Table of Contents

List of Figures

List of Tables

Nomenclature

A	Area	m^2
a	Annular diameter ratio	
C	Coefficient used in correlations	
$C_{1\text{-}4}$	Constant used in correlations	
C_p	Constant-pressure specific heat	J/kg.K
D	Inner diameter	m
D_h	Hydraulic diameter	m
D_o	Outer diameter	m
EB	Energy balance error	
f	Friction factor	
f_{app}	Apparent friction factor	
f_{cr}	Friction factor at Re_{cr}	
f_{qt}	Friction factor at Re_{qt}	
g	Gravitational acceleration	m/s^2
Gr	Grashof number	
Gr^*	Modified Grashof number	
Gz	Graetz number	
h	Heat transfer coefficient	$W/m^2.°C$
I	Current	A
j	Colburn *j*-factor	
j_{cr}	Colburn *j*-factor at Re_{cr}	
j_{qt}	Colburn *j*-factor at Re_{qt}	
k	Thermal conductivity	W/m.K
k_{tube}	Thermal conductivity of tube	W/m.K
L	Length	m
Lh	Hydrodynamic entrance length (Fig. 2.3)	m
Lt	Thermal entrance length	m
M	Measurement or calculated value	
$\dot{m}$	Mass flow rate	kg/s
n	Total	
Nu	Nusselt number	
ΔP	Pressure drop	Pa
Pr	Prandtl number	
Pw	Tube-wall parameter	
Pw^*	Modified tube-wall parameter	
$\dot{Q}_e$	Electrical input rate	W
$\dot{Q}_w$	Water heat transfer rate	W
$\dot{q}$	Heat flux	W/m^2
R	Inner radius	m
r	Radial distance	m
R_{tube}	Thermal resistance	°C/W
Ra	Rayleigh number	
Ra^*	Modified Rayleigh number	
Re	Reynolds number	
Re'	Transitional flow inflection point	
Re_{cr}	Critical Reynolds number	
Re_{qt}	Start of quasi-turbulent flow regime	
Re_t	Start of turbulent flow regime	

ΔRe	Width of transitional flow regime	
Ri	Richardson number	
Ri^*	Modified Richardson number	
T	Temperature	°C or K
t	Tube-wall thickness	m
TG_f	Transition gradient in terms of friction factor results	
TG_j	Transition gradient in terms of Colburn j-factor factor results	
V	Velocity	m/s
V	Voltage	V
x	Distance from inlet	m
z^*	$\pi/(4Gz)$ as in Eq. 2.17	

Greek letters

α	Thermal diffusivity	m^2/s
β	Thermal expansion coefficient	1/K
ε	Surface roughness	m
λ	Annular geometric parameter	
μ	Dynamic viscosity	kg/m.s
ν	Kinematic viscosity	m^2/s
ξ	Turbulent friction factor in Eq. 2.20	
ρ	Density	kg/m^3
σ	Standard deviation	
Υ	Pulsation coefficient	

Superscripts

-	Average

Subscripts

b	Bottom/bulk
c	Cross-section
$cond$	Conduction
$conv$	Convection
cor	Correlation
exp	Experimental
f	Film temperature, $T_f = 0.5(T_b + T_s)$
FC	Forced convection
i	Index/inlet
L	Laminar
m	Mean
o	Outer/outlet
QT	Quasi-turbulent
ref	Reference
s	Surface
SL	Shah and London [1] Nusselt number correlation
T	Turbulent
t	Top
TG	Transition gradient

Abbreviations (also used as italic subscripts)

FC/MC	forced/mixed convection boundary
FCD	forced convection developing region
FCD/MCD	boundary between FCD and MCD regions
FCD/FD	boundary between FCD and FD regions
FD	fully developed region
MCD	mixed convection developing region
MCD/FD	boundary between MCD and FD regions

1. Introduction

1.1. Background

Heat exchangers have a wide range of domestic and industrial applications, especially in the generation and consumption of electrical energy. On the generation side, heat exchangers are indispensable components in the cycles of fossil fuel, nuclear and solar power plants. They are used to transfer heat in boilers from the energy source (fossils, nuclear reaction, solar, etc.) to the fluids (usually steam) used to drive turbines that generate electricity. Downstream of turbines, heat exchangers are used to condense steam and reject heat to the environment. On the consumption side, heat exchangers are again indispensable components and are found in the process, petrochemical, petroleum, transport, sewage treatment, manufacturing and heating, ventilation and air-conditioning industries.

The efficiency of generating energy and using energy directly depends on the effectiveness of heat exchangers. It is therefore critical that sufficient design information is available so that heat exchanger effectiveness can be optimised. In the design process, a selection can be made between a laminar (low heat transfer coefficients and pressure drops) or turbulent (high heat transfer coefficients and pressure drops) flow regime. Because pressure drop is related to pumping power and thus operational running cost, the aim is to obtain high heat transfer coefficients and low pressure drops.

Although pressure drop and heat transfer are usually investigated independently, there exists a direct relationship that is often overlooked [2]. It is desirable to know this relationship, because if it is known then it will be possible to calculate either the heat transfer coefficients or the friction factors when the other variable is available. Furthermore, it will also give additional insight into the trade-off between high heat transfer coefficients and low pressure drops during the design process. Two analogies were developed, based on the similarity between momentum and heat transfer in the boundary layer [3]: the Reynolds number analogy was developed for Prandtl numbers of unity, while the Chilton-Colburn analogy was developed for laminar and turbulent flow over flat plates for Prandtl numbers between 0.6 and 60. The relationship between pressure drop and heat transfer in the laminar and turbulent flow regimes was investigated by Obot and Esen [4] and Allen and Eckert [5], respectively, while Gill [6] proposed correlations for laminar and turbulent flow. Although most heat exchangers operate in the turbulent flow regime, the best compromise between high heat transfer coefficients and low pressure drops might be in the transitional flow regime, between laminar and turbulent flow [7]. Tam *et al*. [8] and Olivier and Meyer [9] investigated pressure drop and heat transfer simultaneously in the transitional flow regime; however, no correlations were developed to quantitatively describe this relationship.

To improve the efficiency of heat exchangers, the heat transfer coefficients can be increased using enhanced tubes, such as finned tubes, twisted tape inserts or helical microfin tubes. As these tubes became more effective, designers decreased the mass flow rate to reduce the pressure drop and thus the pumping power. With time, many of these tubes started operating close to or in the transitional flow regime. Furthermore, corrosion and scaling on the inside of heat exchangers may lead to increased flow resistance and thus decreased mass flow rates, which also cause heat exchangers to

operate in or close to this flow regime. Other factors that might cause transitional flow are design constraints, additional equipment and changes in operating conditions or equipment. In the transitional flow regime, the flow alternates between laminar and turbulent and turbulent eddies occur in flashes, known as turbulent bursts. This might cause the pressure drop to increase by an order of magnitude. Designers are thus usually advised to avoid this flow regime [10], because the flow is believed to be unstable and chaotic, and little design information is available [7].

Flow regimes in tubes have been extensively investigated from as early as 1883, especially focusing on laminar and turbulent flow, while research on the transitional flow regime has been done since the 1990s. As the densities of fluids are dependent on temperature, the addition of heat to the tube wall can lead to mixed convection. This is due to the temperature gradients inside the thermal boundary layer that leads to density differences and buoyancy effects in the presence of gravity [11]. Free convection effects not only increase the heat transfer and pressure drop, but also reduce the thermal entrance length and induce an early transition to turbulent flow [12].

A flow regime map is a valuable tool that can be used to determine whether free convection effects can be neglected (forced convection) or whether it is significant (mixed convection). The first flow regime map for horizontal tubes with a constant surface temperature and constant heat flux boundary condition was developed by Metais and Eckert [13] and Ghajar and Tam [14], respectively. Later, Tam *et al*. [15] developed a unified support vector machine-based flow regime map for horizontal tubes with a constant heat flux boundary condition, which could be used for re-entrant, square-edged and bellmouth inlets. However, because this flow regime map was developed using the experimental data of Ghajar and Tam [16], it was primarily for Rayleigh numbers in the order of 10^6, which was high. The mixed convection boundary in the laminar and transitional flow regimes was developed using experimental data with Prandtl numbers between 23 and 140 (different concentrations of ethylene glycol-water mixtures), which are significantly larger than for water ($Pr \approx 7$). Furthermore, as the Grashof number is proportional to D^3, the relatively large inner diameter of the test section (15.8 mm) led to increased Grashof numbers. This is of significant importance because the Rayleigh number, which was used on the x-axis of their flow regime map, is a product of the Grashof number, which was large due to the large tube diameter, and Prandtl number, which was high because ethylene glycol-water mixtures were used.

For fluid flow in a tube with heat transfer, the thermal entrance length measured from a tube inlet is another very important aspect for design engineers. The reason is that it determines whether the heat transfer coefficients are dependent (developing flow) on or independent (fully developed flow) of axial tube position. When high Prandtl number fluids such as oil are used, the thermal entrance length can become very long, especially at high laminar Reynolds numbers (close to the transitional flow regime). Siegel *et al*. [17] define the thermal entrance length for laminar flow to be the heated length required for the Nusselt number to approach within 5% of the theoretical fully developed value of 4.36, for a constant heat flux boundary condition. To account for mixed convection, Hallman [18] defines the thermal entrance length as the point where the experimental curve of the local Nusselt numbers as a function of axial position crosses, meets or becomes parallel to the constant-property solution given by Siegel *et al*. [17]. However, this definition might lead to inaccurate results because it was found that free convection effects caused the local Nusselt numbers to first decrease near the inlet of the test section, and then increase along the test section until a constant value was reached [19-21].

Cheng and Ou [22] numerically investigated free convection effects in large Prandtl number fluids and found that when the Rayleigh number was greater than 3.75×10^5, the local Nusselt numbers decreased along the tube length and became constant. However, three regions with different heat transfer characteristics were observed from the local Nusselt numbers when the Rayleigh number was less than 3.75×10^5. Although these regions were observed, the boundaries between the three regions and the heat transfer characteristics in each region were not defined qualitatively and quantitatively. What further complicates the local heat transfer characteristics of mixed convection flow is the local laminar-turbulent transition, which occurs along the tube length when the Reynolds number exceeds the critical Reynolds number. Nishi *et al*. [23] give a comprehensive review of the work that has been done on the laminar-turbulent transition along a tube length. Previous studies focused mainly on the effect of inlet disturbances and Reynolds number on the two different flow structures (puffs and slugs), which occur during transition, and not specifically on the effect of free convection on the local heat transfer characteristics.

According to a recent review paper by Meyer [7], the transitional flow regime itself has been mainly investigated by Professor Ghajar from Oklahoma State University and his co-workers [8, 14, 16, 24-30], and by Professor Meyer from the University of Pretoria and his co-workers [9, 31-39]. From literature, it is clear that Ghajar and co-workers broke new ground by investigating the effect of inlet geometries and heating, making it possible for others, such as Meyer and co-workers, to follow. Previous studies focussed on the effects of heating, inlet geometries, enhanced tubes, nanofluids, micro-channels, multiple tubes and annuli.

A comprehensive overview of the available correlations in the transitional flow regime is given by Taler [40]. Hausen proposed the first correlation to predict the overall heat transfer coefficients in the transitional flow regime in 1959. In the 1970s, Gnielinski [41] and Churchill [42] developed correlations for developing and fully developed flow for forced convection conditions [10]. Other heat transfer correlations in the transitional flow regime were also developed by Ghajar and Tam [16], Yu-ting *et al*. [43] and Lu *et al*. [44]. However, the Prandtl number ranges were limited to the test fluids that were used (ethylene glycol-water mixtures [16] and molten salt [43, 44]).

Gnielinski [45] proposed a method to determine the heat transfer coefficients in the transitional flow regime, by applying linear interpolation between laminar flow at a Reynolds number of 2 300 and turbulent flow at a Reynolds number of 4 000. However, the usually cited Reynolds number range of approximately 2 300 to 10 000 is only true for very steady and uniform entry flow with a rounded entrance [10], and is significantly affected by the inlet geometry and free convection effects. Gnielinski [45] mentioned that “no experimental data were found which have allowed checking the Nusselt numbers obtained by the calculation procedure outlined above in the region of linear interpolation, i.e., between $1\,000 < Re < 4\,000$”. The lack of experimental data in the transitional flow regime is most probably the main reason for the limited understanding of and little design information on transitional flow that is available.

Taler [40] recently proposed a heat transfer correlation for transitional and turbulent flow in tubes, which is valid for both a constant surface temperature and constant heat flux boundary condition, and it correlates well with experimental and numerical data [40, 46]. The form of the correlation is such that at a Reynolds number of 2 300 (where transition is assumed to start), the Nusselt number changes depending on the inlet flow condition. Although this correlation accounts for developing flow, this

study shows that the Reynolds number range and heat transfer characteristics in the transitional flow regime are significantly affected by free convection effects. As this correlation is not a function of Grashof number, it is more appropriate for forced convection conditions, rather than mixed convection conditions.

Although the transitional flow regime has been extensively investigated, the Reynolds number boundaries of the transitional flow regime are in general qualitative and rely on visual observations. The result is that the definition of the start and end of the transitional flow regime often rely on subjective decisions (which data points to consider as laminar, transitional or turbulent), which makes it challenging to compare the transitional flow results of different studies. Ghajar and Tam [16] developed correlations to predict the start and end of the transitional flow regime as a function of axial position; however, it did not account for free convection effects. Meyer and Abolarin [37] investigated two methods to determine the boundaries of the transitional flow regime. The first method considered the standard deviation of the temperature measurements. The second method, which was also used by Ndenguma *et al*. [36], used three linear curve fits (on a log-log scale) of the Colburn *j*-factors as a function of Reynolds number, and was more convenient to implement. Although both methods still relied on some subjective decisions, the authors found that reasonable results were obtained when the two methods were used to complement one another.

1.2. Problem statement

Several gaps in the mixed convection literature exist, especially when the flow is still developing. The existing flow regime maps may be very accurate for high Prandtl number fluids, but are only valid for fully developed flow and were developed using high Prandtl number fluids, especially in the laminar flow regime. The result is that when, for example water is used in small diameter tubes, the flow is predicted to be in the forced convection regions, while free convection effects are significant.

In the laminar flow regime, there is not only uncertainty regarding an appropriate correlation for calculating the thermal entrance length, but also regarding the definition of the point of fully developed flow in mixed convection heat transfer. Furthermore, because the laminar heat transfer correlations, which are readily available in heat transfer textbooks, are usually based on analytical solutions to the governing equations, they are restricted to constant fluid properties. The differing behaviour of the local heat transfer characteristics of different Prandtl number fluids when mixed convection effects exist makes it even more challenging to obtain a single correlation. What further complicates the heat transfer characteristics of developing flow is the local transition from laminar to turbulent flow along the tube length above the critical Reynolds number.

The transitional flow regime itself has been extensively investigated. However, no experimental studies have been specifically devoted to the heat transfer characteristics of developing flow, how this flow changes along the tube length, how it differs from that of fully developed flow, and how it is affected by free convection effects. Furthermore, the methods that are used to identify the boundaries of the transitional flow regime rely on subjective decisions and the available correlations do not account for developing flow of low Prandtl number fluids in mixed convection conditions. The lack of experimental data in the transitional flow regime is most probably the main reason for the limited understanding of and little design information on transitional flow that is available.

1.3. Aim

The purpose of this study was to experimentally investigate the heat transfer and pressure drop characteristics of developing and fully developed flow of low Prandtl number fluids in smooth horizontal tubes for forced and mixed convection conditions.

1.4. Objectives

The main objectives of this study were:

- to design, build and commission an experimental set-up that can be used to investigate the heat transfer and pressure drop characteristics of developing and fully developed flow in different test sections;
- to develop flow regime nomenclature and terminology to quantify the boundaries of the different flow regimes mathematically, as well as to define the transition characteristics;
- to evaluate the thermal entrance length correlations for forced convection conditions;
- to develop correlations to determine the thermal entrance length for mixed convection conditions;
- to investigate the effect of free convection on the laminar-turbulent transition along the tube length in the transitional flow regime;
- to develop correlations to predict the local laminar Nusselt numbers of both developing and fully developed flow, which are valid for both high and low Prandtl number fluids;
- to extend the experimental data base with results for developing and fully developed flow for both forced and mixed convection conditions in the transitional flow regime;
- to investigate the influence of axial position, free convection effects and Prandtl number on the heat transfer characteristics of developing flow in the transitional flow regime;
- to develop correlations to predict the average Nusselt number of developing and fully developed flow in the laminar, transitional, quasi-turbulent and turbulent flow regimes;
- to determine the relationship between pressure drop and heat transfer in the laminar, transitional, quasi-turbulent and turbulent flow regimes;
- to use the relationship between pressure drop and heat transfer to develop correlations to predict the friction factors, as a function of Nusselt number, for developing and fully developed flow in the laminar, transitional, quasi-turbulent and turbulent flow regimes;
- to develop flow regime maps for developing and fully developed flow in horizontal tubes with a constant heat flux boundary condition, which are valid for a wide range of tube diameters and Prandtl numbers.

These objectives were met using the results of physical measurements of temperatures, pressure drops and mass flow rates in two smooth horizontal tubes with different tube diameters.

1.5. Original outcomes

The work in this study was published as part of this thesis mainly in four articles. The original contributions of the four articles, with relevant chapters, are as follows:

Chapter 5, Meyer and Everts [47]

- local laminar Nusselt numbers can be divided into three regions (forced convection developing, mixed convection developing and fully developed) instead of two regions (developing and fully developed);

- correlations to predict the thermal entrance length for forced and mixed convective laminar flow;
- correlations to predict the local and average Nusselt numbers of mixed convective developing flow as a function of both Grashof number and modified Grashof number;
- influence of free convection effects on the laminar-turbulent transition along the tube length.

Chapter 6, Everts and Meyer [48]

- flow regime nomenclature (details given in Chapter 3);
- experimental data of developing and fully developed flow in the transitional flow regime;
- the width of the transitional flow regime of developing flow decreased with axial position as the flow developed, as well as with increasing free convection effects (increasing tube diameter and heat flux);
- the width of the transitional flow regime of fully developed flow was independent of axial position, but decreased with increasing free convection effects (increasing tube diameter and heat flux);
- correlations to predict the start and end of the transitional flow regime;
- comparison with experimental results in literature to investigate the influence of Prandtl number.

Chapter 7, Everts and Meyer [49]

- the boundaries of the different flow regimes were the same for pressure drop and heat transfer;
- correlations to predict the friction factors, as a function of Nusselt number, for developing and fully developed flow in the laminar, transitional, quasi-turbulent and turbulent flow regimes;
- correlations to predict the average Nusselt number for developing and fully developed flow in the laminar, transitional, quasi-turbulent and turbulent flow regimes.

Chapter 8, Everts and Meyer [50]

- two flow regime maps for fully developed flow;
- four flow regime maps for developing and fully developed flow;
- forced convection results in the transitional flow regime.

1.6. Scope of work

As the aim of this study was to investigate developing flow in the transitional flow regime, the Reynolds number was varied between approximately 500 and 10 000 to ensure that the transitional and quasi-turbulent flow regimes, as well as sufficient parts of the laminar and turbulent flow regimes, were covered. Two test sections were used, one with an inner diameter and length of 11.5 mm and 9.5 m respectively, and another with an inner diameter and length of 4 mm and 5.5 m respectively. A square-edged inlet was used and the tubes were heated at different constant heat fluxes. The fluid used to conduct the experiments in this study was limited to water, therefore the Prandtl numbers were relatively low (approximately six). A state-of-the-art experimental set-up, which could be used to measure temperatures (up to 128 thermocouples), pressure drops (up to eight tube lengths simultaneously), and a wide range of mass flow rates, for different test sections (up to a length of 10 m) using a constant heat flux boundary condition and different inlet geometries, was designed, built and then commissioned. The test sections were designed, built, validated and tested one after another.

1.7. Overview of thesis

Chapter 2 presents a literature survey of mixed convection heat transfer and pressure drop in the different flow regimes, especially the work on flow in the transitional flow regime done by Professor

Ghajar from Oklahoma State University and his co-workers, and by Professor Meyer from the University of Pretoria and his co-workers. In Chapter 3, details are provided of the experimental set-up, the data reduction method, as well as the results of the uncertainty analysis. Nomenclature and terminology to define the boundaries of the different flow regimes as well as transitional flow characteristics were also developed. Chapter 4 contains the validation of the experimental set-up and data reduction method. Chapter 5 [47] covers the local heat transfer characteristics in the laminar and transitional flow regimes, while Chapter 6 [48] focuses on the heat transfer characteristics of developing and fully developed flow in the transitional flow regime. In Chapter 7 [49], the relationship between heat transfer and pressure drop is investigated, and new flow regime maps for a constant heat flux boundary condition are presented in Chapter 8 [50]. Chapter 9 concludes the thesis and provides some recommendations for further work. Appendix A contains the calibration procedure of the Pt100 probes, thermocouples and pressure transducers, while Appendix B contains the uncertainty analysis of all the relevant parameters.

2. Literature Survey

2.1. Introduction

This chapter summarises fundamentals which are key to many equations and concepts relevant to mixed convection heat transfer and pressure drop. Furthermore, the different flow regimes as well as developing and fully developed flow are briefly discussed. Up to now, the transitional flow regime has mainly been investigated by Professor Afshin Ghajar from Oklahoma State University and Professor Josua Meyer from the University of Pretoria, along with their respective co-workers. Their work will be briefly discussed and compared in order to identify gaps in the literature on transitional flow.

2.2. Non-dimensional parameters

2.2.1. Reynolds number

Reynolds showed as early as 1883 that transition depends on the flow disturbances. Therefore, the surface geometry, surface roughness, flow velocity, surface temperature and type of fluid are all factors which affect the transition from laminar to turbulent flow. Although Stokes identified the ratio of the inertia to viscous forces, the Reynolds number was named after Osborne Reynolds in recognition of his work [7] and can be defined as follows for tube flow [51]:

$$Re = \frac{Inertia\ forces}{Viscous\ forces} = \frac{\rho V D}{\mu} \qquad 2.1$$

When the Reynolds numbers are small (laminar flow), the viscous forces are able to suppress the random fluctuations (due to inertia forces) of the fluid. However, at large Reynolds numbers (turbulent flow), the inertia forces are large compared with the viscous forces. Therefore, the viscous forces are unable to prevent these fluctuations of the fluid.

2.2.2. Friction factor

Pressure drop is an important quantity in the analysis of tube flow, because it is directly related to the power requirements of the system. The friction factor (*f*), also known as the Darcy friction factor, is related to the pressure drop and is named after Henry Darcy [3]:

$$f = \frac{2\Delta P D}{L \rho V^2} \qquad 2.2$$

2.2.3. Nusselt number

When the fluid involves some motion, heat transfer through the fluid layer is by convection, while heat transfer is by conduction when the fluid layer is motionless. The Nusselt number is the ratio of the convection heat transfer to conduction heat transfer, and therefore represents the enhancement of heat transfer through a fluid due to the fluid motion. Hence for pure conduction heat transfer the Nusselt number is one. The Nusselt number is a dimensionless heat transfer coefficient and is named after Wilhelm Nusselt, who made significant contributions to convective heat transfer [52]. The Nusselt number for a circular tube is defined as follows:

$$Nu = \frac{\dot{q}_{conv}}{\dot{q}_{cond}} = \frac{hD}{k} \quad (2.3)$$

2.2.4. Prandtl number

The relative thicknesses and growth of the velocity boundary layer and of the thermal boundary layer are described by the Prandtl number. It is named after Ludwig Prandtl, who introduced the concept of boundary layer in 1904 and made significant contributions to boundary layer theory [52]. The Prandtl number is defined as follows:

$$Pr = \frac{Molecular\ diffusivity\ of\ momentum}{Molecular\ diffusivity\ of\ heat} = \frac{\nu}{\alpha} = \frac{\mu c_p}{k} \quad (2.4)$$

When the Prandtl number is unity, heat and momentum dissipate through the fluid at the same rate, and thus the thicknesses of the thermal and velocity boundary layers are the same. The Prandtl number of liquid metals is very small (*Pr* « 1), which indicates that heat diffuses very quickly and the thermal boundary layer is greater than the velocity boundary layer. On the other hand, the Prandtl number of oils is very large (*Pr* » 1) and therefore heat dissipates very slowly relative to momentum.

2.2.5. Grashof and Rayleigh numbers

Free convection effects can be quantified with the Grashof number, named after Franz Grashof, which represents the ratio of the buoyancy forces to the viscous forces [53]:

$$Gr = \frac{Buoyancy\ force}{Viscous\ force} = \frac{g\beta(T_s - T_b)D^3}{\nu^2} \quad (2.5)$$

Because the temperature difference is not always known for constant heat flux applications, while the heat flux is, the modified Grashof number, which is in effect the product of the Grashof number and Nusselt number, can also be used:

$$Gr^* = GrNu = \frac{g\beta\dot{q}D^4}{\nu^2 k} \quad (2.6)$$

When heat is applied to a tube, free convection effects often become significant and the flow is then dominated by mixed convection rather than forced convection. The Rayleigh numbers can be plotted on a flow regime map (Section 2.10) and used as a guideline to determine whether the flow in a tube is dominated by forced convection or mixed convection. This is a valuable tool because it is used to determine whether or not free convection effects can be neglected during design calculations. The Rayleigh number is the product of the Grashof number and Prandtl number [53]:

$$Ra = GrPr \quad (2.7)$$

$$Ra^* = Gr^*Pr \quad (2.8)$$

2.2.6. Richardson number

The Richardson number gives an indication of the relative magnitudes of free convection and forced convection effects [54]:

$$Ri = \frac{Buoyancy\ forces}{Inertia\ forces} = \frac{g\beta(T_s - T_b)D}{V^2} = \frac{Gr}{Re^2} \quad (2.9)$$

This ratio was obtained by considering the boundary layer equations describing uniform upward flow over a vertical flat heat plate. As a general guideline, the flow can be expected to be dominated by forced convection for $Ri \ll 1$ and by free convection for $Ri \gg 1$. When the Richardson number is approximately one, both free and forced convection effects are significant and the flow is expected to be in the mixed convection flow regime [3, 52-55].

2.2.7. Graetz number

The Graetz number, named after the German phycisist Leo Graetz, can be used as a guideline to determine whether laminar flow is fully developed and is defined as follows [3]:

$$Gz = RePr\frac{D}{x} \tag{2.10}$$

It represents the ratio of the time taken by heat to diffuse radially into the fluid by conduction to the time taken by the fluid to reach an axial distance *x* from the tube inlet. When the inverse of the Graetz number is greater than 0.05, the local Nusselt numbers for both a constant heat flux boundary condition and a constant surface temperature boundary condition become constant. The flow can then be assumed to be fully developed [55]. However, it will be shown in Section 5.3.2 that a value of 0.12 is more appropriate for simultaneously hydrodynamically and thermally developing flow.

2.3. Thermal entrance length

When a fluid at a uniform temperature enters a tube with a different surface temperature (for example, a tube heated at a constant heat flux), the fluid particles adjacent to the surface assume the surface temperature. The result is that the temperature of the fluid near the surface is different from the fluid near the centre-line of the tube. This temperature difference inside the fluid leads to convection heat transfer in the radial direction, as well as the development of a thermal boundary layer. The thickness of the thermal boundary layer increases along the tube length, and once the thermal boundary layers meet in the centre of the tube, the flow is thermally fully developed.

For fluid flow in a tube with heat transfer, the thermal entrance length measured from a tube inlet is a very important aspect for design engineers. This is because it determines whether the heat transfer coefficients are dependent (developing flow) on or independent (fully developed flow) of axial tube position. When high Prandtl number fluids such as oil are used, the thermal entrance length can become very long, especially at high laminar Reynolds numbers (close to the transitional flow regime). For forced convection laminar flow, the thermal entrance length is a function of Reynolds number, Prandtl number and tube diameter. According to authoritative heat transfer textbooks [1, 3, 56-58], the theoretical thermal entrance length for laminar flow can be determined as:

$$Lt_{FC} = CRePrD \tag{2.11}$$

where $C = 0.05$

and for turbulent flow as:

$$Lt = 10D \tag{2.12}$$

However, in literature, very little experimental data with low uncertainties that convincingly quantify the value of *C* as being accurate are available. As will be shown in Section 4.2, it could be because it is very challenging to conduct forced convection experiments in tubes where the flow is completely fully developed and the Nusselt number is 4.36.

Siegel *et al*. [17] defined the thermal entrance length for laminar flow to be the heated length required for the Nusselt number to approach within 5% of the theoretical fully developed value of 4.36 for a constant heat flux boundary condition. A series expansion whose form is similar to the Graetz problem [59] (for a uniform wall temperature) was used, and the coefficient was determined to be 0.0425. However, according to Lienhard and Lienhard [60], the coefficients can vary between 0.028 and 0.053, depending on the Prandtl number and wall boundary condition, when the hydrodynamic and thermal boundary layers develop simultaneously. Similar observations were made by Durst *et al*. [6] in a review paper on hydrodynamic entrance lengths. It was found that the coefficient varied between 0.03 and 0.062 for experimental investigations, while numerical and analytical investigations yielded coefficients between 0.025 and 0.08.

To account for mixed convection, Hallman [18] defined the thermal entrance length as the point where the experimental curve of the local Nusselt numbers as a function of axial position crosses, meets or becomes parallel to the constant-property solution given by Siegel *et al*. [17]. However, this definition might lead to inaccurate results because McComas and Eckert [19], who conducted experiments using air, found that at high Grashof numbers and low Reynolds numbers, the local Nusselt numbers did not continue to decrease until it became fully developed. Free convection effects caused the local Nusselt numbers to decrease near the inlet of the test section and then increase before they became constant.

From the results of Shannon and Depew [20], who conducted experiments using water, it seemed as if free convection effects increased the thermal entrance length. However, Bergles and Simonds [61] reported from the work of Petukhov and Polyakov [62] that the entrance length decreased when free convection effects were significant. Hong *et al*. [63] investigated laminar flow analytically and experimentally and found that at a modified Rayleigh number of 10^6, the fully developed Nusselt number, Nu, was approximately 300% greater than the constant-property prediction (Nu = 4.36), while the thermal entrance length was only one tenth of the constant-property prediction ($1/Gz$ = 0.05). Therefore, although extensive research has been done on the thermal entrance length in the laminar flow regime, some gaps in the mixed convection literature remain. There is not only uncertainty regarding the correlation for calculating the thermal entrance length, but also the definition of the point of fully developed flow in mixed convection heat transfer.

2.4. Fully developed flow

The region after the thermal entrance region is the thermally fully developed flow region and the dimensionless temperature profile $(T_s - T)/(T_s - T_m)$ remains constant. Water is used as the test fluid in this study and because the Prandtl number of water is greater than one, the thermal entrance length is greater than the hydrodynamic entrance length. Once the flow is thermally fully developed, it will be hydrodynamically fully developed as well and therefore it can be said that the flow is fully developed.

In the fully developed region, the dimensionless temperature profile $(T_s - T)/(T_s - T_m)$ is independent of x and the derivative of $(T_s - T)/(T_s - T_m)$ with respect to x is zero. The derivative of $(T_s - T)/(T_s - T_m)$ with respect to r should also be independent of x, because the dimensionless temperature profile remains constant in the fully developed region. This can be mathematically expressed as follows [3]:

$$\frac{\partial}{\partial r}\left(\frac{T_s - T}{T_s - T_m}\right)\Big|_{r=R} = \frac{-(\partial T/\partial r)|_{r=R}}{T_s - T_m} \neq f(x) \qquad 2.13$$

The heat flux to the tube surface can be expressed as follows [3]:

$$\dot{q} = h(x)(T_s - T_m) = k\left.\frac{\partial T}{\partial r}\right|_{r=R} \rightarrow h(x) = \frac{k(\partial T/\partial r)|_{r=R}}{T_s - T_m} \quad 2.14$$

Eq. 2.13 indicates that the local heat transfer coefficient (Eq. 2.14) remains constant (independent of *x*) when the flow is fully developed and the fluid properties (thermal conductivity) remain constant. However, it is important to note that although the dimensionless temperature profile is independent of *x* in the fully developed region, the temperature profile is not. Therefore, the temperature profile may vary along the tube length, which is usually the case.

When a constant heat flux boundary condition is applied, the fluid temperature increases along the tube length, thus the thermal conductivity increases as well. Therefore, from Eq. 2.14, it follows that the heat transfer coefficient will also increase, assuming that the surface-fluid temperature difference remains constant. The small effect of variable thermal conductivity along the tube length can be eliminated by expressing the heat transfer coefficients in terms of the Nusselt number:

$$Nu = \frac{hD}{k} = \frac{D(\partial T/\partial r)|_{r=R}}{T_s - T_m} \quad 2.15$$

From Eq. 2.15, it follows that once the flow is fully developed, the Nusselt number should be constant because the tube radius and temperature difference along the tube length will be constant.

2.5. Flow regimes

Flow inside tubes are traditionally divided into the laminar, transitional and turbulent flow regimes. These three regimes are briefly discussed in Sections 2.5.1 to 2.5.3. The correlations that were used to validate the experimental set-up and data reduction method in Chapter 4 are given in Table 2.1 to Table 2.4.

2.5.1. Laminar flow

Osborne Reynolds investigated laminar flow in 1883 by injecting dye into the flow in a glass tube. Reynolds concluded that the dye streak formed a straight line when the velocities were sufficiently low [64]. Free convection effects play a significant role in the laminar flow regime and it is therefore important to distinguish between free, forced and mixed convection. Free convection occurs when the fluid motion is not created by an external source, but by buoyancy forces, which are caused by the difference in temperature (and thus density) inside the fluid. As indicated in Fig. 2.1, the fluid near the surface of the tube has a higher temperature and lower density and circulates in an upward direction (opposite direction to gravity), while the fluid near the centre-line of the tube has a lower temperature and higher density and therefore circulates downwards. These counter-rotating vortices, also known as free convection effects and secondary flow, are superimposed on the stream-wise main flow and increase the forced convection heat transfer significantly [10]. Tam and Ghajar [10] found that free convection effects increased the laminar Nusselt numbers to approximately 14.5, which is more than 300% greater than the theoretical fully developed forced convection Nusselt number of 4.36 for a constant heat flux boundary condition. On the other hand, forced convection exists when, for example, the fluid motion is forced through a heated or cooled tube by means of a pump. However, the inertia and viscous forces should be significantly higher than the buoyancy forces.

Fig. 2.1: Schematic representation of the counter-rotating vortices caused by free convection effects.

The flow is dominated by mixed convection when a pump is used to create the fluid motion, but free convection effects remain significant. When the flow is dominated by mixed convection, the heat transfer coefficients are not only dependent on the Reynolds and Prandtl numbers, but also on the Grashof number to account for the density variation inside the tube [16]. The state-of-the-art of mixed convection in tubes has been reviewed in book chapters by Aung [65] and Raithby and Hollands [66], as well as in three review articles by Jackson *et al*. [67], Orfi *et al*. [68] and Maré *et al*. [69]. These literature sources show that laminar heat transfer in horizontal circular tubes with a constant heat flux boundary condition has been extensively investigated, especially between the 1950s and 1990s. As the densities of fluids are dependent on temperature, the addition of heat to the tube wall leads to mixed convection, due to the temperature gradients inside the thermal boundary layer, which lead to density differences and buoyancy effects in the presence of gravity [11]. Although much attention has been paid to mixed convection laminar flow, especially when the flow is fully developed, the differing behaviour of the local heat transfer characteristics of different Prandtl number fluids has made it challenging to obtain a single correlation [22].

McComas and Eckert [19], who conducted experiments using air, found that at high Grashof numbers and low Reynolds numbers, free convection effects caused the local Nusselt numbers to first decrease near the inlet of the test section (similar to forced convection flow), and then increase along the test section before a constant value is reached. Similar results were obtained by Shannon and Depew [20] and Barozzi *et al*. [21], who conducted experiments using water. Hong *et al*. [63] investigated laminar flow analytically and experimentally and found that, although free convection effects were significant, the local Nusselt numbers decreased and became constant, and did not increase as was found in other mixed convection studies conducted at high Grashof numbers.

Cheng and Ou [22] numerically investigated free convection effects in large Prandtl number fluids. Similar to the results obtained by Hong *et al*. [63], it was found that when the Rayleigh number was greater than 3.75×10^5, the local Nusselt numbers decreased along the tube length and became constant. However, three regions with different heat transfer mechanisms were observed from the local Nusselt numbers when the Rayleigh number was less than 3.75×10^5. Region 1 was named the Leveque solution region and the local Nusselt numbers decreased with axial position due to the entrance effect. In this region, the convective terms due to free convection were negligible compared with the axial convective term. A minimum Nusselt number was reached once the free convection and entrance effects were balanced. Free convection effects were significant in the intermediate region (Region 2), and caused the local Nusselt numbers to increase along the tube length. The free

convection effects dominated the entrance effects up to a point where the local Nusselt numbers reached a maximum. The local Nusselt numbers then decreased until an asymptotic value was reached in Region 3. Although these three regions were observed by Cheng and Ou [22], the boundaries between the three regions and the heat transfer characteristics in each region were not defined qualitatively and quantitatively (this was done in Section 5.3.3).

2.5.1.1. Laminar flow correlations

Although laminar heat transfer correlations are readily available in heat transfer textbooks, these equations and graphs are usually based on analytical solutions to the governing equations for laminar flow. Therefore, they are restricted to constant fluid properties, while this assumption is not valid in actual practice [61]. Table 2.1 and Table 2.2 contain the correlations that were used to validate the laminar Nusselt numbers and friction factors in Chapter 4. It should be noted that the correlation of Shah and London [1] was adapted from the correlation of Churchill and Ozoe [70].

Table 2.1: Laminar Nusselt number correlations.

Morcos and Bergles [71]

$$Nu = \left\{4.36^2 + \left[0.145\left(\frac{Gr_f^* Pr_f^{1.35}}{Pw_f^{*0.25}}\right)^{0.265}\right]^2\right\}^{1/2} \quad (2.16)$$

$$Pw^* = \frac{Pw}{Nu} = \frac{kD}{k_{tube}t}$$

$3\times10^4 \leq Ra \leq 10^6$; $4 \leq Pr \leq 175$; $2 \leq Pw \leq 66$

Percentage deviation: not specified

Fully developed flow

Shah and London [1]

$$Nu_{SL} = Nu_1 \times Nu_2 - 1 \quad (2.17)$$

where

$$Nu_1 = \left[1 + \left(\frac{\pi/(115.2\ z^*)}{\{1 + (Pr/0.0207)^{2/3}\}^{1/2}\ \{1 + (220\ z^*/\pi)^{-10/9}\}^{3/5}}\right)^{5/3}\right]^{3/10}$$

$$Nu_2 = 5.364\left[1 + (220\ z^*/\pi)^{-10/9}\right]^{3/10}$$

$$z^* = \frac{\pi}{4Gz}$$

Percentage deviation: not specified

Developing and fully developed flow

Table 2.2: Laminar friction factor correlations.

Classical relation by Poiseuille [3]

$$f = \frac{64}{Re} \quad (2.18)$$

$Re \leq 2\,100$

Fully developed flow

Tam *et al.* [8]

$$f_{app} = \frac{4}{Re}\left(16 + \frac{0.00314}{0.00004836 + 0.0609\left(\frac{x/D}{Re}\right)^{1.28}}\right) \quad (2.19)$$

$799 \leq Re \leq 2\,240$; $3 \leq x/D \leq 200$

Percentage deviation: -26.1% to +28.1%

Developing flow

2.5.2. Turbulent flow

Osborne Reynolds also investigated turbulent flow with his dye experiments and found that when the velocity of the fluid was high, the fluid motion was highly unstructured. Random and rapid zigzag formations were observed, which indicated the velocity fluctuations inside the tube [51]. The heat transfer coefficients in the turbulent flow regime are insensitive to different types of boundary conditions and the inertia of the fluid suppresses free convection effects inside the tube. It is therefore not necessary to distinguish between forced and mixed convection, or between a constant heat flux and constant surface temperature boundary condition. Furthermore, the heat transfer coefficients are high in this flow regime due to the rapid mixing of the fluid particles inside the tube.

2.5.2.1. Turbulent flow correlations

Table 2.3 contains some of the available correlations which were used to validate the turbulent Nusselt numbers in Chapter 4.

Table 2.3: Turbulent Nusselt number correlations.

Gnielinski [41] $$Nu = \frac{(\xi/8)(Re-1000)Pr}{1+12.7\sqrt{(\xi/8)}(Pr^{2/3}-1)}\left[1+\left(\frac{D}{L}\right)^{2/3}\right]\left(\frac{Pr}{Pr_s}\right)^{0.11}$$ $\xi = (1.8\log_{10} Re - 1.5)^{-2}$ [72] $3\times10^3 \leq Re \leq 5\times10^6$; $0.5 \leq Pr \leq 2\,000$ Percentage deviation: not specified	2.20
Ghajar and Tam [16] $$Nu = 0.023\, Re^{0.8}\, Pr^{0.385}\, (x/D)^{-0.0054}(\mu/\mu_s)^{0.14}$$ $3 \leq x/D \leq 192$; $7\,000 \leq Re \leq 49\,000$; $4 \leq Pr \leq 34$; $1.1 \leq \mu/\mu_s \leq 1.7$ Percentage deviation: -10.3% to +10.5%	2.21

Table 2.4 contains the correlations of Blasius [51] and Fang *et al*. [73], which were used to validate the isothermal turbulent friction factors in Chapter 7. Allen and Eckert [5] introduced the viscosity correction term to account for the effect of heating, which was used for the diabatic friction factors in Chapter 7.

Table 2.4: Turbulent friction factor correlations.

Blasius [51] $$f = 0.316Re^{-0.25}$$ $3\,000 \leq Re \leq 100\,000$ Percentage deviation: not specified	2.22
Fang *et al*. [73] $$f = 0.25\left[\log\left(\frac{150.39}{Re^{0.98865}} - \frac{152.66}{Re}\right)\right]^{-2}$$ $3\,000 \leq Re \leq 10^8$ Percentage deviation: 0.045% compared with the Colebrook equation [74]	2.23
Allen and Eckert [5] $$f = 0.316Re^{-0.25}\left(\frac{\mu_b}{\mu_s}\right)^{-0.25}$$ $13\times10^3 \leq Re \leq 1.1\times10^5$; $7 \leq Pr \leq 8$ Percentage deviation: not specified	2.24

2.5.3. Transitional flow

According to a recent review paper by Meyer [7], the transitional flow regime has mainly been investigated by Professor Afshin Ghajar from Oklahoma State University and his co-workers, as well as by Professor Josua Meyer from the University of Pretoria and his co-workers. Their contributions are summarised in Sections 2.6 and 2.7, while Section 2.8 briefly covers the laminar-turbulent transition along the tube length.

Although the transitional flow regime has been extensively investigated, the Reynolds number boundaries of the transitional flow regime are in general qualitative and rely on visual observations. The result is that the definition of the start and end of the transitional flow regime often rely on subjective decisions (which data points to consider as laminar, transitional or turbulent), which makes it challenging to compare the transitional flow results of different studies. From the results of this study, as well as those of Everts [75], it follows that the transitional flow regime can be divided into two flow regimes. Therefore, four distinct flow regimes exist: laminar, transitional, quasi-turbulent and turbulent. The upper part of the transitional flow regime (between Re_{qt} and Re_t in Fig. 2.2) has been referred to as the low-Reynolds-number-end regime [76-78]. However, due to the characteristics of this flow regime, it is proposed (based on a comment from a reviewer [47]) in Section 3.8 that it should be named the quasi-turbulent flow regime. Although there is no significant difference between the standard deviation of the temperature fluctuations in the quasi-turbulent and turbulent flow regimes [37], an extension of the straight line (on a log-log scale) of the turbulent Nusselt numbers as a function of Reynolds number overpredicts the Nusselt numbers in the quasi-turbulent flow regime. Therefore, the flow characteristics are similar to turbulent flow, but the flow is not fully turbulent yet.

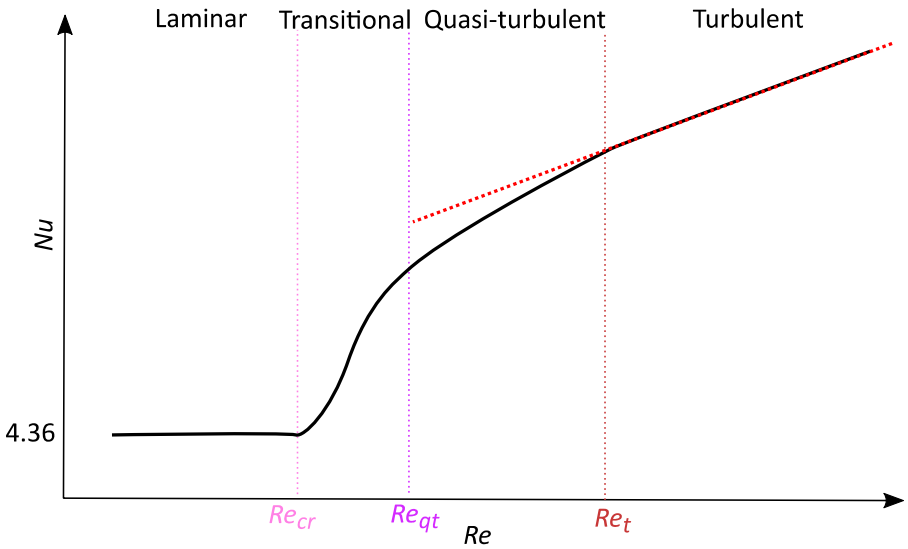

Fig. 2.2: Schematic representation of the different flow regimes in terms of the Nusselt number as a function of Reynolds number.

Ghajar and Tam [16] considered the start of the transitional flow regime as the location where the gradient of the Colburn *j*-factor lines (plotted as a function of Reynolds number) became zero, as it changed from negative to positive. The end of transition was considered as the location where the Colburn *j*-factor lines became parallel to the Colburn *j*-factors predicted by the fully developed turbulent correlations. Although correlations were developed to predict the start and end of the transitional flow regime, they did not account for free convection effects.

Meyer and Abolarin [37] investigated two methods to determine the boundaries of the transitional flow regime. The first method considered the standard deviation of the temperature measurements. It was found that the standard deviation in the laminar and turbulent flow regimes was approximately 0.1 °C, while it increased to 0.2 °C in the transitional flow regime. The second method, which was also used by Ndenguma *et al*. [36], used three linear curve fits (on a log-log scale) of the Colburn *j*-factors as a function of Reynolds number, and was more convenient to implement than the standard deviation method. The Reynolds numbers at the intersection of the lines through the laminar and transitional data, and the transitional and turbulent data, were identified as the start and end of the transitional flow regime respectively. Although these methods still relied on some subjective decisions, the authors found that reasonable results were obtained when the two methods were used to complement one another.

2.5.3.1. Transitional flow correlations

Extensive research has been done in the laminar and turbulent flow regimes and several correlations exist to calculate the heat transfer coefficients and friction factors in these two regimes. However, the transitional and quasi-turbulent flow regimes have not yet been properly understood and the available correlations to predict the heat transfer coefficients and friction factors in these regimes are still very limited [7]. Furthermore, some correlations for heat transfer and pressure drop in the transitional flow regime include the quasi-turbulent flow regime as well, because no clear distinction was made between these two regimes. As mentioned by Tam and Ghajar [10], an understanding of the factors that influence the start and end of the transitional flow regime, as well as an understanding of the heat transfer behaviour in this regime, is required in order to select or develop appropriate heat transfer correlations for transitional flow.

Taler [40] gives a comprehensive overview of the available correlations in the transitional flow regime. The first correlation to predict the overall heat transfer coefficients in the transitional flow regime was proposed by Hausen in 1959; however, many other studies found that their experimental heat transfer data in the transitional flow regime deviated from this equation [79]. Both Gnielinski [41] and Churchill [42] developed correlations for developing and fully developed flow in the transitional flow regime, using different approaches. Gnielinski [41] based his correlation on experimental data of which the majority was for Reynolds numbers greater than 8 000. The result was that the correlation was better suited for turbulent flow. Churchill [42] developed a single correlation for all flow regimes (laminar, transitional and turbulent) by making use of the method proposed by Churchill and Usagi [80]. Because the main purpose was to develop a single correlation for all flow regimes, rather than to develop a precise correlation for transitional flow only, Churchill advised that the coefficients and exponents should be modified when measurements with improved accuracy were available. Tam and Ghajar [10] concluded that both Gnielinski's and Churchill's correlations failed to accurately predict mixed convection data, because they did not deal with the effects of free convection superimposed on the main flow. Furthermore, although Gnielinski's correlations could predict the forced convection Nusselt numbers of different inlets, Churchill's correlation seemed to be restricted to a bellmouth inlet.

Ghajar and Tam [16] developed correlations for developing and fully developed flow for forced and mixed convection conditions for three different inlet geometries. These correlations were developed using experimental data that were obtained using ethylene glycol-water mixtures (Prandtl numbers up to 160) in the laminar and transitional flow regimes, and water in the turbulent flow regime.

Furthermore, a relatively large tube diameter (15.8 mm) was used. This is of significant importance because the fluid properties and tube diameter have a significant influence on the heat transfer characteristics in the laminar and transitional flow regimes, as will be shown in Chapter 6. Yu-ting *et al*. [43] and Lu *et al*. [44] also developed correlations for transitional flow. However, as these correlations were developed for molten salt, the Reynolds number range was between 4 000 and 10 000, while the Prandtl number ranges were 15-18.4 and 4.8-10 respectively.

Gnielinski [45] proposed a method to determine the heat transfer coefficients in the transitional flow regime, by applying linear interpolation between laminar flow at a Reynolds number of 2 300 and turbulent flow at a Reynolds number of 4 000. Although this method was tested using the numerical data of Abraham *et al*. [76], Gnielinski [45] mentioned that "no experimental data were found which have allowed checking the Nusselt numbers obtained by the calculation procedure outlined above in the region of linear interpolation, i.e., between 1 000 < *Re* < 4 000". The lack of experimental data in the transitional flow regime is most probably the main reason for the limited understanding of and little design information on transitional flow that is available. To compile an experimental database for heat transfer in the transitional flow regime using high Prandtl number fluids (7 < *Pr* < 41), as well as to compare it with the proposed correlation of Gnielinski [45], Bertsche *et al*. [79] investigated transitional flow using a constant surface temperature boundary condition. The average heat transfer coefficients along the tube length in the transitional flow regime correlated well with the correlation of Gnielinski [45], and 71.2% of the data were predicted within 15%. However, it should be noted that a limitation of Gnielinski's approach is that the laminar Nusselt number correlation is for developing forced convection flow, and therefore produces a Nusselt number of 4.36 for fully developed flow. In most cases, this will not be correct, as it is shown in Section 4.2 that laminar flow is normally dominated by mixed convection, especially when low Prandtl number fluids, such as water, are used.

Taler [40] proposed a new heat transfer correlation for transitional and turbulent flow in tubes. The correlation is valid for both a constant surface temperature and a constant heat flux boundary condition, and correlates well with experimental data and numerical data [40, 46]. The form of the correlation is such that at a Reynolds number of 2 300 (where transition is assumed to start), the Nusselt number should change continuously depending on the inlet flow condition and boundary condition. However, the usually cited transitional flow Reynolds number range of approximately 2 300 to 10 000 is only true for very steady and uniform entry flow with a rounded entrance, and is significantly affected when the inlet geometry is changed [10]. Furthermore, as will be shown in this study, free convection effects also significantly affect the start and end of the transitional flow regime, as well as the heat transfer characteristics in this flow regime. The correlation of Taler [40] is thus better suited for forced convection transitional flow.

Therefore, although several heat transfer correlations for transitional flow exist, these correlations are restricted to forced convection conditions, specific inlet geometries or high Prandtl number fluids.

2.6. Transitional flow: Work of Ghajar and co-workers

Professor Afshin Ghajar from Oklahoma State University and his co-workers used local temperature and pressure drop measurements along a tube length to investigate the effect of different inlet geometries and heating on the heat transfer coefficients and friction factors [8, 14, 16, 24-30]. Although temperature measurements were taken at 31 stations along the test section, their investigations mainly focused on the fully developed flow results at x/D = 192 (station 22). Constant

heat flux boundary conditions and different ethylene glycol-water mixtures were used, which resulted in high Prandtl numbers (up to 160). Furthermore, due to the combined effects of the relatively large tube diameter (15.8 mm) and high Prandtl numbers, the product of the Grashof and Prandtl numbers were high and in the order of 10^5 to 10^6 [14]. This is of significant importance because this product was not only used in their flow regime map (to determine whether the flow was dominated by forced or mixed convection) [14], but also in their correlations to predict the Nusselt numbers in the laminar and transitional flow regimes [16].

2.6.1. Inlet geometry

Four different inlet geometries were typically used in previous investigations and these are shown schematically in Fig. 2.3. The different inlet geometries are connected to a flow-calming section, which represents different types of inlet distributors. These inlet geometries can be grouped into two categories. In the first category (Fig. 2.3(a) and (b)), an abrupt geometry change occurs between the inlet section and the test section, therefore an additional disturbance is generated as the flow enters the tube. In the second category (Fig. 2.3(c) and (d)), the diameter changes gradually from the inlet section to the test section and no additional turbulence is created at the tube inlet.

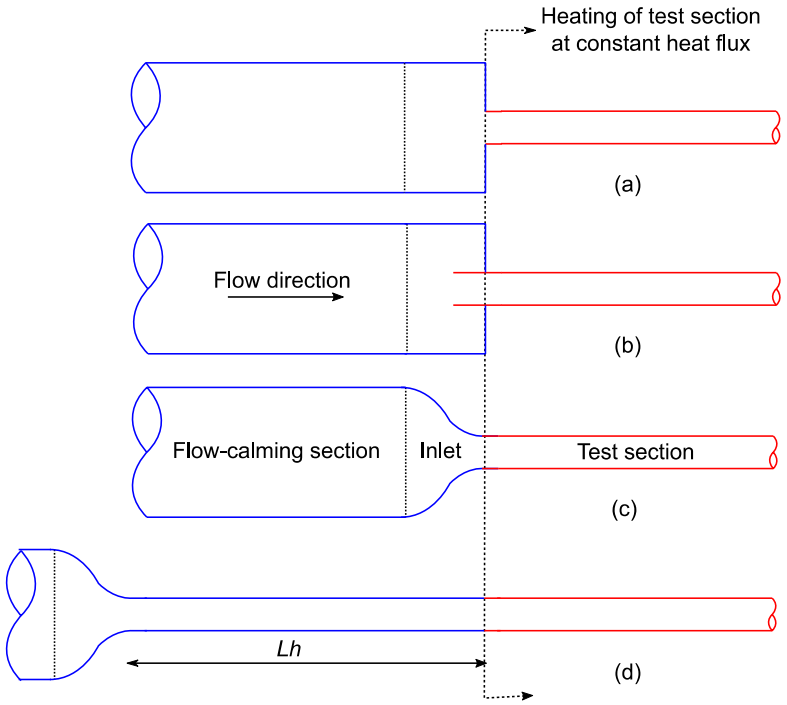

Fig. 2.3: Schematic representation of the different inlet geometries: (a) re-entrant, (b) square-edged, (c) bellmouth and (d) hydrodynamically fully developed. Heating occurs in the red part and blue indicates the unheated part.

The first three inlet geometries were investigated by Ghajar and his co-workers [8, 14, 16, 24-30] and the fourth by Meyer and Olivier [9, 31, 32]:

- Square-edged (Fig. 2.3(a))
  This type of inlet is characterised by a sudden contraction and the inlet of the test section is flush with the inlet section.
- Re-entrant (Fig. 2.3(b))
  This inlet simulates a floating header in a shell-and-tube heat exchanger and contains a square-edged inlet with the test section installed one diameter into the inlet section.

- Bellmouth (Fig. 2.3(c))
  This inlet contains a smooth and gradual contraction. Although the practical application is not common, it is expected to help in the reduction of fouling and to avoid eddies that cause erosion near the tube inlet.
- Hydrodynamically fully developed (Fig. 2.3(d))
  The diameter of this inlet section is the same as that of the test section. This inlet is used to obtain a fully developed velocity profile, because the velocity profiles of the other three inlets are developing.

2.6.1.1. Heat transfer coefficients

Ghajar and Tam [16] investigated laminar, transitional and turbulent flow using different inlet geometries. They found that the inlet that caused the greatest disturbance (re-entrant) led to an earlier transition, while for the bellmouth inlet, which caused the least disturbance, transition only started at Reynolds numbers greater than 3 800. Furthermore, the Reynolds numbers at which transition started (Re_{cr} in Fig. 2.2) increased by 3.4% along the tube length, while the Reynolds numbers at which transition ended (Re_t in Fig. 2.2) increased by as much as 11%. Therefore, although the flow was fully developed, the Reynolds number range in which transition occurred increased along the tube length. However, it was found in this study that the width of the transitional flow regime (ΔRe as defined in Eq. 3.31) decreased along the tube length when the flow was developing and became constant once the flow was fully developed. Ghajar and Tam [14] concluded that the Reynolds numbers at which transition started and ended varied linearly along the entire tube length because the increase in the transition limits was solely due to the variation of the fluid properties along the tube length. The surface and fluid temperatures increased along the length of the tube, thus the viscosity decreased and the Reynolds number increased.

Tam and Ghajar [27] investigated the effect of different inlet geometries on the local heat transfer coefficients, and paid special attention to the bellmouth inlet because the behaviour of this inlet was unusual. The re-entrant and square-edged inlets had no significant influence on the local heat transfer coefficients in the laminar and turbulent flow regimes, and the heat transfer coefficients decreased asymptotically along the tube length as the fluid approached fully developed flow. The same trend was observed with the bellmouth inlet in the laminar flow regime. However, in the turbulent flow regime, the local heat transfer coefficients experienced a significant dip after the inlet, before it started to behave similar to the other inlets. When a bellmouth inlet was used, the boundary layer was first laminar when the flow entered the test section, then went through a transition region to turbulent. This change in boundary layer did not occur in the other two inlets because the inlet disturbances led to a turbulent boundary layer at the inlet of the test section. It was also found that the length of the dip in the local heat transfer coefficients of the bellmouth inlet decreased with increasing Reynolds number, from approximately 140 diameters in the transitional flow regime to 25 diameters in the turbulent flow regime.

The behaviour of the re-entrant and square-edged inlets was similar in the transitional flow regime. The local heat transfer coefficients reached a minimum at approximately x/D = 25 and then increased linearly along the tube length. Newton's law of cooling was used to explain this increasing Nusselt number trend [27]. Once the fluid was fully developed, the surface and fluid temperatures increased linearly along the tube length. However, the authors explained that the rate of increase in the fluid temperature was larger than the rate of increase in the surface temperature. This caused the surface-

fluid temperature difference to decrease along the tube length and the heat transfer coefficients to increase. This reason needs to be investigated as fully developed flow will imply that the surface-fluid temperature difference is constant (Section 2.4). It is also not clear why the rate of heat transfer to the surface and the rate of heat transfer to the fluid are not the same when the flow is fully developed. A possible reason for the increasing heat transfer coefficients along the tube length could rather be the laminar-turbulent transition that occurs along the tube length when the Reynolds number exceeds the critical Reynolds number. This is investigated in Section 5.5.

Tam and Ghajar [27] also investigated the effect of an inlet disturbance on the bellmouth inlet by using three different mesh screens in the flow-calming section just before the bellmouth inlet. They concluded that the Reynolds number at which this unusual behaviour began depended on the inlet disturbance. When the inlet turbulence level was high (coarsest screen), transition occurred at a Reynolds number of 3 470 and when the inlet turbulence level was decreased (finest screen), transition was delayed to 9 640. Furthermore, the axial position at which the boundary layer became unstable and began to change from laminar to turbulent decreased as the Reynolds number was increased. For all three mesh screens, the maximum length of the dip was approximately 175 diameters at the start of the transitional flow regime and decreased to approximately 100 diameters at the end of the transitional flow regime.

2.6.1.2. Friction factors

The effect of different inlet geometries on the fully developed friction factors in the transitional flow regime was investigated in several studies [8, 25, 26] and similar to the heat transfer results, transition was delayed for smoother inlet geometries. Therefore, the Reynolds number range in which transition occurs can be manipulated by changing the inlet geometry.

Ghajar and Madon [25] and Tam *et al.* [8] investigated the effect of inlet geometries on isothermal friction factors for developing and fully developed flow and they developed terminology for developing flow friction factors. The apparent friction refers to the skin friction coefficient in the entrance region of the tube. Therefore, it includes the pressure drop due to the momentum flux during the development of the velocity profile, as well as the shear stresses at the wall. As the skin friction coefficient considers only the pressure drop due to the shear stresses at the tube wall, the local apparent friction factor is greater than the local skin friction coefficient in the entrance region, but equal to the local skin friction coefficient in the fully developed region.

To investigate the laminar apparent friction factors, the same approach as that of Langhaar [81] was used. The apparent friction factor was multiplied by the Reynolds number ($f_{app}Re$) and plotted as a function of the Reynolds number divided by the dimensionless axial position of the pressure taps, $Re/(x/D)$. Ghajar and Madon [25] found that when the Reynolds number was less than 1 500, $f_{app}Re$ was a function of both $Re/(x/D)$ and Reynolds number. However, as the Reynolds number was increased further, $f_{app}Re$ formed an asymptotic curve that was a function of $Re/(x/D)$ only. It was also found that the required tube length for the friction factor to become constant decreased with increasing Reynolds number, but became independent of Reynolds number for Reynolds numbers greater than 1 301.

Tam *et al.* [8] found that when a square-edged inlet was used, the apparent friction factors were independent of Reynolds number for Reynolds numbers less than 2 300 and all the data collapsed onto a single curve. After a certain tube length, this curve approached the fully developed isothermal

constant value of $f_{app}Re = 16$. As the Reynolds number was increased above 2 300, the apparent friction factor became a strong function of Reynolds number. The same trend was observed in the results of the re-entrant inlet. However, it was found that a longer entrance length was required for the apparent friction factors to reach the fully developed friction factors than for the square-edged inlet. Therefore, the additional disturbance caused by the inlet geometry led to a longer entrance region [8, 25].

2.6.2. Heat flux

2.6.2.1. Heat transfer coefficients

When Ghajar and Tam [16] plotted the heat transfer coefficients in terms of the Colburn *j*-factor, the laminar heat transfer results had an almost parallel shift above the line for the laminar forced convection results. This was due to free convection effects, which led to mixed convection. A Nusselt number of approximately 14.5 was obtained, instead of the theoretical fully developed laminar forced convection Nusselt number of 4.36 for a constant heat flux boundary condition. Free convection effects were less evident in the transitional flow regime and could only be noticed from the local heat transfer information, which was the ratio of the heat transfer coefficients at the top and bottom of the test section (h_t/h_b) [10]. When the ratio of h_t/h_b was greater than or equal to 0.8, the flow was assumed to be dominated by forced convection, while the flow was assumed to be dominated by mixed convection when h_t/h_b was less than 0.8.

Ghajar and Tam [16] found that in the laminar flow regime, when the flow was dominated by mixed convection, the heat transfer coefficient was close to unity at the tube inlet, but decreased along the tube length. After approximately 125 diameters, h_t/h_b stabilised at 0.3. Free convection effects therefore required a considerable starting length to become significant, and the flow was dominated by forced convection for the first 20 to 70 diameters of the test section [24]. As expected, h_t/h_b decreased with increasing heat flux in the laminar flow regime, due to the increasing free convection effects [26]. In the transition region, free convection effects were significant at lower Reynolds numbers; however, h_t/h_b increased and approached unity in the upper part. In the turbulent flow regime, the free convection effects were suppressed by the inertia of the fluid and there was no significant difference between the results of the different heat fluxes.

In a review paper by Tam and Ghajar [10], it was noted that although mixed convection was not present in the upper part of the transitional flow regime when a re-entrant or square-edged inlet was used, free convection effects were significant when a bellmouth inlet was used. Ghajar and Tam [16] concluded that free convection effects depended on the Reynolds number, Prandtl number, Grashof number, inlet geometry, boundary condition as well as length-to-diameter ratio of the tube.

2.6.2.2. Friction factors

Tam and Ghajar [26] and Tam *et al.* [8] found that heating had a significant influence on the friction factors in the laminar flow regime, but this effect was less in the transitional flow regime, and negligible in the turbulent flow regime. Tam and Ghajar [26] explained that the velocity profile changed when mixed convection occurred. As the heat flux was increased, the density decreased, and the shear stress due to the change in the velocity profile increased, which led to increased friction factors. In the transitional flow regime, both the start and end of transition were delayed with increasing heat flux. Unlike the results obtained by Tam and Ghajar [26], Tam *et al.* [8, 30] found that the laminar and transitional friction factors decreased when heating was applied. The authors

explained that this was due to the viscosity of the fluid near the surface, which decreased with increasing temperature.

Both increasing and decreasing diabatic friction factors compared with isothermal friction factors are correct. The density and viscosity of the fluid decrease when heat is applied, which leads to decreasing diabatic friction factors. However, the friction factors increase (as was found by Tam and Ghajar [26]) when enough heat is applied so that free convection effects are significant and the increase due to the enhanced mixing caused by free convection effects is more than the decrease in pressure drop caused by the decreased density and viscosity.

2.6.3. Mini- and micro-tubes

Ghajar *et al.* [28] investigated isothermal friction factors in the transitional flow regime using mini- and micro-tubes. Twelve different tube diameters ranging from 337 µm to 2 083 µm were investigated. A channel with a diameter between 200 µm and 3 mm is considered a mini-channel [82], while smaller diameter channels are considered as micro-channels. It was found that when the tube diameter was decreased from 2 083 µm to 667 µm, the critical Reynolds number increased from 1 500 to 2 200. The end of transition remained fixed at a Reynolds number of 4 000 for tube diameters greater than 732 µm, while it ended at a Reynolds number of 3 000 for tubes with diameters of 732 µm and 667 µm. As the tube diameter was decreased further from 667 µm to 337 µm, both the start and end of transition occurred earlier. The critical Reynolds number decreased from 2 200 to 1 300, while the end of transition moved from a Reynolds number of 3 000 to 1 700. This caused the width of the transitional flow regime (in terms of Reynolds number range) to decrease with decreasing tube diameter. Similar results were obtained by Tam *et al.* [30].

The friction factors in the transitional flow regime were not significantly influenced by tube diameter for tube diameters greater than 1 372 µm. However, as the diameter was decreased from 991 µm to 838 µm, the gradient of the friction factors in the transitional flow regime increased. As the diameter was decreased further, the surface roughness became significant relative to the diameter of the tube. The greater relative roughness increased the friction factors (even in the laminar flow regime) and transition occurred earlier. As suggested by Kandlikar [83], Ghajar *et al.* [28] also investigated the results in terms of the constricted flow parameter that discounted the height of the roughness element and only considered the free flow area. These results corresponded significantly better to $64/Re$ in the laminar flow regime. However, transition still occurred earlier with increasing surface roughness. It is therefore important to account for the roughness height when investigating transitional flow in mini- and macro-tubes.

Tam *et al.* [30] also investigated the effect of heating in mini-tubes. Similar to the macro-tube results obtained by Tam *et al.* [8], it was found that the friction factors in the laminar and transitional flow regimes decreased when heating was applied, due to the decrease in viscosity which was caused by the increasing temperature of the fluid near the surface. Furthermore, heating delayed the start of transition, but did not have a significant effect on the end of transition.

2.6.4. Microfin tubes

Tam *et al.* [29] investigated the influence of internal microfin tubes on heat transfer coefficients and friction factors. In the laminar flow regime, the fully developed isothermal friction factors showed an upward parallel shift to $64/Re$ due to the increased surface roughness caused by the microfins. Furthermore, the transitional flow regime was significantly wider than for smooth tubes. The

transitional friction factors went through a steep increase (similar to smooth tubes), which was followed by a relatively constant friction factor before it gradually increased again as the flow approached the turbulent flow regime. In the turbulent flow regime, the friction factors had a significant upward parallel shift from the classical Blasius turbulent friction factor correlation. The friction factors in the transitional and turbulent flow regimes also increased with increasing spiral angle, due to the increased drag on the surface of the tube.

Tam *et al.* [29] concluded from the diabatic friction factor results that the start of transition was both inlet and spiral angle dependent, while the end of transition only depended on the spiral angle. Although heating delayed the start of transition, it had a negligible effect on the end of transition. The diabatic friction factors in the upper part of the transitional flow regime differed significantly for smooth and microfin tubes. For smooth tubes, the friction factors in the transitional flow regime initially experienced an abrupt increase, which was followed by a gradual increase as they approached the turbulent flow regime. However, for microfin tubes, the friction factors experienced an abrupt increase in the entire transitional flow regime. The friction factors in the upper part of the transitional flow regime, as well as the turbulent flow regime, were significantly higher than for the smooth tube, due to the swirling motion induced by the fins.

2.7. Transitional flow: Work of Meyer and co-workers

2.7.1. Smooth tubes

Professor Josua Meyer from the University of Pretoria and his PhD student, Olivier, followed a different experimental approach from that of Ghajar. Meyer pointed out four main differences of their work compared with the work of Ghajar in a recent keynote paper [7]: (1) The fluid was cooled, while Ghajar and his co-workers investigated heating, therefore the fluid characteristics were different. For example, the viscosity near the surface was higher than the bulk, which led to increased shear stress at the surface and therefore higher pressure drops [9]. (2) A constant surface temperature boundary condition (which is of significant practical importance in applications where condensation and evaporation occur) was attempted to be used. A tube-in-tube-type configuration with a very small annulus spacing was required to ensure that the flow rates were very high in the outer tube, while the inner tube was used as the test section. Even with the high flow rates, the surface temperature only remained relatively constant with a maximum temperature difference of 3 °C across the 5 m test section [7]. (3) An additional inlet geometry, the hydrodynamically fully developed inlet, was investigated. (4) Ghajar and his co-workers used local measurements, while Meyer and Olivier used the average measurements across a tube length. Thus, their data contained both developing (laminar and transitional flow regime) and fully developed (turbulent flow regime) flow. Another difference was that Ghajar used distilled water, as well as different ethylene glycol-water mixtures (Prandtl number of up to 160) as the test fluid, while Meyer and Olivier used mainly water ($Pr \approx 7$) with a limited number of experiments with propylene glycol-water mixtures ($Pr \approx 26$).

Similar to the results obtained by Ghajar and co-workers, transition occurred first for the inlet geometry which created the most turbulence. Furthermore, the laminar friction factors were slightly higher than the friction factors predicted by the Poiseuille equation ($f = 64/Re$), but were not influenced by the inlet geometry [33]. The authors explained that the higher friction factors were due to the growing hydrodynamic boundary layer along the surface of the tube, because the flow was still developing. Due to continuity requirements, the retardation of the fluid near the surface caused the

fluid in the centre of the tube to accelerate, which suppressed the boundary layer. This, in turn, led to an increase in shear and therefore higher friction factors [9].

Olivier and Meyer [9] found that the diabatic friction factors in the laminar flow regime were approximately 35% higher than the isothermal friction factors. According to Meyer and Olivier [33], there were two factors that led to increased diabatic friction factors. The first factor, which only contributed to 4% of the increase, was the viscosity difference between the fluid near the surface and the fluid near the centre-line of the tube, which influenced the shear stress at the surface. The second factor was the free convection effects, which distorted the velocity profile in such a way that the velocity gradient was steeper near the surface and therefore led to increased friction factors. Unlike the isothermal results, Olivier and Meyer [9] found that transition for the diabatic friction factors was independent of the inlet geometry. According to Nagendra [84], inlet disturbances have no effect on transition when the product of the Reynolds number, Rayleigh number and diameter-to-length ratio is greater than approximately 10^6. The value of this product varied between 3×10^6 and 3×10^7, which explains why there was no significant difference. Furthermore, the diabatic friction factors experienced a smoother transition from laminar to turbulent flow compared with the isothermal friction factors and the transition region was found to be narrower.

Because a constant surface temperature boundary condition was used, the laminar Nusselt numbers should have been 3.66 for fully developed forced convection flow [85]. However, similar to the results obtained by Ghajar and his co-workers, Olivier and Meyer [9] found that the laminar heat transfer coefficients increased due to free convection effects, which were caused by the temperature (and thus density) difference inside the tube, which enhanced mixing inside the tube. The inlet geometry had a negligible influence on the laminar and turbulent results, as well as on the transitional flow regime [33]. Because the transitional flow regime for the re-entrant, square-edged and bellmouth inlets occurred at the same Reynolds number as for the hydrodynamical fully developed inlet, Meyer and Olivier [33] concluded that free convection effects suppressed the growth of the hydrodynamic boundary layer to such an extent that the flow was hydrodynamically fully developed. However, according to the authors, this could be unique to water or low Prandtl number fluids.

An interesting observation from the propylene glycol-water results was that the Colburn *j*-factors in the transitional flow regime had a negative gradient when the square-edged and bellmouth inlets were used. Olivier and Meyer [9] explained that although the mass flow rate increased, the viscosities (which were obtained from the bulk fluid properties) increased due to the enhanced mixing in the transitional flow regime (it should be noted that the fluid was being cooled), which led to decreasing Reynolds numbers. In contrast to the sharp transition which was found in the propylene glycol-water results, the water results of all four inlet geometries showed a smooth transition from laminar to turbulent flow. Manglik and Bergles [86] obtained a similar trend when they investigated twisted tape inserts. The authors explained that inserts created a swirl effect in the flow, which competed with turbulent flow and led to a smoother transition. Olivier and Meyer [9] explained that in their study, free convection effects inside the tube created a similar swirl motion, which competed with turbulent flow and thus led to a smoother transition.

2.7.2. Enhanced tubes

Meyer and Olivier published two papers on transitional flow inside enhanced tubes with different inlet geometries [31, 32]. Four different types of enhanced tubes were investigated using tubes with outer

diameters of 15.9 mm and 19.1 mm. The tubes had either 25 or 35 fins, which corresponded to helix angles of 18° and 27° respectively. To keep the relative roughness of the tubes the same, the fin heights were 0.4 mm for the 15.9 mm tubes and 0.5 mm for the 19.1 mm tubes. Two smooth tubes with approximately the same diameters were used for comparison purposes.

From the isothermal friction factor results, Meyer and Olivier [32] concluded that the friction factors of the enhanced tubes were higher than for smooth tubes in both the laminar and turbulent flow regimes and transition occurred earlier. This was due to the increased roughness and increased resistance to flow caused by the fins. The tube diameter had a negligible effect, as long as the relative roughness and helix angle were the same. However, the friction factors increased and transition ended earlier with increasing helix angle.

A secondary transition occurred between Reynolds numbers of 3 000 and 10 000 where there was a smooth second increase in friction factors. This was not visible in the results of previous studies where different types of roughness in tubes (in the form of ring inserts of dimpled tubes) were compared. This secondary transition was also found in the diabatic friction factor and heat transfer coefficient results [31]. Meyer and Olivier [32] explained that the fins were probably ineffective to rotate the fluid at low Reynolds numbers, but as the velocity increased, the fins became effective in rotating the fluid. Shah and Sekulić [87] explain that this increase is due to the laminar viscous sublayer (which can account for up to 60% of the fluid's temperature drop in the turbulent flow regime), which is disrupted by the fins. From repeated experiments, the secondary transition region was found to be predictable and not chaotic. Although pressure fluctuations occurred in the transitional flow regime, no fluctuations were observed in the secondary transition region. The secondary transition continued up to a Reynolds number of approximately 10 000, whereafter it continued on the relative roughness curves predicted by the Moody chart.

Similar to the smooth tube results, transition was delayed for smoother inlets, while the inlet geometry had no effect on the laminar and turbulent flow regimes, or on the secondary transition. Transition occurred earlier in the enhanced tubes than in the smooth tube counterparts, and this effect was more pronounced when a bellmouth inlet was used. The authors concluded that the stability of the boundary layer was affected by the roughness due to the fins, thus the ability to maintain laminar flow at high Reynolds numbers was also affected.

The diabatic friction factors of the enhanced tubes were not only higher than the isothermal friction factors, but also higher than the diabatic friction factors of the smooth tubes [31]. Meyer and Olivier [31] explained that the fins had a negative influence in the laminar flow regime because it acted as a barrier for free convection effects and prevented the bulk of the fluid to mix with the fluid near the surface of the tube. As the tubes were cooled from the outside, the relatively unmixed fluid between the fins was at a lower temperature than that of the bulk of the fluid. This led to a higher viscosity and greater shear stress, which led to increased friction factors. The main difference between the results of the isothermal and diabatic friction factors was that, similar to the smooth tube results, transition was independent of the inlet geometry and occurred at a Reynolds number of approximately 2 000 [7].

Similar to the diabatic friction factor results, the fins had a negative influence on the Colburn *j*-factors in the laminar flow regime, because the results of the enhanced tubes were slightly lower than those of the smooth tubes, and the helix angle had no significant influence [31]. Although the fins acted as

a restriction for free convection effects, free convection effects were still significant because the laminar Nusselt numbers were higher than the theoretical value for fully developed forced convection flow (*Nu* = 3.66). Similar to the diabatic smooth tube results [9], transition was independent of the inlet geometry. The turbulent heat transfer coefficients were significantly higher than for smooth tubes and increased with increasing helix angle. Fins with a greater helix angle have the ability to spin the fluid more effectively, leading to enhanced mixing and thus increased heat transfer.

Another enhanced heat transfer technique is to make use of twisted tape inserts. Meyer and Abolarin [37] investigated heat transfer and pressure drop in the transitional flow regime using twisted tape inserts. It was found that when the twist ratio was decreased, both the heat transfer coefficients and friction factors increased, and transition occurred earlier. Furthermore, the extra turbulence created by the twisted tape inserts assisted the flow to transition from laminar to turbulent, therefore the width of the transitional flow regime decreased as the twist ratio was decreased.

2.7.3. Nanofluids

Meyer *et al.* [34] investigated the influence of multi-walled carbon nanotubes (MWCNT) on heat transfer and pressure drop characteristics in the transitional flow regime. Three different volume concentrations of MWCNT (0.33%, 0.75% and 1%) were investigated at a constant heat flux of 13 kW/m^2. Although the critical Reynolds number decreased with increasing nanofluid concentration, it was found that transition was actually delayed, and the decreasing Reynolds numbers were only due to the increasing viscosities of the nanofluids. The delayed transition was due to particle-fluid interaction, which dampened the instability and reduced the turbulent intensity and Reynolds stress in the flow. All three concentrations of nanofluids showed enhancement when the heat transfer results were presented in terms of Nusselt number against Reynolds number. However, the heat transfer coefficients actually decreased with increasing concentration and the increased Nusselt numbers were only due to the high thermal conductivity of the base fluid (3 000 W/m.K) compared with that of water (0.61 W/m.K). Furthermore, when the pressure drops and fluid velocities were compared, it was found that the pressure drop increased with increasing nanofluid concentration due to the increasing viscosity.

2.7.4. Micro-channels

Dirker *et al.* [35] investigated the effect of inlet flow conditions on heat transfer and pressure drop in small-scale rectangular channels. Three different hydraulic diameters (0.57, 0.85 and 1.05 mm) were investigated using a sudden contraction, bellmouth and swirl-inlet. All three inlet geometries had a significant influence on the transitional flow regime; however, for the swirl inlet, the Nusselt numbers and friction factors were higher in all three flow regimes. The swirl effect, together with the altered flow pattern, led to better mixing and therefore increased heat transfer coefficients. As mentioned earlier in this chapter, the work done by Ghajar and co-workers, as well as by Meyer and Olivier, showed that transition was delayed for the bellmouth inlet. However, the results of this study were different because transition occurred first for the bellmouth inlet, and the transition region was wider as well. A possible reason for this could be that the previous investigations considered circular macro-tubes, while rectangular mini-channels were used in this investigation. Therefore, a geometric size relationship between the critical Reynolds number and the channel shape and diameter could exist. Furthermore, transition was delayed when increasing heat fluxes were applied and the friction factors decreased due to the decreasing viscosity of the fluid near the surface of the tube.

2.7.5. Multiple circular tubes

Meyer *et al*. [39] experimentally investigated the maldistribution effects of two adjacent tubes on a centre tube, the presence of a protrusion inlet effect on two adjacent tubes, as well as the effect of the flow asymmetry in the adjacent tubes. It was found that neither the different pitch ratios nor the protrusion inlet affected the heat transfer and pressure drop characteristics in the laminar and turbulent flow regimes; however, the transitional flow regime was significantly affected. Transition was delayed in the multi-tube set-up, compared with the single tube, and the delay in transition was more for the side tubes than for the centre tube.

The isothermal friction factors showed that an increased pitch ratio dampened the inlet disturbances in the centre tube and reduced the flow asymmetry in the side tubes. Therefore, the differences in the critical Reynolds numbers and transition gradients of the three tubes decreased. As the inlet disturbances were dampened in the centre tube, transition was delayed compared with a single tube with a square-edged inlet. For the side tubes, the increased flow asymmetry led to increased critical Reynolds numbers, as well as increased transition gradients. Furthermore, the presence of a protrusion inlet in the centre tube significantly increased the recirculation areas between the tube inlets. The asymmetry of the flow in the side tubes therefore increased, which led to significantly increased critical Reynolds numbers and transition gradients, compared with the multi-tube set-up with a square-edged inlet.

The diabatic friction factors and Colburn *j*-factors indicated that free convection effects not only led to increased critical Reynolds numbers and transition gradients, but also decreased the differences between the results of the tubes in the multi-tube set-up when a square-edged inlet was used. However, free convection effects were not able to dampen the inlet disturbances caused by a protrusion inlet. In the centre tube with the protrusion inlet, free convection effects caused transition to occur at significantly lower mass flow rates, while the severe asymmetric velocity profile in the two side tubes dampened free convection effects and transition started at approximately the same mass flow rate. Although transition occurred earlier in the centre tube, the critical Reynolds numbers in all three tubes increased compared with the isothermal results, due to the decreasing viscosity with increasing temperature. Because the maldistribution effects caused by adjacent tubes and/or a protrusion at the inlet of a tube significantly affected both the heat transfer and pressure drop characteristics in the transitional flow regime, care should be taken during manufacturing to ensure that all the tubes are being installed flush into the header and the tubes are not spaced too close to each other.

2.7.6. Annuli

Ndenguma *et al.* [36, 38] conducted an experimental investigation to determine the average heat transfer coefficients and friction factors in the transitional flow regime of a horizontal concentric annular passage. The annular inlet geometry was that of a 90° T-section fitting, like that found in most practical applications. The flow was simultaneously hydrodynamic and thermally developing and mixed convection condition existed. Different degrees of longitudinal surface temperature uniformity on the inner surface of the annular passage were investigated and it was found that the degree of temperature uniformity on the inner surface of the annular passage decreased the transitional Reynolds number range and led to increased Nusselt numbers and friction factors [36]. When the influence of the annular dimensions was investigated, an annular geometric parameter ($\lambda = aL/D_h$), which takes into consideration both the annular diameter ratio and the hydraulic diameter, was

proposed [38]. It was found that as the annular geometric parameter increased, the magnitudes of the Nusselt numbers and friction factors, as well as the widths of the transitional flow regime, decreased.

2.8. Laminar-turbulent transition along the tube length

When the Reynolds number exceeds the critical Reynolds number, local laminar-turbulent transition occurs along the tube length. Nishi *et al*. [23] give a comprehensive review of the work that has been done on the laminar-turbulent transition along a tube length. It was found that the laminar-turbulent transition does not occur instantaneously, but rather continuously [88]. As the velocity was increased, the turbulent flashes increased until fully developed turbulence was established. Kalinin and Yarkho [89] explain that the turbulent flashes or pulsations can be considered as the alternation of zones with laminar and turbulent structures. This leads to mass flow rate fluctuations, as well as fluctuations in the surface temperatures when heat fluxes are applied to tubes. The turbulent flow structure is referred to as a puff or a slug, depending on the nature of the velocity field at the leading and trailing interfaces [90]. Puffs are usually caused by large disturbances at the inlet, and are observed at lower Reynolds numbers than for slugs. Furthermore, while the length of a puff remains constant as it moves downstream, slugs increase in size as they travel downstream [91]. Previous studies focused mainly on the effect of inlet disturbances and Reynolds number on the two different flow structures (puffs and slugs) that occur during transition.

Although extensive research has been conducted on isothermal flow, only a few studies focused on diabatic flow [92]. Koizumi [92] investigated the influence of free convection effects and inlet flow conditions on the laminar-turbulent transition of fully developed flow using air as the test fluid. Similar to the results obtained by El-Hawary [93], it was found that free convection effects cause laminar-turbulent transition at Reynolds numbers less than the critical Reynolds number. El-Hawary [93] also noted that the effect of the inlet turbulence decreased as free convection effects increased. However, the focus of previous studies was on the onset of fluctuations, indicating the laminar-turbulent transition, and not on the effect of free convection on the local heat transfer characteristics along the tube length during the laminar-turbulent transition.

2.9. Relationship between pressure drop and heat transfer

Although pressure drop and heat transfer are usually investigated independently, there exists a direct relationship that is often overlooked [2]. It is desirable to know this relationship for three reasons: (1) it improves our fundamental understanding of convective heat transfer; (2) it makes it possible to calculate either the heat transfer coefficients or the friction factors when the other variable is available; (3) it gives additional insight into the trade-off between high heat transfer coefficients and low pressure drops during the design process. Two analogies were developed, based on the similarity between momentum and heat transfer in the boundary layer [3]: the Reynolds number analogy was developed for Prandtl numbers of unity, while the Chilton-Colburn analogy was developed for laminar and turbulent flow over flat plates for Prandtl numbers between 0.6 and 60. Obot and Esen [4] developed explicit relationships between pressure drop and heat transfer in the laminar flow regime, and noted that the critical Reynolds number was the same for both the pressure drop and heat transfer results. The relationship between pressure drop and heat transfer in the turbulent flow regime (for $Re > 10\,000$) was investigated by Allen and Eckert [5]. Gill [6] proposed correlations for the laminar and turbulent flow regimes; however, the ranges of the parameters used in the correlations were not given.

Tam *et al*. [8] investigated pressure drop and heat transfer simultaneously, and found similar trends for the pressure drop and heat transfer results in the laminar and turbulent flow regimes. However, transition started slightly earlier for the heat transfer coefficients (Re = 2 298) than for the diabatic friction factors (Re = 2 316). This might be due to the different bulk Reynolds numbers that were used, because the heat transfer results were obtained at x/D = 192, while the friction factors were obtained across a tube length. Furthermore, transition ended significantly earlier for the diabatic friction factors (Re = 3 941) than for heat transfer coefficients (Re = 8 357). Therefore, although both heat transfer coefficients and friction factors increased with increasing Reynolds number in the transitional flow regime, the transitional Reynolds number range was found to be significantly wider for heat transfer than for pressure drop. However, no correlations were developed to quantitatively describe the relationship between pressure drop and heat transfer.

Olivier and Meyer [9] also investigated pressure drop and heat transfer simultaneously and found that the Colburn j-factors and friction factors collapsed onto a single graph when the Colburn j-factors were multiplied by $4Pr^{2/3}$. However, from close inspection, it follows that although this relationship was valid for laminar and turbulent flow, the Colburn j-factors and friction factors in the transitional flow regime did not collapse onto a single graph. Furthermore, this was for cooling in a tube with a constant surface temperature boundary condition, and no specific attention was given to the start and end of the transitional flow regime.

2.10. Mixed convection criteria and flow regime maps

It is important to determine whether free convection effects can be neglected (forced convection dominates) or whether it is significant (mixed convection dominates), because this needs to be taken into consideration when appropriate equations are considered, especially for laminar heat transfer cases. A general guideline in literature [3, 52-54, 60] is that the flow can be expected to be dominated by forced convection for $Ri \ll 1$, by free convection for $Ri \gg 1$ and by mixed convection for $Ri \approx 1$. A more conservative criterion is that the free convection effects should be an order of magnitude greater than the forced convection effects, therefore $Ri > 10$ [52]. However, it should be noted that the Richardson number was obtained by considering the boundary layer equations describing uniform upward flow over a heated vertical flat plate. Because heating a fluid in a horizontal tube leads to secondary flow, mixed convection in tubes are more complicated than in external flows [55]. Mills [55] suggested that when it is not obvious whether forced convection or free convection dominates, the Richardson number criterion for external flow should be used for internal flow to determine whether the flow is dominated by mixed convection. However, it is shown in Chapter 8 that this criterion was too conservative for the internal flow results of this study, because the flow was predicted to be dominated by forced convection, while free convection effects were significant.

Shannon and Depew [20] developed a criterion to predict the convection flow regime for internal laminar flow in horizontal tubes heated at a constant heat flux. Experiments were conducted using water and it was found that free convection effects were significant when the product $Ra^{1/4}/Nu_{FC}$ was greater than 2. As they considered hydrodynamically fully developed flow, the forced convection Nusselt numbers (Nu_{FC}) were obtained using the correlation of Siegel *et al*. [17]. When the flow is simultaneously hydrodynamically and thermally developing, as in this study, the correlation of Shah and London [1] might be more appropriate to use to obtain the forced convection Nusselt numbers. It is shown in Chapter 8 that although the criterion was able to accurately predict the convection flow

regime of the majority of the data of this study, the forced/mixed convection boundary was not predicted correctly. Furthermore, this criterion is valid for laminar flow only.

A flow regime map is a valuable tool that can be used to determine whether free convection effects can be neglected or not. Metais and Eckert [13] developed two flow regime maps for a constant surface temperature boundary condition, one for vertical flow and another for horizontal flow. The forced/mixed convection boundary was arbitrarily defined as the location where the difference between the forced and mixed convection heat transfer coefficients exceeded 10%. Ghajar and Tam [14] found that the flow regime map of Metais and Eckert [13] accurately predicted their turbulent forced convection experimental data, but the laminar and transition data were not predicted correctly. This was due to the constant heat flux boundary condition which was used, while the flow regime map was developed for a constant surface temperature. In the laminar and transitional flow regimes, the boundary condition has a significant influence on the heat transfer characteristics, while turbulent flow is insensitive to different boundary conditions. Furthermore, the influence of free convection effects is also stronger with a constant heat flux boundary condition than with a constant surface temperature boundary condition [14].

A new flow regime map for horizontal tubes with a constant heat flux boundary condition was therefore developed by Ghajar and Tam [14]. The forced/mixed convection boundary was obtained using the ratio of the local peripheral heat transfer coefficients at the top and bottom of the tube (h_t/h_b). The flow was assumed to be dominated by forced convection for $h_t/h_b \geq 0.8$, while mixed convection conditions were assumed for $h_t/h_b < 0.8$. As far as can be determined, this was the first flow regime map for horizontal tubes with a constant heat flux boundary condition, and it also accounted for different inlet geometries (re-entrant, square-edged and bellmouth).

Tam *et al*. [94] improved this flow regime map by making use of the multi-class support vector machines (SVM) method. Three flow regime maps (re-entrant, square-edged and bellmouth inlets) were developed and five flow regimes (forced turbulent, forced transition, mixed transition, forced laminar and mixed laminar) were identified using the Rayleigh and Reynolds numbers. A unified SVM-based flow regime map, which could be used for the re-entrant, square-edged and bellmouth inlets, was developed by Tam *et al*. [15]. The overall accuracy of this flow regime map was also better than that of the three individual SVM-based flow regime maps.

However, as the unified flow regime map of Tam *et al*. [15] was developed using the experimental data of Ghajar and Tam [16], it was primarily for Rayleigh numbers in the order of 10^6, which was high. The laminar heat transfer experiments were conducted using different ethylene glycol-water mixtures, therefore, the forced/mixed convection boundary in the laminar flow regime was developed using experimental data with Prandtl numbers between 23 and 140. Furthermore, due to the relatively large inner diameter of the test section (15.8 mm), the Grashof numbers were high ($Gr \propto D^3$). This is of significant importance because the Rayleigh number, which was used on the *x*-axis of their flow regime map, is a product of the Grashof number, which was large due to the large tube diameter, and Prandtl number, which was high because ethylene glycol-water mixtures were used.

It is shown in Chapter 8 that although the flow regime map of Tam *et al*. [15] could be very accurate for high Prandtl number fluids, it became inaccurate once the Prandtl number and tube diameter were decreased, for example, when water was used in small diameter tubes. The result was that the flow

was predicted to be in the forced convection regions, while free convection effects were significant and the flow was actually dominated by mixed convection.

2.11. Summary and conclusions

This chapter revised a few fundamental concepts, the different flow regimes as well as developing and fully developed flow. A brief overview of previous work done on flow in the transitional flow regime was also given.

It has been found that extensive research has been done on the thermal entrance length in the laminar flow regime; however, there are still some gaps in the mixed convection literature. Although free convection effects have been found to decrease the thermal entrance length, there is not only uncertainty regarding the correlation for calculating the thermal entrance length, but also the definition of the point of fully developed flow in mixed convection heat transfer.

Much attention has also been paid to mixed convection laminar heat transfer in horizontal circular tubes with a constant heat flux boundary condition, especially when the flow is fully developed. While laminar heat transfer correlations are readily available in heat transfer textbooks, these equations and graphs are usually based on analytical solutions to the governing equations for laminar flow. It is therefore restricted to constant fluid properties, while this assumption is not valid in actual practice. Furthermore, the differing behaviour of the local heat transfer characteristics of different Prandtl number fluids makes it challenging to obtain a single correlation. It was found that for Rayleigh numbers less than 3.75×10^5, the local Nusselt numbers did not decrease asymptotically and became constant. The Nusselt numbers decreased near the inlet of the test section, and then increased along the tube length before it became constant. Although three regions were observed in the local laminar Nusselt numbers for mixed convection conditions, the boundaries between the three regions and the heat transfer characteristics in each region were not defined qualitatively and quantitatively.

For transitional flow, Ghajar and co-workers broke new ground with investigating the effect of inlet geometry and heating on transition, making it possible for others, such as Meyer and co-workers, to follow. However, the focus of previous studies was not on the characteristics of developing flow, but rather on the effect of different inlet geometries, enhanced tubes, micro-channels, multiple circular tubes, annular flow and different Prandtl number fluids. In general, it was found that transition was delayed for smoother inlet geometries, as well as increasing heat fluxes, but occurred earlier with increasing surface roughness, helix angle in enhanced tubes, or decreasing twist ratio when twisted tape inserts were used. Therefore, the Reynolds number range in which transition occurred could be manipulated by changing the inlet geometry, heat flux or tube surface. It was also found that the transition region varied when different locations on the tube were considered even though the flow was fully developed. Although literature states that this could be due to the variation of fluid properties with temperature along the tube length, it was found in this study that the width of the transitional flow regime remained constant once the flow was fully developed.

Up to now, no experimental studies have been specifically devoted to the heat transfer characteristics of developing flow in the transitional flow regime, how they change along the tube length, how they differ from that of fully developed flow, and how they are affected by free convection effects. Furthermore, the methods that were used to identify the boundaries of the transitional flow regime not only relied on subjective decisions, but also did not distinguish between the transitional and quasi-

turbulent flow regimes. An understanding of the factors that influence the start and end of the transitional flow regime, as well as an understanding of the heat transfer and pressure drop behaviour in this regime, is required in order to select or develop appropriate heat transfer and pressure drop correlations for transitional flow. As this flow regime has not yet been properly understood, the available correlations to predict the heat transfer coefficients and friction factors are still very limited. The existing correlations are restricted to forced convection conditions, specific inlet geometries or high Prandtl number fluids and no clear distinction has been made between the transitional and quasi-turbulent flow regimes.

Furthermore, although heat transfer and pressure drop are usually investigated independently, a direct relationship exists, which is often overlooked. This relationship has been investigated in the laminar and turbulent flow regimes, and correlations have been developed to quantify these relationships. However, no correlations have been developed to quantitatively describe the relationship between heat transfer and pressure drop in the transitional flow regime. It is important to investigate this relationship, especially in the transitional flow regime, because there is a fundamental gap in the literature on this subject field. This will be the first step before similar relationships can be developed for more complex geometries. Specifically, for complex geometries, it will be much easier for product developers to obtain either the heat transfer coefficients or pressure drops, because this will save time and money. This relationship will enable them to calculate either the heat transfer coefficients or the friction factors, when the other variable is unavailable. Furthermore, it will also give additional insight into the trade-off between high heat transfer coefficients and low pressure drops during the design process.

When selecting appropriate equations, a flow regime map is a valuable tool that can be used to determine whether free convection effects can be neglected (forced convection dominates) or whether it is significant (mixed convection dominates). Although a versatile flow regime map that accounts for different inlet geometries in horizonal tubes is available in literature for constant heat flux boundary condition, this map was developed using experimental data obtained in relatively large diameter tubes and high Prandtl number fluids, especially in the laminar flow regime. Therefore, although the existing flow regime map may be very accurate for high Prandtl number fluids, it may become inaccurate once the Prandtl number and tube diameter are decreased, for example, when water is used in small diameter tubes. The result is that the flow is predicted to be in the forced convection regions, while free convection effects are significant and the flow is actually dominated by mixed convection. Furthermore, the existing flow regime maps were also developed for fully developed flow, while the majority of the flow in heat exchangers might still be developing, especially at high Reynolds numbers close to the transitional flow regime.

Overall, it can be concluded that there are several gaps in the mixed convection literature, especially when the flow is still developing. Thermal entrance length, heat transfer and pressure drop correlations, which are valid for both developing and fully developed laminar and transitional flow in mixed convection conditions, are required, as well as a flow regime map that accounts for low Prandtl number fluids and for developing flow. This will not only enable designers to optimise the design of heat exchangers, but also improve the fundamental understanding of mixed convection developing and fully developed flow.

3. Experimental Set-up and Data Reduction

3.1. Introduction

The purpose of this chapter is to describe the experimental set-up, which was used to conduct heat transfer and pressure drop experiments in smooth horizontal tubes at different heat fluxes as a function of different mass flow rates. An overview of the components of the experimental set-up, the test section, as well as the material, equipment and instrumentation used, is given. The experimental procedure and data reduction method are also discussed and an overview of the results of an uncertainty analysis is given. Furthermore, new nomenclature and terminology to mathematically define and quantify the boundaries of the different flow regimes, as well as the heat transfer and pressure drop characteristics in the transitional flow regime, is presented.

3.2. Experimental set-up

The layout of the experimental set-up is shown in Fig. 3.1. The experimental set-up consisted of a closed-loop system, which circulated water from a storage tank, through the test section and back to the storage tank, using two electronically controlled magnetic gear pumps with a maximum flow rate of 270 ℓ/h. Because the laboratory was permanently temperature-controlled (24 hours per day, 7 days per week) to a constant temperature of 21.8 °C, it was possible to conduct experiments at the same ambient conditions throughout a total period of three years. The test fluid was chosen as water and the capacity of the storage tank was 260 ℓ, which was maintained at a preselected temperature (20 °C) because it was externally connected to a thermostat-controlled bath that cooled the heated water. The water in the storage tank was continuously pumped through a filtration cycle to remove any solid particles that might have entered the system, as well as to enhance mixing and prevent thermal stratification inside the storage tank.

A 0.74 ℓ bladder accumulator was installed upstream of the flow meters and the test section to dampen possible pulsations from the pump, which could have an effect on transition. This ensured a constant pressure and mass flow rate at the inlet of the test section. A bypass valve was inserted after the accumulator to allow a fraction of the water to flow back to the storage tank. During experiments, the supply valve was partially closed and the bypass valve partially opened, so that the pump was operated close to its maximum speed to ensure a preselected mass flow rate of water to the test section. The increased pump speed, as well as the artificial increase in pressure at the pump inlet (monitored using the pressure gauge), led to decreased mass flow rate pulsations [75]. The valve positions were adjusted throughout the experiments to minimise the flow pulsations for all the measurements. A pressure relief valve was installed to allow the water to flow directly to the storage tank if the pressure exceeded the preselected threshold.

Because the mass flow rates varied over a wide range, Coriolis mass flow meters with different flow rate capacities were installed in parallel. The mass flow meter that would produce the most accurate mass flow rate measurements was selected during the experiments. All measurements that were conducted were within the prescribed ranges of the mass flow meters. The mass flow rates were controlled by frequency drives, which were connected to the pump. The required mass flow rate was

therefore obtained by increasing or decreasing the pump speed. Downstream of the mass flow meters, the fluid flowed through a flow-calming section to the test section and mixer, and then back into the storage tank.

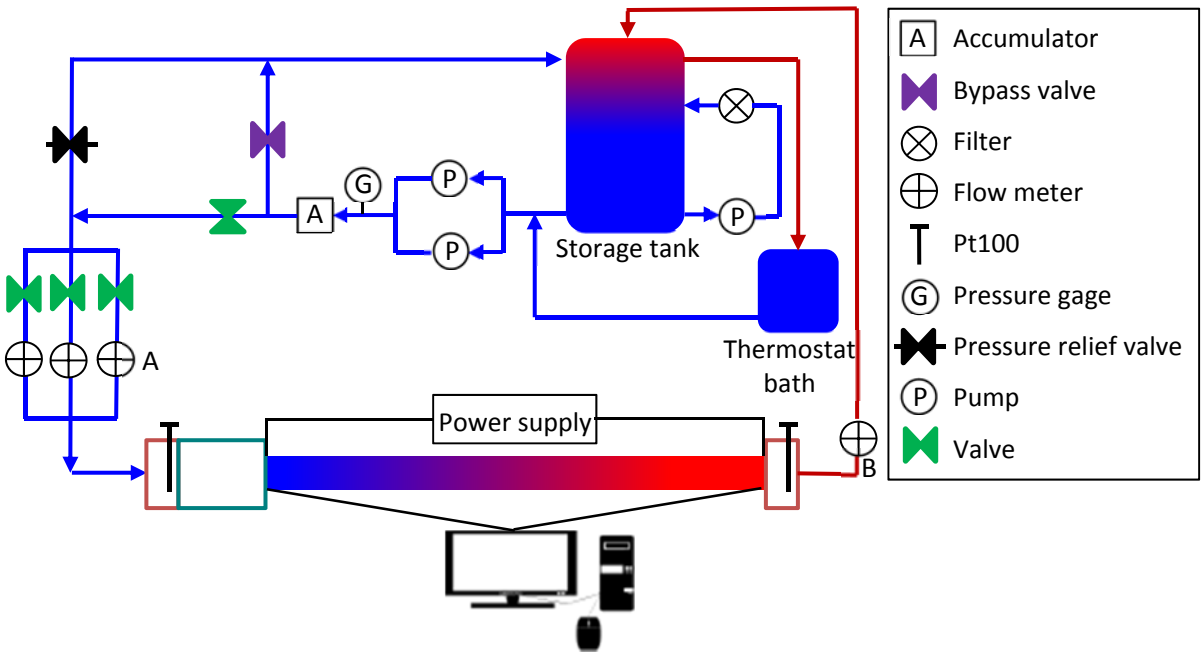

Fig. 3.1: Schematic representation of the experimental set-up used to conduct heat transfer and pressure drop measurements. Water was circulated from the storage tank through the test section and back using two pumps. Flow meter bank A was used to conduct experiments with the 11.5 mm test section and flow meter B was used for the 4 mm test section.

3.3. Flow-calming section

A flow-calming section (Fig. 3.2), similar to the one used by Ghajar [8, 14-16, 24-29, 94], was installed upstream of the test section to straighten the flow. The flow-calming section was made from clear acrylic plastic to ensure that entrained air bubbles could be detected. The acrylic tube had an inner diameter and length of 172 mm and 700 mm respectively. To prevent any temperature gradients inside the flow-calming section, the fluid first flowed through a 100 mm cavity filled with a soft nylon mesh, before it reached a Pt100 probe, where the average inlet temperature was measured. Three perforated acrylic plates with an open-area ratio (OAR) of 0.299 (73 holes with a diameter of 11 mm) were inserted after the Pt100 probe and were followed by tightly packed soda straws (inside diameter 5.1 mm, length 102 mm, OAR of 0.855), between two galvanised steel meshes (wire diameter 0.37 mm, OAR of 0.588). The fluid passed through another galvanised steel mesh (wire diameter 0.37 mm, OAR of 0.588) before leaving the flow-calming section. The inlet section was bolted to the flow-calming section and consisted of a clear acrylic tube with an inside diameter and length of 172 mm and 195 mm respectively. An acetal disc was bolted to the inlet section to obtain a square-edged inlet.

A bleed valve was installed prior to the inlet section to bleed air that entered the flow-calming section. The Pt100 probe connection inside the flow-calming section was used as another bleed valve. The flow-calming section was properly insulated against heat loss using 40 mm thick insulation with a thermal conductivity of 0.034 W/m.K. Peep holes and lids were incorporated into the insulation so that any air bubbles could be detected.

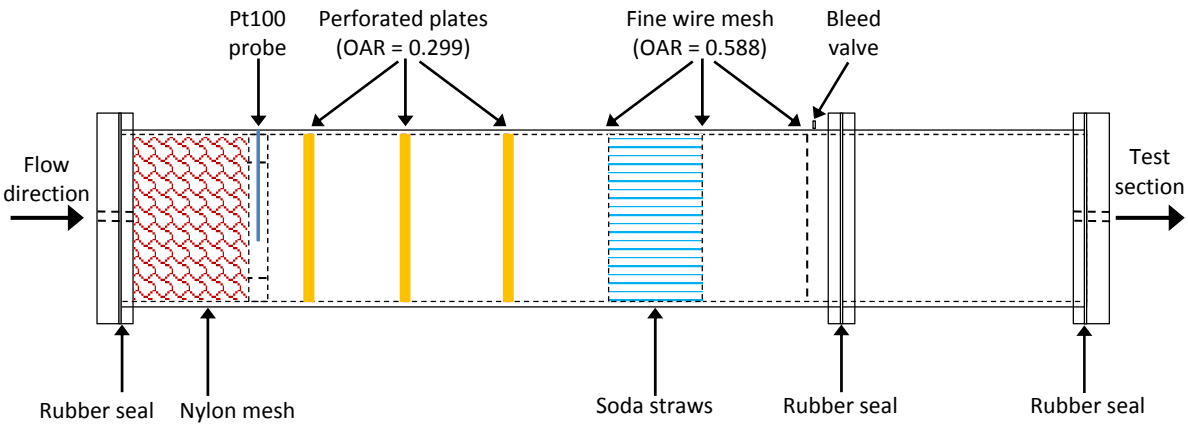

Fig. 3.2: Schematic representation of flow-calming section with a Pt100 probe to measure the inlet water temperature, perforated plates, soda straws and wire meshes.

3.4. Test sections

An acetal disc with a diameter of 260 mm and thickness of 40 mm was used to connect the flow-calming section (Fig. 3.2) to the test sections (Fig. 3.3). The thermal conductivity of acetal is 0.31 W/m.K, which is very low in comparison to the thermal conductivity of the test sections, and thus the acetal disc was also used to prevent axial heat conduction from the test section to the flow-calming section. For a proper square-edged inlet, care was taken to ensure that the start of the test section was flush with the start of the acetal cylinder. Two test sections with inner diameters of 11.5 mm and 4 mm respectively were used to investigate the influence of tube diameter and heating method. The test sections are shown schematically in Fig. 3.3, while the details of the thermocouple stations and pressure taps are summarised in Table 3.1.

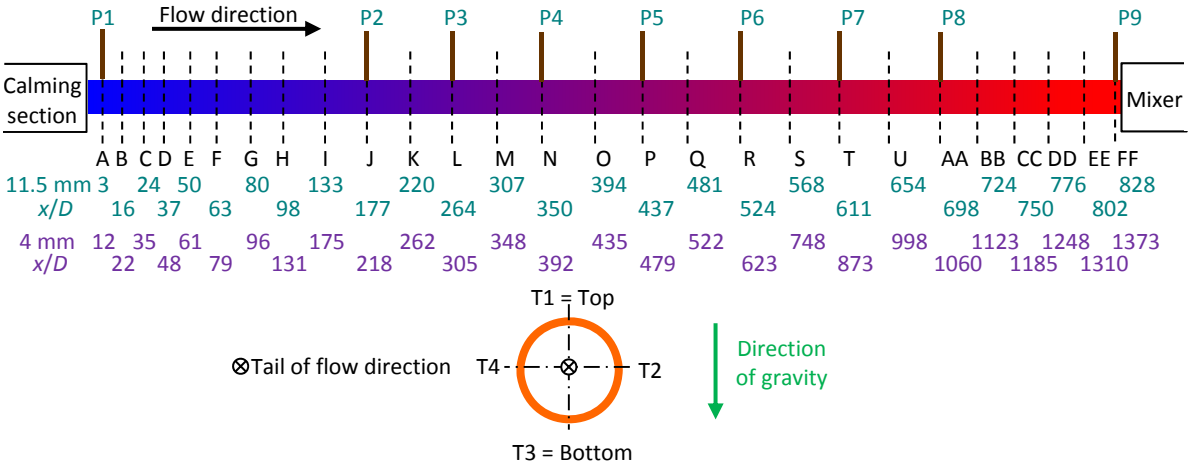

Fig. 3.3: Schematic representation of the test sections indicating the 27 thermocouple stations, A to FF, on the 11.5 mm and 4 mm test sections, as well as the nine pressure taps, P1 to P9, on the 11.5 mm test section. The *x/D* values of the thermocouple stations of both test sections are also given. A cross-sectional view of the test section is included to illustrate the four thermocouple positions spaced around the outside periphery of the tube.

The 11.5 mm test section was manufactured from a hard-drawn copper tube with an average (measured with a split-ball unit and a vernier calliper) inside diameter of 11.52 mm, outside diameter of 12.7 mm and a length of 9.81 m (measured with a measuring tape). However, to prevent possible upstream flow effects from influencing the measurements at the last measuring station (station FF), 300 mm was allowed between the last measuring station (at x = 9.5 m) and the mixer (at x = 9.8 m). The 4 mm test section was manufactured from a seamless 316L stainless steel tube with an inner and

outer diameter of 4 mm and 6 mm respectively and a length of 6 m. However, measurements were only taken across the first 5.5 m. The remaining 500 mm between the last measuring station and mixer was, as with the 11.5 mm test section, to prevent possible upstream effects from influencing the measurements at the last thermocouple station.

Table 3.1: Thermocouple stations and pressure tap locations, as well as number of thermocouples for each thermocouple station in the 11.5 mm and 4 mm test sections.

11.5 mm		**A**	**B**	**C**	**D**	**E**	**F**	**G**	**H**	**I**
		P1								
	x [mm]	37	157	277	427	577	727	927	1 127	1 537
	x/*D*	3	16	24	37	50	63	80	98	133
	n	4	4	4	4	4	4	4	4	4
		J	**K**	**L**	**M**	**N**	**O**	**P**	**Q**	**R**
		P2		**P3**		**P4**		**P5**		
	x [mm]	2 037	2 537	3 037	3 537	4 037	4 537	5 037	5 537	6 037
	x/*D*	177	220	264	307	350	394	437	481	524
	n	4	4	4	4	4	4	4	4	4
		S	**T**	**U**	**AA**	**BB**	**CC**	**DD**	**EE**	**FF**
			P7		**P8**					**P9**
	x [mm]	6 537	7 037	7 537	8 037	8 337	8 637	8 937	9 237	9 537
	x/*D*	568	611	654	698	724	750	776	802	828
	n	4	4	4	4	4	4	4	4	4
4 mm		**A**	**B**	**C**	**D**	**E**	**F**	**G**	**H**	**I**
	x [mm]	47	88	140	192	244	314	383	526	699
	x/*D*	12	22	35	48	61	79	96	131	175
	n	4	4	4	4	4	4	4	4	4
		J	**K**	**L**	**M**	**N**	**O**	**P**	**Q**	**R**
	x [mm]	873	1 047	1 220	1 394	1 567	1 740	1 915	2 088	2 492
	x/*D*	218	262	305	348	392	435	479	522	623
	n	4	4	4	4	4	4	4	4	4
		S	**T**	**U**	**AA**	**BB**	**CC**	**DD**	**EE**	**FF**
	x [mm]	2 992	3 492	3 992	4 242	4 492	4 742	4 992	5 242	5 492
	x/*D*	748	873	998	1 060	1 123	1 185	1 248	1 310	1 373
	n	3	3	3	3	3	3	3	3	3

The average surface roughnesses (ε) of the 11.5 mm copper test section and 4 mm stainless steel test section were measured to be approximately 0.218 µm and 0.138 µm respectively using a surface roughness tester. The relative surface roughnesses (ε/D) were therefore 1.89×10^{-5} and 3.45×10^{-5}, and for all practical purposes, both tubes could be considered as being smooth. The total length of the 11.5 mm and 4 mm test sections provided maximum length-to-inside diameter ratios (x/D) of 828 and 1 373 respectively, while previous investigations by Ghajar and co-workers [8, 16, 24-27, 29] and Meyer and Olivier [9] had maximum values of 400 and 350 respectively. The test sections in this study were thus two to four times longer than the test sections used in previous studies.

T-type thermocouples were used to measure the surface temperatures at 27 selected axial locations on both test sections. The thermocouple stations were spaced closer to each other near the inlet of the test section to accurately obtain the temperature profile of developing flow, while the thermocouple stations were spaced further apart on the rest of the test section where the flow was expected to be fully developed. To compare the developing heat transfer results in the 4 mm and

11.5 mm test sections, the same non-dimensional axial positions were used on both test sections for $x/D < 524$. As the diameter of the 4 mm test section was 2.88 times smaller than that of the 11.5 mm test section, the maximum length-to-inside diameter ratio (x/D) was 1.66 times larger than that of the 11.5 mm test section. To obtain sufficient heat transfer results in the remaining part of the 4 mm test section, the thermocouples were located at 500 mm intervals for $524 < x/D < 873$, and at 250 mm intervals for $873 < x/D < 1\,373$.

To investigate possible circumferential temperature distributions caused by free convection effects along the tube length, four thermocouples (spaced 90° apart around the periphery) were used at each thermocouple station on the 11.5 mm test section, and on the 4 mm test section for $x/D < 524$. The remaining thermocouple stations on the 4 mm test section (stations R to FF) contained thermocouples at the top and bottom of the test section, and one thermocouple on the side only (as shown in Fig. 3.3). The two thermocouples T2 and T4 were positioned on the horizontal water level line and thermocouples T1 and T3 were aligned to the direction of gravity, and were perpendicular to the horizontal line (T4-T2). The third thermocouple alternated between the left (T4 in Fig. 3.3) and right (T2 in Fig. 3.3) side of the test section.

The thermocouples were attached to the 11.5 mm copper test section by first drilling a 0.3 mm indentation into the tube. Solder was inserted into the indentation and heated up to the melting point. The thermocouple was then inserted into the indentation and the heat was removed, allowing the solder to cool down. The thermocouples were carefully checked to ensure good contact with the tube. As the wall thickness of the 4 mm stainless steel tube was 1 mm, the thermocouples were placed into 0.5 mm indentations. A 3D printed jig was used to ensure that all the indentations were drilled to the same depth. The thermocouples were glued to the stainless steel tube using a thermal adhesive with a thermal conductivity of 9 W/m.K, and a curing time of five minutes.

To investigate the pressure drop characteristics of developing flow, nine pressure taps were fixed to the 11.5 mm test section by silver soldering a 30 mm long capillary tube at each pressure tap station (Fig. 3.3). A 1 mm hole was then drilled through the capillary tube and the copper tube. This small diameter was chosen to ensure that the pressure taps did not cause flow obstructions in the test section and that the diameter was less than 10% of the test section's inner diameter [95]. To prevent incorrect pressure drop measurements, care was taken to remove all the burrs from the inside of the test section. A borescope was pulled through the test section to visually inspect and ensure that all the burrs were properly removed. A bush tap with a quick release coupling was inserted over the capillary tubes, and nylon tubing was used to connect the pressure taps to the differential pressure transducers.

The thermal entrance length at a Reynolds number of 2 300 and a Prandtl number of 6 was calculated to be 7.95 m (using Eq. 2.11). The Prandtl number decreases with increasing temperature, which implies that the thermal entrance length will also decrease as the fluid is being heated. Therefore, it was assumed that the flow in the last 1.5 m of the test section would always be fully developed (this was experimentally verified by the local surface-fluid temperature differences). It was further assumed that the pressure drop measurements across the first seven tube lengths ($0\text{ m} < L < 8\text{ m}$) of the test section could contain developing and fully developed flow, depending on the Reynolds number, Prandtl number and heat flux. The pressure drops were measured between the first pressure

tap (P1) and the respective pressure tap (P2 to P8), while the pressure drop of the fully developed region was measured between pressure taps P8 and P9.

Because of limits on the equipment that was available, two different heating methods were used in this study. To obtain a constant heat flux boundary condition in the 11.5 mm copper test section, four constantan wires (which have a high electrical resistance) with a diameter of 0.38 mm were coiled around the test section. The heating wires were connected in parallel to obtain the desired resistance, while limiting the current flowing through each wire. When coiling the heating wire, it was important to consider how close the heating wire could be to the thermocouple junction before affecting the temperature measurements. Everts [75] experimentally investigated different coiling techniques and concluded that a gap of approximately 1 mm between the heating wire and the thermocouple junction was sufficient. Furthermore, when the heating wire was coiled twice over the thermocouple wire, the thermocouple was secured while the temperature measurements remained unaffected. Figure 3.4 shows a schematic representation of the heating wire coiled around the tube and the thermocouple wire.

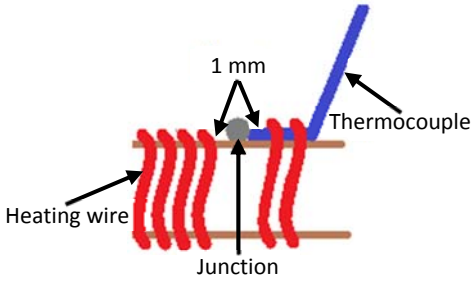

Fig. 3.4: Schematic representation of the heating wire coiled at a thermocouple junction.

A constant heat flux boundary condition was obtained in the 4 mm stainless steel test section by passing current through the tube wall. The resistance of the stainless steel tube was measured to be 0.282 Ω in the temperature-controlled laboratory, using a multimeter. The test section was electrically insulated with Kapton film before it was thermally insulated. Both test sections were thermally insulated with 120 mm thick Armaflex insulation with a thermal conductivity of 0.034 W/m.K. The maximum heat loss was estimated with one-dimensional conduction heat transfer calculations to be less than 3% in both test sections. When axial heat conduction in the tube wall is significant, it needs to be taken into consideration when calculating the local heat transfer coefficients [96, 97]. However, using the criteria of Maranzana *et al*. [98], axial heat conduction was assumed to be negligible in both test sections, because the axial heat conduction number was orders of magnitude less than 0.01.

3.5. Mixer

During laminar flow measurements, significant cross-sectional temperature gradients in the radial and tangential directions developed throughout the test section. Therefore, to obtain a uniform outlet temperature, a mixer (Fig. 3.5) was inserted after the test section to mix the water exiting the test section. The purpose of the mixer was two-fold: to house the splitter plates and to house a Pt100 probe, which was used to measure the outlet temperature.

The mixer design was based on work done by Bakker *et al.* [99], who investigated laminar flow in static mixers with helical splitter plates. The mixer consisted of four copper splitter plates, with a length-to-diameter ratio of 1.5. The elements were positioned and soldered such that the leading edge of an

element was perpendicular to the trailing edge of the next element. Every splitter plate repeatedly split the thermal boundary layers to ensure a uniform temperature gradient in the radial direction. The splitter plates were placed inside the acetal mixer, which directed the fluid to flow over and along the Pt100 probe after it has been mixed. This ensured that the entire Pt100 probe was exposed to the mixed fluid and also eliminated any stagnant recirculation zones. The mixer was insulated with 75 mm thick insulation to prevent any heat loss, and air was bled from the mixer using the Pt100 probe connection to the mixer housing.

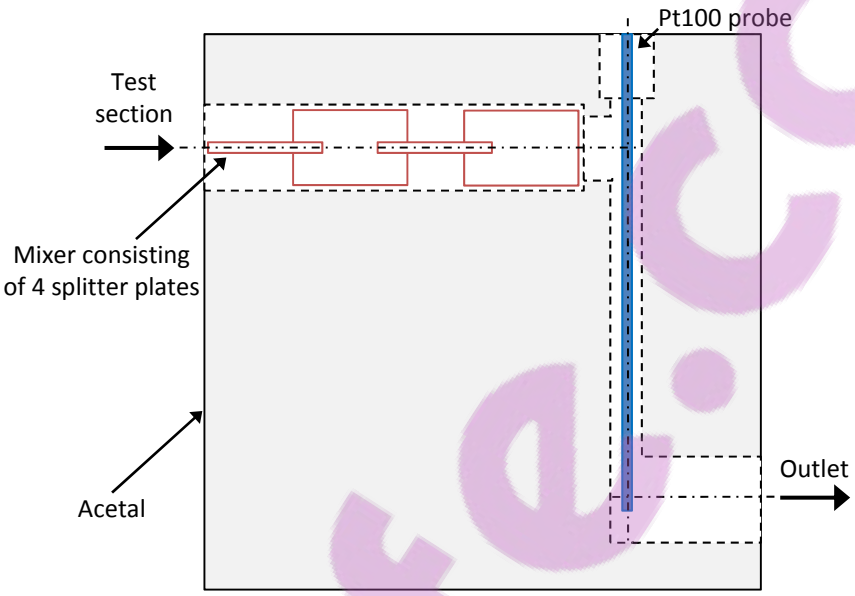

Fig. 3.5: Schematic representation of the mixer with the splitter plates and a Pt100 probe to measure the outlet water temperature.

3.6. Instrumentation

3.6.1. Pt100 probes

Pt100 probes with an accuracy of 0.06 °C were used to measure the temperatures at the inlet of the flow-calming section and at the outlet of the mixer. The Pt100 probes were calibrated between 15 °C and 60 °C inside a thermostat-controlled bath, using a digital thermometer with an accuracy of 0.03 °C. The details of Pt100 probe calibration are given in Appendix A.

3.6.2. Thermocouples

T-type thermocouples with a wire diameter of 0.25 mm and accuracy of 0.1 °C were used to measure the surface temperatures. The thermocouples of both test sections were calibrated in situ to an accuracy of 0.1 °C by pumping water from a thermostat-controlled bath through the flow-calming section, test section and mixer, and back into the thermostat-controlled bath. Reference temperatures were obtained using Pt100 probes at the inlet of the flow-calming section and at the outlet of the mixer, as well as a digital thermometer in the thermostat-controlled bath. The temperature of the thermostat-controlled bath was varied between 20 °C and 60 °C. The thermocouple calibration detail is presented in Appendix A.

3.6.3. Pressure transducers

Differential pressure transducers with interchangeable diaphragms were used to measure the pressure drops in the axial direction along the test section. DP103 pressure transducers were used to

measure the pressure drop across the 1.5 m and 2 m lengths, because diaphragms with a smaller full-scale (and thus higher accuracy) could be used in these pressure transducers. DP15 pressure transducers were used to measure the pressure drop across the other tube lengths. The accuracy of the diaphragms was 0.25% of the full-scale and different diaphragms were used to minimise the uncertainties of the pressure drop measurements. One set of diaphragms was used between Reynolds numbers of 500 and 4 000, and another set between Reynolds numbers of 2 000 and 10 000. The diaphragms with a full-scale smaller than 2.5 kPa were calibrated using a Betz manometer with an accuracy of 2.5 Pa, while the other diaphragms were calibrated using a low pressure controlled air manometer with an accuracy of 10 Pa. The details of the pressure transducer calibration are given in Appendix A.

3.6.4. Flow meters

Three Coriolis flow meters (flow meter bank A in Fig. 3.1) with different measurement ranges were used to measure the mass flow rates in the 11.5 mm test section. For low mass flow rates, a flow meter with a maximum flow rate of 108 ℓ/h was used. For mass flow rates between 60 ℓ/h and 130 ℓ/h, a flow meter with a maximum capacity of 330 ℓ/h was used, while a large flow meter with a maximum limit of 2 180 ℓ/h was used for the higher mass flow rates. The accuracy of the flow meters was 0.05% of the full-scale, thus the accuracy of the three flow meters was 0.054 ℓ/h, 0.165 ℓ/h and 1.09 ℓ/h respectively.

As the diameter of the 4 mm test section was significantly smaller than for the 11.5 mm test section, only a low-flow rate flow meter (flow meter B in Fig. 3.1) was used. This flow meter was located after the mixer and had a maximum flow rate of 108 ℓ/h and accuracy of 0.054 ℓ/h.

3.6.5. Power supply

Two direct current (DC) power supplies were used to heat the 11.5 mm test section. Both power supplies had a maximum power output of 3 kW, maximum voltage of 360 V and maximum current of 15 A. The accuracies of both measured voltages and currents were 0.2% of the nominal value. The maximum supplied power and voltage from each power supply were 525 W and 355 V respectively, at the maximum heat flux of 3 kW/m^2. In an effort to reduce the effect of electromagnetic interference caused by the currents through the coiled wires, two heating wires were connected, with opposing polarities, to each power supply. According to Lenz's law, the opposing directions of current flow should produce two opposing magnetic fields, which will, in turn, largely cancel each other out [100].

As the 4 mm test section was heated by passing current through the stainless tube, a different power supply, with a higher current output, was used. The power supply had a maximum power output of 3 kW, maximum voltage of 40 V and maximum current of 60 A. The electrical resistivity of the tube changed during testing due to the temperature changes. Therefore, current inputs were continuously adjusted to ensure that the desired constant heat flux was obtained throughout the experiments. To account for small variations, the power that was supplied to the test section was logged and averaged.

3.6.6. Control and data logging

The mass flow rate of the pump was controlled by frequency drives that were connected to a personal computer via a data acquisition system. The data acquisition system was used to record the data from the Pt100 probes (temperatures), thermocouples (temperatures), pressure transducers (pressure drops) and flow meters (mass flow rates). The data acquisition system consisted of a personal

computer using National Instruments LabVIEW software. The data acquisition system also consisted of SCXI (Signal Conditioning eXtensions for Instrumentation) hardware, which included terminal blocks, analogue-to-digital converters and multiplexers. A Mathworks MATLAB script was used for the data processing.

3.7. Data reduction

Because a constant heat flux boundary condition was applied to the test section, the average axial temperature of the water increased linearly. The mean fluid temperature, T_m, at a specific tube location, x, was obtained using a linear temperature distribution between the measured inlet, T_i, and measured outlet, T_o, temperatures of the fluid over the tube length, L:

$$T_m = \left(\frac{T_o - T_i}{L}\right) x + T_i \tag{3.1}$$

The bulk fluid temperature, T_b, along a tube length, $L(x)$, measured from the inlet of the test section, was calculated as:

$$T_b = \left(\frac{T_o - T_i}{L}\right) \frac{L(x)}{2} + T_i \tag{3.2}$$

The properties of water (density, ρ, dynamic viscosity, μ, thermal conductivity, k, specific heat, C_p, Prandtl number, Pr, and thermal expansion coefficient, β) were determined using the thermophysical correlations for liquid water [101] at the bulk fluid temperature for the average properties, and at the mean fluid temperature for the local properties at a specific point, x, measured from the inlet of the test section.

The Reynolds number, Re, was calculated as:

$$Re = \frac{\dot{m}D}{\mu A_c} \tag{3.3}$$

where $\dot{m}$ was the measured mass flow rate inside the tube, D was the inner-tube diameter, μ was the dynamic viscosity and A_c the cross-sectional area of the test section ($A_c = \pi/4D^2$).

The electrical input rate ($\dot{Q}_e = VI$) remained constant, resulting in a constant heat flux. The heat transfer rate to the water, $\dot{Q}_w$, was determined from the measured mass flow rate, measured inlet and outlet temperatures of the water and the specific heat, which was calculated at the bulk fluid temperature:

$$\dot{Q}_w = \dot{m}C_p(T_o - T_i) \tag{3.4}$$

The heat transfer rate to the water, $\dot{Q}_w$, was continuously monitored by comparing it with the electrical input rate, $\dot{Q}_e$, of the power supply, which should ideally be equal because the test section was well insulated. The energy balance error, EB, which ideally should be as close as possible to zero, was determined as:

$$EB = \left|\frac{\dot{Q}_e - \dot{Q}_w}{\dot{Q}_e}\right| \times 100 = \left|\frac{VI - \dot{m}C_p(T_o - T_i)}{VI}\right| \times 100 \tag{3.5}$$

The average energy balance error of all the experiments that were conducted was less than 3%, which was in good agreement with the calculations estimating the heat losses through the insulation material.

The heat flux, $\dot{q}$, on the inside of the tube wall was determined from the heat transfer rate to the water, $\dot{Q}_w$, and the inner-surface area, A_s, of the test section along the heated length, L:

$$\dot{q} = \frac{\dot{Q}_w}{A_s} = \frac{\dot{m}C_p(T_o - T_i)}{\pi DL} \quad 3.6$$

The heat transfer rate to the water was used to determine the heat flux, because it was regarded as more accurate than the electrical input rate. Because the energy balance error was not zero, and some losses did occur to the ambient air, the electrical input rate was always slightly higher than the heat transfer rate to the water.

The average of the n temperature measurements at a station (with n = 3 or n = 4) was used as the average outer surface temperature, $T_{s,o}$, at a specific thermocouple station:

$$T_{s,o} = \frac{T_1 + T_2 + \cdots + T_n}{n} \quad 3.7$$

The thermal resistance, R_{tube}, across the tube wall was calculated using the following equation:

$$R_{tube} = \frac{ln\left(\frac{D_o}{D}\right)}{2\pi Lk} \quad 3.8$$

where D_o and D were the measured outside and inside diameters of the tube.

The thermal conductivity of copper is 401 W/m.K, while the thermal conductivity of 316L stainless steel is only 16.3 W/m.K. The temperature differences across the tube wall, ΔT, were calculated using Eqs. 3.8 and 3.9, because the thermal resistance and heat input were known:

$$\Delta T = \dot{Q}_w R_{tube} \quad 3.9$$

The thermal resistance in the 11.5 mm test section was calculated to be 4.05×10^{-6} °C/W for the tube, because the wall thickness was 0.6 mm. Therefore, the temperature difference across the tube wall was approximately 0.004 °C when the maximum heat input (3 kW/m^2) was applied to the test section. The negligible temperature difference led to the assumption that the temperature on the inside surface of the test section was equal to the temperature measurement on the outside surface of the test section, because the temperatures in general could only be measured to an accuracy of 0.1 °C. It was therefore assumed that the surface temperature, determined from Eq. 3.7, was the average surface temperature on the inside of the tube at a measuring station in the 11.5 mm test section.

The thermal resistance in the 4 mm stainless steel tube was calculated to be 3.63×10^{-4} °C/W, which is two orders of magnitude more than in the 11.5 mm copper test section. Although the thermocouples in the 4 mm test section were placed in a 0.5 mm deep indentation in the tube wall, the temperature difference across the remaining 0.5 mm was approximately 0.2 °C when the maximum heat input (8 kW/m^2) was applied to the test section. Because this was not negligible, the temperature difference

calculated using Eqs. 3.8 and 3.9 was subtracted from the measured surface temperatures (Eq. 3.7) to obtain the temperature on the inside of the 4 mm test section.

From this, the inner-surface temperatures, T_s, of the test section were determined as:

$$T_s = T_{s,o} - \Delta T = T_{s,o} - \dot{Q}_w R_{tube} \quad 3.10$$

Because heat was applied to the 4 mm test section by passing current through the tube wall (and not using heating wire coiled around the outer surface of the tube), the finite difference formulations of Ghajar and Kim [102] could be used to determine the inner-surface temperatures. However, the simpler method of Morcos and Bergles [71], which consists of a two-dimensional conduction equation and also accounts for both radial and peripheral heat transfer, was used. The results were compared with those obtained using Eq. 3.9, and it was found that at the maximum heat flux of 8 kW/m^2, the difference was 0.1 °C but reduced to 0.01 °C when the heat flux was decreased to 1 kW/m^2. As this was within the uncertainty of the thermocouples (0.1 °C), it confirmed that Eq. 3.9 could provide reliable results. Therefore, similar to Morcos and Bergles [71], it was decided to use the simpler one-dimensional method (Eq. 3.9) in this study.

The average surface temperature, $\overline{T}_s$, along a tube length, $L(x)$, measured from the inlet of the test section, was calculated as:

$$\overline{T}_s = \frac{1}{L}\int_0^L T_s(x)\, dx \quad 3.11$$

The heat transfer coefficients, h, were then determined from the following equation, because the heat flux, $\dot{q}$, surface temperature, T_s, and mean fluid temperature, T_m, were known:

$$h = \frac{\dot{q}}{(T_s - T_m)} \quad 3.12$$

The Nusselt numbers, Nu, were determined from the heat transfer coefficients as follows:

$$Nu = \frac{hD}{k} \quad 3.13$$

The heat transfer results were also investigated in terms of the Colburn j-factors to account for the variations in the Prandtl numbers:

$$j = \frac{Nu}{RePr^{\frac{1}{3}}} \quad 3.14$$

The Graetz numbers, Gz, were determined as:

$$Gz = RePr\frac{D}{x} \quad 3.15$$

while the Grashof numbers, Gr, were determined using the following equation:

$$Gr = \frac{g\beta(T_s - T_m)D^3}{\nu^2} \quad (3.16)$$

where 9.81 m/s^2 was used for the gravitational acceleration, g, and the kinematic viscosity was obtained from the density and dynamic viscosity ($\nu = \mu/\rho$).

The modified Grashof numbers, Gr^*, which are a function of heat flux instead of temperature differences, are the product of the Grashof numbers and Nusselt numbers and were determined as follows:

$$Gr^* = GrNu = \frac{g\beta\dot{q}D^4}{\nu^2 k} \quad (3.17)$$

The Rayleigh numbers, Ra, were determined as the product of the Grashof numbers and Prandtl numbers:

$$Ra = GrPr \quad (3.18)$$

$$Ra^* = Gr^*Pr \quad (3.19)$$

The Richardson numbers, Ri, were determined from the Grashof and Reynolds numbers:

$$Ri = \frac{Gr}{Re^2} \quad (3.20)$$

$$Ri^* = \frac{Gr^*}{Re^2} \quad (3.21)$$

Eqs. 3.12-3.21 were for the local values at a specific axial position along the tube length. The average values along a tube length, $L(x)$, measured from the inlet of the test section, were obtained by using the bulk fluid temperature (Eq. 3.2) and average surface temperature (Eq. 3.11) instead of the mean fluid temperature (Eq. 3.1) and local surface temperature (Eq. 3.10).

The friction factors, f, were calculated from the mass flow rate and pressure drop measurements, ΔP, between two pressure taps, which were apart from each other a length $L(x)$, using the bulk fluid properties (Eq. 3.2):

$$f = \frac{2\Delta PD}{L(x)\rho_b V^2} = \frac{\Delta P\rho_b D^5\pi^2}{8\dot{m}^2 L(x)} \quad (3.22)$$

In general, in this study, the percentage error of a measurement or calculated value was determined as %error = $|M_{exp} - M_{cor}|/M_{ref} \times 100$. When the experimental set-up and data reduction method were validated in Chapter 4, M_{ref} was obtained from existing correlations in literature, M_{cor}. However, when the accuracies of the correlations and flow regime maps that were developed in Chapters 5-8 were determined, M_{ref} was obtained from the experimental data, M_{exp}. The average percentage error was taken as the average of the absolute errors of the data points.

3.8. Flow regime nomenclature

Although the Reynolds number boundaries between the laminar and transitional flow regimes have been described in literature, the descriptions are in general qualitative and relied on visual observations, which were subjective. Furthermore, in most of these cases, no clear distinction between the transitional and quasi-turbulent flow regimes was made. When large databases are collected, it is challenging to objectively and consistently identify the different boundaries. The result is that different transition outcomes can be generated by different people from the same data. Therefore, for the purposes of this study, the boundaries between the flow regimes, as well as terminology to define transitional flow characteristics, were quantified mathematically, in order to determine it computationally.

Fig. 3.6 is a schematic representation of the flow regimes in terms of the Nusselt numbers (Fig. 3.6(a)), Colburn *j*-factors (Fig. 3.6(b)) and friction factors (Fig. 3.6(c)) as a function of Reynolds number. The boundaries of the different flow regimes (Re_{cr}, Re_{qt} and Re_t) are indicated on the *x*-axis. Furthermore, the gradients of the Nusselt number (*dNu*/*dRe*), Colburn *j*-factor (*dj*/*dRe*) and friction factor (*df*/*dRe*) lines in the different flow regimes are defined along the *L*-*L*, *TG*-*TG*, *QT*-*QT* and *T*-*T* lines.

The boundaries of the transitional flow regime (Re_{cr} and Re_{qt}) could be identified from the standard deviation of the temperature and mass flow rate measurements (see, for example, Fig. 6.4 and Fig. 6.5). However, this could not be used to identify the start of the turbulent flow regime, Re_t, because there was no significant difference between the standard deviations of the mass flow rate and temperature measurements in the quasi-turbulent and turbulent flow regimes [37]. The Nusselt numbers and Colburn *j*-factors were used to define the boundaries of the different flow regimes, because these parameters are generally available (when the experimental data of other studies are analysed and investigated), while the temperature and mass flow rate measurements are not necessarily available. The results in terms of the Nusselt number and Colburn *j*-factor lines were used complementary, as it was found that some boundaries were easier to identify using the Nusselt number lines, and others using the Colburn *j*-factor lines. Furthermore, as will be shown in Fig. 7.5, the flow regime boundaries are the same for the pressure drop and heat transfer results. Therefore, the boundaries identified using the Nusselt number and Colburn *j*-factor results are also valid for the friction factor results.

3.8.1. Flow regime boundaries

3.8.1.1. Start of the transitional flow regime, Re_{cr}

The start of the transitional flow regime (and end of the laminar flow regime), Re_{cr}, was defined similarly to Ghajar and Tam [16] as:

$$Re = Re_{cr} \text{ when: } \left(\frac{dj}{dRe}\right)_{i-2:i} = 0 \qquad 3.23$$

The notation *i*-2:*i* indicates that at an arbitrary point *i*, the gradient was obtained using the three data points at *Re*(*i*-2), *Re*(*i*-1) and *Re*(*i*), for increasing Reynolds numbers. The effect of using less and more data points was investigated and it was found that three data points in general gave the best results.

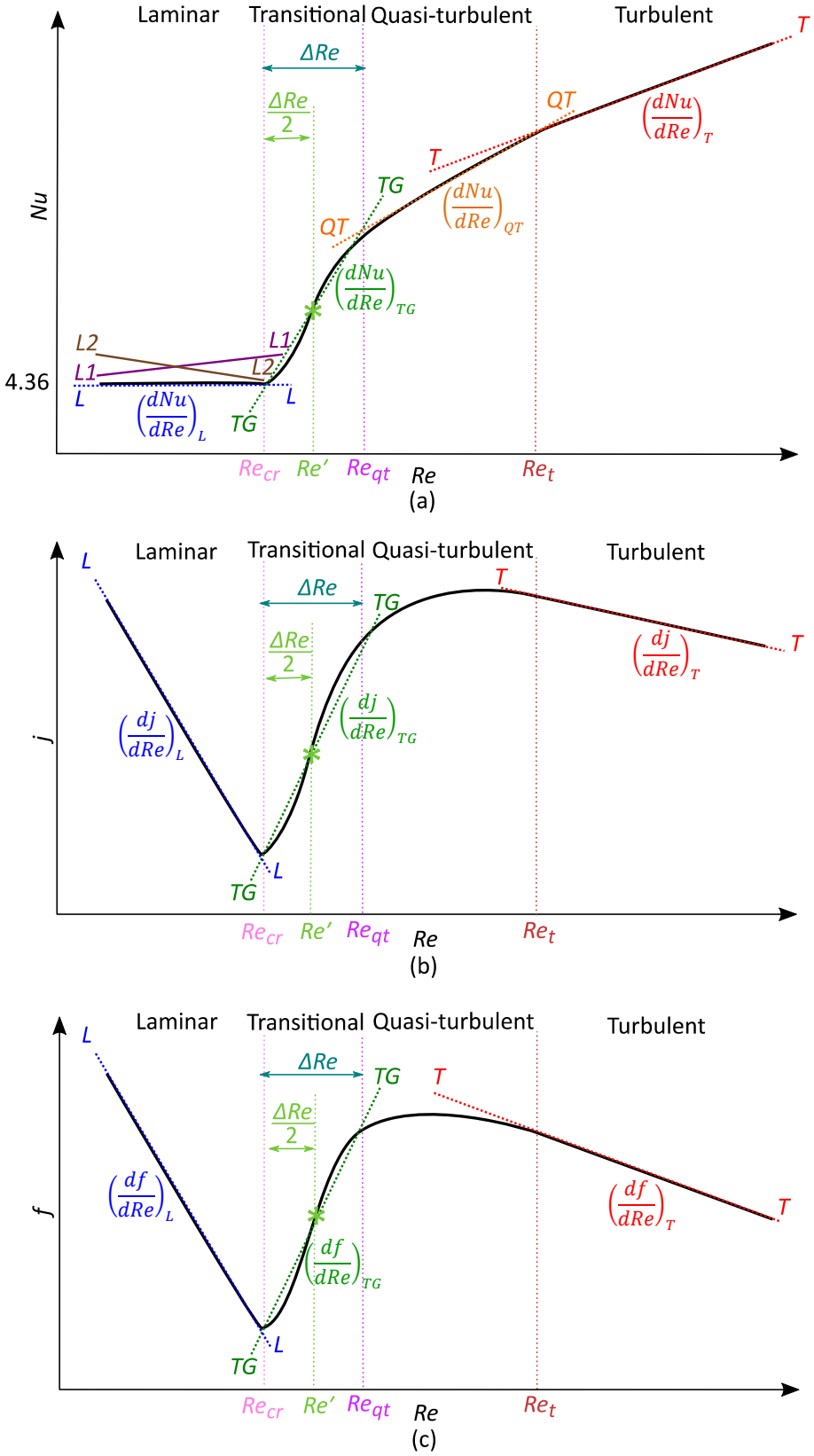

Fig. 3.6: Schematic representation of the different flow regimes in terms of (a) Nusselt number, (b) Colburn *j*-factor and (c) friction factor as a function of Reynolds number.

Figure 3.7 contains the Colburn *j*-factor gradients, *dj/dRe*, as a function of Reynolds number at *x/D* = 98 and heat flux of 3 kW/m^2 in the 11.5 mm test section. Figure 3.7 indicates that the critical Reynolds number was at 2 540, where the gradient changed from negative (laminar flow) to positive (transitional flow).

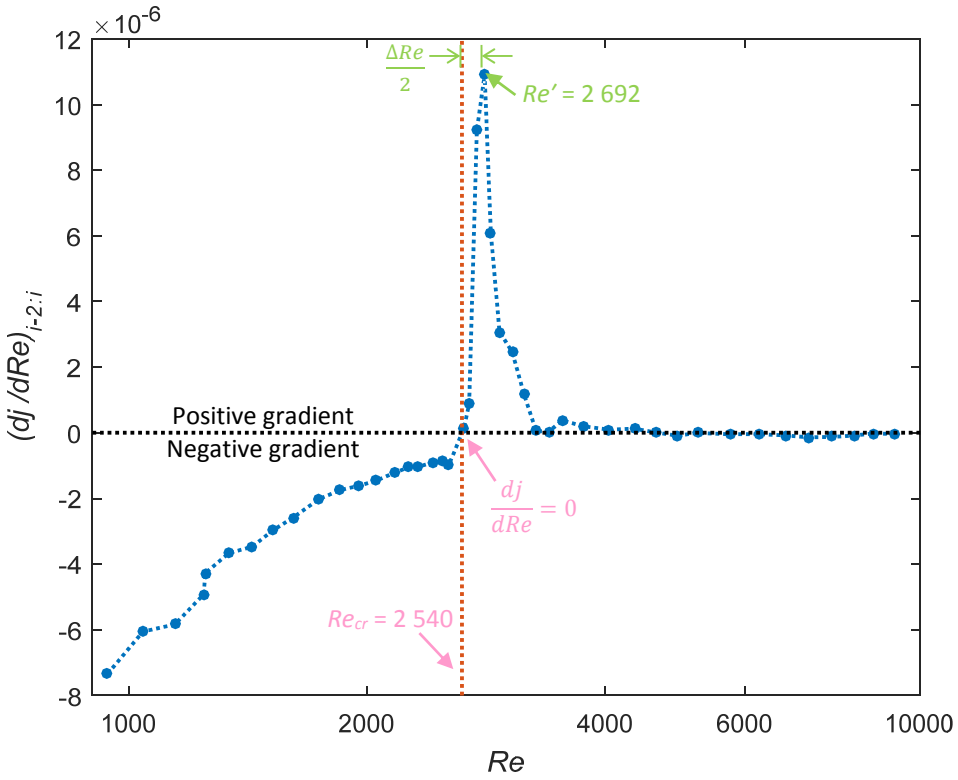

Fig. 3.7: Colburn *j*-factor gradient as a function of Reynolds number to obtain the start of the transitional flow regime at *x/D* = 98 and a heat flux of 3 kW/m^2 in the 11.5 mm test section.

3.8.1.2. Start of the quasi-turbulent flow regime, Re_{qt}

The end of transition (Re_{qt}), which is also the start of the quasi-turbulent flow regime, was not as clear and easy to identify as the start of transition. This challenge also had implications for accurately identifying the start of the turbulent flow regime (Re_t in Section 3.8.1.3). This possibly explains why, in literature, the quasi-turbulent flow regime is often regarded as part of either the transitional or turbulent flow regimes. However, as was found by Everts [75], as well as in Chapters 6 and 7, the flow characteristics and heat transfer coefficients in the quasi-turbulent flow regime are unique and not exactly the same as the transitional or turbulent flow regimes. The flow characteristics are similar to turbulent flow, because there is a negligible difference between the standard deviation of the temperature measurements in the quasi-turbulent and turbulent flow regimes [37]. However, the heat transfer coefficients in the quasi-turbulent flow regime are overpredicted by turbulent heat transfer correlations. Because the flow is not fully turbulent yet, this flow regime was named quasi-turbulent. The start of the quasi-turbulent flow regime was defined as:

$$Re = Re_{qt} \text{ when: } \left(\frac{d^2Nu}{dRe^2}\right)_{i:i+2} \geq -0.00015 \qquad 3.24$$

The notation *i*:*i*+2 indicates that at an arbitrary point *i*, the gradient was obtained using the three data points at *Re*(*i*), *Re*(*i*+1) and *Re*(*i*+2) for increasing Reynolds numbers (while Eq. 3.23 used the results at the previous two Reynolds numbers).

Figure 3.8(a) and (b) contain the Nusselt number gradients (dNu/dRe) and gradient of the Nusselt number gradients (d^2Nu/dRe^2) respectively, as a function of Reynolds number at x/D = 98 and heat flux of 3 kW/m^2 in the 11.5 mm test section. Figure 3.8(a) indicates that the start of the quasi-turbulent flow regime corresponded to the point where the trend of the gradient of the line dNu/dRe changed. From Fig. 3.8(b), it follows that the quasi-turbulent flow regime started at a Reynolds number of 3 052 where d^2Nu/dRe^2 was approximately -6.9×10^{-5}. Similar graphs were generated for all the thermocouple stations at all heat fluxes in both test sections, and it was found that the quasi-turbulent flow regime started when d^2Nu/dRe^2 was greater than -0.00015. It was found that this could be used as a satisfactory general criterion for almost all data.

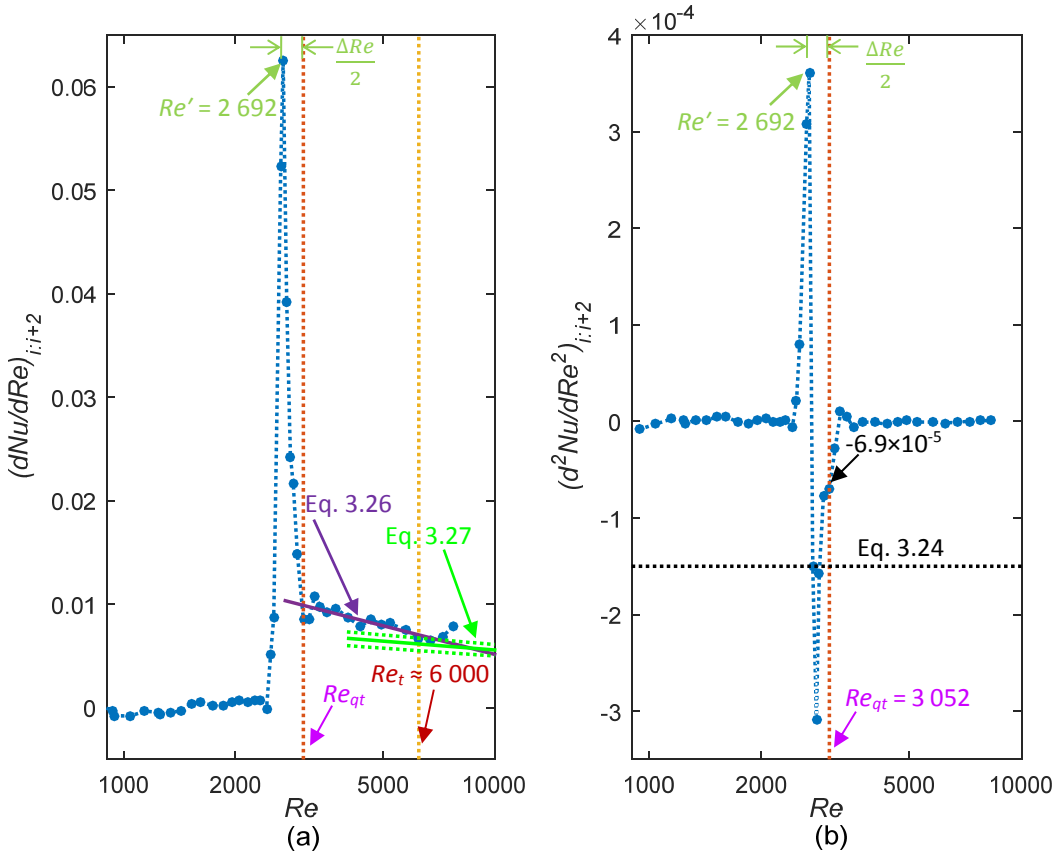

Fig. 3.8: (a) Nusselt number gradient and (b) gradient of Nusselt number gradients, as a function of Reynolds number at x/D = 98 and a heat flux of 3 kW/m^2 in the 11.5 mm test section.

3.8.1.3. Start of the turbulent flow regime, Re_t

The Reynolds number that corresponded to the start of the turbulent flow regime was the most challenging to obtain. The flow is considered as fully turbulent, once the Nusselt number and Colburn *j*-factor lines fall onto or become parallel to the heat transfer coefficients predicted by fully turbulent correlations, for example, the Colburn equation [3]. Although it follows from Fig. 3.8(a) that this Reynolds number corresponded to the point where the trend of the Nusselt number gradients changed (gradient decreased and became approximately constant), it was challenging to quantify it mathematically/numerically. It was found that the start of the turbulent flow regime (and end of

quasi-turbulent flow regime), Re_t, could be defined as the Reynolds number at the intersection of the trendlines through the Nusselt number gradients in the quasi-turbulent ($(dNu/dRe)_{QT}$) and the turbulent ($(dNu/dRe)_T$) flow regimes:

$$Re = Re_t \text{ when: } \left(\frac{dNu}{dRe}\right)_{QT} = \left(\frac{dNu}{dRe}\right)_T \quad 3.25$$

where

$$\left(\frac{dNu}{dRe}\right)_{QT} = 0.7054Re^{-0.534} \quad 3.26$$

$$\left(\frac{dNu}{dRe}\right)_T = 0.0352Re^{-0.2} \quad 3.27$$

Equation 3.26 was obtained by doing a power curve fit through all the Nusselt number gradients in the quasi-turbulent flow regime ($Re_{cr} < Re < 6\,000$) of all the thermocouple stations at the different heat fluxes in both test sections, and is represented by the solid purple line in Fig. 3.8(a). Equation 3.27 was obtained by taking the derivative of the Colburn equation [3] (which is valid for fully turbulent flow) with respect to Reynolds number, and is indicated by the solid green line in Fig. 3.8(a). Due to the relatively high uncertainties (because of the small temperature differences) in the turbulent flow regime, an uncertainty of 10% is indicated by the dotted green lines. From Fig. 3.8(a), it followed that the flow became fully turbulent at a Reynolds number of approximately 6 000, with an uncertainty of approximately 10%. Because a single trend line (Eq. 3.26) was obtained through all the data in the quasi-turbulent flow regime, this value was true for all the results. However, this can be refined with experimental data (with low uncertainties, especially in the quasi-turbulent and turbulent flow regimes) by obtaining individual trendlines through data in the quasi-turbulent flow regime.

3.8.2. Flow characteristics

3.8.2.1. Laminar flow regime

As summarised in Fig. 5.1(a), the local laminar Nusselt numbers can be divided into three regions: forced convection developing (FCD), mixed convection developing (MCD) and fully developed (FD). The trend of the Nusselt numbers as a function of Reynolds number is significantly affected by the heat transfer characteristics of these three regions.

3.8.2.1.1. Forced convection developing (FCD)

When the flow is still developing, the local Nusselt numbers decrease along the tube length, as the thermal boundary layer develops (entrance effects). As the thermal boundary layer thickness is very thin in this region, free convection effects are negligible. The thermal entrance length increases with increasing Reynolds number, therefore at a fixed axial position, the thermal boundary layer thickness decreases and the Nusselt numbers increase. The Nusselt numbers therefore increase with increasing Reynolds number and form a diagonal line with a positive gradient (line *L*1-*L*1 in Fig. 3.6):

$$\frac{dNu}{dRe} > 0 \quad 3.28$$

3.8.2.1.2. Mixed convection developing (MCD)

In this region, the thermal boundary layer thickness is sufficient for free convection effects to be significant. As the flow is still developing, the thermal boundary layer thickness increases along the

tube length. It is shown in Fig. 5.6 that free convection effects decrease the thermal entrance length, therefore at a fixed axial position, the thermal boundary layer thickness increases and the Nusselt number decreases (entrance effects). However, free convection effects increase with increasing thermal boundary layer thickness, which may lead to increasing Nusselt numbers along the tube length (free convection effects).

When the decrease in Nusselt number (due to the shorter thermal entrance length) is more than the increase due to free convection effects, entrance effects dominate and $(dNu/dRe)_L > 0$ (Eq. 3.28). However, when free convection effects dominate the entrance effects, the Nusselt numbers decrease with increasing Reynolds number, because the thermal boundary layer thickness and free convection effects decrease (line *L*2-*L*2 in Fig. 3.6):

$$\frac{dNu}{dRe} < 0 \qquad 3.29$$

3.8.2.1.3. Fully developed (FD)

For fully developed forced convection flow, the Nusselt numbers form a horizontal line and should be equal to 4.36:

$$\frac{dNu}{dRe} = 0 \qquad 3.30$$

When the flow is dominated by mixed convection, the Nusselt numbers should be greater than 4.36. The Nusselt numbers decrease with increasing Reynolds number, because the free convection effects decrease, therefore $(dNu/dRe)_L < 0$ (Eq. 3.29).

3.8.2.2. Transitional flow regime

Previous work that has been done on flow in the transitional flow regime concludes that the transitional flow regime can be manipulated by changing the inlet geometry and heat flux, and that it varies when different locations on the test section are considered. In order to quantify these changes in the transitional flow regime, the width of the transitional flow regime, ΔRe, and the transition gradients, TG_f and TG_j, are defined.

3.8.2.2.1. Width of the transitional flow regime

The width of the transitional flow regime represents the Reynolds number range in which transition occurs:

$$\Delta Re = Re_{qt} - Re_{cr} \qquad 3.31$$

3.8.2.2.2. Transition gradient

The transition gradient, TG_j (indicated by the dotted green *TG*-*TG* line in Fig. 3.6(b)), represents the straight line between the Colburn *j*-factors at the start (Re_{cr}) and end (Re_{qt}) of the transitional flow regime:

$$TG_j = \frac{j_{qt} - j_{cr}}{Re_{qt} - Re_{cr}} \qquad 3.32$$

Similarly, the transition gradient for friction factors represents the straight line between the friction factors at the start (Re_{cr}) and end (Re_{qt}) of the transitional flow regime:

$$TG_f = \frac{f_{qt} - f_{cr}}{Re_{qt} - Re_{cr}} \quad 3.33$$

The transition gradients give good indications of how the heat transfer and pressure drop characteristics change in the transitional flow regime.

3.8.2.2.3. Transitional flow inflection point, *Re'*

Figures 3.7 and 3.8(a) indicate that when *dNu/dRe* is plotted as a function of Reynolds number, *dNu/dRe* reaches a prominent maximum at *Re'*, which is in the middle of the transitional flow regime. Furthermore, when d^2Nu/dRe^2 is plotted as a function of Reynolds number in Fig. 3.8(b), it follows that in the transitional flow regime the gradient first increases with increasing Reynolds number up to a maximum, then it decreases (to negative gradients) to a minimum at the next Reynolds number increment, before it increases again. Therefore, the inflection point in the transitional flow regime is where d^2Nu/dRe^2 changes from the maximum to the minimum.

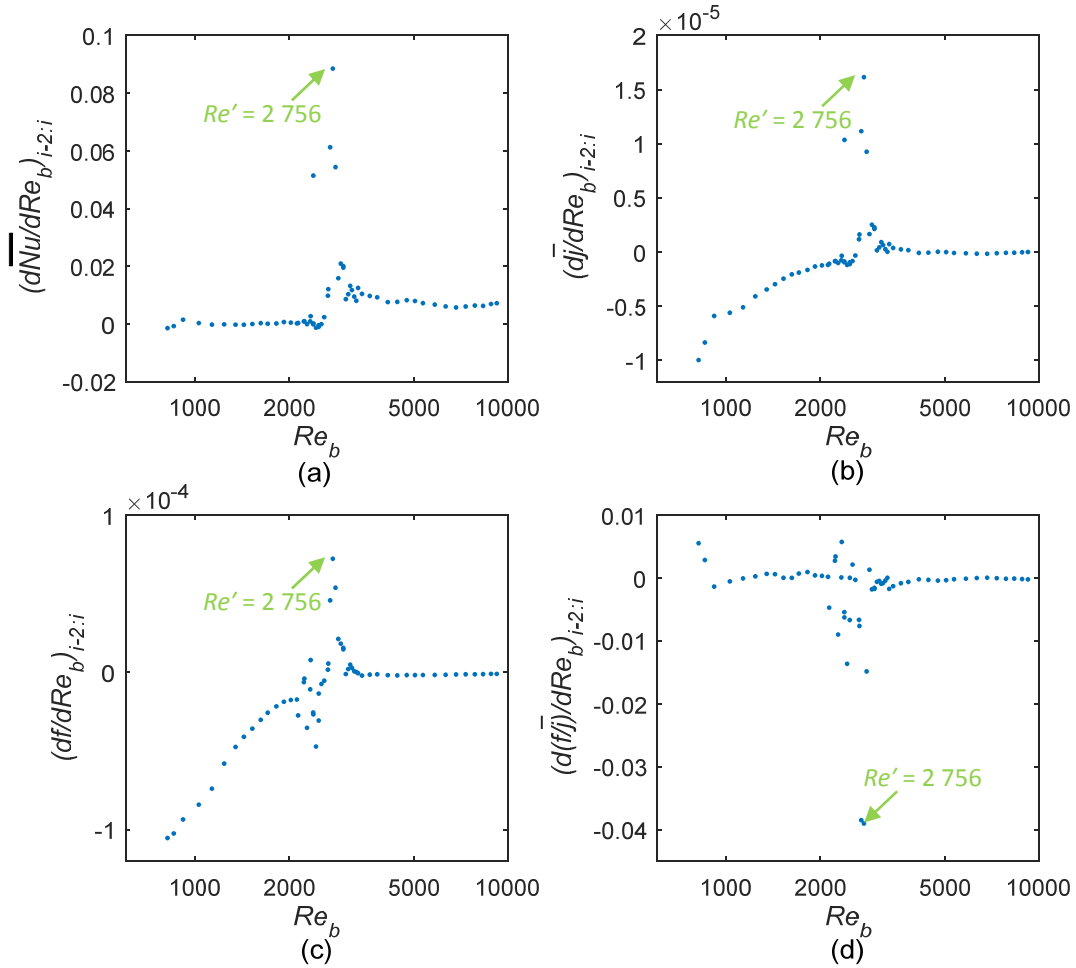

Fig. 3.9: Gradients of the average (a) Nusselt numbers, (b) Colburn *j*-factors, (c) friction factors and (d) *f/j*-factors, as a function of bulk Reynolds number for 0 m < *L* < 2 m at a heat flux of 1 kW/m², to identify the inflection point in the transitional flow regime.

Figure 3.9 shows the gradients of the average Nusselt numbers, Colburn *j*-factors, friction factors and *f*/*j*-factors as a function of bulk Reynolds number for 0 m < *L* < 2 m at a heat flux of 1 kW/m^2. From this figure, it follows that all the gradients reach a maximum at a bulk Reynolds number of 2 756. Therefore, the inflection point does not only exist in the heat transfer results, but also the in the pressure drop results, as well as in the relationship between pressure drop and heat transfer results.

From Fig. 3.6, it follows that the Nusselt numbers, Colburn *j*-factors and friction factors increase in the transitional flow regime. However, as schematically indicated (and exaggerated) by the 's'-curve in Fig. 3.6, it follows from Fig. 3.7 to Fig. 3.9 that the increase in heat transfer coefficients and friction factors with increasing Reynolds number, increases with increasing Reynolds number in the lower half of the transitional flow regime and then decreases in the upper half as the flow approaches the quasi-turbulent flow regime.

The inflection point in the transitional flow regime is where the trend of the flow characteristics changes and is in the middle of the transitional flow regime:

$$Re' = \frac{Re_{cr} + Re_{qt}}{2} = Re_{cr} + \frac{\Delta Re}{2} \qquad 3.34$$

It was found that the inflection point predicted using Eq. 3.34 is within 4% of the middle of the transitional flow regime (obtained using Eqs. 3.23 and 3.24). Therefore, as Re_{cr} and *Re*' are simpler to obtain than Re_{qt}, Eq. 3.34 can also be used to obtain the start of the quasi-turbulent flow regime. For this study, the physical mechanism of *Re*' was not investigated.

3.8.2.3. Quasi-turbulent flow regime

Not much research has been devoted to the heat transfer and pressure drop characteristics in this flow regime and it is often regarded as part of the transitional flow regime because the flow is not fully turbulent yet [76]. Although the heat transfer characteristics are closer to those of turbulent flow, an extension of the straight line (on a log-log scale) of the turbulent Nusselt numbers as a function of Reynolds number overpredicts the Nusselt numbers in this regime [7], therefore $(dNu/dRe)_{QT} > (dNu/dRe)_T$. Figure 3.8(a) indicates that *dNu*/*dRe* decreases from 0.0098 to 0.0066, as the Reynolds number is increased and the flow approaches fully turbulent flow. The Nusselt numbers in the quasi-turbulent flow regime increase with increasing Reynolds number and form a diagonal line (Fig. 3.6(a)). However, the Colburn *j*-factors in this regime increase and then decrease slightly with increasing Reynolds number, forming a concave curve as the flow regime changes from transitional to fully turbulent (Fig. 3.6(b)).

3.8.2.4. Turbulent flow regime

The Colburn *j*-factor is proportional to Nusselt number, but inversely to Reynolds number. Therefore, although the turbulent Nusselt numbers increase with increasing Reynolds number, the increase in Nusselt number is less than the increase in Reynolds number, which leads to decreasing Colburn *j*-factors in the turbulent flow regime.

3.9. Uncertainties

The method suggested by Dunn [103] was used to calculate the uncertainties of the parameters obtained in the data reduction. All uncertainties were calculated within the 95% confidence interval.

The uncertainty analysis method and results are given in Appendix B. Table 3.2 summarises the instruments with their ranges and accuracies, as specified by the manufacturers.

Table 3.2: Ranges and accuracies of measuring instruments.

Instrument	Range	Accuracy
Pt100 probe	-100 °C – 250 °C	0.06 °C
Thermocouple	< 150 °C	0.1 °C
Flow Meter		
CMFS010	0 – 110 ℓ/h	0.055 ℓ/h
CMFS015	0 – 330 ℓ/h	0.165 ℓ/h
CMF025	0 – 2 180 ℓ/h	1.09 ℓ/h
Pressure Transducer		
0.55 kPa diaphragm	0 – 0.55 kPa	1.375 Pa
0.86 kPa diaphragm	0 – 0.86 kPa	2.15 Pa
1.4 kPa diaphragm	0 – 1.4 kPa	3.5 Pa
2.2 kPa diaphragm	0 – 2.2 kPa	5.5 Pa
3.5 kPa diaphragm	0 – 3.5 kPa	8.75 Pa
5.5 kPa diaphragm	0 – 5.5 kPa	13.75 Pa
8.6 kPa diaphragm	0 – 8.6 kPa	21.5 Pa

The results of the uncertainty analysis are summarised in Table 3.3 for three different heat fluxes in the 4 mm and 11.5 mm test sections. The nomenclature defined in Section 3.8 was used to distinguish the different flow regimes. It should be noted that although the Nusselt number, Colburn *j*-factor, Grashof number, Rayleigh number and Richardson number uncertainties at a heat flux of 1 kW/m^2 in the 4 mm test section were high in the quasi-turbulent flow regime, the focus of these forced convection results were on the laminar and turbulent flow regimes. Measurements were only taken up to the quasi-turbulent flow regime to ensure that the entire transitional flow regime was covered.

Table 3.3 indicates that the Reynolds number uncertainty was less than 2% in all four flow regimes and was not significantly affected by heat flux. Similarly, the uncertainty of the Graetz number did not change significantly with heat flux or Reynolds number. However, it was less for the 11.5 mm test section because the larger tube diameter and longer tube length led to decreased uncertainties.

The magnitude and trend of the Nusselt number and Colburn *j*-factor uncertainties were similar. The uncertainties remained approximately constant in the laminar flow regime, but decreased with increasing heat flux and tube diameter. The laminar forced and mixed convection uncertainties were less than 10% and 5% respectively. In the transitional flow regime, the temperature fluctuations caused the uncertainties to increase to approximately 10% (depending on the heat flux). The uncertainties in the quasi-turbulent and turbulent flow regimes increased with increasing Reynolds number and the average Nusselt number uncertainty at a Reynolds number of 6 000 was 13%.

The trends of the Grashof number, Rayleigh number and Richardson number were similar. As the Rayleigh number is proportional to *Gr* and the Richardson number proportional to Gr^2, the Rayleigh number uncertainties were slightly higher and the Richardson number uncertainties significantly higher than the Grashof number uncertainties. In the laminar flow regime, the Grashof number uncertainties at a heat flux of 1 kW/m^2 in the 4 mm test section were approximately 8%, but decreased to 6% when the heat flux was increased to 3 kW/m^2. As the tube diameter was increased to 11.5 mm, the Grashof number uncertainties at a heat flux of 3 kW/m^2 decreased further to approximately 2%.

This was mainly due to the increasing surface-fluid temperature differences that led to decreased temperature uncertainties. As the Reynolds number was increased, the surface-fluid temperature difference decreased, which caused the Grashof number uncertainties at a heat flux of 3 kW/m^2 in the 11.5 mm test section to increase to up to 4.5% and 6.6% in the quasi-turbulent and turbulent flow regimes respectively. In the transitional flow regime, the uncertainties were also higher (up to 5.2% at a heat flux of 3 kW/m^2 in the 11.5 mm test section), due to the temperature fluctuations.

Table 3.3: Uncertainty analysis results (in percentage, %) for three heat fluxes in the 4 mm and 11.5 mm test sections.

		4 mm			11.5 mm		
		1 kW/m^2	3 kW/m^2	8 kW/m^2	1 kW/m^2	2 kW/m^2	3 kW/m^2
Re	Laminar	1.5 - 1.6	1.5 - 1.6	1.5 - 1.6	1.1 - 2.1	1.1 - 1.5	1.1 - 1.4
	Transition	1.5 - 1.7	1.5 - 1.7	1.5 - 2.4	1.1	1.1	1.1
	Quasi-turbulent	1.5	1.5	1.5	1.1	1.1	1.1
	Turbulent	-	1.5	1.5	1.1	1.1	1.1
Gz	Laminar	5.3	5.3	5.3	2.6 - 3.1	2.5 - 2.8	2.5 - 2.7
	Transition	5.3	5.3	5.3 - 5.6	2.5 - 2.6	2.5 - 2.6	2.5 - 2.6
	Quasi-turbulent	5.3	5.3	5.3	2.5 - 2.6	2.5 - 2.6	2.5 - 2.6
	Turbulent	-	5.3	5.3	2.5	2.5	2.5 - 2.6
Nu	Laminar	5.1 - 5.6	2.7 - 2.9	2.2 - 2.3	3.9 - 4.1	3.0 - 3.1	3.0 - 3.2
	Transition	5.3 - 17	2.7 - 8.5	2.2 - 9.8	4.0 - 12	3.0 - 9.5	3.0 - 5.6
	Quasi-turbulent	19 - 79	7.1 - 19	3.7 -6.5	6.5 - 12	4.0 - 6.2	3.6 - 4.6
	Turbulent	-	20 - 22	6.7 - 9.3	12 - 17	6.1 - 9.3	4.9 - 6.6
j	Laminar	5.4 – 5.9	3.2 - 3.4	2.8 - 2.9	4.1 - 4.6	3.3 - 3.5	3.0 - 3.2
	Transition	5.6 - 18	3.2 - 8.7	2.8 - 10	4.2 - 13	3.3 - 9.6	3.0 - 5.6
	Quasi-turbulent	19 - 79	7.3 - 19	4.07 - 6.7	6.6 - 12	4.2 - 6.3	3.6 - 4.6
	Turbulent	-	20 - 22	6.9 - 9.5	12 - 17	6.3 - 9.3	4.9 - 6.6
Gr	Laminar	7.6 - 8.0	6.3	6.1	3.1 - 3.3	2.5 - 2.7	2.3 - 2.5
	Transition	7.9 - 19	6.3 - 9.4	6.1 - 10	3.2 - 12	2.5 - 9.2	2.3 - 5.2
	Quasi-turbulent	20 - 79	8.1 - 20	6.5 - 7.7	6.4 - 13	3.8 - 6.3	3.1 - 4.5
	Turbulent	-	21 - 23	7.8 - 9.3	13 - 18	6.4 - 9.6	4.8 - 6.6
*Gr**	Laminar	8.5 - 9.0	8.4	8.4	3.2 - 3.9	3.1 - 3.3	3.0 - 3.1
	Transition	8.9 - 10	8.4 - 9.0	8.4 - 9.7	3.9 - 8.3	3.3 - 7.0	3.1 - 3.8
	Quasi-turbulent	9.1 - 13	8.4 - 8.9	8.4	4.2 - 6.9	3.3 - 4.1	3.1 - 3.5
	Turbulent	-	8.9 - 9.1	8.4 - 8.5	6.9 - 10	4.2 - 5.8	3.6 - 4.4
Ra	Laminar	8.0 - 8.4	6.7	6.5	3.8 - 4.0	3.4 - 3.5	3.3 - 3.4
	Transition	8.2 - 19	6.7 - 9.7	6.5 - 11	3.9 - 12	3.4 - 9.4	3.3 - 5.7
	Quasi-turbulent	20 - 79	8.5 - 20	6.9 - 8.0	6.8 - 13	4.5 - 6.7	3.9 - 5.0
	Turbulent	-	21 - 24	8.1 - 9.6	13 - 18	6.8 - 9.8	5.3 - 7.0
*Ra**	Laminar	8.8 - 9.2	8.7	8.7	3.9 - 4.5	3.8 - 4.0	3.8 - 3.9
	Transition	9.2 - 10	8.7 - 9.4	8.7 - 10	4.6 - 8.6	4.0 - 7.4	3.8 - 4.4
	Quasi-turbulent	9.4 - 13	8.8 - 9.2	8.7	4.8 - 7.3	4.0 - 4.7	3.9 - 4.2
	Turbulent	-	9.2 - 9.4	8.7 - 8.8	7.3 - 10	4.8 - 6.3	4.3 - 5.0
Ri	Laminar	12	11	11	3.8 - 5.3	3.3 - 4.0	3.2 - 3.8
	Transition	12 - 21	11 - 13	11 - 14	3.8 - 12	3.4 - 9.4	3.2 - 5.7
	Quasi-turbulent	22 - 80	12 - 22	11 - 12	6.8 - 13	4.4 - 6.7	3.8 - 5.0
	Turbulent	-	23 - 25	12 - 13	13 - 18	6.8 - 9.8	5.3 - 7.0
*Ri**	Laminar	12	12	12	4.1 - 5.5	3.8 - 4.3	3.7 - 4.3
	Transition	12 - 13	13	12 - 14	4.5 - 8.6	4.0 - 7.4	3.8 - 4.3
	Quasi-turbulent	13 - 15	12 - 13	12	4.7 - 7.2	3.9 - 4.6	3.8 - 4.1
	Turbulent	-	13	12	7.2 - 10	4.8 - 6.2	4.2 - 4.9

Because the modified Grashof numbers, modified Rayleigh numbers and modified Richardson numbers are a function of heat flux (which remained constant) and not temperature difference (which decreased with increasing Reynolds number), the uncertainties did not change significantly as the Reynolds number was increased from laminar to turbulent flow. However, as expected, it decreased significantly with increasing heat flux and tube diameter.

Table 3.4: Friction factor uncertainties (in percentage, %) in the 11.5 mm test section at different heat fluxes.

		0 kW/m^2	1 kW/m^2	2 kW/m^2	3 kW/m^2
0 m < *L* < 2 m	Laminar	2.9 – 15	2.8 - 16	2.8 – 11	2.9 – 11
	Transition	2.8 – 7.4	4.5 - 17	4.0 – 9.4	4.5 – 15
	Quasi-turbulent	1.1 – 6.0	2.2 - 4.3	2.1 – 4.4	2.0 – 3.8
	Turbulent	1.0 – 2.5	1.0 - 3.2	1.0 - 3.5	1.1 – 2.3
0 m < *L* < 3 m	Laminar	2.5 – 11	7.5 - 57	7.6 – 43	7.7 – 39
	Transition	3.1 – 9.5	5.0 - 20	6.3 – 12	5.6 – 13
	Quasi-turbulent	1.2 – 6.3	2.7 - 5.0	2.6 – 5.2	2.8 – 5.0
	Turbulent	1.4 – 3.9	1.5 - 3.4	1.4 – 3.3	1.4 – 3.2
0 m < *L* < 4 m	Laminar	3.0 – 16	1.9 - 11	2.2 – 11	2.5 – 36
	Transition	1.9 – 10	3.9 - 11	5.6 – 11	5.6 – 13
	Quasi-turbulent	1.0 – 6.0	1.8 - 3.7	1.7 – 4.4	2.8 – 5.0
	Turbulent	1.0 - 2.5	1.0 - 2.5	1.0 - 2.6	1.4 - 3.2
0 m < *L* < 5 m	Laminar	9.5 – 46	1.6 - 8.7	1.9 – 8.6	2.2 – 36
	Transition	5.0 – 13	3.7 - 12	6.1 – 10	4.4 – 16
	Quasi-turbulent	2.4 – 7.4	1.8 - 3.5	1.8 – 4.6	2.0 – 5.2
	Turbulent	1.4 - 3.8	1.1 – 2.4	1.1 – 2.6	1.1 – 2.1
0 m < *L* < 6 m	Laminar	3.1 – 16	1.5 – 7.6	1.8 – 23	2.0 – 36
	Transition	3.0 – 7.1	3.1 – 12	4.1 – 10	4.3 – 13
	Quasi-turbulent	1.0 – 5.9	1.7 – 3.0	1.6 – 3.7	1.7 – 4.2
	Turbulent	1.0 - 2.5	1.0 – 2.3	1.0 – 2.5	1.0 – 1.9
0 m < *L* < 7 m	Laminar	9.8 – 52	1.4 – 7.2	1.7 – 6.8	2.0 – 36
	Transition	6.0 – 11	3.1 – 8.7	3.6 – 7.3	3.9 – 11
	Quasi-turbulent	2.4 – 7.4	1.7 – 2.9	1.7 – 3.4	1.8 – 4.0
	Turbulent	1.4 – 3.8	1.0 – 2.4	1.0 – 2.5	1.0 – 2.0
0 m < *L* < 8 m	Laminar	3.2 – 16	1.5 – 6.7	1.8 – 8.1	2.0 – 7.5
	Transition	2.9 – 8.5	2.9 – 7.3	3.3 – 7.4	3.8 – 9.3
	Quasi-turbulent	1.1 – 5.9	1.9 – 2.9	1.9 – 3.3	2.1 – 3.8
	Turbulent	1.0 - 2.5	1.3 – 2.8	1.2 – 2.8	1.2 – 2.6
8 m < *L* < 9.5 m	Laminar	10 – 54	4.2 – 27	4.5 – 20	4.8 – 15
	Transition	7.0 – 12	-	-	-
	Quasi-turbulent	2.4 – 10	1.6 – 4.9	1.6 – 4.1	1.7 – 3.9
	Turbulent	1.4 – 3.8	1.0 – 2.1	1.0 – 2.3	1.0 – 1.8

Table 3.4 summarises the friction factor uncertainties at different heat fluxes for different tube lengths in the 11.5 mm test section. The laminar friction factor uncertainties across the tube lengths 0 m < *L* < 2 m, 0 m < *L* < 3 m and 8 m < *L* < 9.5 m were higher (average uncertainty of 13%) than for the other tube lengths. This was due to the limitations of the pressure transducer diaphragms, because smaller suitable diaphragms were not commercially available. The laminar friction factor uncertainties for the other tube lengths were approximately 10% at the minimum Reynolds number and decreased to approximately 2%. In the transitional flow regime, the mass flow rate fluctuations caused the

uncertainties to increase to 16%, while the uncertainties in the turbulent flow regime were less than 4%.

3.10. Experimental procedure

Steady-state conditions were reached after approximately one hour after initiating an experiment. Steady-state conditions were assumed once there was no increase or decrease in temperatures, pressure drops and mass flow rates, within a period of approximately two minutes. Different time periods were considered and a period of approximately two minutes was found to be sufficient. After the initial steady state was achieved, the mass flow rate was increased in large increments in the laminar and turbulent regions, and in smaller increments in the regions where transition was noticed. The time required to reach steady state depended on the mass flow rate inside the test section and the heat flux. In the laminar flow regime, at very low Reynolds numbers, approximately 30 minutes was required to reach steady-state conditions. As the mass flow rate was increased, the time required for steady state decreased to 20 minutes. Although the mass flow rates in the transitional flow regime were greater than in the laminar flow regime, up to one hour was required to reach steady state due to the mass flow rate and temperature fluctuations inside the tube. In the quasi-turbulent and turbulent flow regimes, approximately 15 minutes was required to reach steady state. Data were only captured once steady-state conditions were obtained.

According to Olivier and Meyer [9] and Meyer [7], the effects of hysteresis are negligible in the transitional flow regime; therefore, the experiments were only conducted for increasing Reynolds numbers. Due to the large number of data points, as well as the time required to reach steady state, the experiments were divided into two categories: experiments were first conducted for laminar and transitional flow between Reynolds numbers of 500 and 4 000, and then for transitional, quasi-turbulent and turbulent flow between Reynolds numbers of 2 000 and 10 000. The experiments started at the minimum mass flow rate (corresponding to Re = 500 or Re = 2 000) and ended at the maximum flow rate (corresponding to Re = 4 000 or Re = 10 000). The Reynolds number was increased by increasing the mass flow rate using the frequency drives connected to the pumps. The supply and bypass valves were continuously adjusted to ensure that the pumps operated close to their maximum speeds, to reduce mass flow rate pulsations. Different heat fluxes were applied to the test sections by adjusting the applied voltage of the power supplies. After steady state had been reached, 200 measuring points (temperature, pressure and mass flow rate) were captured at a frequency of 10 Hz. The average value of the 200 measuring points was then used as one data point in the calculations.

The thermocouples and pressure transducers were recalibrated every six months to prevent any experimental drift, and the differences between the calibration factors were found to be insignificant. To ensure that the results are reliable and repeatable, the experiments were repeated two or three times and the difference in the results was less than 2% in the laminar, quasi-turbulent and turbulent flow regimes and approximately 5% in the transitional flow regime. Furthermore, statistical significant experiments were conducted three years later after the initial experiments and compared well with the initial measurements. This indicated that no significant drift in the instrumentation and experiments occurred.

3.11. Experimental test matrix

Table 3.5 summarises the experiments conducted at different mass flow rates and heat fluxes for the 11.5 mm and 4 mm test sections. A total of 648 tests were conducted, which consisted of 648 mass flow rate measurements, 70 301 temperature measurements and 2 536 pressure drop measurements.

Table 3.5: Experimental test matrix.

Test section	Heat flux [kW/m^2]	Reynolds number range	Mass flow rate measurements	Temperature measurements[‡]	Pressure drop measurements
11.5 mm	0	507 ≤ *Re* ≤ 9 615	131	14 279	1 048
	1	597 ≤ *Re* ≤ 9 280	69	7 521	552
	2	894 ≤ *Re* ≤ 9 376	62	6 758	496
	3	1 061 ≤ *Re* ≤ 9 509	55	5 995	440
4 mm	0.5	913 ≤ *Re* ≤ 3 303	32	3 456	-
	1	965 ≤ *Re* ≤ 6 021	67	7 236	-
	2	947 ≤ *Re* ≤ 7 176	66	7 128	-
	3	1 005 ≤ *Re* ≤ 6 963	62	6 696	-
	4	885 ≤ *Re* ≤ 7 848	57	6 156	-
	8	1 746 ≤ *Re* ≤ 8 203	47	5 076	-
Total			648	70 301	2 536

[‡]3 or 4 thermocouples per station

Because this study was a continuation of the experimental work that had been done for the research for the master's degree, the results of that study [75] were also used. Table 3.6 summarises the experimental test matrix of the previous study and more details regarding the experimental set-up and results are available in Everts [75].

Table 3.6: Experimental test matrix of Everts [75].

Test section	Heat flux [kW/m^2]	Reynolds number range	Mass flow rate measurements	Temperature measurements	Pressure drop measurements
11.5 mm	0	538 ≤ *Re* ≤ 14 968	47	2 256	47
	0.065	303 ≤ *Re* ≤ 1 793	28	1 344	-
	6.5	460 ≤ *Re* ≤ 9 630	111	5 382	111
	8	470 ≤ *Re* ≤ 9 600	103	4 944	103
	9.5	470 ≤ *Re* ≤ 9 800	109	5 232	109
Total			398	19 158	370

Table 3.7: Experimental test matrix of studies from literature.

Study	Estimated number of mass flow rate measurements				*Pr*
	Laminar	Transitional	Turbulent	Total	
Meyer *et al*. [34][1]	30	86	150	266	6 - 9
Meyer and Abolarin [37][1]	32	30	154	216	3 - 7
Kupper [104]	22	-	-	22	4 - 9
Chen [105]	33	10	5	48	4 - 285
Strickland [106]	13	37	32	82	3 - 158
Meyer and Tang [107]	34	-	-	34	35

[1] These experiments were conducted in the same laboratory at the University of Pretoria, under the supervision of Professor Josua Meyer. Grote and Abolarin were both graduate students.

For a part of this study, experimental results from literature [34, 71, 101, 104-106] were used. The difference between the results of this study and literature is that the Prandtl number in this study varied between 3 and 7, while the Prandtl number of almost all the experiments conducted in literature was significantly higher (up to Prandtl numbers of 285). This study, together with those works of literature, therefore ensured that a wider range of Prandtl number data were available to use for interpretation and the development of correlations.

3.12. Summary, conclusions and recommendations

The experimental set-up, data reduction method and experimental procedure were described in this chapter. Experiments were conducted using two different test sections with a square-edged inlet for both. The 11.5 mm test section consisted of a smooth circular copper tube with a length of 9.8 m, while the 4 mm test section consisted of a smooth circular stainless steel tube with a length of 6 m. The Reynolds number was varied between 500 and 10 000 and water was used as the test fluid. The surface temperatures were measured at 27 thermocouple stations on each test section, while the inlet and outlet temperatures of the fluid were obtained from Pt100 probes inside the flow-calming section and mixer respectively. To investigate the pressure drop of both developing and fully developed flow, the pressure drop measurements were taken across eight different tube lengths inside the 11.5 mm test section.

A constant heat flux boundary condition was obtained using two different methods. Heating wires were coiled around the 11.5 mm test section, while current was passed directly through the tube wall of the 4 mm test section. Different heat fluxes were applied to each test section, by adjusting the current through the heating wire (in the 11.5 mm test section) or through the tube wall (in the 4 mm test section). The test sections were properly insulated and the maximum heat loss was estimated to be less than 3%.

Literature shows that the Reynolds number boundaries of the transitional flow regime were in general qualitatively identified through visual observations, which were subjective. Furthermore, in most of these cases, no clear distinction between the transitional and quasi-turbulent flow regimes was made. Therefore, the boundaries between the flow regimes, as well as terminology to define transitional flow characteristics, were quantified mathematically in order to determine it computationally. However, the definition of the boundary between the quasi-turbulent and turbulent flow regimes can be improved by using experimental data with lower uncertainties (experiments conducted at higher heat fluxes) in the quasi-turbulent and turbulent flow regimes. The inflection point was found to be in the middle of the transitional flow regime, and was prominent in the heat transfer and pressure drop results, as well as when the relationship between pressure drop and heat transfer was investigated. It is recommended that the physical mechanism of this point should be investigated, because it might improve our fundamental understanding of the heat transfer and pressure drop characteristics in the transitional flow regime.

Adequate time after the start, as well as between Reynolds number increments, was allowed to ensure that steady-state conditions were always obtained. The measurements were only taken once there was no significant increase or decrease in temperatures, pressure drops and mass flow rates, within a period of approximately two minutes. Care was also taken during the experiments to ensure that there was always sufficient back pressure and a high enough pump speed to reduce the effect of flow pulsations.

An uncertainty analysis was conducted and the Reynolds number uncertainty remained approximately constant at 1.5% for all Reynolds numbers and heat fluxes in the laminar and turbulent flow regimes, but increased to approximately 2% in the transitional flow regime. For the Nusselt numbers and Colburn *j*-factors, the laminar forced convection and mixed convection uncertainties were less than 10% and 5% respectively. In the transitional flow regime, the uncertainties increased to approximately 10% due to temperature fluctuations. The average Nusselt number uncertainty at a Reynolds number of 6 000 was 13%. The trends of the Grashof number, Rayleigh number and Richardson number uncertainties were similar; however, the Rayleigh number uncertainties were slightly higher and the Richardson number uncertainties significantly higher than the Grashof number uncertainties. In the laminar flow regime, the Grashof number uncertainties at a heat flux of 1 kW/m^2 in the 4 mm test section were approximately 8%, but decreased to 6% when the heat flux was increased to 3 kW/m^2. As the tube diameter was increased to 11.5 mm, the uncertainties decreased further to approximately 2%. However, it increased with increasing Reynolds number to 4.5% and 6.6% in the quasi-turbulent and turbulent flow regimes respectively, at a heat flux of 3 kW/m^2 in the 11.5 mm test section. In the transitional flow regime, the uncertainties increased due to the temperature fluctuations. The laminar friction factor uncertainties were approximately 10% at the minimum Reynolds number and decreased to approximately 2%. However, the laminar friction factor uncertainties across some tube lengths were higher (average uncertainty of 13%) due to the limitations of the pressure transducer diaphragms. In the transitional flow regime, the mass flow rate fluctuations caused the uncertainties to increase to 16%, while the uncertainties in the turbulent flow regime were less than 4%.

4. Validation

4.1. Introduction

This chapter validates the experimental set-up and data reduction method by comparing the heat transfer and pressure drop data with existing correlations as well as with experimental data from previous studies. This validation ensures that the results presented in Chapters 5 to 8 can be used with confidence. For heat transfer, the local laminar Nusselt numbers are validated for forced convection conditions in Section 4.2 and for mixed convection conditions in Section 4.3. The average laminar Nusselt numbers are validated in Section 4.4 and the average turbulent Nusselt numbers are validated in Section 4.5. In each section, the Nusselt numbers are first validated for the 11.5 mm test section and then for the 4 mm test section. For pressure drop, the isothermal friction factors are validated for fully developed and developing flow in Section 4.6.

4.2. Local laminar Nusselt numbers (forced convection)

For fully developed laminar flow in a circular smooth tube with a constant heat flux boundary condition, literature indicates that the Nusselt number should be 4.36 [3], which is indicated by the black dotted line in Fig. 4.1. The local Nusselt numbers at a bulk Reynolds number of 941 and heat flux of 60 W/m^2 are represented by the blue markers in Fig. 4.1. Although it was very challenging to obtain forced convection conditions in macro-tubes, the average fully developed Nusselt number ($50 < x/D < 827$) was 4.75, which was within 8.9% of the theoretical Nusselt number of 4.36. The local Nusselt numbers also correlated well with the correlation of Shah and London [1] for simultaneously hydrodynamically and thermally developing flow (Eq. 2.17), with an average deviation of 19%, while the deviation between $x/D = 567$ and $x/D = 724$ was less than 3%. The local surface temperatures, measured by the thermocouples at a station, were also checked (especially comparing the temperatures at the top to the temperatures at the bottom) and the average deviation between the temperature measurements was calculated to be 0.04 °C. This was within the uncertainty range of the thermocouples and it could therefore be concluded that fully developed forced convection conditions were successfully obtained in the laminar flow regime.

Although the uncertainty was very high (56%) at the first thermocouple station (due to the very small surface-fluid temperature difference), it decreased along the test section to a minimum of 30%. The thermocouple uncertainty was 0.1 °C, while the surface-fluid temperature difference at the first thermocouple station was only 0.16 °C, and increased along the test section to 0.24 °C. Furthermore, the difference between the inlet and outlet temperatures across the tube length of 9.5 m was 0.63 °C, and the average surface-fluid temperature only was 0.23 °C. It was therefore very challenging to experimentally obtain forced convection conditions with low uncertainties, which could explain why so little experimental data that shows forced convection conditions is available in literature.

As the diameter of the 11.5 mm test section was 2.88 times greater than the 4 mm test section, the Grashof number, and thus free convection effects, could be expected to be approximately 24 times fewer in the 4 mm test section ($Gr \propto D^3$). A higher heat flux (and thus decreased uncertainties) could therefore be applied, while still obtaining forced convection conditions. The local Nusselt numbers at a bulk Reynolds number of 1 000 were compared for heat fluxes of 0.5 kW/m^2 (green markers) and

1 kW/m^2 (red markers) in Fig. 4.1. This figure indicates that there was no significant difference between the Nusselt numbers of the two heat fluxes, which confirms that free convection effects were negligible. The average Nusselt number between x/D = 873 and x/D = 1 373 was 4.46 at a heat flux of 0.5 kW/m^2, and 4.58 at a heat flux of 1 kW/m^2, which was within 2.3% and 5% of the theoretical Nusselt number of 4.36. Fully developed forced convection conditions were thus successfully obtained. However, because the uncertainties were lower at a heat flux of 1 kW/m^2 (due to the increased temperature differences), it was decided to use a heat flux of 1 kW/m^2 in the 4 mm test section for the forced convection investigation. The results also correlated very well with the correlation of Shah and London [1] with an average deviation of 1.7%.

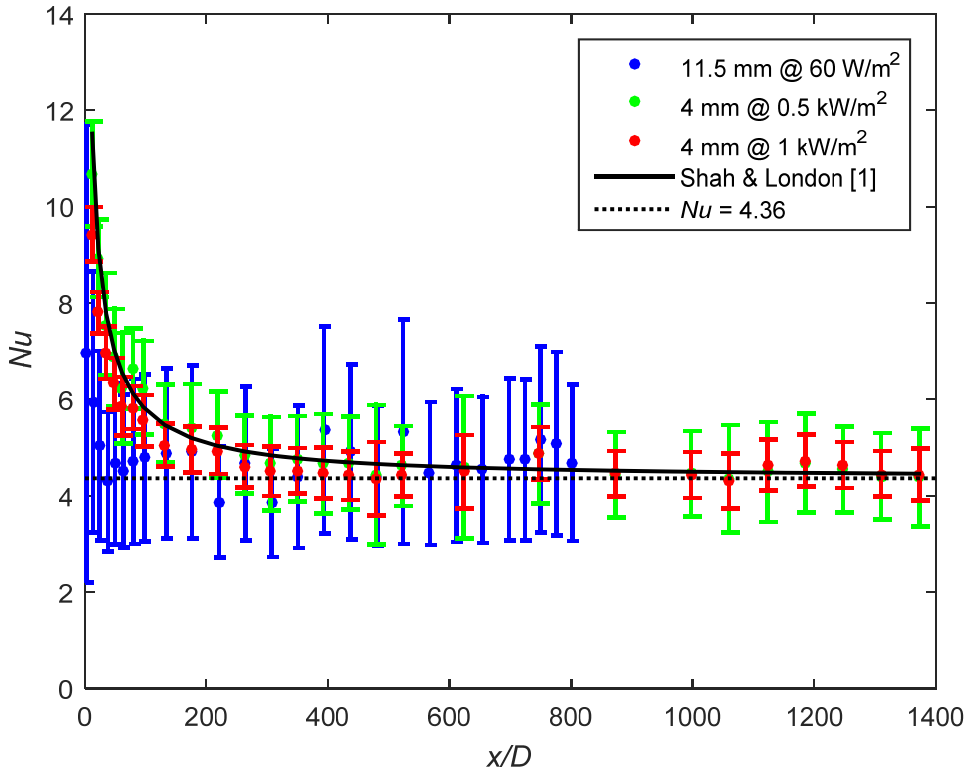

Fig. 4.1: Comparison with literature of local laminar forced convection Nusselt numbers as a function of axial position. The 60 W/m^2 results in the 11.5 mm test section are at a bulk Reynolds number of 941, bulk Grashof number of 1.67×10^4 and bulk Prandtl number of 6.75. The 1 kW/m^2 results in the 4 mm test section are at a bulk Reynolds number of 965, bulk Grashof number of 253 and bulk Prandtl number of 6.0.

It was found that of the 891 fully developed laminar experimental data points in the 4 mm and 11.5 mm test sections, forced convection conditions (fully developed Nusselt numbers within 10% of the theoretical fully developed Nusselt number of 4.36) existed in only 5.4% of all the experiments. A Nusselt number increase of less than 20% and 50% was obtained in only 13% and 24% of the data respectively, while an increase of at least 100% was found in more than 60% of the data. Therefore, it is very challenging to experimentally obtain forced convection conditions. Forced convection conditions in the laminar flow regime could only be validated in this study at very low heat fluxes for 21 different mass flow rates. Therefore, in most experiments, not only from this study, but also from literature summarised in Table 3.7, mixed convection conditions existed rather than forced convection conditions.

4.3. Local laminar Nusselt numbers (mixed convection)

To validate the local laminar Nusselt numbers for mixed convection conditions, experiments were conducted in the 11.5 mm test section at a heat flux of 1 kW/m^2 and a bulk Reynolds number of 1 041. Experiments were also conducted in the 4 mm test section at a bulk Reynolds number of 1 005 and heat flux of 3 kW/m^2. The results in both test sections were compared with the correlation of Morcos and Bergles [71], which is given with its ranges in Table 2.1. The heat transfer coefficients in the laminar flow regime were very sensitive to the heating or cooling methodology, Prandtl number, forced and mixed convection conditions, as well as developing and fully developed flow. It was found that limited correlations, which were suitable for the conditions (developing mixed convection laminar flow with low Prandtl numbers) of this study, were available from literature. The correlation of Morcos and Bergles [71] was the only correlation available that partially suited the parameter ranges (only the tube wall-parameter, *Pw*, was not within the specified ranges) of this study.

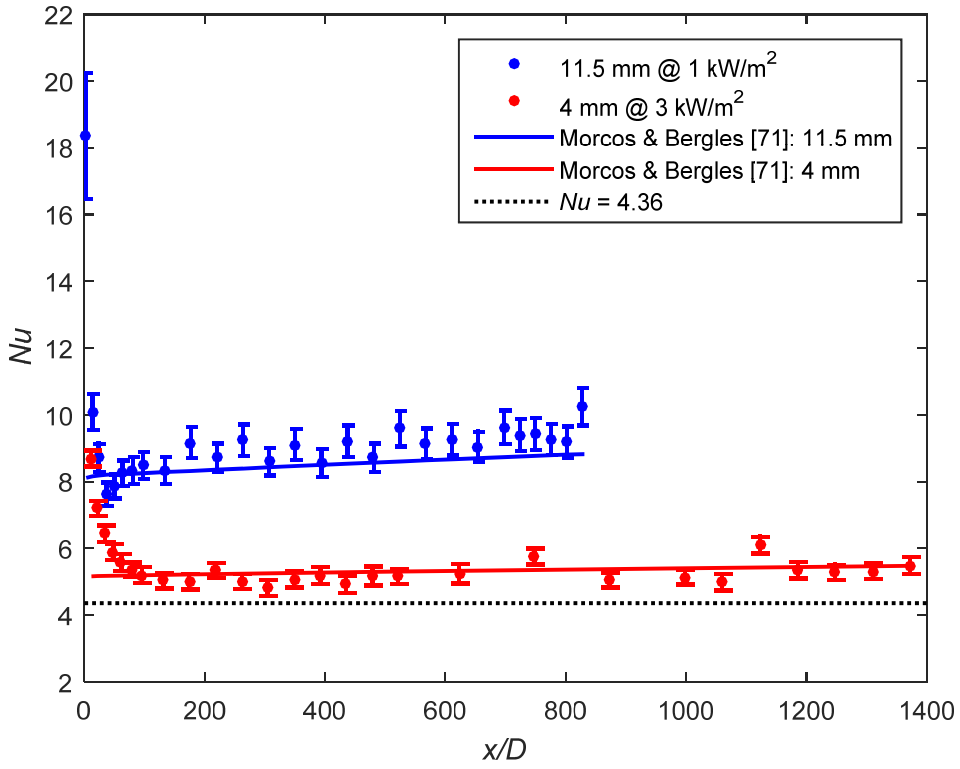

Fig. 4.2: Comparison with literature of local laminar mixed convection Nusselt numbers as a function of axial position. The results in the 11.5 mm test section are at a bulk Reynolds number of 1 041, bulk Grashof number of 1.04×10^5 and bulk Prandtl number of 5.9. The results in the 4 mm test section are at a bulk Reynolds number of 1 005, bulk Grashof number of 1.1×10^5 and bulk Prandtl number of 4.9.

Figure 4.2 indicates that the Nusselt numbers in both test sections correlated well with the correlation of Morcos and Bergles [71]. The average deviation between x/*D* = 37 and *x*/*D* = 827 in the 11.5 mm test section was 6%, while the average deviation between x/*D* = 79 and *x*/*D* = 1 373 in the 4 mm test section was 4%. Exact correlation was not expected because the range of the tube-wall parameter in the Morcos and Bergles correlation [71] was between 2 and 66, while it was approximately 0.03 and 0.15 in the 11.5 mm and 4 mm test sections respectively, during this validation. Furthermore, this correlation was developed for fully developed flow, while developing flow existed near the inlet of the test section. However, all the other parameters were within the specified ranges of the correlation.

4.4. Average laminar Nusselt numbers

The average Nusselt numbers were obtained by using the bulk fluid temperature between the inlet and outlet of the test section and the average surface temperature across the test section. A heat flux of 1 kW/m^2 was applied to the 11.5 mm test section and the bulk Reynolds numbers varied between 600 and 2 000. In the 4 mm test section, the bulk Reynolds numbers varied between 900 and 2 000 at a heat flux of 3 kW/m^2. The results were compared with the correlation of Morcos and Bergles [71] in Fig. 4.3.

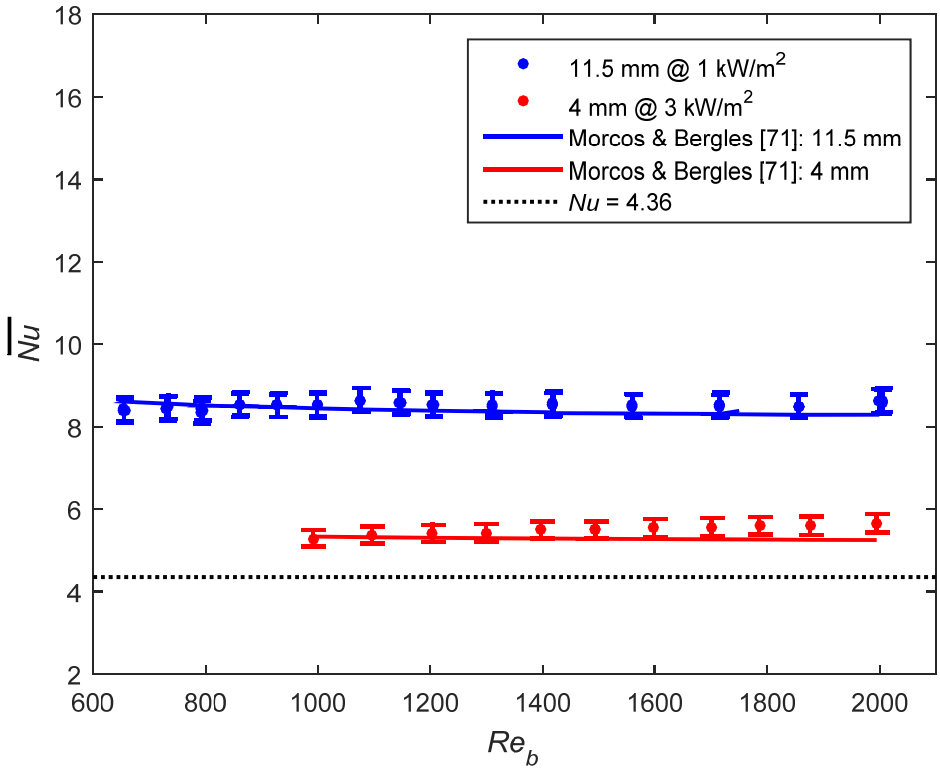

Fig. 4.3: Comparison with literature of average laminar Nusselt numbers as a function of bulk Reynolds number. The results in the 11.5 mm test section are for bulk Reynolds numbers between 600 and 2 000 at a heat flux of 1 kW/m^2. The results in the 4 mm test section are for bulk Reynolds numbers between 900 and 2 000 at a heat flux of 3 kW/m^2.

As expected, the laminar Nusselt numbers in both test sections were significantly higher than the theoretical Nusselt number of 4.36 due to free convection effects and the fact that the test sections contained developing flow. The Grashof number is proportional to D^3, therefore free convection effects increase with increasing tube diameter. Furthermore, as will be shown in Section 5.3.2, free convection effects decrease the thermal entrance length. Therefore, the increased Nusselt numbers were mainly due to free convection effects in the 11.5 mm test section and due to developing flow in the 4 mm test section (due to the longer thermal entrance length).

The average Nusselt numbers in both test sections correlated very well with the correlation of Morcos and Bergles [71], with an average deviation of 2% and 4% in the 11.5 mm and 4 mm test section respectively. Similar to local laminar Nusselt numbers, exact correlation was not expected because the boundaries of the tube-wall parameter (*Pw*) were specified to be between 2 and 66, while the tube-wall parameter was approximately 0.03 and 0.15 in the 11.5 mm and 4 mm test sections respectively, during this validation. Furthermore, the Rayleigh numbers in the 4 mm test section varied between 4.8×10^3 and 6.5×10^3, while the correlation of Morcos and Bergles [71] was developed

for Rayleigh numbers greater than 3×10^4. Although the Rayleigh numbers were slightly lower, the results correlated well and a maximum deviation of 7.3% was found at a Reynolds number of 2 000 where the Rayleigh number was the lowest (4.8×10^3). However, all the other parameters were within the specified ranges of the correlation.

4.5. Average turbulent Nusselt numbers

To validate the average turbulent Nusselt numbers, the bulk Reynolds number was varied between 4 000 and 10 000 in the 11.5 mm test section at a heat flux of 3 kW/m^2. A heat flux 8 kW/m^2 was applied to the 4 mm test section and the bulk Reynolds number was varied between 4 600 and 8 600. The average Nusselt numbers were compared with the correlations of Ghajar and Tam [16] and Gnielinski [41], as well as the experimental data of Meyer *et al*. [34], in Fig. 4.4. These two correlations, as well as their ranges, were summarised in Table 2.3. Meyer *et al*. [34] also used a constant heat flux boundary condition and applied a heat flux of 13 kW/m^2 to the test section.

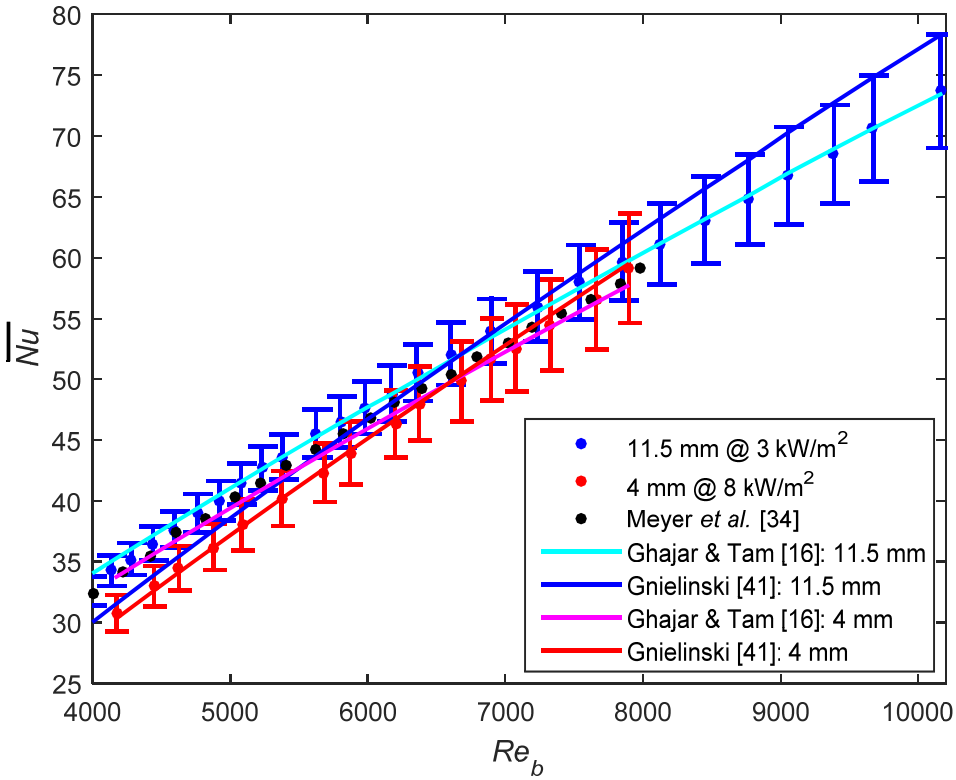

Fig. 4.4: Comparison with literature of the average turbulent Nusselt numbers as a function of bulk Reynolds number. The bulk Reynolds numbers in the 11.5 mm test section varied between 4 000 and 10 000 at a heat flux of 3 kW/m^2. A heat flux of 8 kW/m^2 was applied to the 4 mm test section and the bulk Reynolds numbers varied between 4 600 and 8 600.

The Nusselt numbers in the 11.5 mm test section correlated very well with the correlation of Ghajar and Tam [16] with an average deviation of less than 1%. As expected, a maximum deviation of 4% was obtained at a Reynolds number of 4 000, because this correlation was developed for Reynolds numbers greater than 7 000. For Reynolds numbers greater than 5 000, the average deviation was 0.4% and the maximum deviation only 1%. The data also correlated well with the correlation of Gnielinski [41] and the average deviation was 5%. A maximum deviation of 10% was obtained at a Reynolds number of 4 100, while a minimum deviation of 0.4% was obtained at a Reynolds number of 6 900. The average deviation between Reynolds numbers of 4 000 and 6 000 was 6%, while it was 1%

between Reynolds numbers of 6 000 and 8 000, and 5% between Reynolds numbers of 8 000 and 10 000.

Furthermore, the Nusselt numbers in the 11.5 mm test section correlated well with the experimental data of Meyer *et al*. [34] and a maximum deviation of 8% was found at a Reynolds number of 7 800. The average deviation between Reynolds numbers of 4 000 and 8 000 was 6%, while a minimum deviation of 4% was found at a Reynolds number of 4 000. Although the experiments were conducted at different heat fluxes, the data correlated well with the experimental data of Meyer *et al*. [34], because free convection effects were suppressed by the velocity of the fluid. Therefore, there was no significant difference between the Nusselt numbers of the different heat fluxes in the turbulent flow regime.

The average turbulent Nusselt numbers in the 4 mm test section correlated very well with the equation of Gnielinski [41] for the entire Reynolds number range and the average deviation was less than 1%. The results also correlated well with the correlation of Ghajar and Tam [16] with an average deviation of 3.2%. Similar to the 11.5 mm test section, the maximum deviation of 9% was found at the minimum Reynolds number of 4 200.

Figure 4.4 shows that the uncertainties of the Nusselt numbers of both test sections increased with increasing Reynolds numbers. This was due to higher temperature uncertainties caused by the decreasing surface-fluid temperature differences, as well as the decreasing temperature differences between the inlet and outlet of the test section, as the Reynolds number increased.

4.6. Isothermal friction factors

The fully developed and developing isothermal friction factors between bulk Reynolds numbers of 500 and 10 000 were compared with existing correlations in Fig. 4.5. As will be shown in Section 5.3.2, it was found that for simultaneously hydrodynamically and thermally developing flow, a coefficient of 0.12 should be used instead of 0.05, which was used to calculate the thermal entrance length ($Lt = CRePrD$ [3]) of this test section. However, average measurements across a tube length were considered for the friction factors that dampened the small changes in the local measurements. Furthermore, Fig. 5.4 indicates that the difference between the local laminar Nusselt numbers at $1/Gz = 0.05$ and $1/Gz = 0.12$ was only 4.4%. Therefore, for the average measurements across $8\text{ m} < L < 9.5\text{ m}$ the flow can be considered as fully developed. The pressure drop across the first 2 m of the test section was used to validate developing flow. Therefore, the flow in this tube length was developing in the laminar and transitional flow regimes, and fully developed in the turbulent flow regime.

A total of 115 data points were considered in the fully developed section and 109 data points in the developing section. The measurements were made without any heat transfer to eliminate the effect of varying viscosity and density. In the laminar flow regime, the developing and fully developed isothermal friction factors were compared with Poiseuille flow friction factor of $64/Re$ [51] for fully developed flow and the correlation of Tam *et al.* [8] for developing flow. In the turbulent flow regime, the results were compared with the correlations of Blasius [51] and Fang *et al*. [73]. The laminar and turbulent correlations are summarised in Table 2.2 and Table 2.4 respectively.

The friction factors predicted using the correlation of Tam *et al.* [8] were slightly larger than $64/Re$ [51]. As the Reynolds number was increased, the difference between the two correlations increased,

and the maximum difference of 8.6% was found at a Reynolds number of 2 300. The maximum wall shear stress was found at the inlet of the test section, where the velocity boundary layer was the thinnest. Therefore, the maximum pressure drops and friction factors were found at the inlet of the test section. This explains why the friction factors for developing flow (correlation of Tam *et al.* [8]) were higher than for fully developed flow (64/*Re* [51]). Furthermore, the difference increased with increasing Reynolds number, because the thermal entrance length increased and a larger portion of the tube contained developing flow.

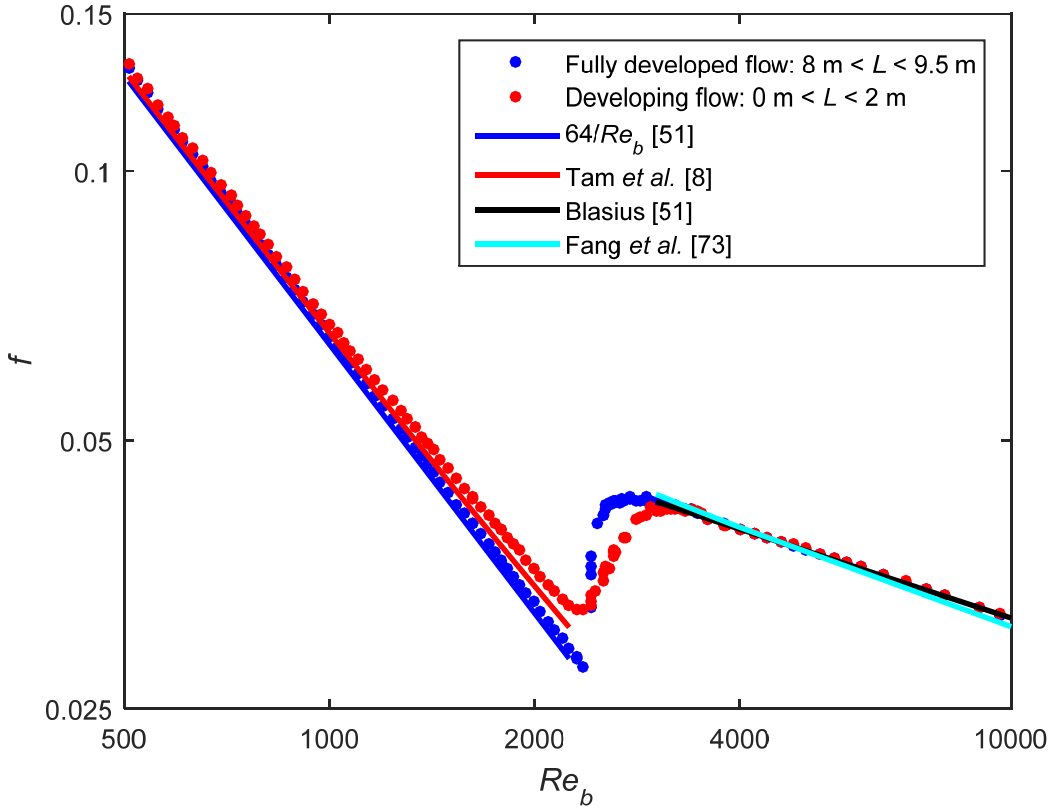

Fig. 4.5: Comparison with literature of fully developed and developing isothermal friction factors as a function of Reynolds number between bulk Reynolds numbers of 500 and 10 000.

The laminar fully developed friction factors correlated well with 64/*Re* [51], with an average deviation of 2.5% between Reynolds numbers of 500 and 2 000, confirming that the fully developed flow assumption was correct. A maximum deviation of 3.5% occurred at a Reynolds number of 2 362 where transition started. The laminar developing flow friction factors correlated well with the friction factors predicted by the correlation of Tam *et al.* [8], with an average deviation of 3.3% between Reynolds numbers of 500 and 2 300. A maximum deviation of 9.6% occurred at a Reynolds number of 2 361 where transition started.

The fully developed turbulent friction factors correlated very well with the correlations of Blasius [51] and Fang *et al*. [73], with an average deviation of 0.3% and 1.1% respectively, between Reynolds numbers of 3 000 and 10 000. The turbulent friction factors in the developing section also correlated very well with the correlations of Blasius [51] and Fang *et al*. [73], with average deviations of 0.35% and 1.2% respectively, between Reynolds numbers of 3 500 and 10 000.

4.7. Conclusions

The experimental set-up and data reduction method for heat transfer and pressure drop were validated in this chapter. The conclusions were presented in the order of local laminar Nusselt numbers for forced and mixed convection conditions, average mixed convection laminar Nusselt numbers, average forced convection turbulent Nusselt numbers and isothermal fully developed and developing friction factors.

It was very challenging to obtain forced convection conditions in macro-tubes, and only a very small heat flux could be applied. The average fully developed Nusselt number ($50 < x/D < 827$) in the 11.5 mm test section at a Reynolds number of 941 and heat flux of only 60 W/m² was found to be 4.75. This was within 8.9% of the theoretical value of 4.36 for fully developed forced convection laminar flow. Forced convection conditions at a Reynolds number of 965 in the 4 mm test section were obtained at a heat flux of 1 kW/m². The average Nusselt number between $x/D = 307$ and $x/D = 1\,373$ was 4.5, which was within 3.4% of the theoretical fully developed forced convection Nusselt number of 4.36. The results in both test sections also correlated well with literature with an average deviation of 19% in the 11.5 mm test section, while the deviation between $x/D = 567$ and $x/D = 724$ was less than 3%. An average deviation of 6% was obtained in the 4 mm test section, while the deviation between $x/D = 307$ and $x/D = 1\,373$ was 1.7%.

The local Nusselt numbers were also validated for mixed convection conditions to account for free convection effects. The results in both test sections correlated well with literature with an average deviation of 6% between $x/D = 37$ and $x/D = 827$ in the 11.5 mm test section, and an average deviation of 4% between $x/D = 79$ and $x/D = 1\,373$ in the 4 mm test section.

The average laminar Nusselt numbers were significantly higher than the theoretical Nusselt number of 4.36 for fully developed laminar forced convection flow, as it should be, due to free convection effects. The results in both the 11.5 mm and 4 mm test sections correlated well with literature with an average deviation of 2% and 4% respectively. Furthermore, the average turbulent Nusselt numbers in the 11.5 mm and 4 mm test sections between Reynolds numbers of 4 000 and 10 000 correlated very well with literature with an average deviation of less than 5% and 3.2% respectively.

The fully developed isothermal friction factors were validated by using the pressure drop measurements across the last 1.5 m of the test section. The laminar friction factors correlated well with literature and the average deviation between Reynolds numbers of 500 and 2 000 was 2.5%, while a maximum deviation of 3.5% occurred at a Reynolds number of 2 362 where transition started. In the turbulent flow regime, the average deviation with literature was less than 1% between Reynolds numbers of 3 000 and 10 000.

To validate the developing flow isothermal friction factors, pressure drop measurements were taken across the first 2 m of the test section, therefore the flow was developing in the laminar and transitional flow regimes and fully developed in the turbulent flow regime. The laminar friction factors correlated well with developing flow correlations and the average deviation between Reynolds numbers of 500 and 2 300 was 3.3%, while a maximum deviation of 9.6% was found at a Reynolds number of 2 361 where transition started. The turbulent results were also compared with literature and the average deviation between Reynolds numbers of 3 000 and 10 000 was less than 1%.

Therefore, the heat transfer coefficients and friction factors correlated well with existing correlations. Although two different heating methods were used in the 11.5 mm and 4 mm test sections, accurate results were obtained using both methods. The experimental set-up and data reduction method could therefore be considered as validated and reliable results could be expected for other heat fluxes and mass flow rates of experiments that were conducted.

5. Local Heat Transfer in the Laminar and Transitional Flow Regimes

5.1. Introduction

In this chapter, the effects of free convection on the development of the local heat transfer characteristics along the tube length are investigated. The specific objectives are: (1) to evaluate the thermal entrance length correlations for forced convection conditions, (2) to develop correlations to determine the thermal entrance length for mixed convection conditions, (3) to develop correlations to predict the local and average Nusselt numbers of both developing and fully developed flow which are valid for both high and low Prandtl number fluids, as well as (4) to investigate the effect of free convection on the laminar-turbulent transition along the tube length in the transitional flow regime. Most of the results contained in this chapter were published in Meyer and Everts [47].

5.2. Heat transfer regions for laminar and transitional flow

It was found from analysing the experimental data of this study and literature [34, 37] that all mixed convection data in the laminar and transitional flow regimes could be represented as shown schematically in Fig. 5.1. It shows the effect of Grashof number (free convection effects) on the local Nusselt numbers, as a function of axial position, in the laminar flow regime (Fig. 5.1(a)), on the critical Reynolds number (Fig. 5.1(b)), and on the laminar-turbulent transition for mixed convection conditions in the transitional flow regime (Fig. 5.1(d)). The effect of Reynolds number on the laminar-turbulent transition for forced convection conditions in the transitional flow regime is schematically illustrated in Fig. 5.1(c).

In Fig. 5.1(a), (b) and (d), the red line, 1, represents forced convection conditions, while lines 2 to 4 represent increasing values of Grashof number (thus increased free convection effects). However, in Fig. 5.1(c), the red dashed line, 1, represents the critical Reynolds number, while lines 2 to 4 represent increasing values of Reynolds number. Furthermore, three different regions were identified in the laminar flow regime (Fig. 5.1(a)): forced convection developing (FCD), mixed convection developing (MCD) and fully developed (FD). When the Reynolds number exceeded the critical Reynolds number, four different regions were identified in the transitional flow regime (Fig. 5.1(c) and (d)): laminar, transition, quasi-turbulent and turbulent. However, these regions could not be identified at the critical Reynolds number (Fig. 5.1(b)). The names of these four flow regions were based on the nomenclature of the four flow regimes identified and quantified in Section 3.8.

The trends shown in Fig. 5.1 are supported by experimental data in Sections 5.3 and 5.5. The reasons why only the trends are shown schematically and not according to scale are: (1) the laminar results of the different Grashof numbers in the FCD region were very close to each other, and (2) the FCD region formed only a small part of the tube length, which made it difficult to identify the trends. This was also true for (3) the Nusselt numbers near the inlet of the test section in the transitional flow regime. It was also found that in the transitional flow regime, (4) the laminar-turbulent transition was very dependent on Reynolds number and Grashof number, which made it challenging to obtain and compare results for different Grashof numbers at a fixed Reynolds number, and vice versa.

Furthermore, (5) some scatter existed in the experimental data, which made it challenging to illustrate clear trends.

5.2.1. Laminar flow regime (Fig. 5.1(a))

If the Grashof number is so low that the flow can be considered as forced convection, the results will follow the red forced convection line. As the flow developed axially from the tube inlet, all the results initially followed the red forced convection line. When the Grashof number was increased, free convection effects became significant and the results deviated from the red line. Furthermore, as indicated by points D, G and J, the axial position at which the results deviated from the red line (FCD/MCD) decreased with increasing Grashof number.

In the forced convection developing (FCD) region, the gradient of the Nusselt number lines decreased slightly with increasing Grashof number, because the thermal entrance length decreased. However, this difference was very small because free convection effects were negligible in this region. In the mixed convection developing (MCD) region, the Nusselt numbers increased along the tube length, because the flow developed and free convection effects increased. As indicated by lines D-E, G-H and J-K, the gradient of the Nusselt number lines increased with Grashof number.

For forced convection conditions, the flow is considered as fully developed when the Nusselt numbers are within 5% of the theoretical Nusselt number of 4.36 and becomes constant. For simultaneously hydrodynamically and thermally developing flow (see Section 5.3.2), this value corresponds to $x/D = 0.12RePr$ (indicated by the purple dotted line) and not $x/D = 0.05RePr$ (indicated by the teal dotted line). As indicated by points E, H and K, the axial position at which the flow became fully developed decreased with increasing Grashof number. In the fully developed (FD) region, the Nusselt numbers and free convection effects were constant along the tube length, because the flow was fully developed. However, the magnitude of the Nusselt numbers increased with increasing Grashof number (points C, F, I and L).

5.2.2. Critical Reynolds number (Fig. 5.1(b))

At the critical Reynolds number, the local Nusselt numbers decreased along the tube length near the inlet of the test section, and then became constant. No MCD regions (Fig. 5.1(a)) were observed. As the thermal entrance length decreased with increasing Grashof number, the Nusselt number gradients near the inlet of the test section (A-D, A-F and A-H) decreased and the Nusselt numbers became constant earlier along the tube length (points B, D, F and H). The Nusselt numbers remained constant further along the tube length. However, the magnitude of the Nusselt numbers increased with increasing Grashof numbers (points C, E, G and I).

5.2.3. Forced convection laminar-turbulent transition (Fig. 5.1(c))

When the Reynolds number exceeds the critical Reynolds number and the flow is in the transitional flow regime, laminar-turbulent transition occurs along the tube length. When forced convection conditions existed and the Reynolds number was increased above the critical Reynolds number (red and blue lines), the trends were similar. However, the axial position at which the Nusselt numbers became constant decreased (points B and D). Furthermore, the magnitude of the Nusselt numbers increased (points C and E) due to the increased fluid velocity that enhanced mixing inside the test section.

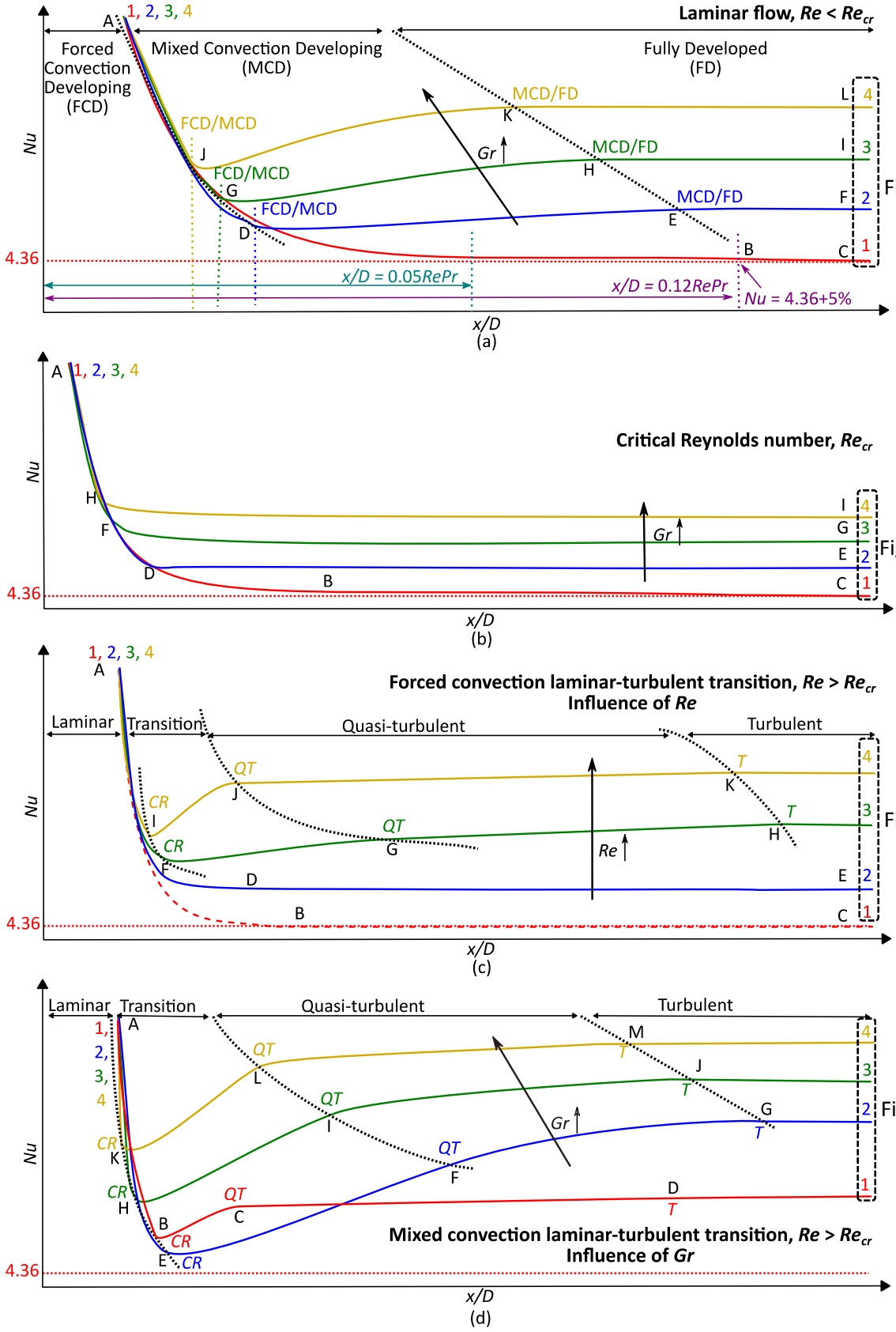

Fig. 5.3

Fig. 5.12

Fig. 5.13

Fig. 5.15

Fig. 5.1: Schematic representation of the developing Nusselt numbers showing the effects of (a) Grashof number in the laminar flow regime, (b) Grashof number at the critical Reynolds number, (c) Reynolds number on the forced convection laminar-turbulent transition and (d) Grashof number on the mixed convection laminar-turbulent transition.

As the Reynolds number increased further (green and yellow lines), four regions (laminar, transition, quasi-turbulent and turbulent) can be identified. The heat transfer characteristics in the laminar region were similar to those of the laminar FCD region (Fig. 5.1(a)). Therefore, the gradient of the Nusselt number lines in the laminar region (lines A-F and A-I) decreased with increasing Reynolds number, because the thermal entrance length increased.

The axial position at which the Nusselt numbers started to increase (points F and I), decreased with increasing Reynolds number. In the transitional flow regime, fluctuations occurred inside the test section because the flow alternated between laminar and turbulent flow [89]. As shown in Fig. 6.5, these fluctuations increased along the tube length, leading to increased mixing, therefore enhanced heat transfer and increased Nusselt numbers. The gradient of the Nusselt numbers (lines F-G and I-J) increased with increasing Reynolds number, which implied that the transition from the laminar to the quasi-turbulent regions occurred faster (points G and J) and the transition region decreased.

In the quasi-turbulent region, the flow characteristics were similar to turbulent flow; however, the flow was not yet turbulent and the local Nusselt numbers increased along the tube length. The gradient of the Nusselt number lines in the quasi-turbulent region (lines G-H and J-K) decreased with increasing Reynolds number and approached zero as the flow approached the turbulent region. The axial position at which the Nusselt numbers became constant (points H and K) also decreased with increasing Reynolds number. However, as this decrease was less than for points G and J, the width of the quasi-turbulent region increased slightly with increasing Reynolds number. The magnitude of the Nusselt numbers in the quasi-turbulent and turbulent regions increased with increasing Reynolds number due to the enhanced mixing inside the tube.

5.2.4. Mixed convection laminar-turbulent transition (Fig. 5.1(d))

When mixed convection conditions existed, the Nusselt numbers decreased along the tube length near the inlet of the test section. The axial position at which the Nusselt numbers started to increase (points E, H and K) decreased with increasing Grashof number and the gradient of the Nusselt number lines in the transition region (lines E-F, H-I and K-L) increased. Therefore, the width of the transition region decreased with Grashof number. In the quasi-turbulent region, the gradient of the Nusselt number lines (lines F-G, I-J and L-M) decreased with increasing Grashof number and the magnitude of the Nusselt numbers increased. The axial position at which the Nusselt numbers became constant (points G, J and M) decreased with increasing Grashof number. The Nusselt numbers in the turbulent region remained constant along the tube length. However, it increased with increasing Grashof number.

Although the laminar-turbulent transition occurred faster with increasing Grashof number when the flow was dominated by mixed convection (blue, green and yellow lines), a different trend was observed when free convection effects first became significant at very low Grashof numbers (red and blue lines). As free convection effects became significant, the effect was to first disturb the fluctuations inside the test section and cause transition to occur slower; therefore, the free convection effects had a dampening effect. However, as the Grashof number was increased, the fluctuations inside the test section increased significantly with increasing free convection effects (as shown in Fig. 6.4), which caused the flow to transition faster from laminar to turbulent.

5.3. Laminar Flow

The results in this section are directly related to Fig. 5.1(a). Points A-L in Fig. 5.2, Fig. 5.3, Fig. 5.6, Fig. 5.7 and Fig. 5.8 correspond to the labels used in Fig. 5.1(a).

5.3.1. Local Nusselt numbers

To investigate the effect of free convection on the local laminar Nusselt numbers, the Nusselt numbers as a function of axial position at a bulk Reynolds number of approximately 1 800 are compared for different heat fluxes in the 4 mm test section. The correlation of Shah and London [1], which is valid for simultaneously hydrodynamically and thermally developing forced convection flow, is indicated by the solid red line, while the theoretically fully developed forced convection Nusselt number of 4.36 is indicated by the horizontal red dotted line. The vertical black dotted line indicates the fully developed flow condition of $1/Gz \geq 0.05$ (Eq. 2.11).

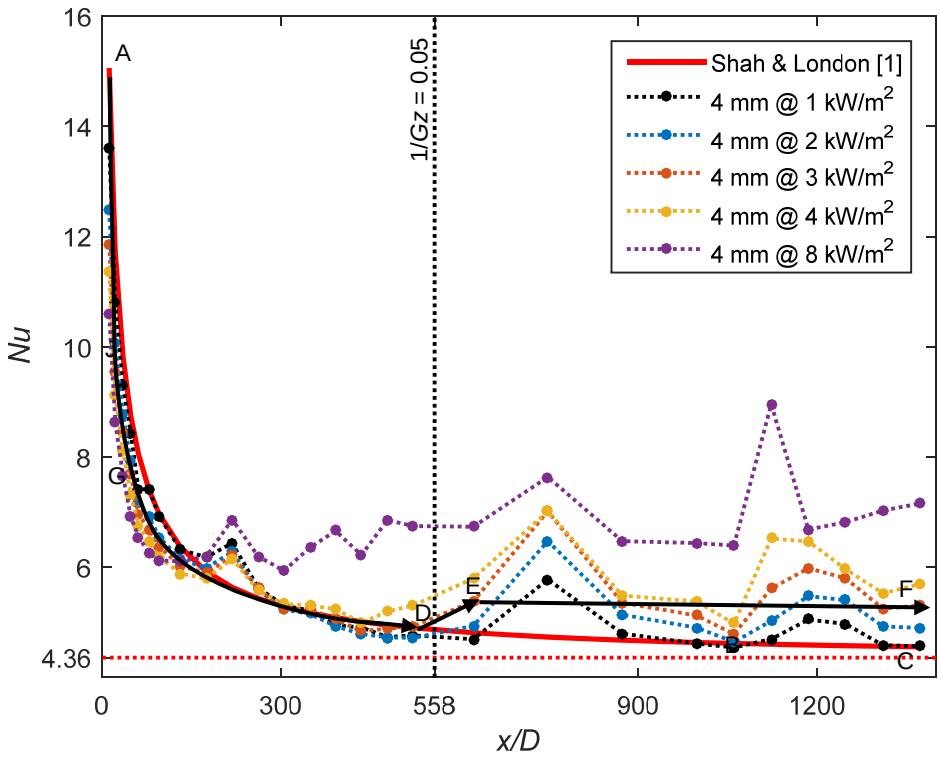

Fig. 5.2: Comparison of Nusselt numbers as a function of axial position at a bulk Reynolds number of 1 800 for different heat fluxes using water as the test fluid. The forced convection results are indicated by points A-B-C along the solid red line, while arrows A-D-E-F indicate the trend at a heat flux of 3 kW/m^2.

As expected, the maximum Nusselt numbers were found at the inlet of the test section, because the thickness of the thermal boundary layer was a minimum. It then decreased along line A-B-C as the thermal boundary layer thickness increased and the flow approached fully developed flow. The forced convection data are indicated by the black markers and correspond very well to the correlation of Shah and London [1] (red line in Fig. 5.3). This formed the 'lower boundary' of the local Nusselt numbers and corresponds to the red line in Fig. 5.1(a). As the heat flux was increased, the Nusselt numbers began to increase and deviate from this line (point D), because free convection effects became significant. This trend is illustrated by the red and blue lines in Fig. 5.1(a). The Nusselt numbers increased with axial position (arrow D-E), but became constant once the flow was fully developed (arrow E-F).

To further investigate the effect of free convection on the local laminar Nusselt numbers, the Nusselt numbers as a function of axial position at a bulk Reynolds number of approximately 1 800 are compared for different heat fluxes and tube diameters (cf. Fig. 5.3). Also included are the experimental data at a heat flux of 4 kW/m^2 in a 19 mm test section [37]. The solid markers represent the results (at different heat fluxes) in the 4 mm test section, while the star and square markers represent the results in the 11.5 mm and 19 mm test sections respectively.

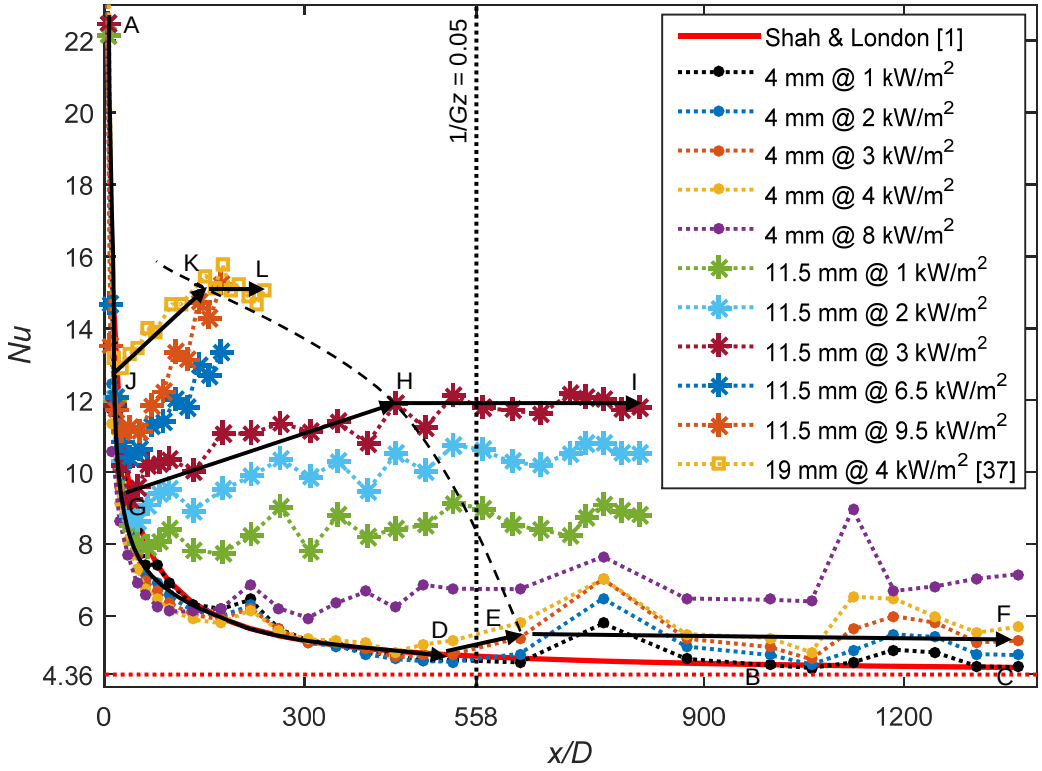

Fig. 5.3: Comparison of Nusselt numbers as a function of axial position at a bulk Reynolds number of 1 800 for different heat fluxes and tube diameters using water as the test fluid. Also included are the experimental data at a heat flux of 4 kW/m^2 in a 19 mm test section [37]. The solid markers represent the results (at different heat fluxes) in the 4 mm test section, while the star and square markers represent the results in the 11.5 mm and 19 mm test sections respectively. The forced convection results are indicated by points A-B-C along the solid red line. Arrows A-D-E-F and A-G-H-I indicate the trend at a heat flux of 3 kW/m^2 in the 4 mm and 11.5 mm test sections while arrows A-J-K-L indicate the trend at a heat flux of 4 kW/m^2 in the 19 mm test section.

Points D, G and J in Fig. 5.3 (schematically illustrated in Fig. 5.1(a)) indicate that as the Grashof number was increased from 917 (point D) to 20 915 (point G) and 198 401 (point J), by increasing the tube diameter and heat flux, free convection effects caused the local Nusselt numbers to deviate from the forced convection results earlier along the test section. Furthermore, the gradient of the Nusselt number lines near the inlet of the test section (arrows A-G and A-J) decreased with increasing Grashof number. Therefore, free convection effects caused the Nusselt numbers to develop faster along the tube length.

Arrows D-E, G-H and J-K in Fig. 5.3, schematically illustrated in Fig. 5.1(a), indicate that as the heat flux and tube diameter were increased, the magnitude and gradient of the Nusselt numbers increased. When the Grashof number was increased by an order of magnitude (points G and J), the Nusselt number gradient increased from 0.0067 (points G-H) to 0.0203 (points J-K), which is also an order of magnitude greater. This can be expected because the Grashof number, and thus free convection

effects, increased with increasing heat flux and tube diameter, which led to enhanced heat transfer inside the test section and thus increased Nusselt numbers. Furthermore, as will be shown in Section 5.3.2, free convection effects caused the flow to develop faster, which also explains why the Nusselt number gradient increased.

Therefore, unlike the forced convection results, the local Nusselt numbers did not decrease and became constant, *but decreased to a minimum and then increased before they became constant and the flow fully developed*. This was due to the combined effects of free convection and developing flow. A similar trend was observed by Cheng and Ou [22], who explained that the local Nusselt numbers decreased near the inlet due to the entrance effect and free convection effects were negligible. At the minimum Nusselt number (for example, points D, G and J in Fig. 5.3), the entrance and free convection effects were equal, but then the Nusselt numbers began to increase once the free convection effects began to dominate the entrance effects. As the flow was not yet fully developed when it began to deviate from the forced convection line, free convection effects increased along the tube length [48], which caused the Nusselt numbers to increase along the tube length.

The Nusselt numbers became constant once the flow was fully developed and the surface-fluid temperature difference became constant (for example, points E, H and K in Fig. 5.1(a) and Fig. 5.3). Points E, H and K in Fig. 5.3 indicate that thermal entrance length decreased significantly with increasing Grashof number, because the Nusselt numbers became constant earlier along the test section. This trend is indicated by the black dotted MCD/FD-line in Fig. 5.1(a) and Fig. 5.3. Furthermore, as schematically illustrated in Fig. 5.1(a), free convection effects also caused the magnitude of the fully developed Nusselt numbers to increase.

5.3.2. Thermal entrance lengths

Figure 5.4 summarises the local Nusselt numbers as a function of the inverse of the Graetz number for bulk Reynolds numbers between 1 000 and 2 000 at heat fluxes of 0.5 kW/m^2 (filled markers) and 1 kW/m^2 (empty markers) in the 4 mm test section. (It should be noted that the results obtained in the 11.5 mm test section were not used in this graph due to greater uncertainties than for the 4 mm test section.) The vertical black dotted line indicates the fully developed flow condition of $1/Gz \geq 0.05$ (Eq. 2.11). Also included in this figure are the correlations of Siegel *et al*. [17] for hydrodynamically fully developed and thermally developing flow, and of Shah and London [1] for simultaneously hydrodynamically and thermally developing flow. The theoretical Nusselt number of 4.36 for fully developed forced convection laminar flow is indicated by the horizontal black dotted line, while a 5% and 10% increase from this Nusselt number is indicated by the horizontal blue and red dotted lines respectively.

As the correlation of Siegel *et al*. [17] was developed for hydrodynamically fully developed flow, the predicted Nusselt numbers were lower than for the correlation of Shah and London [1], because the flow developed faster. Siegel *et al*. [17] considered the flow to be fully developed once the local Nusselt numbers were within 5% of the theoretical fully developed Nusselt number of 4.36 and reported that this should occur at $1/Gz \geq 0.0425$ (as indicated in Fig. 5.4). Figure 5.4 indicates that the correlation of Shah and London [1] only crossed the 5%-line at $1/Gz \approx 0.11$. As the flow in this study was also simultaneously hydrodynamically and thermally developing, the trend of the local Nusselt numbers correlated better with the correlation of Shah and London [1].

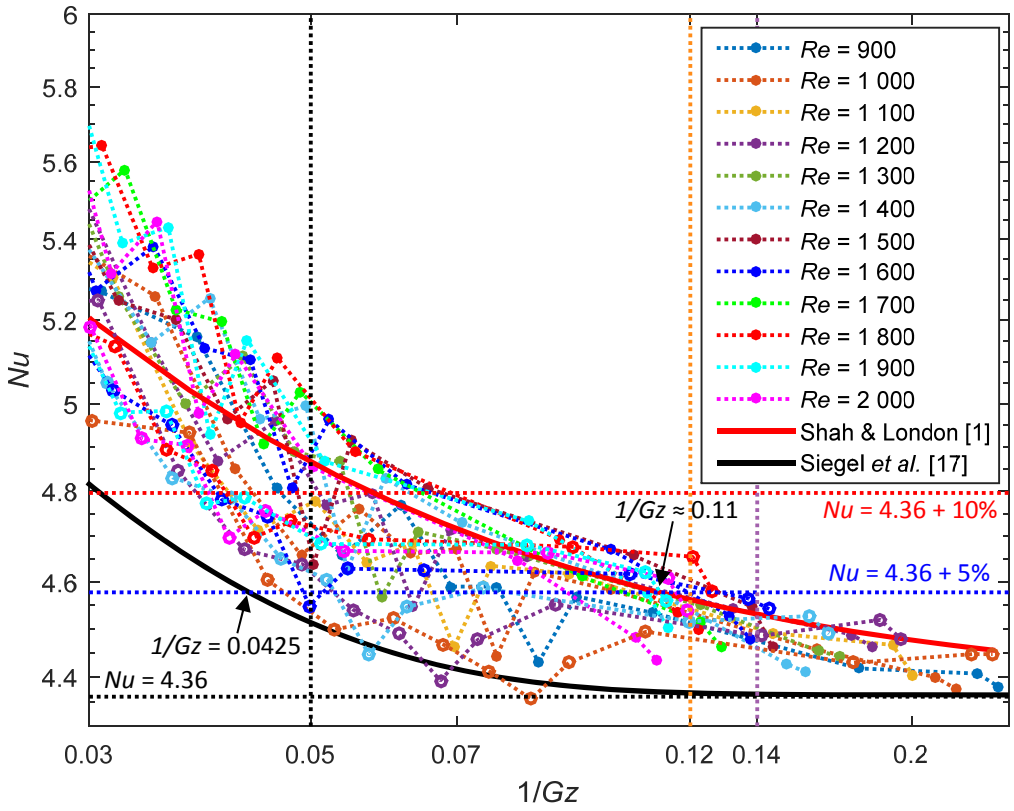

Fig. 5.4: Local Nusselt numbers as a function of the inverse of the Graetz number for bulk Reynolds numbers between 900 and 2 000 in the 4 mm test section. The filled and empty markers represent the results at heat fluxes of 0.5 kW/m² and 1 kW/m² respectively.

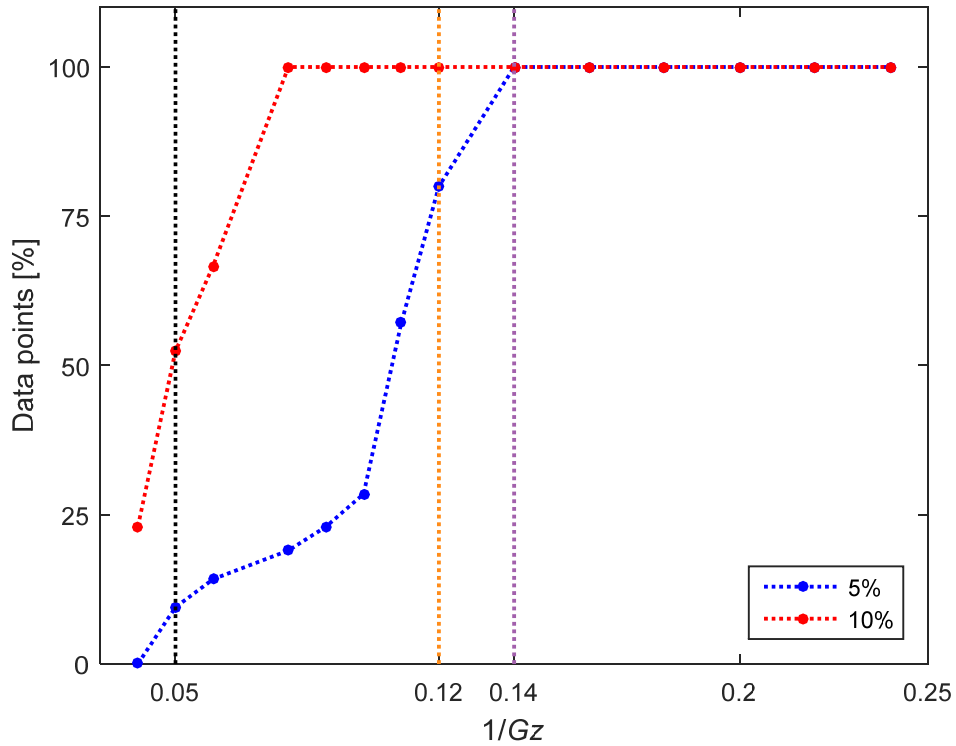

Fig. 5.5: Percentage data points in Fig. 5.4 within 5% and 10% of the theoretical Nusselt number of 4.36.

Figure 5.5 shows the percentage data points within 5% and 10% of the theoretical Nusselt number of 4.36 as a function of $1/Gz$. This graph indicates that at $1/Gz = 0.05$ (indicated by the black dotted line), only 10% of the experimental data points were within 5% (thus fully developed). It therefore means that $C = 0.05$ (Eq. 2.11), as used in most subject literature, is inaccurate. At $1/Gz = 0.12$ (indicated by the orange dotted line), 80% of the experimental data points were within 5% and all the experimental data points within 10%. This corresponded well to the value of $1/Gz \approx 0.11$ where the correlation of Shah and London [1] crossed the 5%-line. At $1/Gz = 0.14$ (indicated by the purple dotted line), all the experimental data points were within 5%. Acknowledging the uncertainty of the study's forced convection data (average uncertainty of 18% and 10% for heat fluxes of 0.5 kW/m^2 and 1 kW/m^2 respectively), it is clear that $1/Gz \geq 0.12$ is a more accurate/conservative criterion for fully developed flow when the flow is simultaneously hydrodynamically and thermally developing. However, a conservative value of $1/Gz \geq 0.14$ will ensure that all the Nusselt numbers are within 5% of the theoretical Nusselt number of 4.36. It can therefore be concluded that the theoretical thermal entrance length correlation (Eq. 2.11) is better suited for hydrodynamically fully developed flow. A longer thermal entrance length is required for simultaneously hydrodynamically and thermally developing flow, therefore a coefficient of 0.12 is recommended.

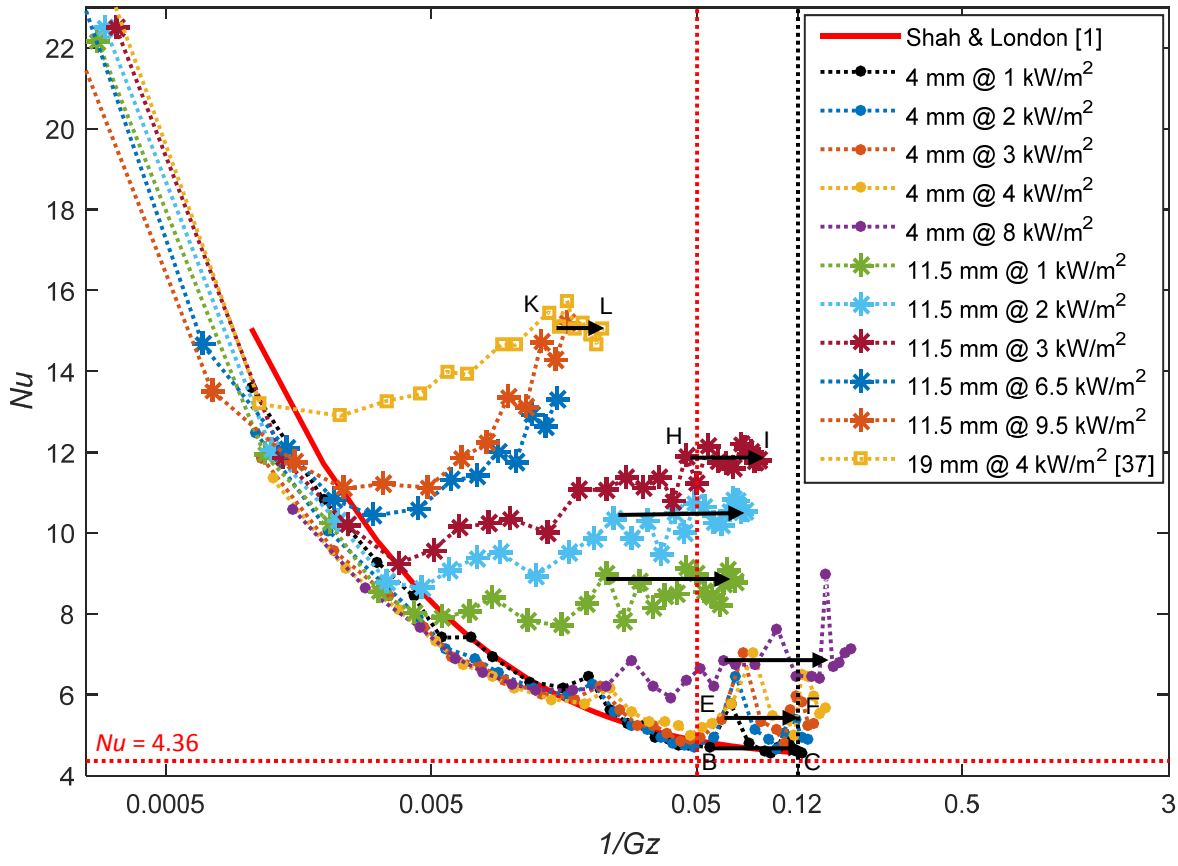

Fig. 5.6: Comparison of local Nusselt numbers against the inverse of the Graetz number, at a bulk Reynolds number of 1 800 for different heat fluxes and tube diameters.

The mixed convection results in Fig. 5.3 are plotted against the inverse of the Graetz number in Fig. 5.6. The horizontal red dotted line represents the theoretical Nusselt number of 4.36 for fully developed forced convection laminar flow, while the vertical red dotted line indicates $1/Gz = 0.05$, which is the thermal entrance length predicted using Eq. 2.11. The vertical black dotted line indicates

$1/Gz = 0.12$, which is the forced convection thermal entrance length for simultaneously hydrodynamically and thermally developing flow, found in Fig. 5.4. The fully developed data are indicated using black horizontal arrows and these arrows indicate that, similar to Fig. 5.3, the location ($1/Gz$) at which the flow became fully developed decreased significantly with increasing tube diameter (thus increasing Grashof number). However, for a fixed tube diameter, the value of $1/Gz$ increased with increasing heat flux, because $1/Gz$ was inversely proportional to the Prandtl number, which decreased with increasing temperature. As can be expected, Fig. 5.6 indicates that both forced convection thermal entrance length conditions ($1/Gz = 0.05$ and $1/Gz = 0.12$) became increasingly inaccurate at higher Grashof numbers (11.5 mm test section and 19 mm test section) and should therefore be adjusted when mixed convection conditions exist, especially at high Grashof numbers.

5.3.3. Boundaries between FCD, MCD and FD laminar regions

For laminar flow, three different regions (FCD, MCD and FD in Fig. 5.1(a)) were identified and correlations were developed to quantify the FCD/MCD and MCD/FD boundaries. The ranges of the correlations are summarised in Table 5.1.

Table 5.1: Ranges of correlations to predict the FCD/MCD boundary (Eqs. 5.1 and 5.2) and the MCD/FD boundary (Eqs. 5.3 and 5.4).

	Re	*Pr*	*Gr*	*Gr**	*Gz*	*D* [mm]
FCD/MCD 5.1, 5.2	48 - 3 217	2.9 - 282	2.48 - 4.51×10^5	541 - 4.01×10^6	2.6 - 1.14×10^5	3 - 19
MCD/FD 5.3, 5.4	467 - 3 217	2.9 - 53	30.6 - 4.51×10^5	2.48 – 6.02×10^5	2.6 - 3.49×10^4	4 - 19

5.3.3.1. FCD/MCD boundary

To determine the FCD/MCD boundary, the Nusselt numbers in Fig. 5.3 were evaluated in terms of $(1/Gz)Gr^{0.57}Pr^{0.4}$ to account for mixed convection conditions (Gr) and different test fluids (Pr). Figure 5.7(a) indicates that the FCD/MCD boundary (points B, D, G and J) can be estimated to be at $(1/Gz)Gr^{0.57}Pr^{0.4} = C_1$, where the constant C_1 is approximately equal to 2.4.

Using the boundary $(1/Gz)Gr^{0.57}Pr^{0.4} = C_1$, the entrance length required for the flow to be in the MCD region can be determined as follows, and can also be written as a function of the forced convection thermal entrance length, Lt_{FC}, (using $C = 0.12$):

$$Lt_{MCD} = \frac{C_1 RePr^{0.6} D}{Gr^{0.57}} = \frac{C_1 Lt_{FC}}{0.12 Gr^{0.57} Pr^{0.4}} \qquad 5.1$$

From Eq. 5.1, it follows that similar to Eq. 2.11, the entrance length for mixed convection developing flow, $Lt_{MCD,}$ increased with increasing Reynolds number, Prandtl number and tube diameter. However, it was inversely proportional to the Grashof number and therefore decreased as free convection effects increased. Furthermore, the entrance length was a weaker function of Prandtl number (compared with forced convection) once free convection effects became significant. This was expected, because the fluid properties (density and viscosity) were accounted for in the Reynolds number and Grashof number.

Similarly for the modified Grashof number, Fig. 5.7(b) indicates that the FCD/MCD boundary (points B, D, G and J in Fig. 5.7(b), corresponding to the same points in Fig. 5.1(a) and Fig. 5.3), can be

estimated to be at $(1/Gz)Gr^{*0.45}Pr^{0.4} = C_2$, where the constant C_2 is approximately equal to 2.1. Using the boundary $(1/Gz)Gr^{*0.45}Pr^{0.4} = C_2$, the length required for the flow to be in the MCD region was determined as:

$$Lt_{MCD} = \frac{C_2 RePr^{0.6} D}{Gr^{*0.45}} = \frac{C_2 Lt_{FC}}{0.12 Gr^{*0.45} Pr^{0.4}} \qquad 5.2$$

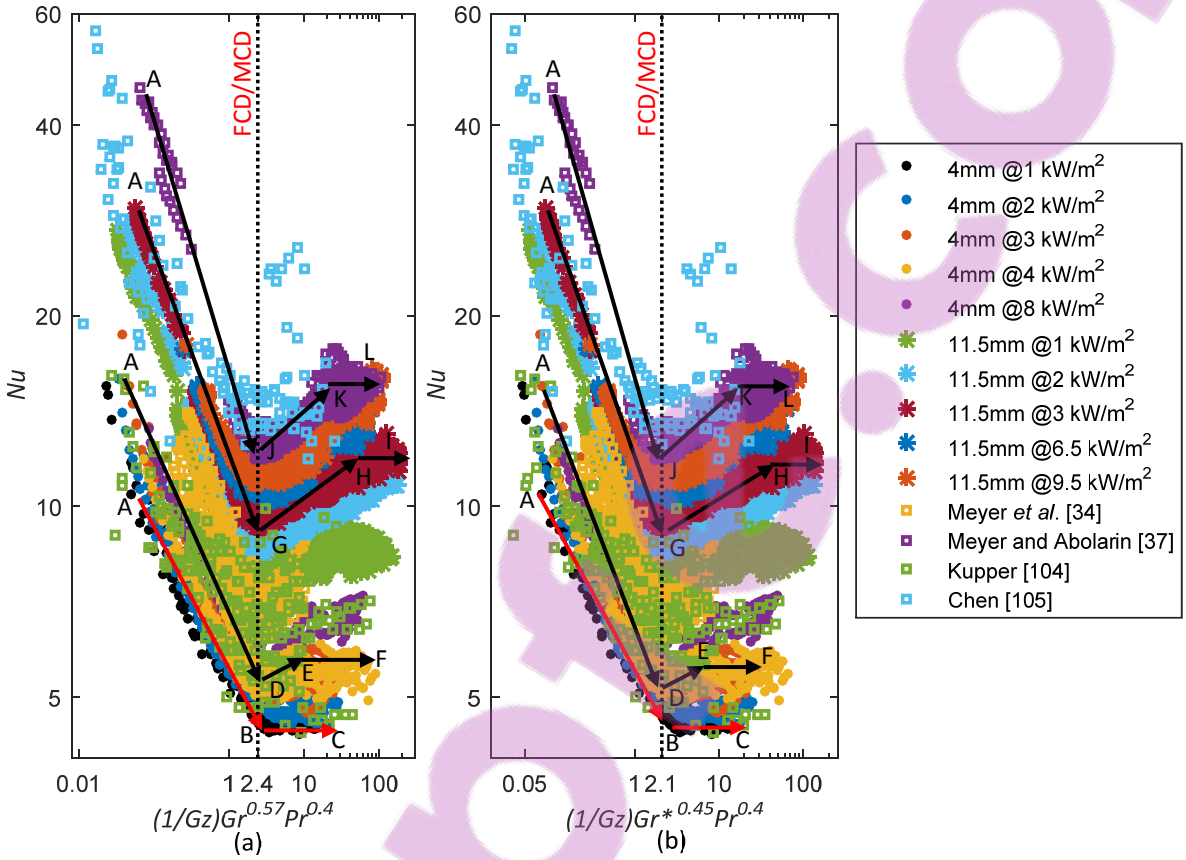

Fig. 5.7: Nusselt numbers as a function of (a) $(1/Gz)Gr^{0.57}Pr^{0.4}$ and (b) $(1/Gz)Gr^{*0.45}Pr^{0.4}$, to determine the FCD/MCD boundary. The solid markers represent the results (at different heat fluxes) in the 4 mm test section, while the star and square markers represent the results in the 11.5 mm and literature [34, 37, 104, 105] respectively. The forced convection results are indicated by red arrows A-B-C. Arrows A-D-E-F and A-G-H-I indicate the trend at a heat flux of 3 kW/m² in the 4 mm and 11.5 mm test sections, while arrows A-J-K-L indicate the trend at a heat flux of 4 kW/m² in the 19 mm test section.

5.3.3.2. MCD/FCD boundary

Figure 5.1(a) indicates that the location at which the flow became fully developed (MCD/FD boundary) was not as distinct as the FCD/MCD boundary, because the gradient of the Nusselt numbers did not change from negative to positive, but gradually from positive to zero. Figure 5.6 indicates that the forced convection thermal entrance length equations became increasingly inaccurate when the Grashof numbers were increased. Experimental data for high Prandtl number fluids in the MCD region are rare, because the increased viscosity prevents free convection effects to dominate the entrance effects. This boundary was therefore developed mainly with water data; however, a single case of 60% diethylene glycol data at a Reynolds number of approximately 1 600 [105] was included, because free convection effects dominated the entrance effects in a small part of the test section. As the Prandtl numbers varied between 45.7 and 53, this case extended the Prandtl number range of this boundary.

To determine the MCD/FD boundary, the Nusselt numbers were plotted (Fig. 5.8(a)) in terms of $(1/Gz)Gr^{0.4}Pr^{1.65}(x/D)^{0.3}$, to account for mixed convection conditions (Gr) and different test fluids (Pr). It was found that the non-dimensional axial distance (x/D) had to be included, because the thermal boundary layer thickness, and thus free convection effects, changed along the tube length when the flow was developing. Points B, E, H and K in Fig. 5.8(a) (corresponding to the same points in Fig. 5.1(a) and Fig. 5.3) indicate that the MCD/FD boundary was estimated to be at $(1/Gz)Gr^{0.4}Pr^{1.65}(x/D)^{0.3} = C_3$, where the constant C_3 is approximately equal to 130.

Using the boundary $(1/Gz)Gr^{0.4}Pr^{1.65}(x/D)^{0.3} = C_3$, the length required for the flow to become fully developed during mixed convection conditions was determined as:

$$Lt_{FD} = D\left(\frac{C_3 Re}{Gr^{0.4}Pr^{0.65}}\right)^{10/13} = \frac{Lt_{FC}}{0.12}\left(\frac{C_3}{Re^{0.3}Pr^{1.95}Gr^{0.4}}\right)^{10/13} \quad 5.3$$

From Eq. 5.3, it follows that the thermal entrance length was proportional to the Reynolds number and tube diameter, but inversely to the Grashof number and Prandtl number. This explains why fully developed flow (or very close to) was obtained in the experimental data set of Chen [105], although the maximum length-to-inside diameter ratio was only 400 and the Prandtl number high ($45 < Pr < 53$).

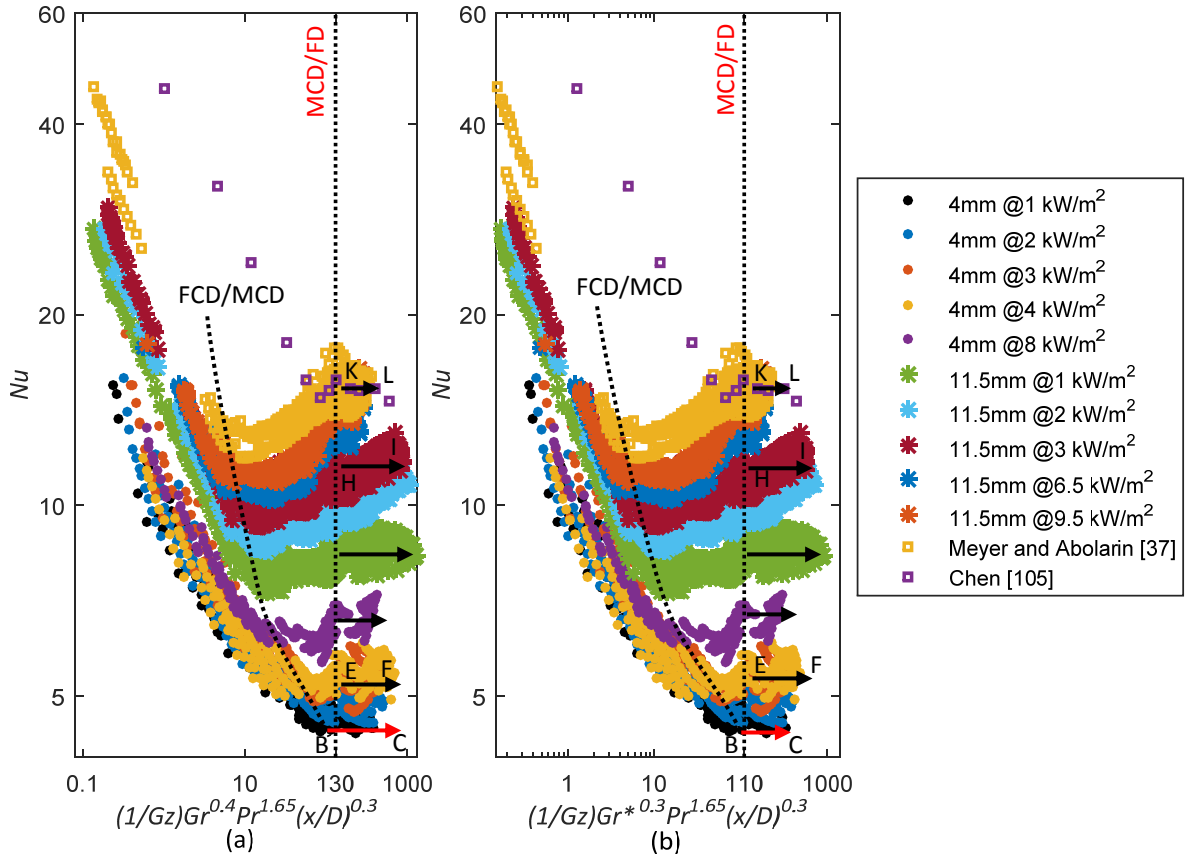

Fig. 5.8: Nusselt numbers as a function of (a) $(1/Gz)Gr^{0.4}Pr^{1.65}(x/D)^{0.3}$ and (b) $(1/Gz)Gr^{*\,0.3}Pr^{1.65}(x/D)^{0.3}$ to determine the MCD/FD boundary. The solid markers represent the results (at different heat fluxes) in the 4 mm test section, while the star and square markers represent the results in the 11.5 mm test section and literature [37, 105] respectively.

The same procedure was then repeated for the modified Grashof number. Points B, E, H and K in Fig. 5.8(b) (corresponding to the same points in Fig. 5.1(a) and Fig. 5.3) indicate that the MCD/FD boundary

was estimated to be at $(1/Gz)Gr^{*0.3}Pr^{1.65}(x/D)^{0.3} = C_4$, where the constant C_4 is approximately equal to 110. The length required for the flow to become fully developed during mixed convection conditions, as a function of Gr^*, was determined as:

$$Lt_{FD} = D\left(\frac{C_4 Re}{Gr^{*\,0.3}Pr^{0.65}}\right)^{10/13} = \frac{Lt_{FC}}{0.12}\left(\frac{C_4}{Gr^{*\,0.3}Re^{0.3}Pr^{1.95}}\right)^{10/13} \quad 5.4$$

5.3.3.3. Conditions for no MCD region

Cheng and Ou [22] numerically investigated free convection effects in large Prandtl number fluids and found that when the Rayleigh number was greater than 3.75×10^5, the local Nusselt numbers decreased along the tube length and became constant. Similar results were also obtained in literature [34, 63, 105-107] when higher Prandtl number fluids, such as glycols and nanofluids, were used. Figure 5.9 contains three cases of local Nusselt numbers as a function of axial position of experimental data from literature [105-107] using high Prandtl number fluids. From all three data sets, it follows that the Nusselt numbers decreased near the inlet of the test section and then became constant, indicating that the flow was fully developed. As the Nusselt numbers did not increase with axial position before they became constant, the MCD region became negligible, and the local Nusselt numbers changed from the FCD region directly to the FD region. However, the fully developed Nusselt numbers were significantly higher than 4.36 (indicated by the horizontal black dotted line), confirming that mixed convection conditions existed, and it also increased with increasing Prandtl number.

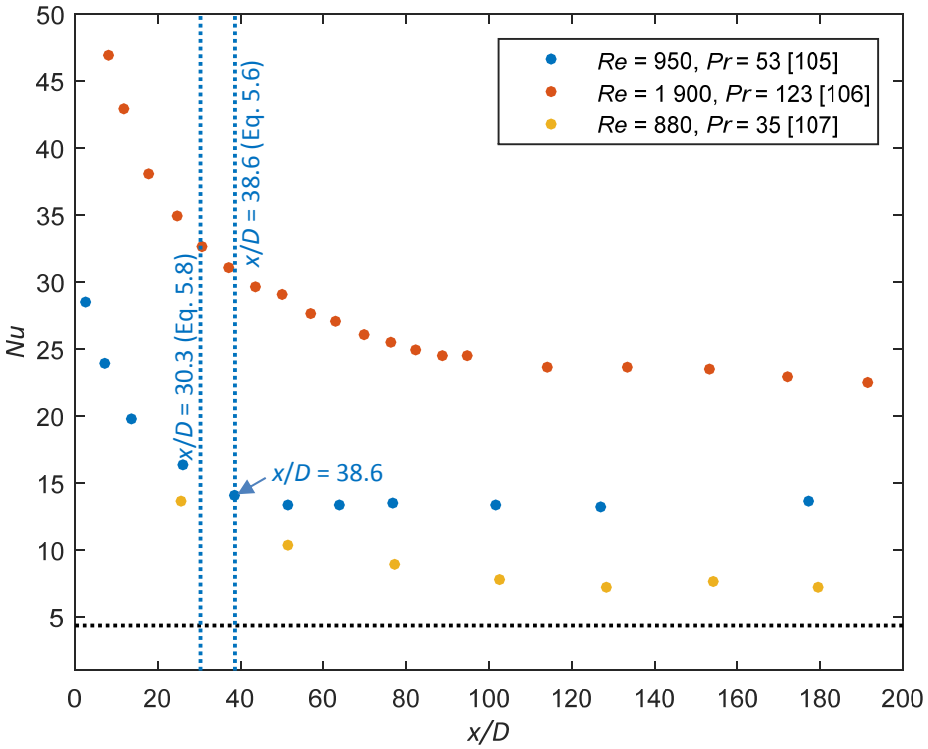

Fig. 5.9: Local Nusselt numbers as a function of axial position of experimental data from literature [105-107] using high Prandtl number fluids.

To investigate the influence of Prandtl number on free convection effects, the fluid properties of water and ethylene glycol are compared in Section 6.4. Due to the significantly higher viscosity in the centre

of the tube, it was found that the free convection effects were restricted to the thermal boundary layer and did not lead to secondary flow, which assists in the diffusion of the heat from the surface to the centre of the tube.

The Grashof number, $Gr_{FCD/FD}$, where the FCD/MCD and MCD/FD boundaries become equal will represent the point where the MCD region is negligble. Thus at this condition the flow will change from the FCD region to the FD region without any MCD region. This is schematically illustrated by the purple line in Fig. 5.10.

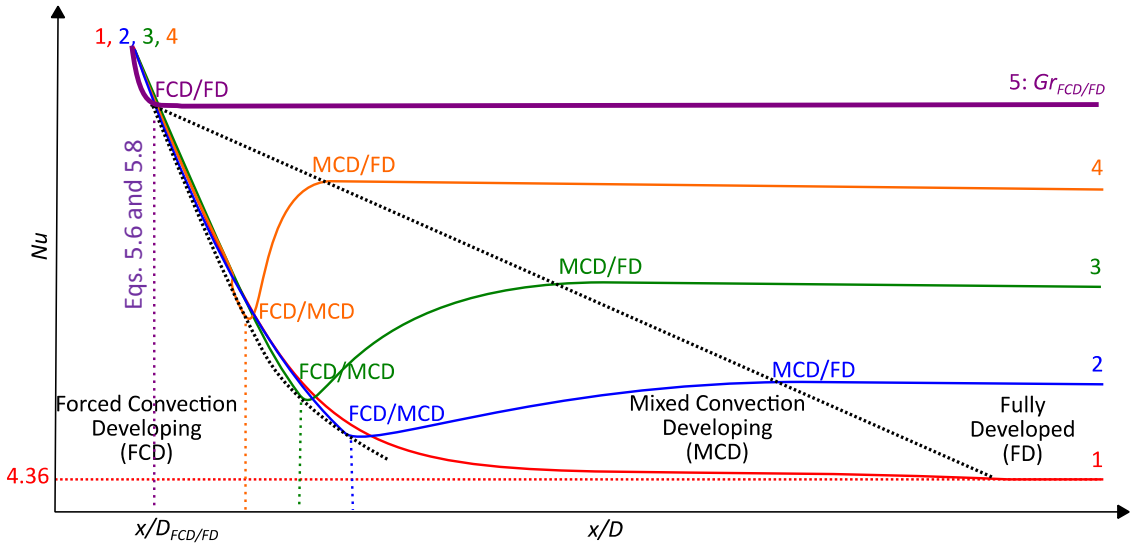

Fig. 5.10: Schematic representation of the effect of Grashof number on the local Nusselt numbers as a function of axial position, indicating the conditions of no MCD region.

For the MCD region to become negligble, Eqs. 5.1 and 5.3 were solved simultaneously as $Lt_{MCD} = Lt_{FD}$:

$$Gr_{FCD/FD} \geq 1.78 \times 10^{-5} Re^{0.88} Pr^{4.19} \quad 5.5$$

Equation 5.5 was then substituted into Eq. 5.1 to obtain the location where the FCD/MCD and MCD/FD boundaries become equal:

$$\frac{x_{FCD/FD}}{D} = \frac{1223 Re^{0.5}}{Pr^{1.79}} \quad 5.6$$

The same procedure was then repeated for the modified Grashof number, using Eqs. 5.2 and 5.4:

$$Gr^*_{FCD/FD} \geq 2.03x10^{-6} Re^{1.05} Pr^{5.02} \quad 5.7$$

$$\frac{x_{FCD/FD}}{D} = \frac{766 Re^{0.526}}{Pr^{1.658}} \quad 5.8$$

From Eqs. 5.6 and 5.8, it follows that the FCD/FD boundary was dependent on the ratio of the Reynolds number to the Prandtl number. Equations 5.5 to 5.8 were verified using the experimental data of Chen [105] (blue markers in Fig. 5.9). This figure indicates that the Nusselt numbers became approximately constant at x/D = 38.6, while Eqs. 5.6 and 5.8 predicted the FCD/FD boundary to be at x/D = 38.6 and x/D = 30.3 (within approximately 20%) respectively.

As Eqs. 5.6 and 5.8 produced different results for Fig. 5.9, their sensitivity towards Prandtl number was evaluated for different cases of Reynolds number and Prandtl number and the results are summarised in Table 5.2. This table indicates that the deviation between the correlations at a Prandtl number of three was approximately 14%. It then decreased to 3% when the Prandtl number was increased to seven, but increased to 22% as the Prandtl number was increased to 50. This is as expected, because most of the data that were used to develop these correlations were at a Prandtl number of approximately seven. Less data had Prandtl numbers as low as three, while only a single case of 60% diethylene glycol ($45.7 < Pr < 53$) data at a Reynolds number of approximately 1 600 [105] was used to develop Eqs. 5.3 and 5.4. The Prandtl number in Table 5.2 was not increased further, because Eqs. 5.3 and 5.4 were limited to Prandtl numbers up to 53. The accuracy of Eqs. 5.6 and 5.8 for high and low Prandtl number fluids can be improved when more experimental data with high Prandtl numbers are available to modify Eqs. 5.3 and 5.4.

Table 5.2: Verification of FCD/MCD and MCD/FD boundaries using Eqs. 5.6 and 5.8.

	x/D (Eq. 5.6)	x/D (Eq. 5.8)	% difference
Re = 500, Pr = 3	3 827	3 257	16.1
Re = 500, Pr = 7	840	799	4.9
Re = 500, Pr = 50	25	31	20.9
Re = 1 000, Pr = 3	5 412	4 690	14.3
Re = 1 000, Pr = 7	1 188	1 151	3.1
Re = 1 000, Pr = 50	35	44	22.7
Re = 2 000, Pr = 3	7 654	6 753	12.5
Re = 2 000, Pr = 7	1 680	1 657	1.3
Re = 2 000, Pr = 50	50	64	24.5

5.3.4. Local Nusselt number correlations

To develop a correlation that accurately predicts the local Nusselt numbers in all three regions (Fig. 5.1(a)), three separate correlations were first developed for the FCD, MCD and FD regions. It was found that the heat transfer characteristics in the MCD and FD regions were similar, because both correlations were a function of Grashof number (or modified Grashof number), Prandtl number and Graetz number. Therefore, a combined correlation for the MCD and the FD regions was developed. The method of Churchill and Usagi [80] was used to combine the equation for the FCD region (Nu_1) and the combined MCD and FD regions (Nu_2), and it was found that the results did not improve significantly for exponents larger than six. Equations 5.9 and 5.10 can be used to calculate the local Nusselt numbers in terms of the Grashof number and modified Grashof number and are thus valid for all three laminar regions:

$$Nu = 4.36 + (Nu_1^6 + Nu_2^6)^{1/6} \qquad 5.9$$
$$Nu_1 = (0.33Gz^{0.54} - 0.84)Pr^{-0.2}$$
$$Nu_2 = (0.207Gr^{0.305} - 1.19)Pr^{0.5}Gz^{-0.08}$$

$$Nu = 4.36 + (Nu_1^6 + Nu_2^6)^{1/6} \qquad 5.10$$
$$Nu_1 = (0.33Gz^{0.54} - 0.84)Pr^{-0.2}$$
$$Nu_2 = (0.202Gr^{*\,0.254} - 1.23)Pr^{0.45}Gz^{-0.06}$$

Table 5.3 summarises the ranges and performance of the correlations compared with the experimental results of this study, using 5 680 data points, and this study and literature [34, 101, 104,

105, 107-109], using a total of 7 675 data points. Table 5.3 indicates that both correlations predicted almost all the data (99%) of this study within 20%. Furthermore, approximately 80% of the experimental data of this study and literature [34, 37, 104, 105, 107-109] were predicted within 10%.

Table 5.3: Overall performance and ranges of the local laminar Nusselt number correlations. The value of *n* represents the number of data points and Ave %, the average deviation.

Eq.	This study only				This study and literature [34, 37, 104, 105, 107-109]			
	n	±10 % [%]	±20% [%]	Ave %	*n*	±10% [%]	±20% [%]	Ave %
Gr: 5.9	5 680	87	99	5.4	7 675	78	94	7.4
*Gr**: 5.10	5 680	89	99	5.3	7 675	78	94	7.3
Range	467 ≤ *Re* ≤ 3 217, 3 ≤ *Pr* ≤ 7.4, 2.6 ≤ *Gz* ≤ 5 589, 30 ≤ *Gr* ≤ 2.49×10^5, 541 ≤ *Gr** ≤ 4.01×10^6				48 ≤ *Re* ≤ 3 217, 2.9 ≤ *Pr* ≤ 282, 2.6 ≤ *Gz* ≤ 1.14×10^5, 5.5 ≤ *Gr* ≤ 4.51×10^5, 41.3 ≤ *Gr** ≤ 7.27×10^6			

To determine the validity/accuracy of the correlations for Prandtl numbers less than one, the performance of the correlations was determined using experimental data conducted using air as the test fluid. Apart from the experimental data of McComas and Eckert [19], limited experimental data using air, which gives the Reynolds number, Nusselt number, Grashof number and axial position of each data point, were available in literature. The performance of Eqs. 5.9 and 5.10 was determined using 34 experimental data points obtained using air at $Re \approx 740$, $Pr \approx 0.7$ and $3.34 < Gr < 491$. It was found that Eq. 5.9 could predict 71% of the data within 20% and the average deviation was 15%, while Eq. 5.10 could predict 80% of the data within 20% and the average deviation was 13%

5.3.5. Average laminar Nusselt numbers

Shah [110] developed a correlation to determine the average Nusselt numbers of developing flow; however, it was limited to constant fluid properties. The available average mixed convection Nusselt number correlations are valid for a constant surface temperature boundary condition [111, 112] and not for a constant heat flux boundary condition. Therefore, the local Nusselt number correlations (FCD region (Nu_1) and combined MCD and FD regions (Nu_2) in Eqs. 5.9 and 5.10) were combined and integrated along the tube length, L. The following correlation was obtained to calculate the average laminar Nusselt number over a length, L, measured from the tube inlet:

$$\overline{Nu} = 4.36 + \overline{Nu}_1 + \overline{Nu}_2 \tag{5.11}$$

$$\overline{Nu}_1 = \frac{1}{L}\int_0^{Lt_{MCD}} Nu_1\, dL = \frac{1}{L}\left(-0.84\, Pr_b^{-0.2} Lt_{MCD} + 0.72(Re_b D)^{0.54} Pr_b^{0.34} Lt_{MCD}^{0.46}\right)$$

$$\overline{Nu}_2 = \frac{1}{L}\int_{Lt_{MCD}}^{L} Nu_2\, dL = \left(0.207 Gr_b^{0.305} - 1.19\right) Pr_b^{0.42} (Re_b D)^{-0.08} (L - Lt_{MCD})$$

$$Lt_{MCD} = \frac{2.4 Re_b Pr_b^{0.6} D}{Gr_b^{0.57}} \text{ for } L > Lt_{MCD}$$

$$Lt_{MCD} = L \text{ for } L < Lt_{MCD}$$

In this equation, as well as Eq. 5.12, the Reynolds numbers, Prandtl numbers and Grashof numbers were evaluated at the bulk fluid temperature. Similarly, Eq. 5.12 was developed to calculate the Nusselt numbers as a function of the modified Grashof number:

$$\overline{Nu} = 4.36 + \overline{Nu}_1 + \overline{Nu}_2 \qquad 5.12$$

$$\overline{Nu}_1 = \frac{1}{L}\int_0^{Lt_{MCD}} Nu_1\, dL = \frac{1}{L}(-0.84\, Pr_b^{-0.2} Lt_{MCD} + 0.72(Re_b D)^{0.54} Pr_b^{0.34} Lt_{MCD}^{0.46})$$

$$\overline{Nu}_2 = \frac{1}{L}\int_{Lt_{MCD}}^{L} Nu_2\, dL = \left(0.202 Gr_b^{*\,0.254} - 1.23\right) Pr_b^{0.39} (Re_b D)^{-0.06} (L - Lt_{MCD})$$

$$Lt_{MCD} = \frac{2.1 Re_b Pr_b^{0.6} D}{Gr_b^{*\,0.45}} \text{ for } L > Lt_{MCD}$$

$$Lt_{MCD} = L \text{ for } L < Lt_{MCD}$$

Thus, Eq. 5.11 is in terms of Grashof number while Eq. 5.12 is in terms of the modified Grashof number. Table 5.4 summarises the ranges and performance of Eqs. 5.11 and 5.12 using 495 experimental data points of this study. Table 5.4 indicates that both correlations performed very well and could predict 95% of the data within 10% and all the data within 20%.

Table 5.4: Overall performance and ranges of the average laminar Nusselt number correlations. The value of *n* represents the number of data points and Ave %, the average deviation.

Eq.	Experimental data from this study			
	n	±10 % [%]	±20% [%]	Ave %
Gr: 5.11	495	98	100	3.6
*Gr**: 5.12	495	95	100	3.6
Range	48 ≤ *Re* ≤ 3 217, 2.9 ≤ *Pr* ≤ 282, 2.6 ≤ *Gz* ≤ 1.14×10^5, 5.5 ≤ *Gr* ≤ 4.51×10^5, 41.3 ≤ *Gr** ≤ 7.27×10^6			

5.4. Quasi-turbulent and turbulent flow

Limited results in the quasi-turbulent and turbulent flow regimes are presented in this chapter, because it is only required to link the results given in Fig. 5.3 and Fig. 5.11, to Fig. 5.14. Figure 5.11 compares the Nusselt numbers as a function of axial position for bulk Reynolds numbers between 4 000 and 8 000 at heat fluxes of 3 kW/m^2 and 8 kW/m^2 in the 4 mm test section, and at heat fluxes of 1 kW/m^2 and 3 kW/m^2 in the 11.5 mm test section.

The thermal entrance length for turbulent flow (normally taken as approximately 10*D* [3]) can be regarded as negligible, because the Nusselt numbers remained constant along the entire tube length. Furthermore, the magnitude of the Nusselt numbers increased with increasing Reynolds numbers due to the enhanced mixing inside the test section. As expected, at a specific Reynolds number, for example, 8 000, there was no significant difference between the magnitude of the Nusselt numbers in the different test sections and at different heat fluxes, confirming that free convection effects were negligible. However, Fig. 5.11(b) (this figure is selected as it is easy to distinguish) indicates that at Reynolds numbers between 4 000 and 7 000, the Nusselt numbers increased slightly along the tube length. This increase became lower as the Reynolds number was increased and at a Reynolds number of 8 000, the Nusselt numbers were constant along the entire tube length. Therefore, the flow was not yet fully turbulent (at 4 000 < *Re* < 7 000), but still in the quasi-turbulent regime, which is the

upper part of the transitional flow regime. In this flow regime, the flow approaches turbulent flow and the heat transfer characteristics are similar to turbulent flow. However, as the flow is not fully turbulent yet, turbulent heat transfer corrections overpredict the Nusselt numbers in this region [7].

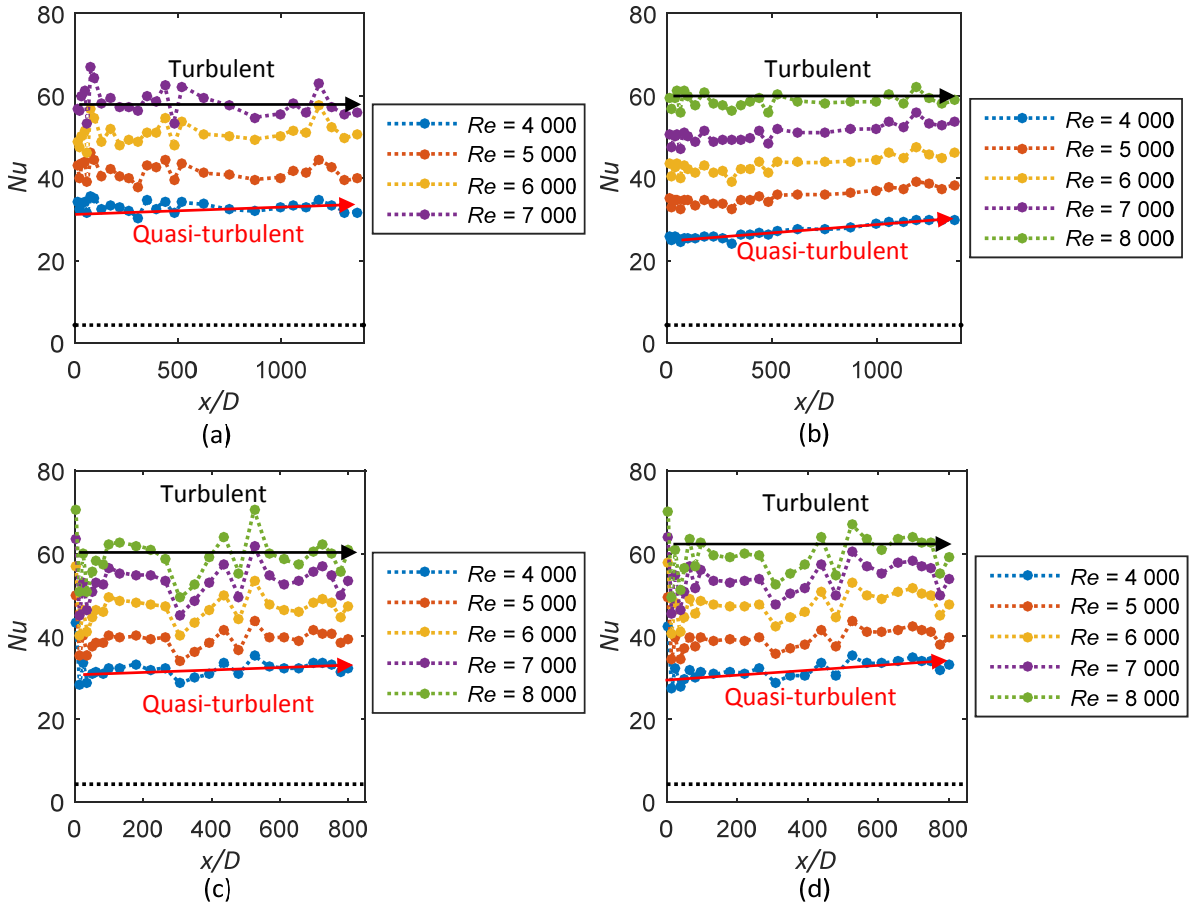

Fig. 5.11: Comparison of Nusselt numbers as a function of axial position for bulk Reynolds numbers between 4 000 and 8 000 at a heat flux of (a) 3 kW/m² and (b) 8 kW/m² in the 4 mm test section, and at a heat flux of (c) 1 kW/m² and (d) 3 kW/m² in the 11.5 mm test section. The red and black arrows indicate the trends in the quasi-turbulent and turbulent flow regimes respectively.

5.5. Transitional flow

5.5.1. Critical Reynolds number

The critical Reynolds number corresponds to the Reynolds number before fluctuations in mass flow rate and temperature occur and was obtained using the nomenclature defined in Section 3.8.1.1. Figure 5.12 contains the local Nusselt numbers as a function of axial position at the bulk critical Reynolds number at different heat fluxes in the 4 mm and 11.5 mm test sections. The results in this graph are directly aligned to Fig. 5.1(b).

It is shown in Fig. 6.6 that the start of the transitional flow regime was affected by free convection effects, therefore different critical Reynolds numbers were obtained for the different heat fluxes and tube diameters. Figure 5.12 indicates that, at the critical Reynolds number, the local Nusselt numbers decreased along the tube length and then became constant. As schematically illustrated in Fig. 5.1(b), it follows from points B, D, F and H in Fig. 5.12 that the axial position at which the Nusselt numbers became constant, decreased with increasing heat flux and tube diameter (thus increasing free

convection effects). Furthermore, the magnitude of the fully developed Nusselt numbers increased with increasing Grashof number (points C, E, G and I in Fig. 5.1(b) and Fig. 5.12).

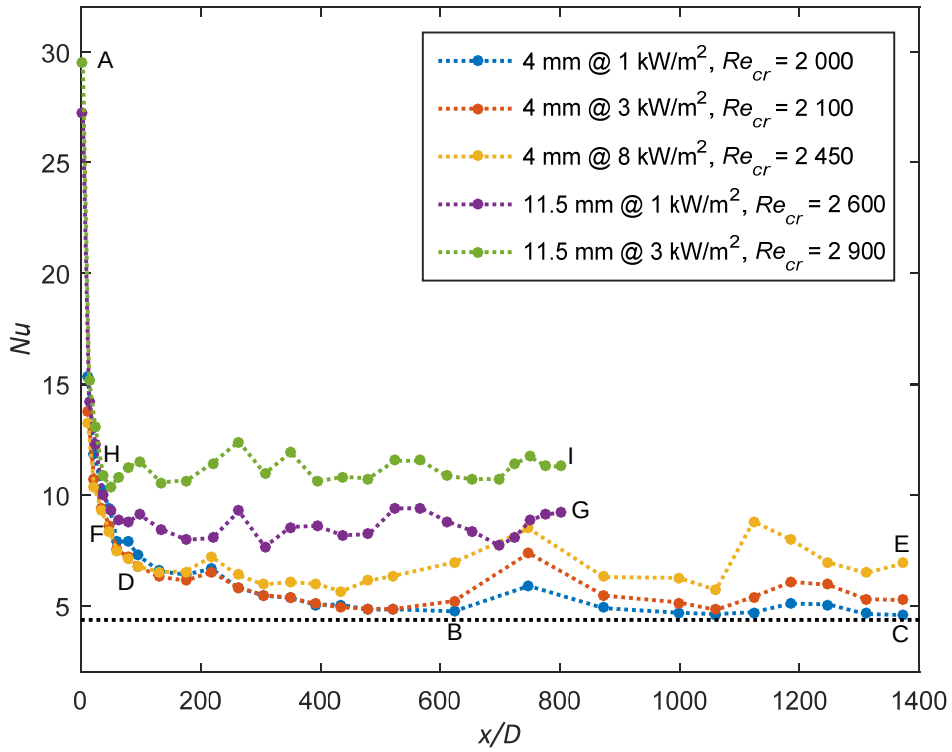

Fig. 5.12: Local Nusselt numbers as a function of axial position at the critical Reynolds number at different heat fluxes in the 4 mm and 11.5 mm test sections.

5.5.2. Forced convection laminar-turbulent transition

The results in this section are directly aligned to Fig. 5.1(c). Figure 5.13 compares the local Nusselt numbers as a function of axial position for different bulk Reynolds numbers in the transitional flow regime at a heat flux of 1 kW/m^2 in the 4 mm test section; therefore, the flow was dominated by forced convection conditions. For comparison purposes, the theoretical Nusselt number of 4.36 for fully developed laminar forced convection flow, is indicated by the black dotted line. Figure 5.13 indicates that for Reynolds numbers between 2 000 and 2 200, the trend of the local Nusselt numbers was similar to that of the critical Reynolds number (Fig. 5.1(b)). However, the location at which the Nusselt numbers became constant decreased with increasing Reynolds number (points B and D in Fig. 5.13 and Fig. 5.1(c)). Furthermore, as schematically illustrated in Fig. 5.1(c), points C and E indicate that the fluctuations inside the test section as well as the increased fluid velocity led to enhanced mixing, therefore the magnitude of the Nusselt numbers increased.

At Reynolds numbers greater than 2 200, the local Nusselt numbers decreased (laminar) near the inlet of the test section, then increased significantly (transition) with axial position, forming a 'dip'. It then increased slightly (quasi-turbulent) before it became constant (turbulent). As shown schematically by the green and yellow lines in Fig. 5.1(c), four different regions can be distinguished and the different regions are indicated by the dotted red lines in Fig. 5.13 for a Reynolds number of 2 400. Due to the small heat flux that was applied (to ensure forced convection conditions), the temperature and Nusselt number uncertainties increased, which made it challenging to distinguish between the quasi-turbulent and turbulent flow regions.

The local Nusselt number trend was similar to laminar flow when the flow entered the test section. However, due to the higher fluid velocity, the flow did not remain laminar, but passed through a transition and quasi-turbulent region before it became turbulent. Lines A-F and A-I indicate that the gradient of the Nusselt number lines in the laminar region decreased with increasing Reynolds number, because the thermal entrance length increased.

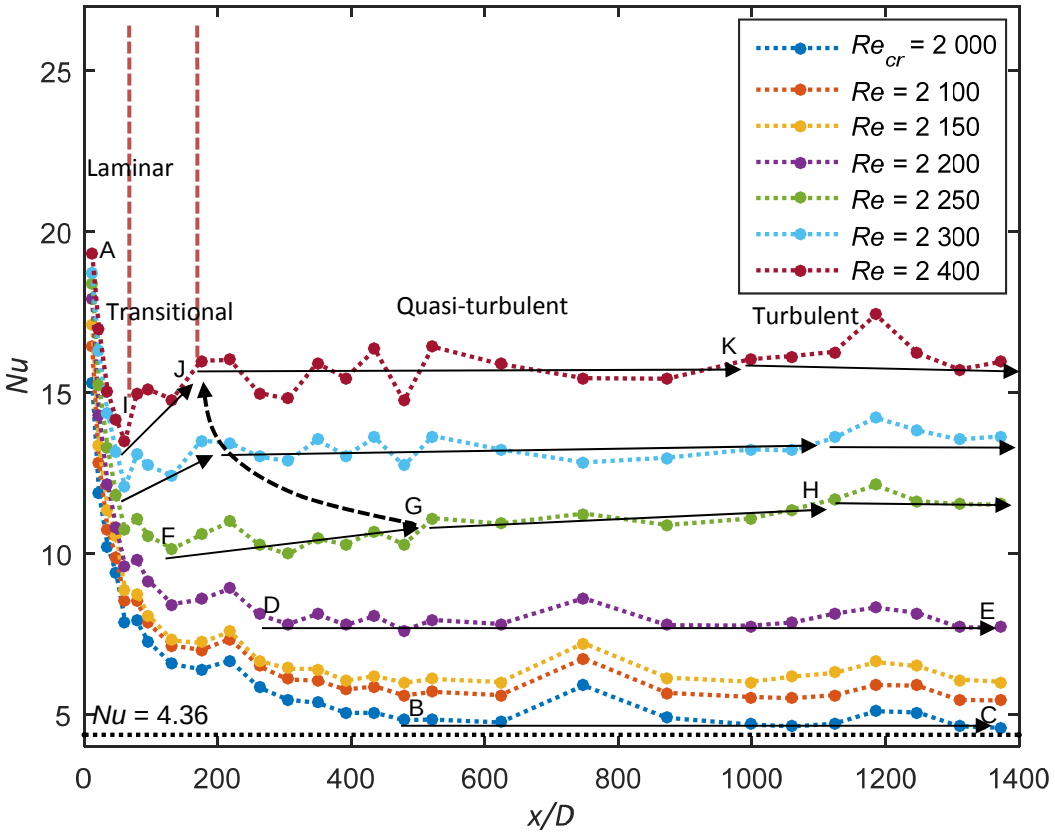

Fig. 5.13: Local Nusselt numbers as a function of axial position for bulk Reynolds numbers between 2 000 and 2 400 at a heat flux of 1 kW/m^2 in the 4 mm test section.

In the transition region, it was found that as the Reynolds number was increased, the depth of the dip increased, the width decreased and the trough (points F and I) occurred earlier. This caused the gradient of the Nusselt number lines in the transition region to increase with increasing Reynolds number (lines F-G and I-J), which implies that the transition from the laminar to the quasi-turbulent regions occurred faster.

Similar to Fig. 5.11, the magnitude of the Nusselt numbers in the quasi-turbulent and turbulent regions increased as the Reynolds number was increased, due to the enhanced mixing inside the test section (points H and K). Furthermore, the gradient of the Nusselt number lines in the quasi-turbulent region decreased with increasing Reynolds number, because the flow approached the turbulent flow regime where the Nusselt numbers remained constant. As schematically illustrated in Fig. 5.1(c), it seems that the location at which the Nusselt numbers became constant (points H and K in Fig. 5.12) decreased with increasing Reynolds number. This confirmed that the transition from laminar to turbulent occurred faster with increasing Reynolds number.

It can thus be concluded that the transitional flow regime in terms of fluid velocity (Reynolds number), between the laminar and turbulent flow regimes, was caused by the local transition region as a function of axial position. This transition region occurred when the inlet velocity was high enough for mass flow rate and temperature fluctuations to occur, which caused the velocity profile of the fluid to change from laminar to turbulent along the tube length.

5.5.3. Mixed convection laminar-turbulent transition

The results in this section are directly aligned to Fig. 5.1(d). Figure 5.14 compares the Nusselt numbers as a function of axial position for transitional bulk Reynolds numbers at heat fluxes of 1 kW/m^2 and 3 kW/m^2 in the 4 mm and 11.5 mm test sections. The results in Fig. 5.14(a) are for forced convection conditions, while the results in Fig. 5.14(b) to (d) are for mixed convection conditions. As will be shown in Fig. 6.6, the start and end of the transitional flow regime are affected by free convection effects, therefore different Reynolds number ranges are used for the different heat fluxes and tube diameters in Fig. 5.14. In each graph, the dark blue data represent the results at the bulk critical Reynolds number, while the other colours represent the results at Reynolds number increments of 100. For comparison purposes, the theoretical Nusselt number of 4.36, for fully developed laminar forced convection flow, is indicated by the black dotted line.

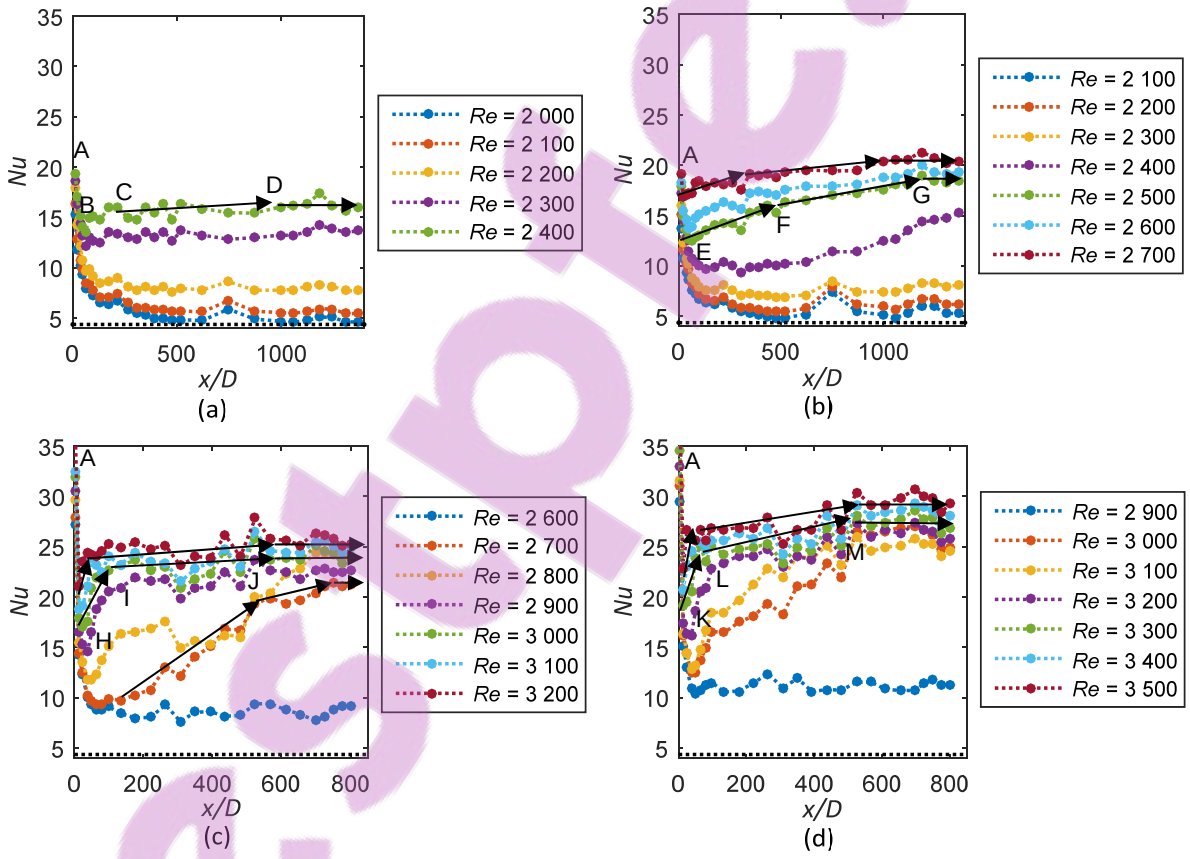

Fig. 5.14: Comparison of Nusselt numbers as a function of axial position for transitional bulk Reynolds numbers at a heat flux of (a) 1 kW/m^2 (forced convection) and (b) 3 kW/m^2 in the 4 mm test section, and at a heat flux of (c) 1 kW/m^2 and (d) 3 kW/m^2 in the 11.5 mm test section. The dark blue data represent the results at the bulk critical Reynolds number, while the other colours represent the results at Reynolds number increments of 100.

For clarification, the results indicated by the green markers (at a bulk Reynolds number of Re_{cr} + 400) in Fig. 5.14(a) to (d) are summarised in Fig. 5.15. Points E, H and K indicate that the axial position at which the Nusselt numbers started to increase, decreased with increasing free convection effects.

Furthermore, arrows E-F, H-I and K-L indicate that the gradient of the Nusselt number lines in the transition region increased with increasing heat flux and tube diameter, thus increasing Grashof number in Fig. 5.1(d). Although free convection effects caused the flow to transition faster from the laminar to the quasi-turbulent regions (points F, I and L), a significant tube length was still required for the flow to transition to fully turbulent flow. Arrows F-G, I-J and L-M indicate that the gradient of the Nusselt number lines in the quasi-turbulent region decreased with increasing free convection effects. In the turbulent region (points G, J and M), the magnitude of the Nusselt numbers increased with increasing heat flux and tube diameter; however, the Nusselt numbers remained constant along the tube length, because the free convection effects were constant.

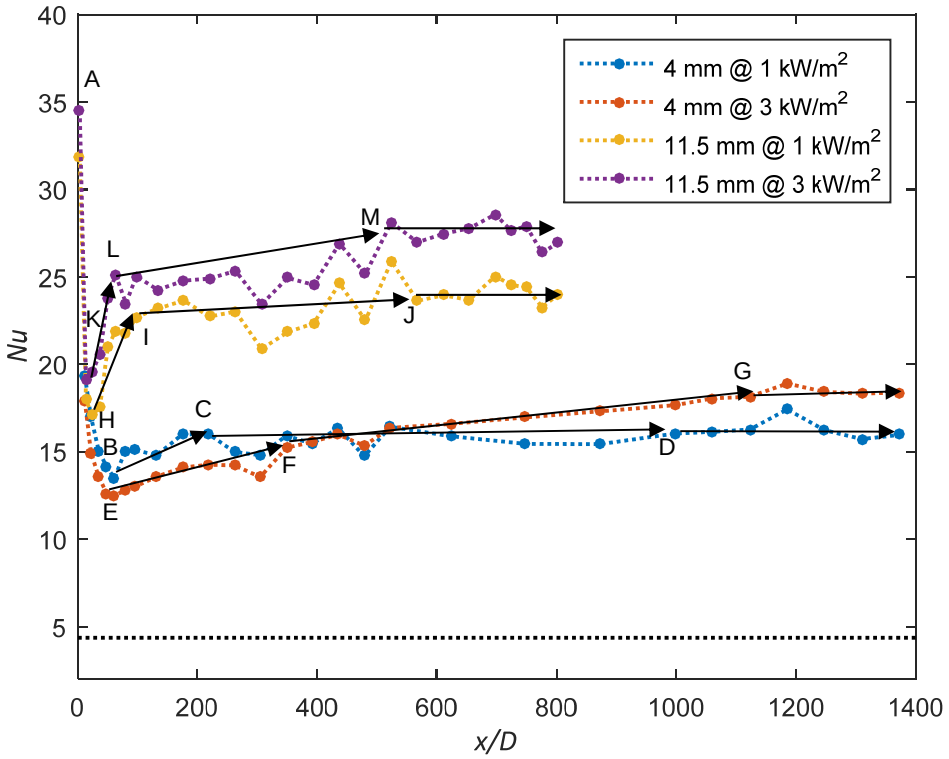

Fig. 5.15: Local Nusselt numbers as a function of axial position at a bulk Reynolds number of Re_{cr} + 400 at heat fluxes of 1 kW/m² and 3 kW/m² in the 4 mm and 11.5 mm test sections.

Although it follows from the results in Fig. 5.15 that free convection effects caused the laminar-turbulent transition to occur faster, free convection effects initially caused the flow to transition slower compared with forced convection conditions (points C and F). The same was true for the transition from the quasi-turbulent to turbulent regions (points D and G). Therefore, once free convection effects became significant, it first disturbed the fluctuations inside the test section and caused transition to occur slower. However, as free convection effects were increased (by increasing the tube diameter and heat flux), the fluctuations inside the test section were enhanced (as shown in Fig. 6.4), which caused the flow to transition faster from laminar to turbulent.

5.6. Conclusions and recommendations

The purpose of this chapter was to experimentally investigate the effects of free convection on the development of the local heat transfer characteristics in smooth horizontal circular tubes, heated with a constant heat flux. It was found that a longer thermal entrance length was required when the flow was simultaneously hydrodynamically and thermally developing (as in this study), than when the flow

was hydrodynamically fully developed and thermally developing. A coefficient of at least 0.12 (and not 0.05 as suggested in most literature) was therefore suggested for simultaneously hydrodynamically and thermally developing forced convection laminar flow. As the heat flux and tube diameter were increased, free convection effects became significant, which not only led to increased Nusselt numbers, but also to a decreased thermal entrance length. Correlations were developed to calculate the thermal entrance length for mixed convection conditions.

Three different regions (FCD, MCD and FD) were identified in the local laminar heat transfer results and nomenclature and correlations were developed to define and quantify the boundaries of these regions. Correlations were also developed to calculate the local and average laminar Nusselt numbers of mixed convection developing flow.

The laminar-turbulent transition along the tube length occurred faster with increasing Reynolds number, due to the increased velocity of the fluid. However, this transition was also influenced by free convection effects. Free convection effects initially disturbed the fluctuations inside the test section, causing a slower laminar-turbulent transition compared with forced convection conditions. However, as the free convection effects were increased further, the fluctuations inside the test section were enhanced. The enhanced mixing caused the laminar-turbulent transition along the tube length to occur faster and the magnitude of the Nusselt numbers to increase.

When the Reynolds number exceeded the critical Reynolds number, four different regions were identified; however, the boundaries and heat transfer characteristics of these regions in the transitional flow regime were not quantified. The reason was that the laminar-turbulent transition along the tube length was significantly affected by fluid velocity as well as free convection effects, and occurred faster with both increasing Reynolds number and Grashof number. It is recommended that this should be further investigated to develop correlations to determine the boundaries of the different regions in the transitional flow regime, as well as to predict the local Nusselt numbers as a function of axial position.

Experimental data from literature were used to ensure that a wider range of Prandtl number data were available to use for the interpretation of the results of this study and the development of correlations. However, it is recommended that experiments with higher Prandtl numbers (such as ethylene glycol-water mixtures) should be conducted using the same or a modified experimental set-up. The results can then be compared with the low Prandtl number results obtained in this study to improve the accuracy and extend the ranges of the local and average laminar Nusselt number correlations that were developed in this chapter. Furthermore, for Prandtl numbers less than one, the thermal boundary layer develops faster than the hydrodynamic boundary. It will thus be valuable to also conduct experiments using air to determine the validity/accuracy of the correlations when the thermal boundary layer develops faster than the hydrodynamic boundary layer.

Because corrosion and scaling are common problems in heat exchangers, which not only increase the pressure drop, but also affect the heat transfer performance, it is recommended that experiments should be conducted using tubes with different values of surface roughness. Thermal entrance length correlations that account for surface roughness can then be developed, because it would be expected that the flow would develop faster with increasing surface roughness. Furthermore, the influence of surface roughness on the laminar-turbulent transition along the tube length can also be investigated.

6. Heat Transfer in the Transitional Flow Regime

6.1. Introduction

In this chapter, the influence of axial position, free convection effects and Prandtl number on the heat transfer characteristics of developing and fully developed transitional flow along the tube length are investigated. Correlations to determine the start and end of the transitional flow regime are also developed. Most of the results contained in this chapter were published in Everts and Meyer [48].

6.2. Influence of axial position

To investigate the influence of axial position on the heat transfer characteristics in the transitional flow regime, the Nusselt numbers and Colburn j-factors at a heat flux of 1 kW/m^2 in the 4 mm test section are compared as a function of Reynolds number for different axial positions in Fig. 6.1. To avoid any influences of free convection effects, a low heat flux was chosen to ensure that the flow was dominated by forced convection conditions. Although experiments in general were conducted up to a Reynolds number of 10 000, the Reynolds number was not increased above 6 000 for the forced convection experiments, because the uncertainty of the heat transfer coefficients became too large due to the small temperature differences inside the test section. However, the transitional flow regime, as well as sufficient parts of the laminar and quasi-turbulent flow regimes, was covered.

Between Reynolds numbers of 900 and approximately 2 000 (depending on the tube location), the flow was laminar ($(dj/dRe)_L < 0$). The theoretical fully developed forced convection Nusselt number of 4.36 is indicated by the black dotted line. Figure 6.1(a) indicates that, at a fixed Reynolds number, the laminar Nusselt numbers were a maximum near the inlet of the test section (x/D = 22) and then decreased to approximately 4.36 as the flow developed along the tube length. For $x/D \geq 479$, the laminar Nusselt numbers were in very good agreement (average deviation of 6.4%) with the theoretical Nusselt number of 4.36, which confirmed that fully developed forced convection conditions were successfully obtained. As free convection effects were negligible and the flow was still developing for $x/D < 479$, entrance effects dominated and $(dNu/dRe)_L > 0$ (Eq. 3.28). However, the gradient of the laminar Nusselt numbers, $(dNu/dRe)_L$, decreased and approached zero as x/D increased and the flow approached fully developed flow (Eq. 3.30).

As indicated by the vertical dotted lines in Fig. 6.1(b), the transitional flow regime started (Re_{cr}) at a Reynolds number of 1 900 at x/D = 22, and at a Reynolds number of 2 047 at x/D = 1 311. However, the isothermal friction factors in Fig. 7.1 indicate that transition started at the same moment in time along the entire test section. As the temperature gradient across the test section was zero during the isothermal experiments, the critical Reynolds numbers of the different tube lengths (developing and fully developed flow) were the same. The increasing critical Reynolds numbers in Fig. 6.1(b) were only due to the temperature gradient along the tube length, and the decreasing viscosity with increasing temperature (this will be investigated in Fig. 6.3).

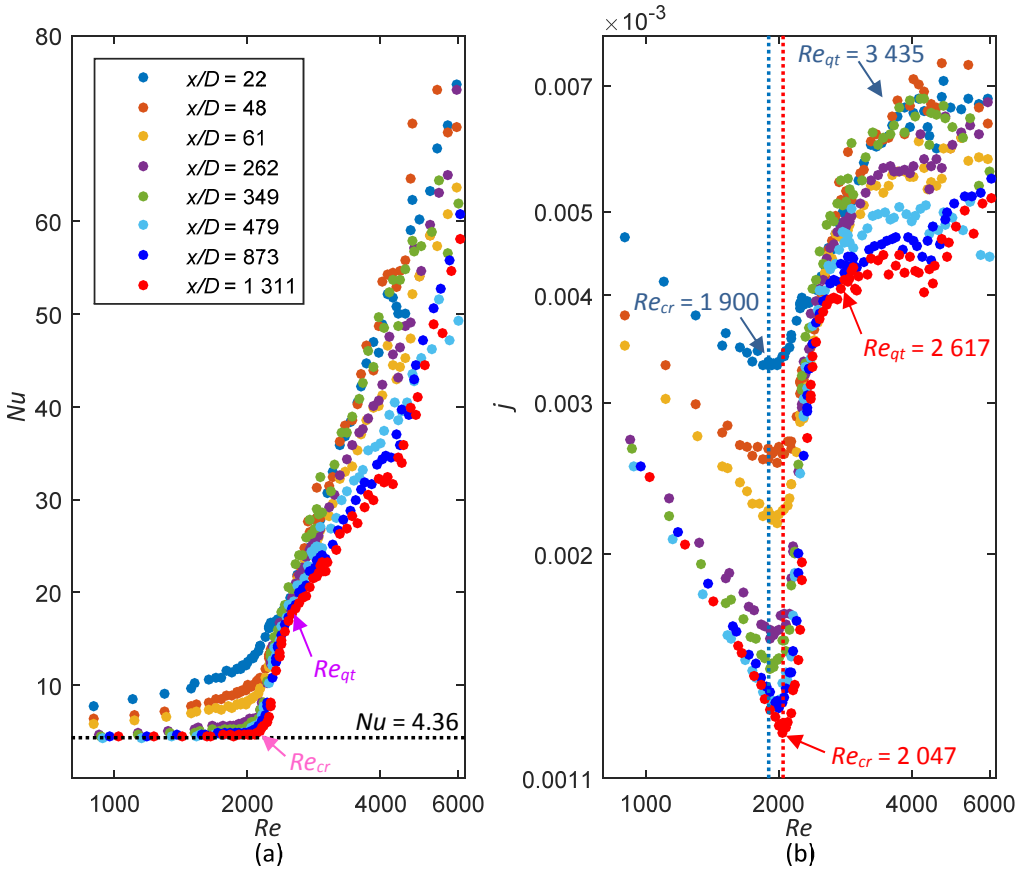

Fig. 6.1: Comparison of (a) Nusselt numbers and (b) Colburn *j*-factors as a function of Reynolds number at a heat flux of 1 kW/m^2 in the 4 mm test section. The start of the transitional flow regime at *x/D* = 22 and *x/D* = 1 311 is indicated by the vertical dotted lines.

The end of the transitional flow regime (Re_{qt}) became more pronounced as the flow developed along the tube length. The Colburn *j*-factors in Fig. 6.1(b) indicate that the Reynolds number at which transition ended (Re_{qt}), decreased from 3 435 at x/D = 22 to 2 617 at x/D = 1 311. This caused the width of the transitional flow regime (ΔRe) to decrease from a Reynolds number range of 1 535 to 570. As ΔRe decreased, the transition gradient (TG_j in Fig. 3.6) increased along the tube length. Figure 5.13 indicates that as the Reynolds number in the transitional flow regime was increased, the transition region inside the test section decreased and a larger portion of the test section contained flow in the quasi-turbulent and turbulent regions. This implies that at two fixed axial positions, for example, x/D = 48 and x/D = 1 311, x/D = 48 experienced transition for a wider range of Reynolds numbers, which explains why ΔRe decreased along the tube length. As there was no significant difference in the transition gradient for x/D > 479 in Fig. 6.1(b), it follows that ΔRe became constant once the flow was fully developed.

As expected, the trend of the heat transfer coefficients in the quasi-turbulent flow regime remained approximately constant along the tube length, because the flow was almost turbulent (and thus fully developed). The scatter in the Nusselt numbers and Colburn *j*-factors in this flow regime was due to the small temperature differences, and thus increased uncertainties. If one thermocouple station measured a slightly higher (or lower) temperature (although it was within the uncertainty of the thermocouple), the Nusselt numbers and Colburn *j*-factors were also higher (or lower) compared with the rest.

6.3. Influence of free convection

To investigate the influence of free convection, the Nusselt numbers and Colburn *j*-factors were compared at heat fluxes of 3 kW/m^2 (Fig. 6.2(a) and (b)) and 8 kW/m^2 (Fig. 6.2(c) and (d)) in the 4 mm test section and at a heat flux of 3 kW/m^2 in the 11.5 mm test section (Fig. 6.2(e) and (f)). Although the bulk Reynolds number in the 4 mm test section was not decreased below 1 800 at a heat flux of 8 kW/m^2 (the outlet temperature exceeded 70 °C), a sufficient part of the laminar flow regime was still covered. Furthermore, the Reynolds number in the 4 mm test section was not increased above 8 000, because the temperature differences became too small and the uncertainties too high to obtain accurate and reliable results. The results are discussed in the following order: laminar flow (Section 6.3.1), quasi-turbulent and turbulent flow (Section 6.3.2) and transitional flow (Section 6.3.3).

6.3.1. Laminar flow

Figure 6.2(a) indicates that, as expected, free convection effects caused the laminar Nusselt numbers to increase above 4.36, and increased further with increasing heat flux (Fig. 6.2(c)) and tube diameter (Fig. 6.2(e)). When comparing the laminar Colburn *j*-factors of the two heat fluxes in the 4 mm test section (Fig. 6.2(b) and (d)), it follows that between $x/D = 22$ and $x/D = 61$, there was no significant difference in the trend and magnitude of the Colburn *j*-factors. The heat transfer coefficients fell into the FCD region for $22 \leq x/D \leq 262$ and $22 \leq x/D \leq 61$, at heat fluxes of 3 kW/m^2 and 8 kW/m^2 respectively. Therefore, it was not affected by heat flux and $dNu/dRe > 0$ because entrance effects dominated (Eq. 3.28).

For $x/D > 262$ and $x/D > 96$ at heat fluxes of 3 kW/m^2 and 8 kW/m^2 respectively, in the 4 mm test section, and for $x/D > 24$ in the 11.5 mm test section, the flow was in the MCD region. As summarised in Fig. 5.1(a), the thermal entrance length decreased with increasing Grashof number, thus increasing tube diameter and heat flux. The thermal boundary layer therefore developed faster and the heat transfer coefficients fell into the MCD region at smaller values of x/D. In this region, free convection effects increased along the tube length, as well as with increasing heat flux and tube diameter, which caused $(dNu/dRe)_L$ and $(dj/dRe)_L$ to decrease. Figure 6.2(e) indicates that the difference between the laminar Colburn *j*-factors of the different thermocouple stations was a maximum at a Reynolds number of 800, but became negligible as the Reynolds number was increased to 2 500. This was due to the decreasing thermal boundary layer thickness with increasing Reynolds number, which led to decreased free convection effects and thus $dNu/dRe < 0$.

6.3.2. Quasi-turbulent and turbulent flow

As will be discussed in Section 6.3.3, transition was delayed with increasing heat flux and tube diameter, while there was no significant difference in the start of the turbulent flow regime. The flow became fully turbulent at a Reynolds number of approximately 6 000, therefore the width of the quasi-turbulent flow regime decreased with increasing free convection effects. As expected, there was no significant difference between the turbulent heat transfer coefficients of the different heat fluxes and tube diameters, because free convection effects were suppressed by the velocity of the fluid. The scatter in heat transfer coefficients in these flow regimes decreased with increasing heat flux and tube diameter, due to the increased temperatures that led to decreased uncertainties.

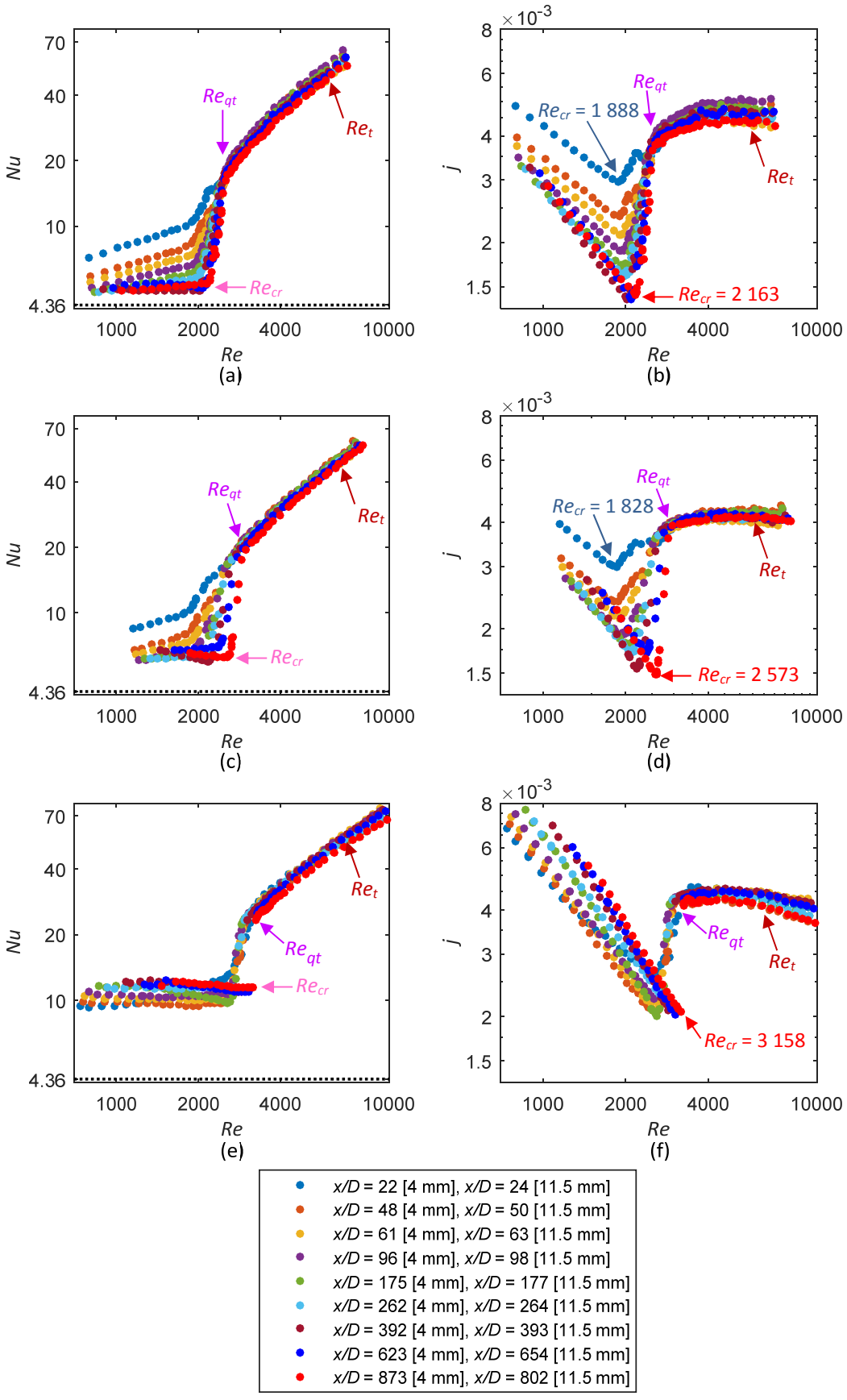

Fig. 6.2: Comparison of (a) Nusselt numbers and (b) Colburn *j*-factors at a heat flux of 3 kW/m² and (c) Nusselt numbers and (d) Colburn *j*-factors at a heat flux of 8 kW/m² in the 4mm test section, and (e) Nusselt numbers and (f) Colburn *j*-factors at a heat flux of 3 kW/m² in the 11.5 mm test section, as a function of Reynolds number.

6.3.3. Transitional flow

Figure 6.2(b) and (d) indicate that free convection effects (due to the increased heat flux) caused transition to occur earlier between x/D = 22 and x/D = 61 (Re_{cr} = 1 888 and Re_{cr} = 1 828 at x/D = 22 for heat fluxes of 3 kW/m^2 and 8 kW/m^2 respectively), while it was delayed as x/D was increased further (Re_{cr} = 2 163 and Re_{cr} = 2 573 at x/D = 873 for heat fluxes of 3 kW/m^2 and 8 kW/m^2 respectively). To investigate this, Fig. 6.3 compares the surface temperatures and local Reynolds numbers as a function of axial position at the bulk critical Reynolds number at heat fluxes of 1 kW/m^2 (forced convection), 3 kW/m^2 and 8 kW/m^2 in the 4 mm test section. Figure 6.3(a) indicates that the temperature gradient along the test section increased significantly with increased heat flux. As the Reynolds number is inversely proportional to viscosity (which decreased with increasing temperature), the critical Reynolds numbers in Fig. 6.3(b) increased along the tube length, although transition started at the same moment in time (same bulk critical Reynolds number) along the entire test section (Fig. 6.5). Figure 6.3(b) indicates that for x/D less than 95.7, the critical Reynolds numbers decreased with increasing heat flux, because transition occurred earlier (at lower mass flow rates); however, as x/D was increased further, the critical Reynolds numbers increased due to the increased temperature gradients along the test section.

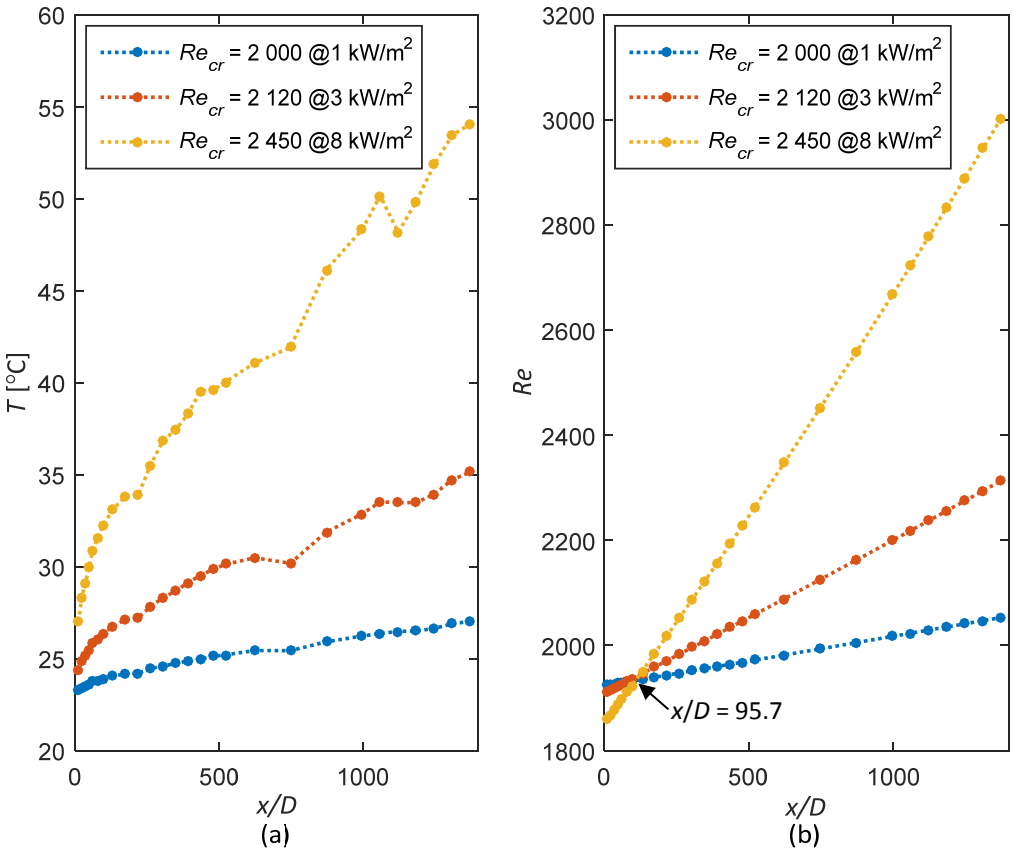

Fig. 6.3: Comparison of (a) surface temperatures and (b) local Reynolds numbers as a function of axial position at the bulk critical Reynolds number at heat fluxes of 1 kW/m^2 (forced convection), 3 kW/m^2 and 8 kW/m^2 in the 4 mm test section.

Figure 6.4 contains the standard deviation of the mass flow rate measurements as a function of mass flow rate at heat fluxes of 1 kW/m^2 (forced convection), 3 kW/m^2 and 8 kW/m^2 in the 4 mm test section. The start of transition corresponded to the point where mass flow rate fluctuations occurred, therefore the standard deviation of the mass flow rate measurements began to increase. Kalinin and

Yarkho [89] explained that, in the transitional flow regime, the flow alternates between laminar and turbulent flow. This leads to oscillations (or fluctuations) due to a stability loss that is the "origination, development, and association of disturbance nuclei inside the laminar stream". Figure 6.4 indicates that at a heat flux of 1 kW/m^2, transition occurred at a mass flow rate of 0.00566 kg/s, while it occurred at 0.00561 kg/s and 0.00544 kg/s when the heat flux was increased to 3 kW/m^2 and 8 kW/m^2 respectively. As is evident from Fig. 6.3(b) for x/D < 95.7, free convection effects caused transition to occur earlier (with reference to mass flow rate). This is as expected since it follows from Fig. 6.4, as well as the findings of Kalinin and Yarkho [89], that the fluctuations increased with increasing heat flux applied which caused the flow to become unstable (thus transition to start) at lower Reynolds numbers.

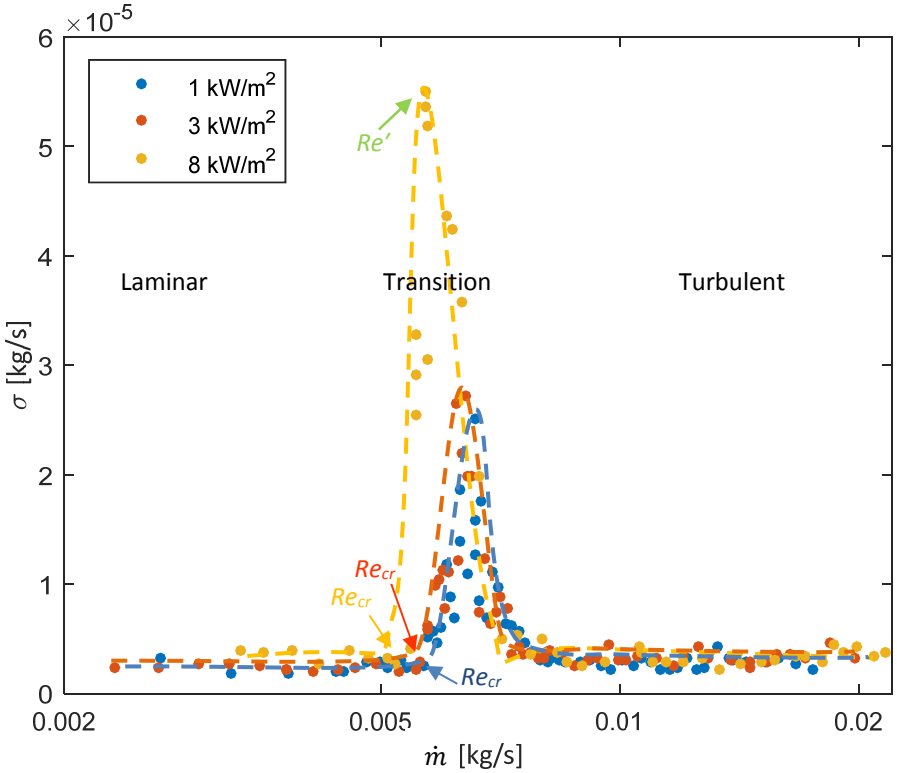

Fig. 6.4: Standard deviation of the mass flow rate measurements as a function of mass flow rate at heat fluxes of 1 kW/m^2 (forced convection), 3 kW/m^2 and 8 kW/m^2 in the 4 mm test section.

Figure 6.5 compares the standard deviations of the temperature measurements at the top of the 4 mm test section as a function of axial position for laminar, transitional, quasi-turbulent and turbulent bulk Reynolds numbers at a heat flux of 8 kW/m^2. As expected, the standard deviations were a minimum in the laminar flow regime ($Re < Re_{cr}$). Once transition started ($Re > Re_{cr}$), the standard deviation increased along the entire test section, indicating that fluctuations occurred. Similar to the isothermal results in Fig. 7.1, transition started at the same moment in time along the entire test section. Furthermore, the standard deviation also increased along the test section from 0.05 °C at x/D = 48 to 0.27 °C at x/D = 1 373. This is due to the development of the thermal boundary layer that led to increased free convection effects, as well as due to the characteristics of the turbulent slugs that lead to the laminar-turbulent transition along the tube length. Slugs are disturbances that increase along the tube length (because the velocity of the slug front is greater than its tail section) up to the size of the test section's cross-section [89]. Similar to the mass flow rate fluctuations in Fig. 6.4, the temperature fluctuations in the transitional flow regime increased with increasing Reynolds

number ($Re > Re_{cr}$ and $Re >> Re_{cr}$). At $Re = Re_{qt}$, fluctuations were significant for $x/D < 600$, but were negligible for $x/D > 600$. Thus, the first part of the test section contained flow in the transitional flow regime, while the last part of the test section contained flow in the quasi-turbulent flow regime. This is in good agreement with the findings of Kalinin and Yarkho [89] that the pulsation coefficient (which is the fraction of a period of time during which the flow is turbulent, therefore $\Upsilon = 0$ for laminar flow and $\Upsilon = 1$ for turbulent flow) increases along the tube length. Although the start of transition was independent of axial position (occurred at the same moment in time), the end of transition was not.

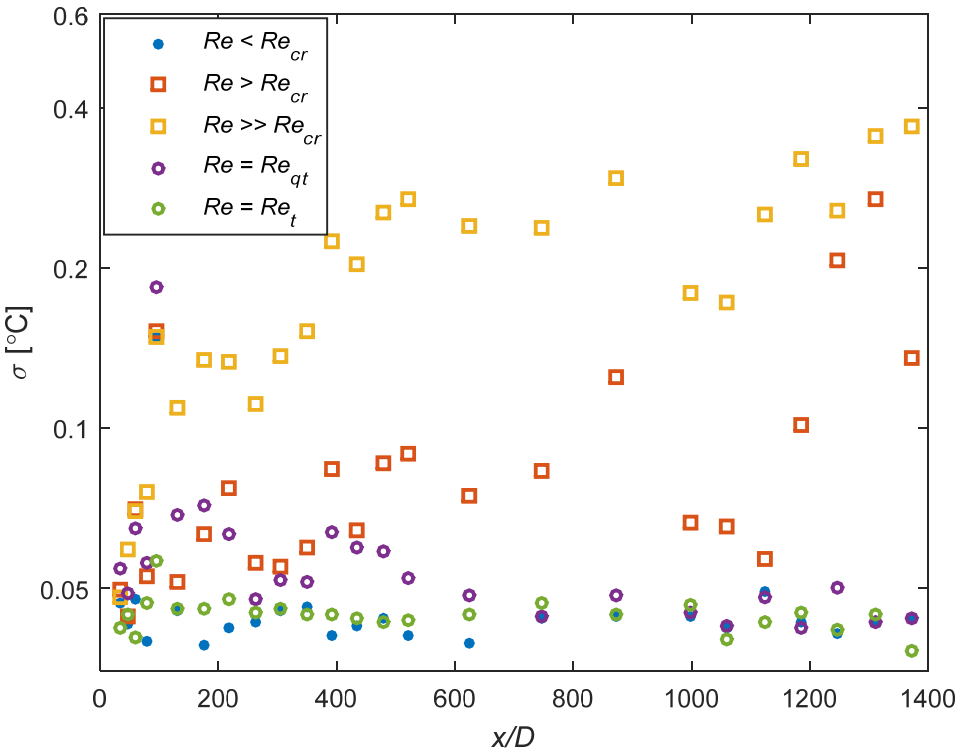

Fig. 6.5: Standard deviation of surface temperatures at the top of the 4 mm test section as a function of axial position at different bulk Reynolds numbers and a heat flux of 8 kW/m^2.

The Reynolds numbers at which the transitional flow regime started (Re_{cr}) and ended (Re_{qt}) for the results in Fig. 6.2, as well as additional heat fluxes, are summarised in Fig. 6.6(a) to (c), while Fig. 6.6(d) compares the width of the transition flow regime (ΔRe). In Fig. 6.6(c), the empty markers represent the start of the transitional flow regime, while the filled markers represent the end of the transitional flow regime. Although transition occurred at the same moment in time along the entire test section (Fig. 6.5) and earlier with increasing free convection effects (Fig. 6.4), Fig. 6.6(a) indicates that the critical Reynolds numbers increased along the tube length and the gradient of the critical Reynolds numbers increased with increasing heat flux and tube diameter.

Furthermore, near the inlet of the test section, the Reynolds number at which transition ended decreased significantly with increasing axial position, but increased as x/D was increased further. Figure 6.6(d) indicates that ΔRe decreased along the tube length when the flow was developing, and became approximately constant once the flow was fully developed. Since transition started at the same moment in time along the entire test section and ΔRe decreased along the test section (Fig. 6.6(d)), it can be concluded that Re_{qt} occurred earlier as the flow developed along the test section, but at the same moment in time once the flow was fully developed. This is as expected because Fig. 5.14

indicates that the transition region inside the test section decreased with increasing Reynolds number (fluid velocity) and/or Grashof number (free convection effects). Therefore, at a fixed Reynolds number, part of the test section could be in the transition region, while the remaining part of the test section could already be in the quasi-turbulent or even turbulent region.

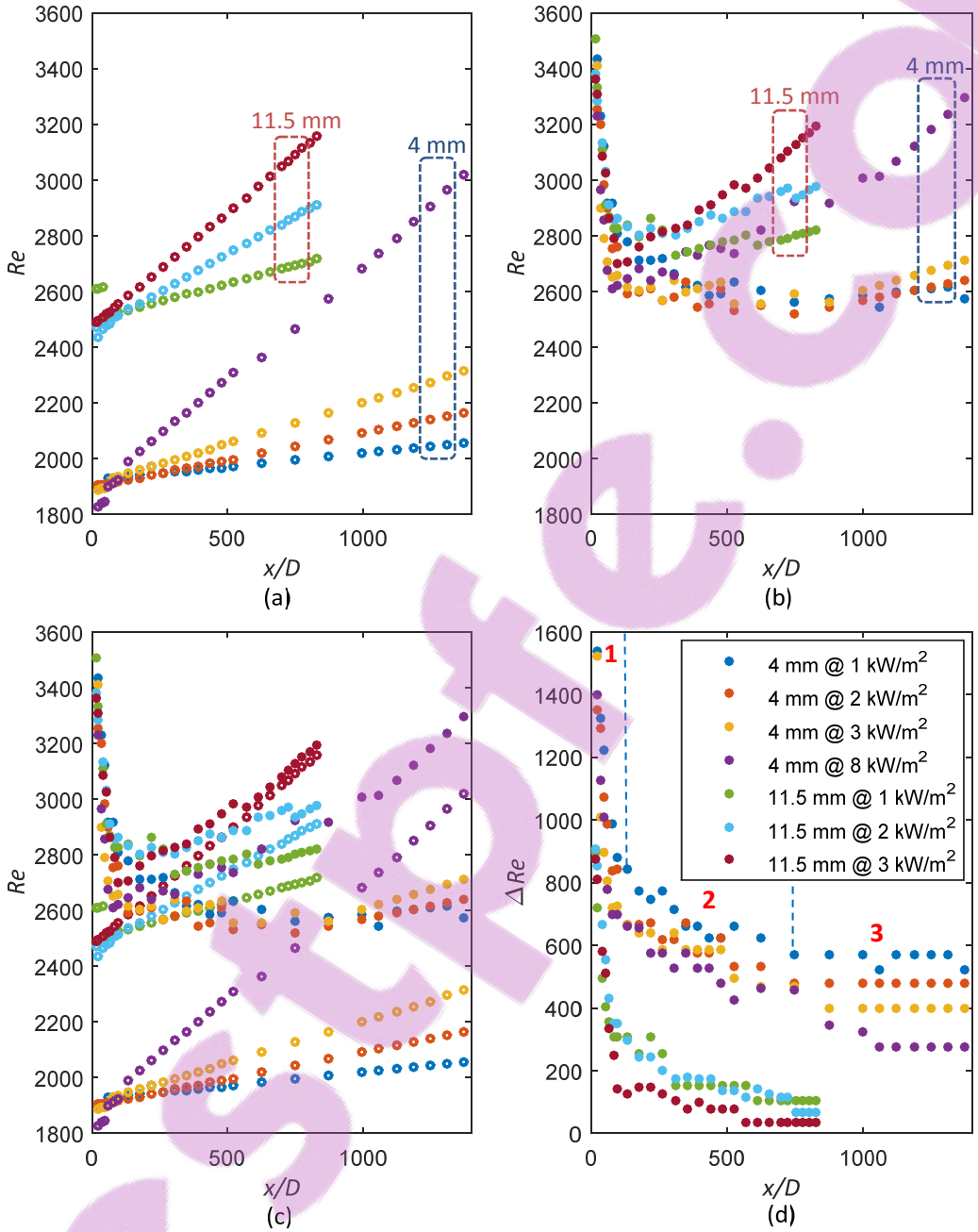

Fig. 6.6: Comparison of (a) Reynolds numbers at which transition started, (b) Reynolds numbers at which transition ended, (c) Reynolds numbers at which transition started and ended and (d) width of the transitional flow regime, as a function of axial position for different heat fluxes in the 4 mm and 11.5 mm test sections. In Fig. 6.6(c), the empty markers represent the start of transition, while the filled markers represent the end of transition.

Figures 6.2 and 6.6(a) indicate that transition occurred significantly earlier in the 4 mm test section ($Re_{cr} \approx 1\,900$) than in the 11.5 mm test section ($Re_{cr} \approx 2\,500$). There are two possible reasons for this: (1) Reynolds number was proportional to tube diameter and therefore increased with increasing tube diameter. (2) A greater contraction ratio (ratio of the flow-calming section diameter to the test section

diameter) to the 4 mm test section caused a different disturbance of the boundary layer at the inlet of the test section, which caused transition to occur earlier. The contraction ratio in the 4 mm test section was 60.5, while it was 14.9 in the 11.5 mm test section, and approximately 10 in the work of Ghajar and co-workers [8, 14, 16, 24-27, 106].

Figure 6.6(d) indicates that when the flow was fully developed in the 4 mm test section, Δ*Re* was 580 at a heat flux of 1 kW/m^2, but decreased to 270 when the heat flux was increased to 8 kW/m^2. As free convection effects were increased further by increasing the tube diameter, Δ*Re* decreased from approximately 100 at a heat flux of 1 kW/m^2, to 35 at a heat flux of 3 kW/m^2. At this heat flux, severe fluctuations occurred inside the test section and the flow regime continuously alternated between the laminar and quasi-turbulent flow regimes. After time (up to one hour), the flow stabilised at the critical Reynolds number and then in the quasi-turbulent flow regime at the next increasing experimental Reynolds number increment. Therefore, the transitional flow regime became negligible and Δ*Re* of 35 was the smallest possible pump increment. This confirms that free convection effects caused the transition region (in terms of axial position) to decrease and become negligible at the end of the test section (where the flow was fully developed). This, in turn, caused the transitional flow regime (in terms of Reynolds number) to become negligible when the flow was fully developed, as was found in Fig. 6.2(e) and (f).

Figure 6.6(d) also indicates that when free convection effects were negligible (1 kW/m^2 in the 4 mm test section), Δ*Re* gradually decreased and became constant at a Reynolds number range of 570 at x/D = 748. As the heat flux (and thus free convection effects) was increased, the axial position at which Δ*Re* became constant increased, while the opposite trend was observed in the 11.5 mm test section. For the 4 mm test section, the average Grashof number in the transitional flow regime was approximately 100 at a heat flux of 1 kW/m^2, and increased to 500 and 2 000 as the heat flux was increased to 3 kW/m^2 and 8 kW/m^2 respectively. In the 11.5 mm test section, the average transitional Grashof number at heat fluxes of 1 kW/m^2 and 3 kW/m^2 was approximately 7 000 and 15 000, which was an order of magnitude more than in the 4 mm test section. Figure 5.15 indicates that once free convection effects became significant, the fluctuations inside the test section were disturbed and transition occurred slower compared with forced convection conditions. However, as the Grashof number was increased further, the fluctuations were enhanced and caused transition to occur faster.

Figure 6.6(d) indicates that the transitional flow regime of developing and fully developed flow can be divided into three regions in terms of axial position. As these regions were affected by free convection effects, it was only indicated for the forced convection case (1 kW/m^2 in the 4 mm test section). In Region 1, Δ*Re* decreased significantly along the tube length as the thermal boundary layer thickness increased. Due to the small thermal boundary layer thickness, free convection effects had a negligible influence on Δ*Re*. In Region 2, the thermal boundary layer thickness was sufficient for free convection effects to become significant. Therefore, Δ*Re* decreased with axial position (due to the increasing thermal boundary layer thickness and increasing mass flow rate and temperature fluctuations) as well as with increasing heat flux and tube diameter, because free convection effects caused the flow to transition faster from laminar to turbulent. Once the flow was fully developed (Region 3), Δ*Re* was independent of axial position. However, it decreased significantly with increasing heat flux and tube diameter, and even became negligible when the Grashof number was very high (3 kW/m^2 in the 11.5 mm test section).

Similar to Fig. 6.1(b), the transition gradients in Fig. 6.2(b), (d) and (f) increased along the test section as the flow approached fully developed flow, as well as with increased free convection effects due to increased heat fluxes and tube diameter. Figure 6.7 compares the transition gradient, TG_j, as a function of axial position for different heat fluxes in the 4 mm and 11.5 mm test sections. An overall trend in this graph is that the transition gradient increased as the flow developed along the tube length as well as with increasing free convection effects. This is as expected because Fig. 5.14 indicates that the laminar-turbulent transition along the tube length occurred faster, causing ΔRe to decrease.

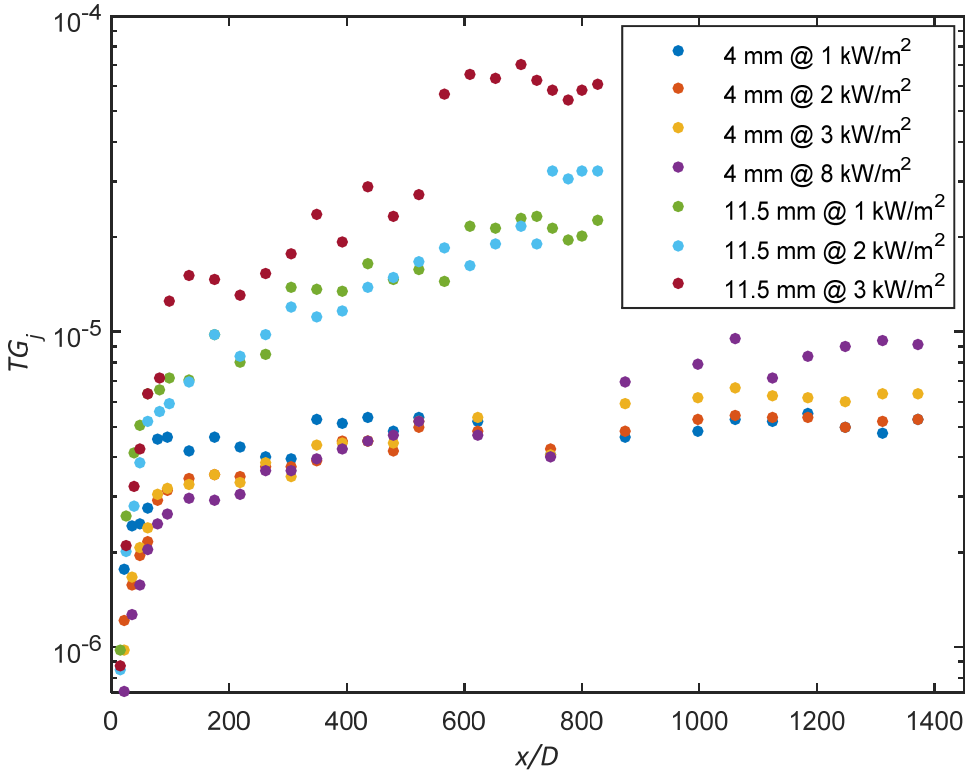

Fig. 6.7: Comparison of the transition gradients as a function of axial position for different heat fluxes in the 4 mm and 11.5 mm test sections.

However, from close inspection, it follows that when x/D was less than 479, the transition gradient in the 4 mm test section decreased with increasing heat flux. Figure 6.2 indicates that, near the inlet of the test section ($x/D < 96$), the critical Reynolds number decreased with increasing heat flux, but the magnitude of the Colburn j-factor at the critical Reynolds number increased. This caused the transition gradient to increase slightly (it should be noted that a log scale was used for the y-axis in Fig. 6.7 to better illustrate the detail in the 4 mm test section). Between $x/D = 96$ and $x/D = 479$ in the 4 mm test section, both the critical Reynolds number and the magnitude of the Colburn j-factors at the critical Reynolds number increased with increasing heat flux, which led to a decreased transition gradient. When x/D was greater than 479, the increase in critical Reynolds number with increasing heat flux (due to the increased temperature gradient) was sufficient for the transition gradient to increase, although the magnitude of the Colburn j-factor at the critical Reynolds number increased.

Once the flow was fully developed, the transition gradient became approximately constant along the tube length (since ΔRe remained constant), but increased with increasing free convection effects (since ΔRe decreased). As the transitional flow regime became negligible in the 11.5 mm test section

when the flow was fully developed (Fig. 6.2(e) and (f)), the transition gradient was expected to tend to infinity ($TG_j \rightarrow \infty$). However, this was not the case as the changes in the *y*-scale (Colburn *j*-factor) were much smaller than the changes in the *x*-scale (Reynolds number). Although the transition gradient was very small, 7.03×10^{-5}, it was still 14.8 times more than the forced convection case in the 4 mm test section. It was not experimentally possible to obtain a Reynolds number increment of less than 35, and the transition gradient will only tend to infinity if the Reynolds number increment tends to zero.

6.3.4. Summary

To summarise the effect of free convection on the heat transfer coefficients in the different flow regimes, the Colburn *j*-factors as a function of Reynolds number are compared in Fig. 6.8 for different heat fluxes at $x/D = 873$ in the 4 mm test section and at $x/D = 802$ in the 11.5 mm test section. Furthermore, the effect of free convection on the heat transfer coefficients in the different flow regimes is schematically illustrated in Fig. 6.9. Points A to N in Fig. 6.8 correspond to the labels used in Fig. 6.9. The results at a heat flux of 1 kW/m^2 in the 4 mm test section (line A-B-C) in Fig. 6.8 and the solid black line A-B-C-D-E in Fig. 6.9 represent forced convection conditions, therefore the Grashof numbers were the lowest. The Grashof numbers increased as the heat flux was increased to 3 kW/m^2 in the 4 mm test section (line F-G-H-D) and increased further when the tube diameter was increased to 11.5 mm. Therefore, the maximum Grashof numbers were obtained at a heat flux of 3 kW/m^2 in the 11.5 mm test section (line L-M-N-D-E).

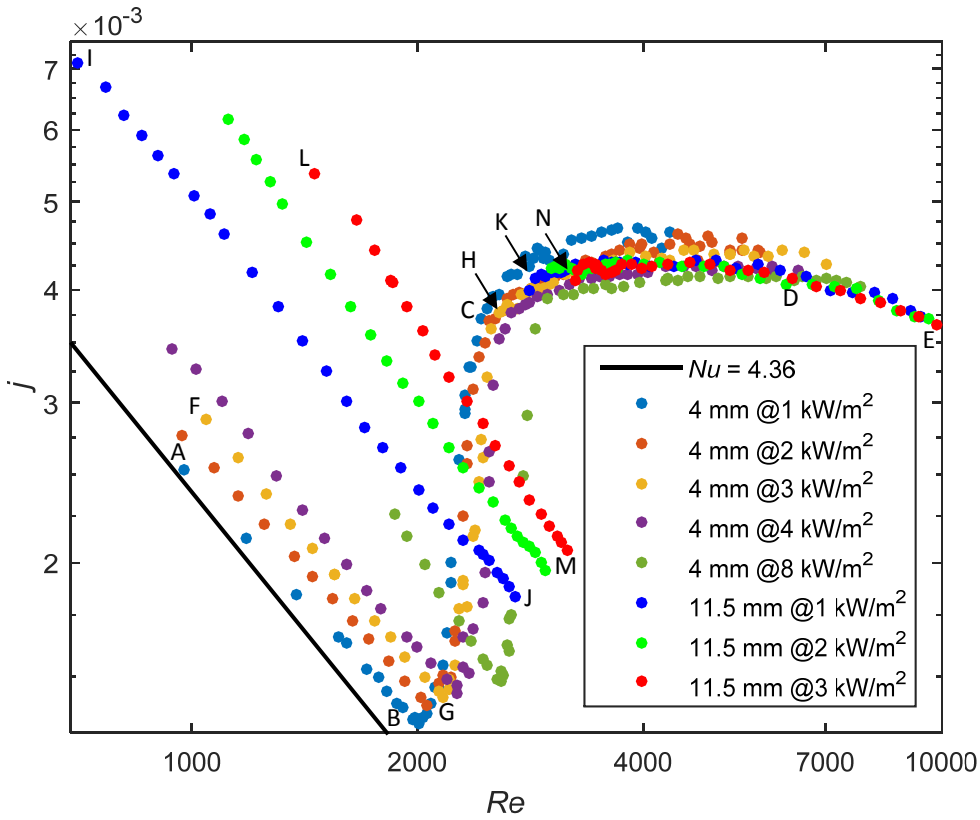

Fig. 6.8: Comparison of Colburn *j*-factors as a function of Reynolds number for different heat fluxes in the 4 mm and 11.5 mm test sections.

Figure 6.8 indicates that as free convection effects (and thus Grashof number) were increased, due to increasing heat flux (lines A-B and F-G) and tube diameter (lines I-J and L-M), the magnitude of the

laminar Colburn *j*-factors increased and $(dj/dRe)_L$ decreased. Points B and G indicate that the start of transition, Re_{cr}, was delayed from a Reynolds number of 2 005 to 2 163 when the heat flux was increased from 1 kW/m^2 to 3 kW/m^2 in the 4 mm test section, due to the decreasing viscosity with increasing temperature. Points G and M indicate that, at a fixed heat flux of 3 kW/m^2, transition was also significantly delayed from a Reynolds number of 2 163 to 3 176, as the tube diameter was increased from 4 mm to 11.5 mm. The critical Reynolds number therefore increased with increasing Grashof number (free convection effects), as indicated by points B, G, J, M and P in Fig. 6.9.

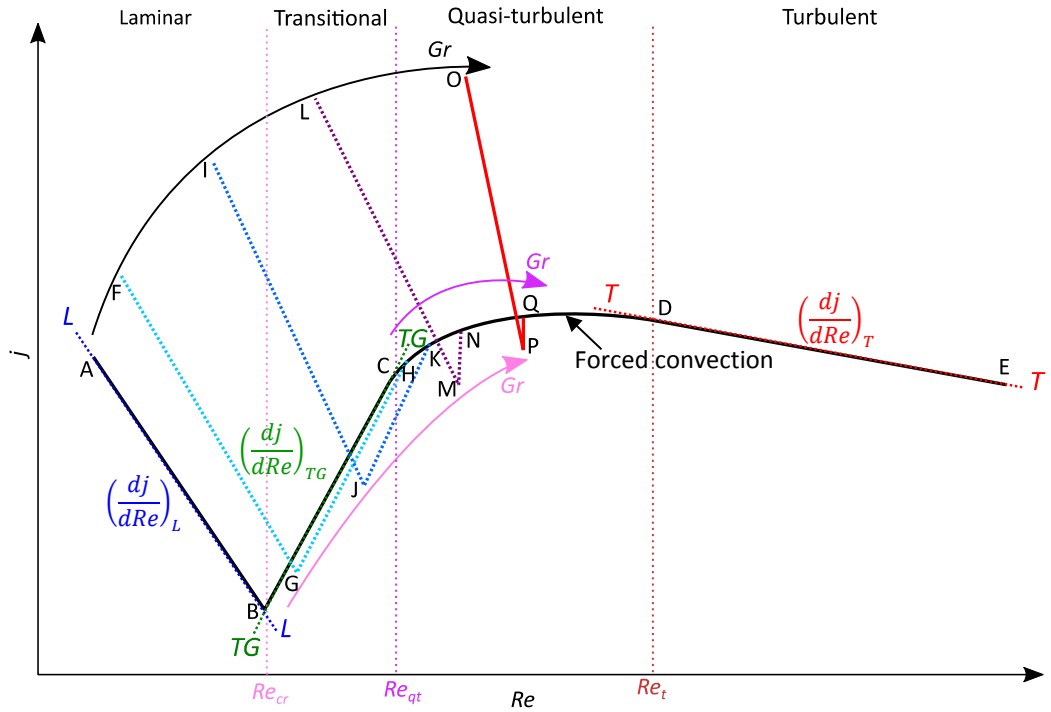

Fig. 6.9: Schematic representation of the influence of Grashof number on the different flow regimes when the heat transfer coefficients are investigated in terms of the Colburn *j*-factor as a function of Reynolds number.

Free convection effects caused the flow inside the test section to transition faster from laminar to turbulent (Fig. 5.1(d)). Therefore, as the heat flux and tube diameter (Grashof number) were increased, the transition gradient ($(dj/dRe)_{TG}$) increased from 6.9×10^{-6} at a heat flux of 1 kW/m^2 in the 4 mm test section (line B-C) to 6.1×10^{-5} at a heat flux of 3 kW/m^2 in the 11.5 mm test section (line M-N), and the width of the transitional flow regime (ΔRe) decreased from a Reynolds number range of 873 to 35. When the Grashof number was high enough, as in the 11.5 mm test section, the transitional flow regime became negligible when the flow was fully developed. The flow alternated between the laminar and quasi-turbulent flow regimes, stabilising as laminar at the critical Reynolds number (point M) and in the quasi-turbulent flow regime at the next Reynolds number increment (point N), therefore skipping the entire transitional flow regime.

Points C, H, K and N in Fig. 6.8 indicate that the end of the transitional flow regime, Re_{qt}, was delayed with increased heat flux and tube diameter (thus Grashof number in Fig. 6.9). As expected, the turbulent flow regime was unaffected by heat flux or tube diameter, because the free convection effects were suppressed by the inertia of the fluid. The flow became fully turbulent, Re_t, at approximately the same Reynolds number of 6 000 (point D). As the start of the quasi-turbulent flow regime, Re_{qt}, was delayed, while the start of the turbulent flow regime was unaffected, the width of

the quasi-turbulent flow regime decreased with increasing free convection effects. It can therefore be postulated that if the Grashof number is significantly increased and tends to infinity (line O-P-Q-D-E in Fig. 6.9), the width of both the transitional and quasi-turbulent flow regimes might become negligible for fully developed flow. Therefore, the flow regime might change from laminar to turbulent without any noteworthy transitional and quasi-turbulent flow regimes.

6.4. Influence of Prandtl number

Ghajar and co-workers did the pioneering work on transitional flow, investigating the effects of heat flux and inlet geometries. Strickland, a master's student of Professor Ghajar, did the heat transfer experiments using a square-edged inlet [106]. Three different test fluids were used and the ranges of the experiments conducted with each test fluid are summarised in Table 6.1.

Table 6.1: Summary of experimental data of Strickland [106].

	Distilled water	60% ethylene glycol	100% ethylene glycol
Re	3 639 – 50 529	1 180 – 12 456	280 – 3 328
Pr	3.44 – 6.24	16.8 – 55.29	95.89 – 157.8
Nu	31.3 – 232	12.9 – 146.3	15 – 80.2
Gr	$6.3\times10^4 - 2.3\times10^6$	$2.6\times10^3 - 2\times10^5$	$1\times10^3 - 1.6\times10^4$
$\dot{q}$ [kW/m^2]	13.5 – 62.8	4.8 – 57.9	6.1 – 28.8

Table 6.1 indicates that pure ethylene glycol and distilled water were used for the laminar and turbulent flow regimes respectively, while a mixture of 60% ethylene glycol (by mass fraction) and water was used for the transitional flow regime, as well as part of the laminar and quasi-turbulent flow regimes. As their focus was on fully developed flow, and to avoid any entrance effects, the data at $x/D = 192$ (station 22) were mainly used to investigate the heat transfer characteristics in the transitional flow regime (although the test section contained 31 thermocouple stations).

To investigate the effect of Prandtl number and tube diameter, Fig. 6.10 compares the results of Strickland [106] with the results of this study at $x/D \approx 176$ and $x/D \approx 219$ in the 4 mm and 11.5 mm test sections. These thermocouple stations were chosen because they were the closest to $x/D = 192$, which was used by Strickland [106]. The results of Strickland were obtained at different heat fluxes and are indicated by the square markers, while the results in the 4 mm and 11.5 mm test sections were obtained at a heat flux of 3 kW/m^2 and are indicated by the empty and filled circles respectively.

Although the laminar data of Strickland [106] were obtained at different heat fluxes (4.9 kW/m^2 to 28.8 kW/m^2), Fig. 6.10 indicates that, unlike the results of Fig. 6.8, the laminar heat transfer coefficients were not significantly affected. This is due to the difference in the fluid properties of water and ethylene glycol. When the fluid properties of water ($Pr \approx 7$) and ethylene glycol ($Pr \approx 100$) were investigated between temperatures of 20 °C and 80 °C, it was found that the specific heat and thermal conductivity of ethylene glycol were up to 50% and 60% respectively less than water, which led to greater temperature differences. However, the density was 12% higher and the viscosity an order of magnitude higher than that of water. As the viscosity of ethylene glycol is a strong function of temperature, free convection effects were significant, but were restricted to the thermal boundary layer (higher temperature and lower viscosity), due to the significantly higher viscosity in the centre of the tube. Therefore, free convection effects could not lead to significant secondary flow, which assisted in the diffusion of the heat from the surface to the centre of the tube, and significantly increased the heat transfer coefficients. Figure 6.10 also indicates that there was no significant

discontinuity between the 100% ethylene glycol and 60% ethylene glycol results in the laminar flow regime, because both test fluids had high viscosities which restricted free convection effects to the thermal boundary layer.

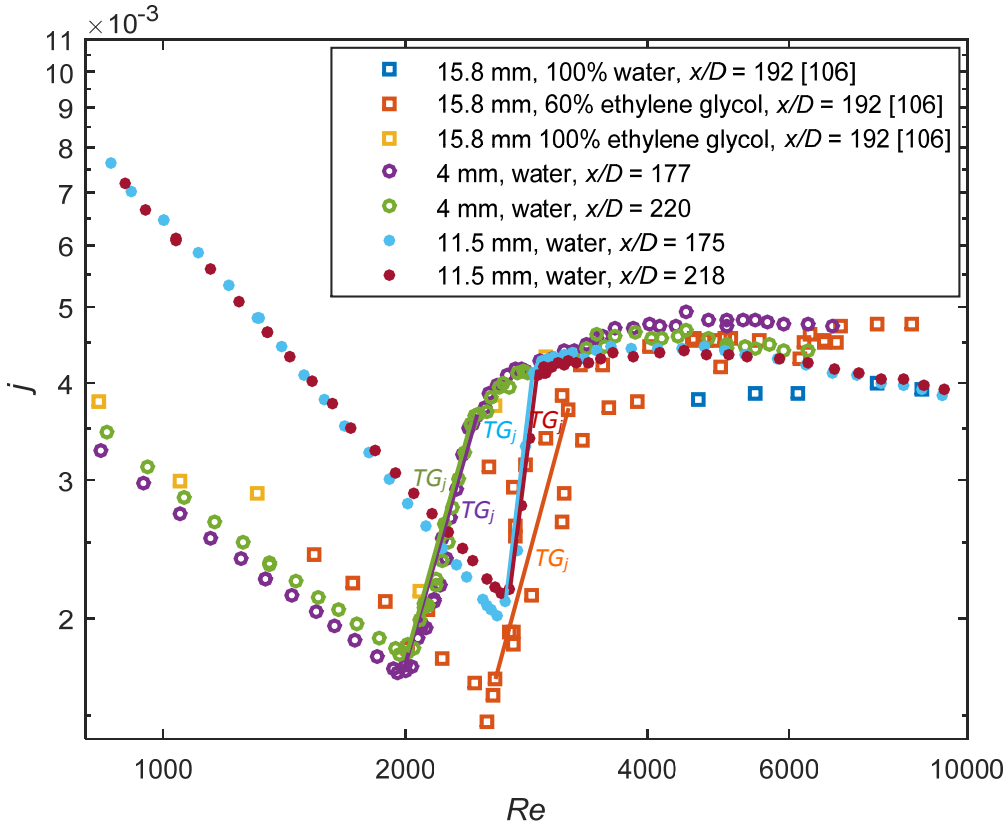

Fig. 6.10: Comparison of Colburn *j*-factors as a function of Reynolds number of the experimental data of Strickland [106] at *x*/*D* = 192 with the experimental data of this study at *x*/*D* = 177 and *x*/*D* = 220 in the 4 mm test section and at *x*/*D* = 175 and *x*/*D* = 218 in the 11.5 mm test section. The solid lines illustrate the transition gradient of each experimental data set.

Figure 6.10 indicates that free convection effects led to a decreased laminar Colburn *j*-factor gradient when the tube diameter was increased from 4 mm to 11.5 mm. Although the tube diameter used by Strickland [106] was 1.37 times and 3.97 times larger than the 11.5 mm and 4 mm test sections respectively, free convection effects were suppressed by the significantly higher viscosity of ethylene glycol. In the 4 mm test section, the laminar Colburn *j*-factors increased between *x*/*D* = 176 and *x*/*D* = 219, because free convection effects increased with increasing thermal boundary layer thickness. However, the difference between the two stations in the 11.5 mm test section was negligible at Reynolds numbers less than 2 000, because the increased free convection effects caused the thermal boundary layer thickness to develop significantly faster.

Transition occurred first in the 4 mm test section at Reynolds numbers of 1 959 and 1 971, then in Strickland's test section at a Reynolds number of 2 524, and last in the 11.5 mm test section at Reynolds numbers of 2 602 and 2 637. Figure 6.6(a) indicates that the critical Reynolds number increased with increasing heat flux and tube diameter. However, the increased viscosity of ethylene glycol caused the critical Reynolds number in Strickland's test section to decrease compared with the 11.5 mm test section.

The solid lines in Fig. 6.10 indicate the transition gradients of each test section. Due to the different heat fluxes and test fluids which were used by Strickland [106], scatter existed in the transitional flow regime, which made it challenging to determine the transition gradient. However, it was estimated to be 3.38×10^{-6}, while the transition gradients of the 4 mm and 11.5 mm test sections were approximately 4.25×10^{-6} and 9.13×10^{-6} respectively. Increased free convection effects led to an increased transition gradient when the tube diameter was increased from 4 mm to 11.5 mm; however, there was a negligible difference between the transition gradients of the two thermocouple stations in each test section. The increased viscosity of 60% ethylene glycol led to decreased free convection effects, therefore the flow transitioned slower from laminar to turbulent, causing the transition gradient to decrease and the width of the transitional flow regime to increase.

The results of the 4 mm and 11.5 mm test sections in the quasi-turbulent and turbulent flow regimes compared fairly well with the results of Strickland [106]. As free convection effects were suppressed by the inertia of the fluid, the heat transfer coefficients were independent of fluid properties, heat flux and tube diameter. Some scatter and discontinuities were expected in the turbulent flow regime, because the temperature differences decreased, which led to increased uncertainties.

6.5. Correlations: start and end of the transitional flow regime

Ghajar and Tam [14] developed the following correlations to predict the start and end of the transitional flow regime for a square-edged inlet:

$$Re_{cr} = 2524 - 0.82\left(192 - \frac{x}{D}\right) \quad 6.1$$

$$Re_{qt} = 8791 - 7.69\left(192 - \frac{x}{D}\right) \quad 6.2$$

As these equations were developed for x/D values between 3 and 192, the start and end of transition were predicted to be at Reynolds numbers of 2 369 - 2 524 and 7 337 - 8 791 respectively, for $3 \leq x/D \leq 192$. The result is that ΔRe varied between a Reynolds number range of 4 968 and 6 267. When comparing these predictions to the results in Fig. 6.6, it was found that Eq. 6.1 predicted Re_{cr} in the 11.5 mm test section within 4.5%, but overpredicted Re_{cr} in the 4 mm test section with 26%. As Eq. 6.2 significantly overpredicted Re_{qt} in both test sections, ΔRe was also significantly overpredicted.

Figure 6.6(c) indicates that both the Reynolds numbers at which transition started and ended were influenced by axial position and free convection effects. As Eqs. 6.1 and 6.2 are a function of axial position only and do not account for any free convection effects, correlations were developed for a square-edged inlet that accounted for both axial position (x/D) and free convection effects (Gr and Gr^*). The critical Reynolds number was divided by $Gr^{0.077}$ to account for mixed convection conditions, and plotted against axial position in Fig. 6.11(a). A linear trend line was fitted through the data points to obtain the following correlation:

$$Re_{cr} = \left(0.1972\frac{x}{D} + 1156.7\right) Gr^{0.077} \quad 6.3$$

From Eq. 6.3, it follows that the critical Reynolds number increased linearly along the test section (as was found in Fig. 6.6(a) due to the decreasing viscosity with temperature) and the gradient of the line was influenced by the Grashof number, thus free convection effects. To develop a correlation that is

a function of heat flux and not temperature difference, the following correlation in terms of the modified Grashof number was obtained from Fig. 6.11(c):

$$Re_{cr} = \left(0.209\frac{x}{D} + 1044.4\right) Gr^{*0.07} \quad 6.4$$

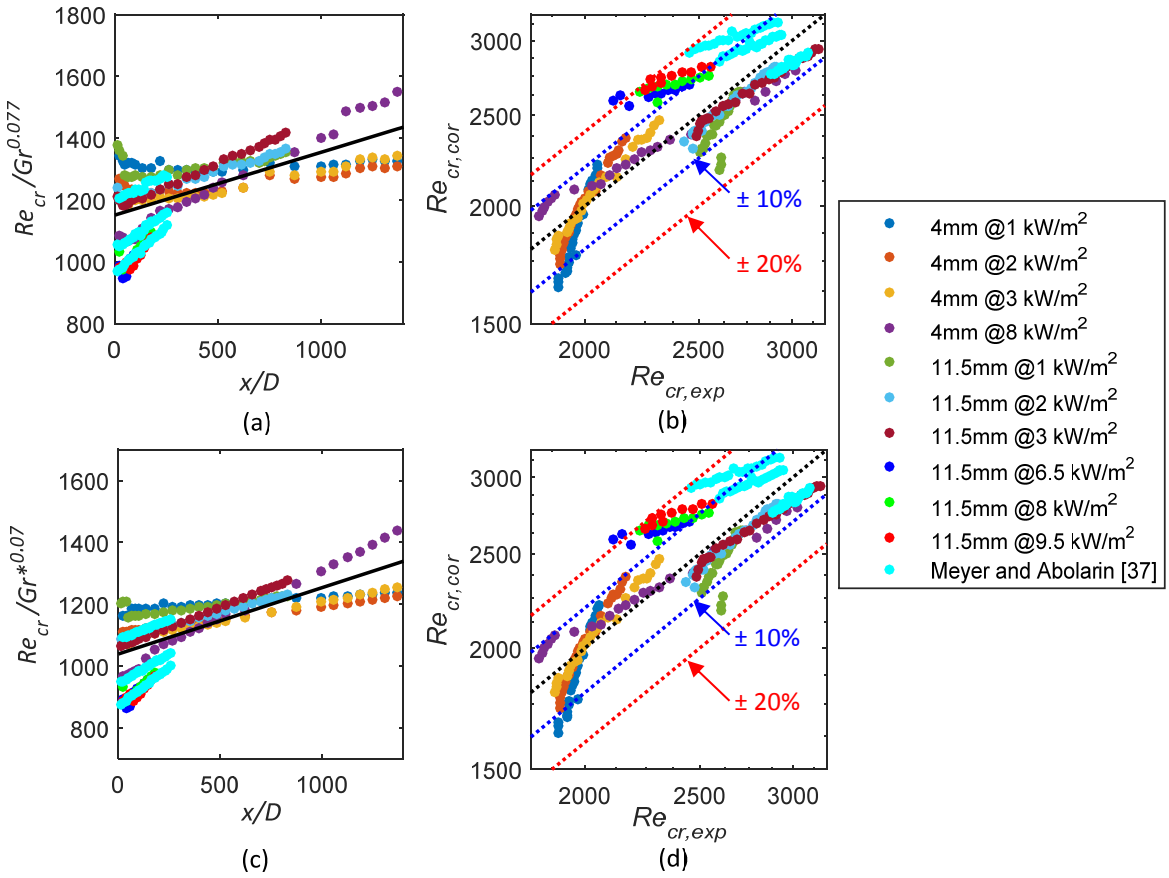

Fig. 6.11: Comparison of (a) $Re_{cr}/Gr^{0.077}$ as a function of axial position, (b) deviation between Eq. 6.3 and experimental data and literature, (c) $Re_{cr}/Gr^{*\,0.07}$ as a function of axial position and (d) deviation between Eq. 6.4 and experimental data and literature.

The Reynolds number at which transition ended (Re_{qt}) was divided by the Grashof number to account for mixed convection conditions, and the results (Re_{qt}/Gr) were plotted against the Grashof number in Fig. 6.12(a). It was found that it was not necessary to include the axial position (x/D), because the Grashof number is a function of tube location (temperature difference and thermal properties vary along the tube length). A power curve fit was done through the data points to obtain the following correlation:

$$\frac{Re_{qt}}{Gr} = 2504\ Gr^{-0.982} \quad 6.5$$

$$Re_{qt} = 2504\ Gr^{0.018} \quad 6.6$$

Similarly, a correlation was developed in terms of the modified Grashof number (Fig. 6.12(c)):

$$\frac{Re_{qt}}{Gr^*} = 2313.2\ Gr^{*-0.98} \quad 6.7$$

$$Re_{qt} = 2313.2\ Gr^{*\,0.02} \quad 6.8$$

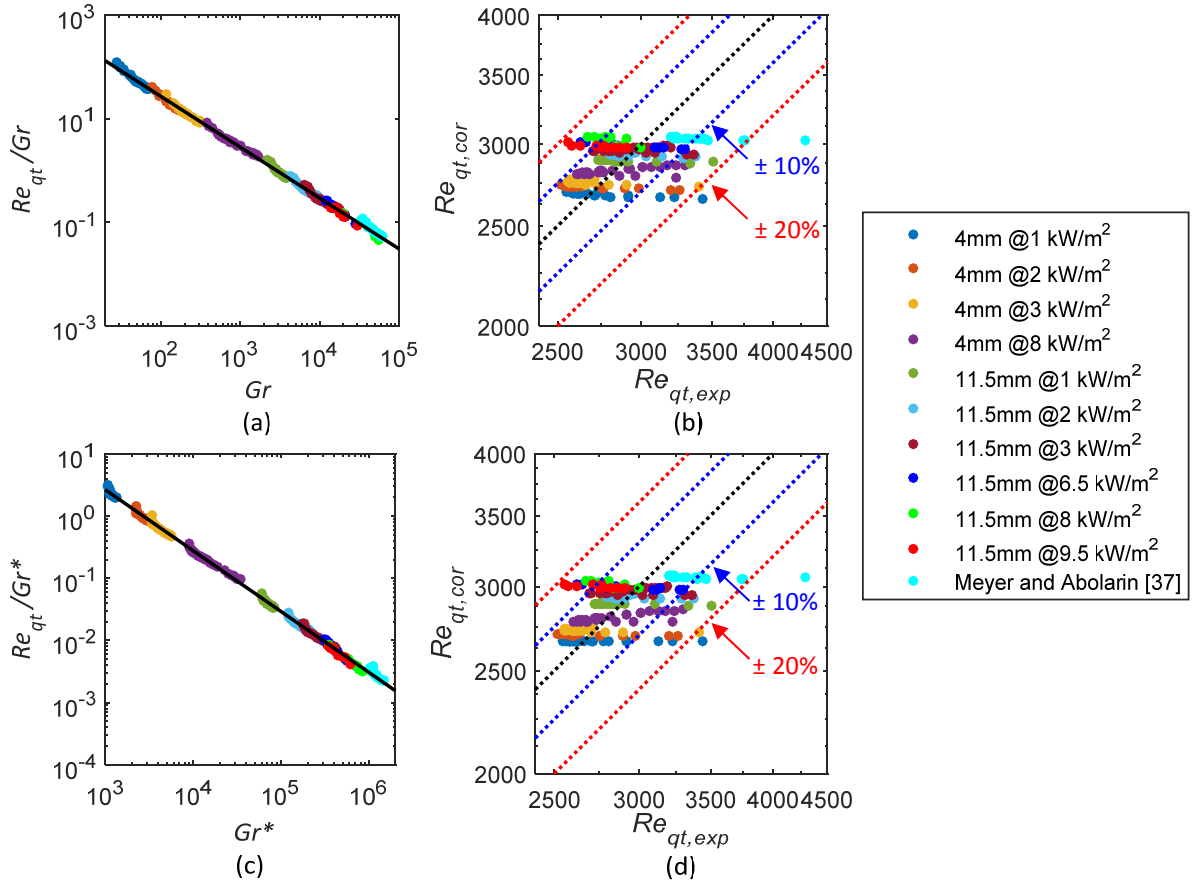

Fig. 6.12: Comparison of (a) Re_{qt}/Gr as a function of Grashof number, (b) deviation between Eq. 6.6 and experimental data and literature, (c) Re_{qt}/Gr^* as a function of modified Grashof number and (d) deviation between Eq. 6.8 and experimental data and literature.

Table 6.2: Overall performance and ranges of the correlations to predict the start and end of the transitional flow regime for a square-edged inlet.

	Eq.	This study only				This study and literature [37]			
		n	±10% [%]	±20% [%]	Ave %	*n*	±10% [%]	±20% [%]	Ave %
Re_{cr}	*Gr*: 6.3	212	83	99.5	6.1	272	81	99.6	6.6
	*Gr**: 6.4	212	82	99.5	5.8	272	80	99.6	6.4
		1 828 ≤ *Re* ≤ 3 158, 3.8 ≤ *Pr* ≤ 6.9, 923 ≤ *Gr* ≤ 7.62×10⁴, 1.08×10³ ≤ *Gr** ≤ 1.11×10⁶, 13.63 ≤ *x*/*D* ≤ 1 373, 4 mm ≤ *D* ≤ 11.5 mm				1 828 ≤ *Re* ≤ 3 158, 3.8 ≤ *Pr* ≤ 6.9, 923 ≤ *Gr* ≤ 2.62×10⁵, 1.08×10³ ≤ *Gr** ≤ 4.42×10⁶, 12.63 ≤ *x*/*D* ≤ 1 373, 4 mm ≤ *D* ≤ 19 mm			
Re_{qt}	*Gr*: 6.6	212	89	99.5	5.6	272	85	99	6.1
	*Gr**: 6.8	212	89	99.5	5.6	272	85	99	6.1
		2 519 ≤ *Re* ≤ 3 506, 4 ≤ *Pr* ≤ 7.5, 28 ≤ *Gr* ≤ 5.76×10⁴, 1.1×10³ ≤ *Gr** ≤ 8.36×10⁵, 13.63 ≤ *x*/*D* ≤ 1 373, 4 mm ≤ *D* ≤ 11.5 mm				2 365 ≤ *Re* ≤ 4 287, 4 ≤ *Pr* ≤ 7.5, 28 ≤ *Gr* ≤ 6.14×10⁴, 1.1×10³ ≤ *Gr** ≤ 1.46×10⁶, 13.63 ≤ *x*/*D* ≤ 1 373, 4 mm ≤ *D* ≤ 19 mm			

Eqs. 6.3, 6.4, 6.6 and 6.8 were compared with experimental results of this study and literature, and the performance and ranges of the correlations are summarised in Table 6.2. This table indicates that the Re_{cr} correlations could predict 80% of the data within 10% and approximately all the data within 20%. The Re_{qt} correlations could predict 85% of the data within 10% and the average deviation was approximately 6%.

6.6. Conclusions and recommendations

The purpose of this chapter was to experimentally investigate the influence of axial position, free convection effects and Prandtl number on the heat transfer characteristics of developing and fully developed flow in smooth tubes in the transitional flow regime. The Reynolds number was varied between 700 and 10 000 to ensure that the transitional and quasi-turbulent flow regimes, as well as sufficient parts of the laminar and turbulent flow regimes, were covered.

The local Reynolds numbers, Nusselt numbers, Colburn *j*-factors and Grashof numbers were calculated at each of the 27 thermocouple stations in both test sections and then compared. It was found that the Reynolds number at which transition started was independent of axial position for both developing and fully developed flow and transition occurred at the same moment in time along the whole tube length. However, the end of transition was dependent on axial position when the flow was developing and occurred earlier as the flow approached fully developed flow. Once the flow was fully developed, the end of transition became independent of axial position. Free convection effects affected both the start and end of the transitional flow regime and caused the Reynolds number range of the transitional flow regime to decrease. Correlations were developed to determine the start and end of the transitional flow regime for developing and fully developed flow in mixed convection conditions.

The transitional flow regime across the tube length was divided into three regions. In the first region, the width of the transitional flow regime decreased significantly with axial position as the thermal boundary layer thickness increased and free convection effects were negligible. In Region 2, the width of the transitional flow regime decreased with axial position due to the development of the thermal boundary layer and increased mass flow rate and temperature fluctuations, as well as with free convection effects. In the fully developed region (Region 3), the width of the transitional flow regime was independent of axial position, but decreased significantly with increasing free convection effects. At high Grashof numbers, free convection effects even caused the transitional flow regime to become negligible when the flow was fully developed and the flow alternated between the laminar and the quasi-turbulent flow regimes.

As the Prandtl number was increased, the increased viscosity restricted free convection effects to the thermal boundary layer. This prevented free convection effects to assist in the diffusion of heat from the surface to the centre of the tube, thus enhancing heat transfer and leading to a faster laminar-turbulent transition along the tube length. The result was that the transition gradient decreased and the width of the transitional flow regime increased.

Therefore, the heat transfer characteristics of developing flow in the transitional flow regime changed as the flow developed and differed significantly from fully developed flow, especially when mixed convection conditions existed. Furthermore, the transitional flow regime was also significantly affected when the Prandtl number was increased. Although high Prandtl number data from literature

were used in this chapter to investigate the influence of Prandtl number, it will be beneficial to conduct experiments using the same experimental set-up, but with higher Prandtl number fluids (such as ethylene glycol-water mixtures). This will be beneficial for the following reasons: (1) improving the comparison of results obtained using different Prandtl number fluids, (2) extending the experimental data base of heat transfer results in the transitional flow regime, and (3) extending the ranges of the correlations to more accurately predict the start and end of the transitional flow regime.

The influence of surface roughness in the transitional flow regime should also be investigated using tubes with different values of relative roughness, because corrosion and scaling which commonly occur in heat exchangers will increase the surface roughness of the tubes. It would be expected that the transitional flow regime will occur earlier with increasing surface roughness, due to the increased turbulence caused by the surface roughness. The correlations of the boundaries of the transitional flow regime can then be revised in order to account for surface roughness as well.

7. Relationship between Pressure Drop and Heat Transfer

7.1. Introduction

This chapter experimentally investigates the relationship between the local pressure drop and heat transfer characteristics of developing and fully developed flow of low Prandtl number fluids in smooth horizontal tubes at different heat fluxes. Laminar, quasi-turbulent and turbulent flow are also dealt with to ensure good alignment with the regimes to the transitional flow regime. Most of the results contained in this chapter were published in Everts and Meyer [49].

7.2. Pressure drop

The isothermal friction factors as a function of bulk Reynolds number for different tube lengths are compared in Fig. 7.1. For fully developed isothermal flow, the laminar friction factors should be equal to 64/*Re*, which is indicated by the solid blue line. Although the pressure drop increased with increasing fluid velocity, the friction factor was inversely proportional to the velocity squared (Eq. 3.22), therefore the friction factor decreased with increasing Reynolds number.

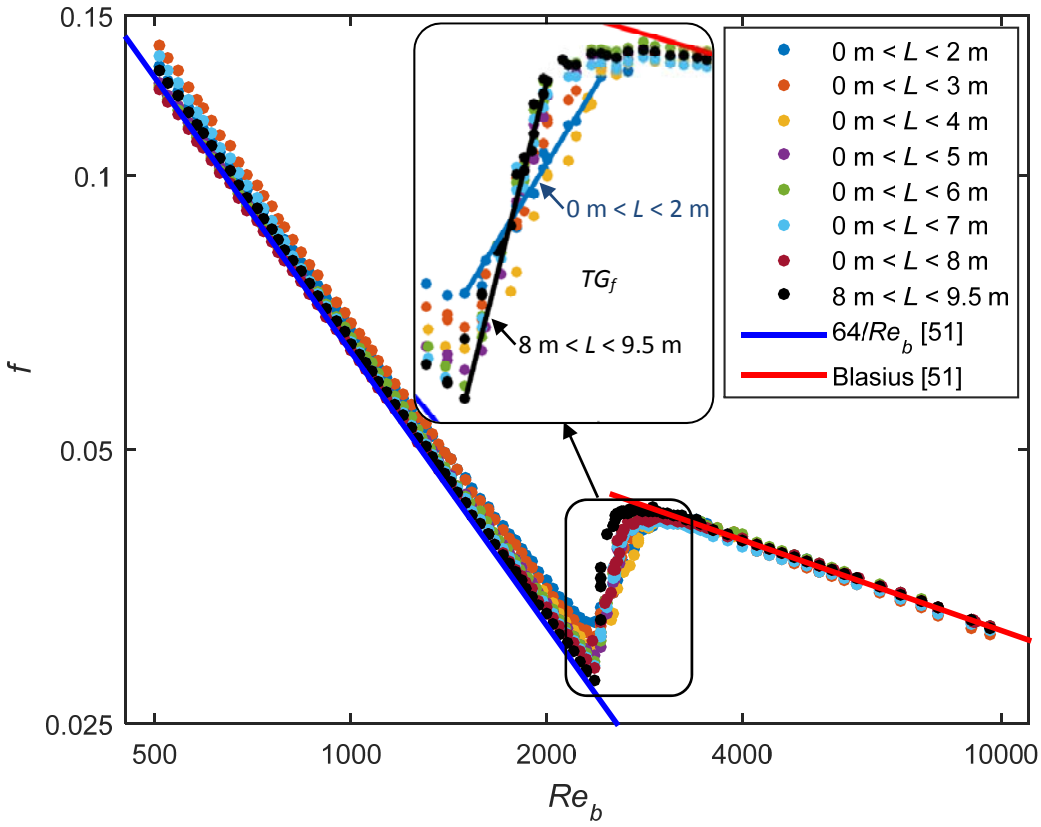

Fig. 7.1: Comparison of isothermal friction factors as a function of bulk Reynolds number across different tube lengths.

Figure 7.1 indicates that, at a fixed Reynolds number of 2 000, the laminar friction factors decreased and approached the solid blue line as the tube length increased. The friction factors of developing

flow were higher than for fully developed flow, because the maximum wall shear stress was found at the inlet of the test section where the hydrodynamic boundary layer was the thinnest. As the tube length was increased, a larger portion of the tube length contained fully developed flow, therefore the average friction factors decreased and approached the fully developed friction factors. Once the flow was fully developed, for example, over the last part of the tube length (8 m < L < 9.5 m), the friction factors corresponded very well to 64/Re and the average deviation was 2.5%. This trend was clear for Reynolds numbers larger than 2 000, but challenging to identify for Reynolds numbers less than 1 000, due to the uncertainties of the friction factors that increased with decreasing Reynolds numbers.

From the detailed view in Fig. 7.1, it follows that the transition gradient, TG_f, increased with increasing tube length, thus it increased as the flow approached fully developed flow. The gradient of the first tube length over which the pressure drop was measured (0 m < L < 2 m) was approximately 1.9×10^{-5} and is indicated by the solid blue line. The gradient of the last tube length (8 m < L < 9.5 m), which contained fully developed flow only, was approximately 4.6×10^{-5} and is indicated by the solid black line. As transition started at the same Reynolds number of 2 361 for all tube lengths, the start of transition was independent of tube length. However, the Reynolds number at which transition ended decreased from 2 809 for 0 m < L < 2 m, to 2 622 for 8 m < L < 9.5 m (fully developed flow).

To investigate the effect of free convection on the friction factors of developing and fully developed flow, the friction factors as a function of bulk Reynolds number at different heat fluxes and tube lengths are compared in Fig. 7.2. This figure indicates that as the heat flux was increased, the laminar friction factors increased slightly. This trend became more prominent as the tube length was increased and the flow approached fully developed flow (Fig. 7.2(h)), because free convection effects increased as the thermal boundary layer thickness increased.

The Reynolds number at which transition started increased with increasing heat flux; however, Fig. 6.3 indicates that this was only due to the decreasing viscosity with increasing temperature, and that free convection effects actually caused transition to occur at lower mass flow rates (Fig. 6.4). Similar to the isothermal results, the transition gradient increased with increasing tube length (flow approached fully developed flow), which caused the width of the transitional flow regime, ΔRe, to decrease. Furthermore, the width of the transitional flow regime also decreased with increasing heat flux. This is as expected, because Fig. 5.15 indicates that as free convection effects were increased by increasing the heat flux and/or tube diameter, the flow transitioned faster from laminar to turbulent along the tube length. This led to a decreased transition region along the test section, and also a decreased transitional flow regime in terms of Reynolds number (as summarised in Fig. 6.9).

Figure 7.2(h) indicates that once the flow was fully developed and free convection effects were significant, the transitional flow regime became negligible and it seemed as if $TG_f \rightarrow \infty$ at Re_{cr}. However, this was not the case as the changes in the y-scale (friction factor) were much smaller than the changes in the x-scale (Reynolds number). Although TG_f was actually a small value of 4.2×10^{-5}, it was still 4.6 times greater than for 0 m < L < 2 m (Fig. 7.2(a)). Severe fluctuations occurred inside the test section and after time (up to one hour), the flow stabilised at the critical Reynolds number and then in the quasi-turbulent flow regime at the next increasing experimental Reynolds number increment. Similar results were obtained in Fig. 6.2 when the local heat transfer coefficients of developing and fully developed flow were investigated.

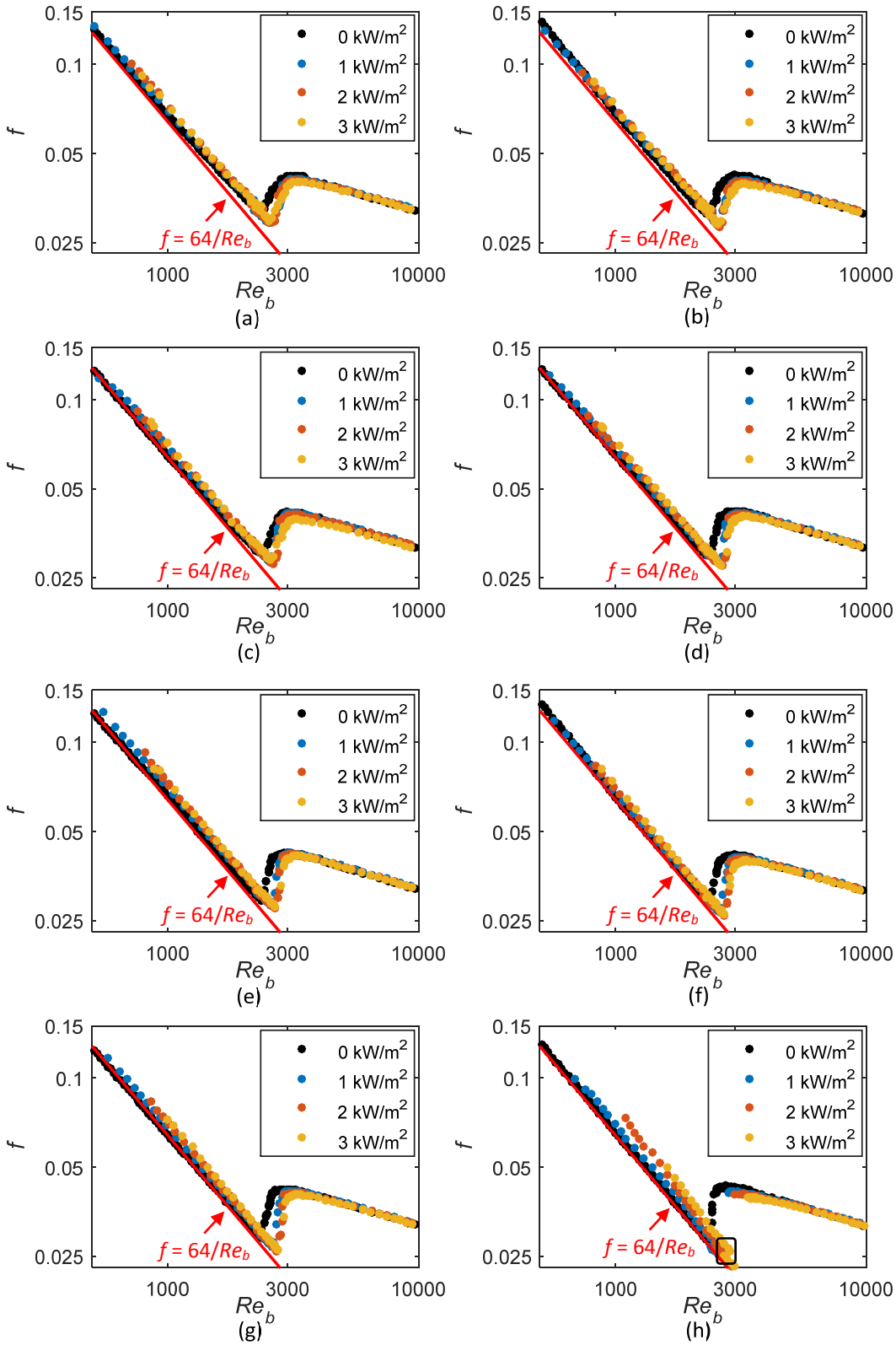

Fig. 7.2: Comparison of friction factors as a function of bulk Reynolds number at different heat fluxes across (a) 0 m ≤ *L* ≤ 2 m, (b) 0 m ≤ *L* ≤ 3 m, (c) 0 m ≤ *L* ≤ 4 m, (d) 0 m ≤ *L* ≤ 5 m, (e) 0 m ≤ *L* ≤ 6 m, (f) 0 m ≤ *L* ≤ 7 m, (g) 0 m ≤ *L* ≤ 8 m and (h) 8 m ≤ *L* ≤ 9.5 m. The heat flux of 0 kW/m^2 indicates isothermal flow. The black rectangle in Fig. 7.2(h) indicates the region where different pressure transducers had to be used because of pressure transducer diaphragm range limitations.

As expected, there was no significant difference between the results of the different tube lengths and heat fluxes in the quasi-turbulent and turbulent flow regimes, because the flow was fully developed and free convection effect were suppressed by the velocity of the fluid.

From the black rectangle in Fig. 7.2(h), it follows that a discontinuity existed between Reynolds numbers of 2 700 and 2 900. This was due to the different pressure transducer diaphragms that were used to conduct experiments between Reynolds numbers of 500 and 4 000, and between 2 000 and 10 000. At a Reynolds number of 2 880, friction factors of 0.02596 and 0.02368 were obtained using the two different pressure transducer diaphragms. Because this difference was only 1.6%, which is less than the friction factor uncertainty of approximately 5% at this heat flux and Reynolds number, it was considered to be negligible. Slight discontinuities existed in the friction factors of the other tube lengths as well; however, it was even less due to the longer tube lengths and lower uncertainties.

Similar to Langhaar [81], the friction factor results in Fig. 7.2 were investigated in terms of the product of the friction factor and Reynolds number (fRe), as a function of the dimensionless axial distance ((x/D)/Re) in Fig. 7.3. For fully developed laminar flow, fRe should be equal to 64, which is indicated by the solid red line. As indicated by the arrows, the different flow regimes can also be identified in Fig. 7.3.

From the isothermal results (black markers in Fig. 7.3), it follows that the laminar friction factors formed a diagonal line (with a negative gradient) near the inlet of the test section (Fig. 7.3(a)), but the gradient of this line approached zero as the flow approached fully developed flow (Fig. 7.3(h)). Although Tam *et al*. [8] found that heating caused the friction factors to decrease in the laminar and transitional flow regimes, the opposite trend is found in Fig. 7.2 and Fig. 7.3. Similar to the results obtained by Tam and Ghajar [26], the laminar friction factors increased with increasing heat flux. This increase became more significant as the tube length increased and the flow approached fully developed flow, because free convection effects increased with increasing boundary layer thickness. Tam and Ghajar [26] explained that the velocity profile changed when mixed convection occurred. As the heat flux was increased, the density decreased, and the shear stress due to the change in the velocity profile increased, which led to increased friction factors. However, the decreasing density and viscosity with increasing temperature could also lead to decreased pressure drops and friction factors, as was found by Tam *et al*. [8].

Figure 6.3 indicates that the surface temperatures increase with increasing heat flux, which lead to increased Reynolds numbers due to the decreasing viscosity with increasing temperature. Therefore, when the flow was fully developed (8 m < L < 9.8 m in Fig. 7.2(h)) at a fixed Reynolds number of approximately 1 650, the viscosity decreased by 32% when the heat flux was increased from 1 kW/m^2 to 3 kW/m^2. Furthermore, the mass flow rate, and thus fluid velocity as well, decreased by approximately 35%. Although the decreased density and viscosity caused the pressure drop across the tube length to decrease by 50%, the significantly lower fluid velocities caused the friction factors to increase by 13% ($f \propto 1/V^2$). However, when the viscosity decreases significantly with temperature (for example when ethylene glycol is used), the decrease in pressure drop might be more than the increase due to the decreased fluid velocity, which will then lead to decreased friction factors (as was found by Tam *et al*. [8]).

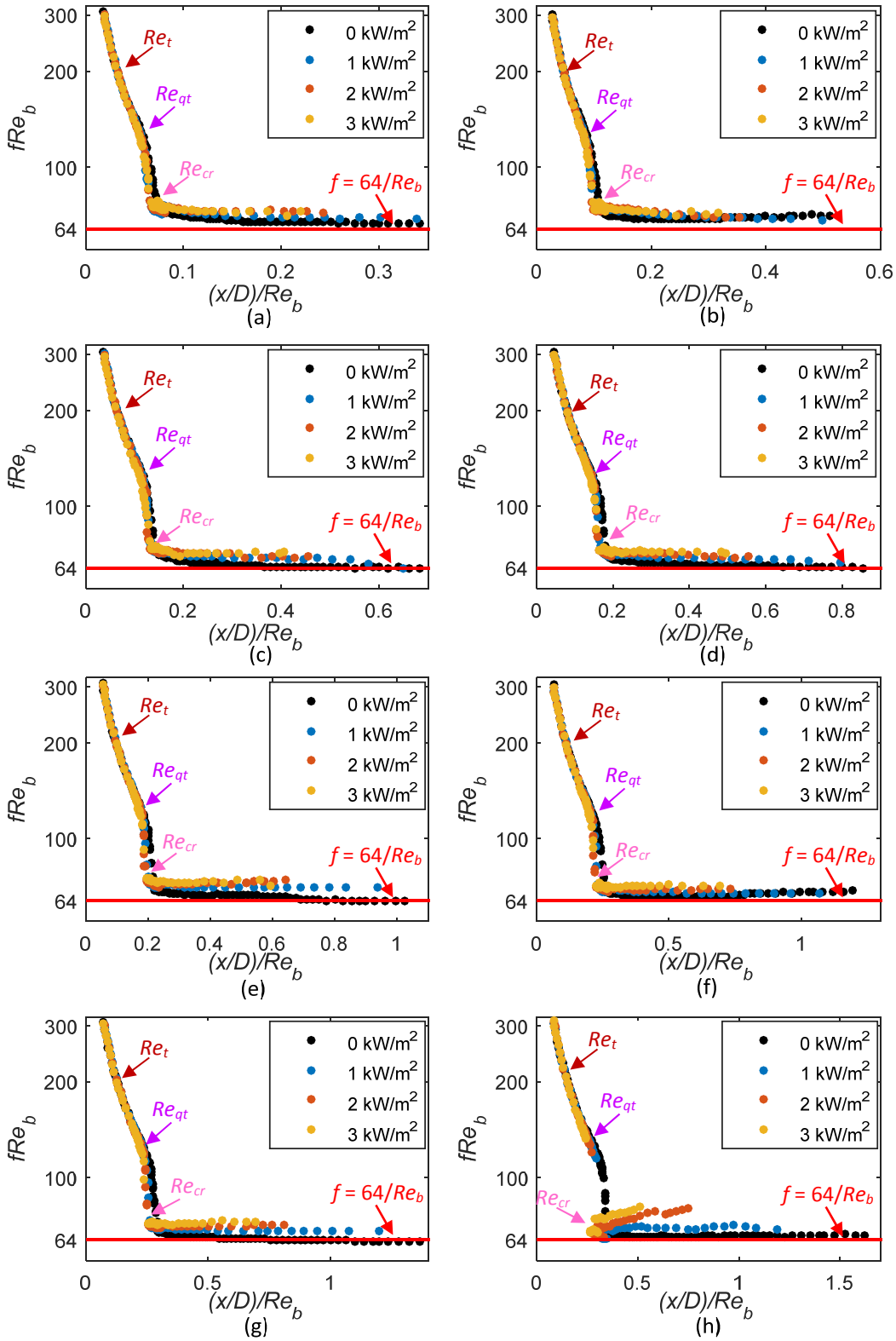

Fig. 7.3: Comparison of the product of the friction factor and bulk Reynolds number (fRe_b) as a function of dimensionless axial distance ($(x/D)/Re_b$) for (a) 0 m ≤ L ≤ 2 m, (b) 0 m ≤ L ≤ 3 m, (c) 0 m ≤ L ≤ 4 m, (d) 0 m ≤ L ≤ 5 m, (e) 0 m ≤ L ≤ 6 m, (f) 0 m ≤ L ≤ 7 m, (g) 0 m ≤ L ≤ 8 m, and (h) 8 m ≤ L ≤ 9.5 m. The heat flux of 0 kW/m^2 indicates isothermal flow.

At the critical Reynolds number, *fRe* increased significantly. Although the boundary between quasi-turbulent and turbulent flow regimes was challenging to identify in Fig. 7.2, it shows prominently in Fig. 7.3. In the quasi-turbulent flow regime, the gradient of *fRe* increased (compared with the transitional flow regime), while it decreased (compared with the quasi-turbulent flow regime) in the turbulent flow regime.

7.3. Heat transfer

Fig. 7.4 compares the average Colburn *j*-factors of the different tube lengths as a function of bulk Reynolds number at different heat fluxes. The solid red line indicates the Colburn *j*-factors calculated using the theoretical Nusselt number of 4.36, which is valid for fully developed forced convection laminar flow, and a Prandtl number of 6.8. Figure 7.4 indicates that the Colburn *j*-factors were significantly higher than for $Nu = 4.36$, due to free convection effects, as well as the fact that the flow was still developing. Metais and Eckert [13] considered free convection effects to be significant when the Nusselt numbers were at least 10% greater than the corresponding forced convection Nusselt numbers. At a Reynolds number of 1 500, the average fully developed Nusselt number (corresponding to the Colburn *j*-factors in Fig. 7.4(h)) was approximately 8.95 at a heat flux of 1 kW/m^2, and increased to 12.46 at a heat flux of 3 kW/m^2. Because this was 105% and 186% respectively greater than 4.36, it can be concluded that free convection effects were significant.

Figure 7.4(a) indicates that, at a Reynolds number of 1 500, the difference between the Colburn *j*-factors at heat fluxes of 1 kW/m^2 and 3 kW/m^2 was approximately 25%, but increased to 61% when the flow was fully developed (Fig. 7.4(a)). Therefore, as the tube length increased and the flow approached fully developed flow, the difference between the Colburn *j*-factors of the different heat fluxes increased, because free convection effects increased with increasing thermal boundary layer thickness. This increase in laminar Colburn *j*-factors was also significantly more than for the laminar friction factors in Fig. 7.2.

Similar to the friction factor results in Fig. 7.2, the critical Reynolds number increased with increasing heat flux. Near the inlet of the test section ($0 \text{ m} < L < 2 \text{ m}$ in Fig. 7.4(a)), transition started at Reynolds numbers of 2 520 and 2 532 at heat fluxes of 1 kW/m^2 and 3 kW/m^2 respectively. However, when the flow was fully developed ($8 \text{ m} < L < 9.5 \text{ m}$ in Fig. 7.4(h)), transition was delayed to Reynolds numbers of 2 641 and 3 142 for heat fluxes of 1 kW/m^2 and 3 kW/m^2 respectively. The difference between the critical Reynolds numbers of the two heat fluxes thus increased along the tube length from a Reynolds number range of 12 (Fig. 7.4(a)) to 541 (Fig. 7.4(h)). Section 6.3.3, as well as the isothermal results in Fig. 7.1, indicates that transition occurred at the same moment in time along the entire test section and that the increasing critical Reynolds numbers along the tube length were due to the decreasing viscosity with increasing temperature. Furthermore, the temperature gradient along the test section increased with increasing heat flux (Fig. 6.3), which led to greater critical Reynolds number variations.

Figure 7.4 also indicates that the transition gradient, TG_j, increased not only as the flow approached fully developed flow, but also with increasing heat flux, because free convection effects caused the flow to transition faster from laminar to turbulent along the tube length. Similar to Fig. 7.2(h), the severe fluctuations due to free convection effects caused the transitional flow regime of fully developed flow (Fig. 7.4(h)) to become negligible and the flow alternated between the laminar and quasi-turbulent flow regimes.

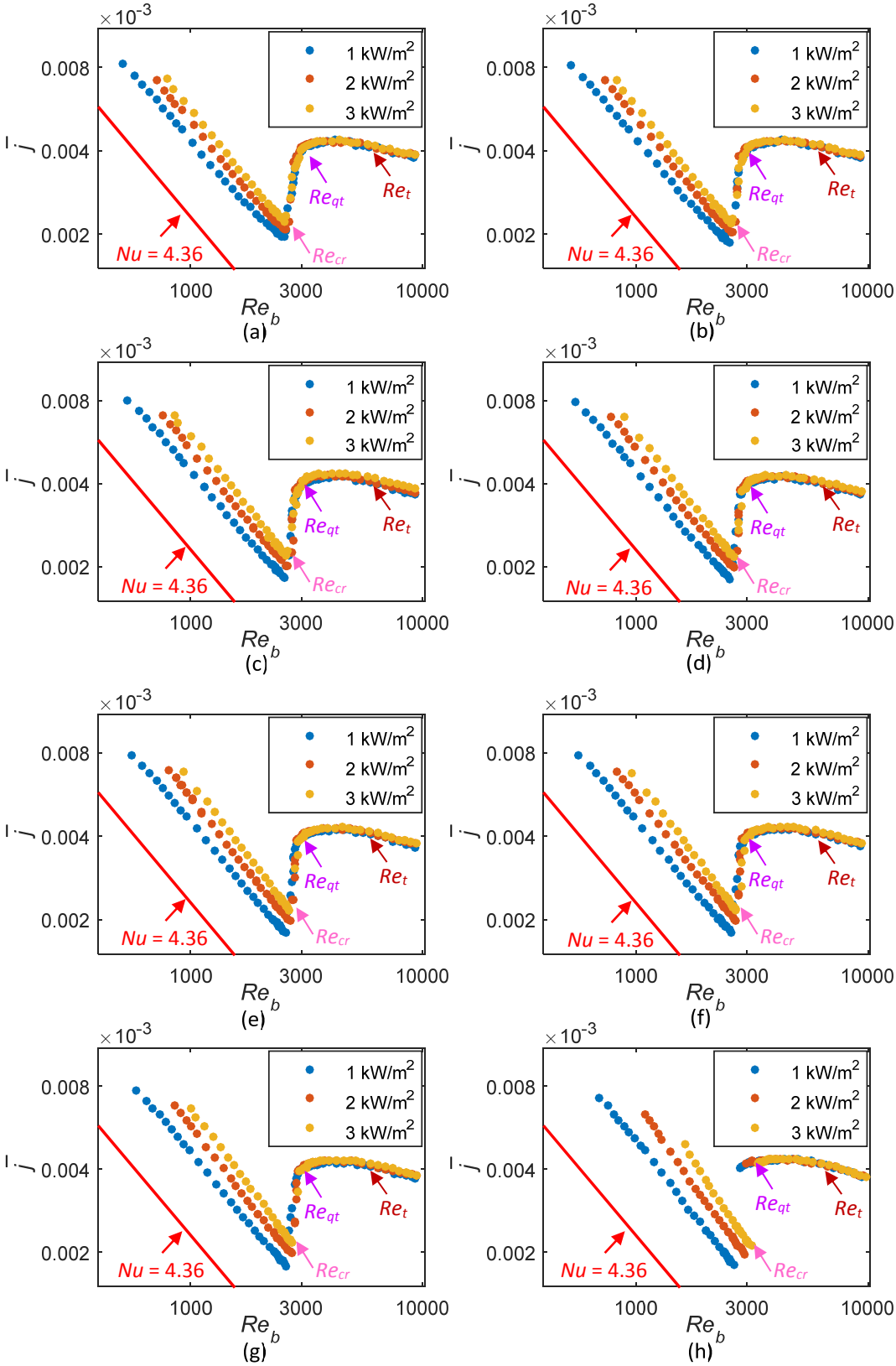

Fig. 7.4: Comparison of average Colburn *j*-factors as a function of bulk Reynolds number at different heat fluxes across (a) 0 m ≤ *L* ≤ 2 m, (b) 0 m ≤ *L* ≤ 3 m, (c) 0 m ≤ *L* ≤ 4 m, (d) 0 m ≤ *L* ≤ 5 m, (e) 0 m ≤ *L* ≤ 6 m, (f) 0 m ≤ *L* ≤ 7 m, (g) 0 m ≤ *L* ≤ 8 m and (h) 8 m ≤ *L* ≤ 9.5 m.

As summarised in Fig. 6.9, free convection effects did not significantly affect the magnitude of the heat transfer coefficients in the quasi-turbulent flow regime; however, it decreased the width of this regime, because the Reynolds number at which transition ended increased, while the Reynolds number at which the flow became fully turbulent remained unaffected. Similar results were obtained in Fig. 7.4(h), because free convection effects caused the width of the quasi-turbulent flow regime to decrease from a Reynolds number range of approximately 3 200 to 2 640, when the heat flux was increased from 1 kW/m^2 to 3 kW/m^2. Furthermore, the width of the quasi-turbulent flow regime also decreased as the flow approached fully developed flow. From Fig. 7.4(a) and (h), it follows that at a heat flux of 3 kW/m^2, the width of the quasi-turbulent flow regime decreased from a Reynolds number range of 3 010 when the flow was developing, to 2 640 when the flow was fully developed. As expected, there was no significant difference between the results of the different tube lengths and heat fluxes in the turbulent flow regime, because the flow was fully developed and the free convection effects were suppressed by the inertia forces of the fluid.

7.4. Relationship between pressure drop and heat transfer

When comparing the friction factor results (Fig. 7.2) and Colburn *j*-factor results (Fig. 7.4) as a function of Reynolds number, it follows that the trends were similar. This was expected because the Chilton-Colburn analogy [3], which was developed for laminar and turbulent flow over flat plates, determined that the relationship between friction factor (pressure drop) and Colburn *j*-factor (heat transfer) was directly proportional. However, it has not been shown before that this relationship is valid in the transitional flow regime.

As the pressure drop and heat transfer data were measured simultaneously during the experiments, the average friction factors and Colburn *j*-factors for 0 m < L < 8 m at heat fluxes of 1 kW/m^2 and 3 kW/m^2 were plotted on the same graph in Fig. 7.5. Although the results are only given for this tube length and heat fluxes, graphs were generated for the other tube lengths and heat fluxes as well and similar observations were made. The boundaries of the different flow regimes (Re_{cr}, Re_{qt} and Re_t) are indicated by the dotted lines (coloured according to the heat flux).

In the laminar flow regime, both friction factors and Colburn *j*-factors decreased with increasing Reynolds number, therefore both gradients were negative. At a fixed Reynolds number of 2 370, the increase in friction factors between the two heat fluxes was 4%, while the increase in Colburn *j*-factors was 29%. Therefore, free convection effects had a greater influence on the heat transfer coefficients than on the friction factors in the laminar flow regime.

At a heat flux of 3 kW/m^2, the gradients of both friction factors (df/dRe) and Colburn *j*-factors (dj/dRe) changed from negative to positive at a Reynolds number of 2 740, which indicated the start of the transitional flow regime (Re_{cr}). In the transitional flow regime, both friction factors and Colburn *j*-factors increased with increasing Reynolds number, therefore the gradients were positive. Transition ended (Re_{qt}) at a Reynolds number of approximately 3 019, where the gradient of both the friction factor and the Colburn *j*-factor lines decreased compared with the transitional flow regime ($(df/dRe)_{QT} < (df/dRe)_{TG}$ and $(dj/dRe)_{QT} < (dj/dRe)_{TG}$).

In the quasi-turbulent flow regime, both the friction factors and Colburn *j*-factors first increased with increasing Reynolds number (although the gradients were significantly less than in the transitional flow regime), and then decreased as the Reynolds number was increased further, forming a concave

curve. However, because the gradient of the Colburn *j*-factors was less than for the friction factors, the concave curve of the Colburn *j*-factors was flatter than for the friction factors. Near the end of the quasi-turbulent flow regime, the trends of the friction factors and Colburn *j*-factors were similar to the turbulent flow regime (decreased with increasing Reynolds number); however, it was not fully turbulent yet. The Colburn *j*-factors indicate that the flow only became fully turbulent at a Reynolds number of approximately 5 955 (Re_t), where both friction factors and Colburn *j*-factors decreased with increasing Reynolds number and correlated very well with the correlations of Allen and Eckert [5] and Ghajar and Tam [16]. This corresponds well to Re_t = 6 000, which was obtained in Section 3.8.1.3 and Fig. 6.2.

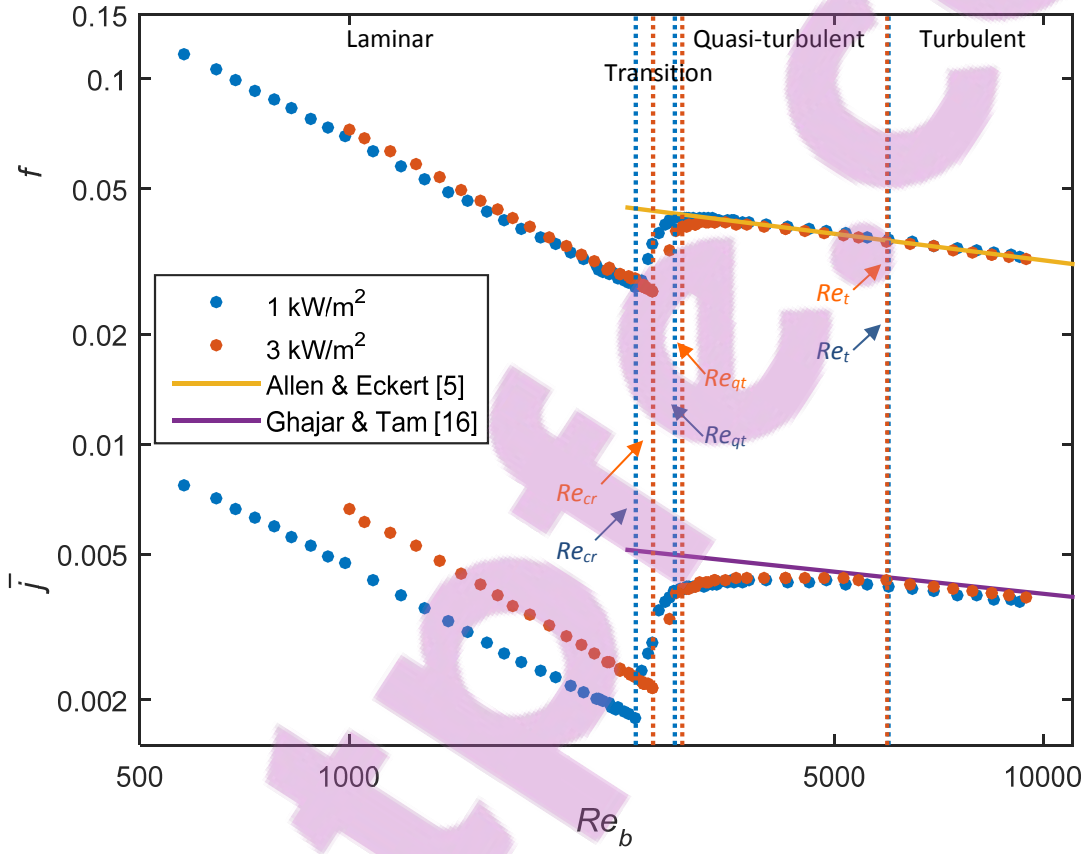

Fig. 7.5: Comparison of the pressure drop and heat transfer results in terms of the friction factors and average Colburn *j*-factors for 0 m < *L* < 8 m as a function of bulk Reynolds number at heat fluxes of 1 kW/m² and 3 kW/m².

Therefore, the boundaries of the different flow regimes, especially the transitional flow regime, were the same for pressure drop and heat transfer for all the experiments. This corresponds to the Chilton-Colburn analogy [3], which shows that there is a direct relationship between friction factor (pressure drop) and Colburn *j*-factor (heat transfer) for laminar and turbulent flow over flat plates. Similar findings were also made by Everts [75]. However, Tam *et al.* [8] found that the transition region, ΔRe, was wider for heat transfer than for pressure drop. A possible explanation is that the authors considered the quasi-turbulent flow regime as part of the transitional flow regime when the Colburn *j*-factors were investigated, while it was considered as part of the turbulent flow regime when the friction factors were investigated.

To investigate the relationship between pressure drop and heat transfer, *f*/*j*-factors were obtained by dividing the friction factors by the Colburn *j*-factors. The results are summarised in Fig. 7.6 for tube lengths of 0 m < *L* < 2 m (Fig. 7.2(a) and Fig. 7.4(a)) and 0 m < *L* < 8 m (Fig. 7.2(g) and Fig. 7.4(g)), at a heat flux of 3 kW/m^2. Figure 7.6 indicated that the *f*/*j*-factors in the laminar flow regime increased with increasing Reynolds number. Because the results differed significantly for the two tube lengths, it can be concluded that the *f*/*j*-factors in the laminar flow regime were affected by developing flow and free convection effects. In the transitional flow regime, the *f*/*j*-factors decreased significantly with increasing Reynolds number; however, this decrease was slightly less for 0 m < *L* < 2 m than for 0 m < *L* < 8 m. Although the *f*/*j*-factors continued to decrease in the quasi-turbulent flow regime, the gradient of the *f*/*j*-factors increased compared with the transitional flow regime, and approached zero in the turbulent flow regime. Furthermore, as the Reynolds number was increased, the difference in the *f*/*j*-factors of the two tube lengths decreased, and became negligible in the turbulent flow regime because the flow was fully developed and free convection effects were suppressed.

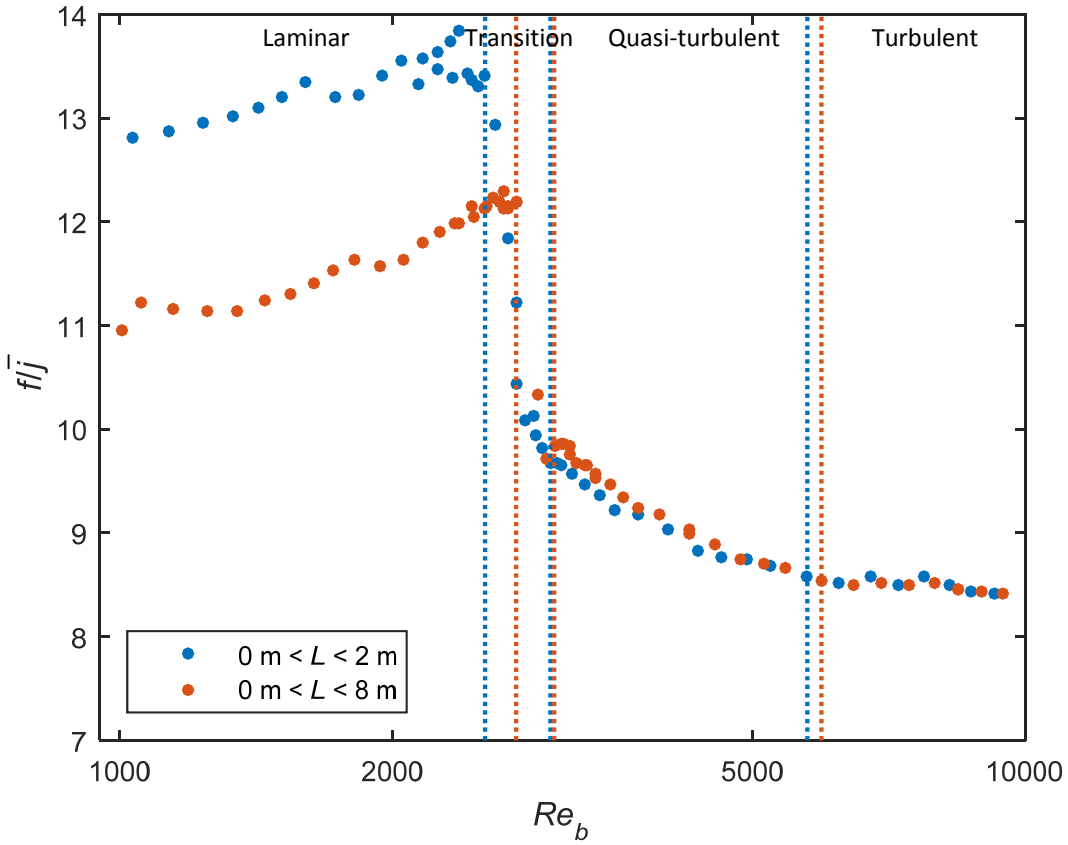

Fig. 7.6: Comparison of the friction factors divided by the average Colburn *j*-factors as a function of bulk Reynolds number for 0 m < *L* < 2 m and 0 m < *L* < 8 m at a heat flux of 3 kW/m^2.

Figure 7.6 indicates that the *f*/*j*-factors can also be used to identify the boundaries of the different flow regimes when pressure drop and heat transfer are investigated simultaneously. This can be used in addition to the criteria for the flow regime boundaries presented in Section 3.8.1, and will also ensure a better understanding of the trade-off between pressure drop and heat transfer in the different flow regimes.

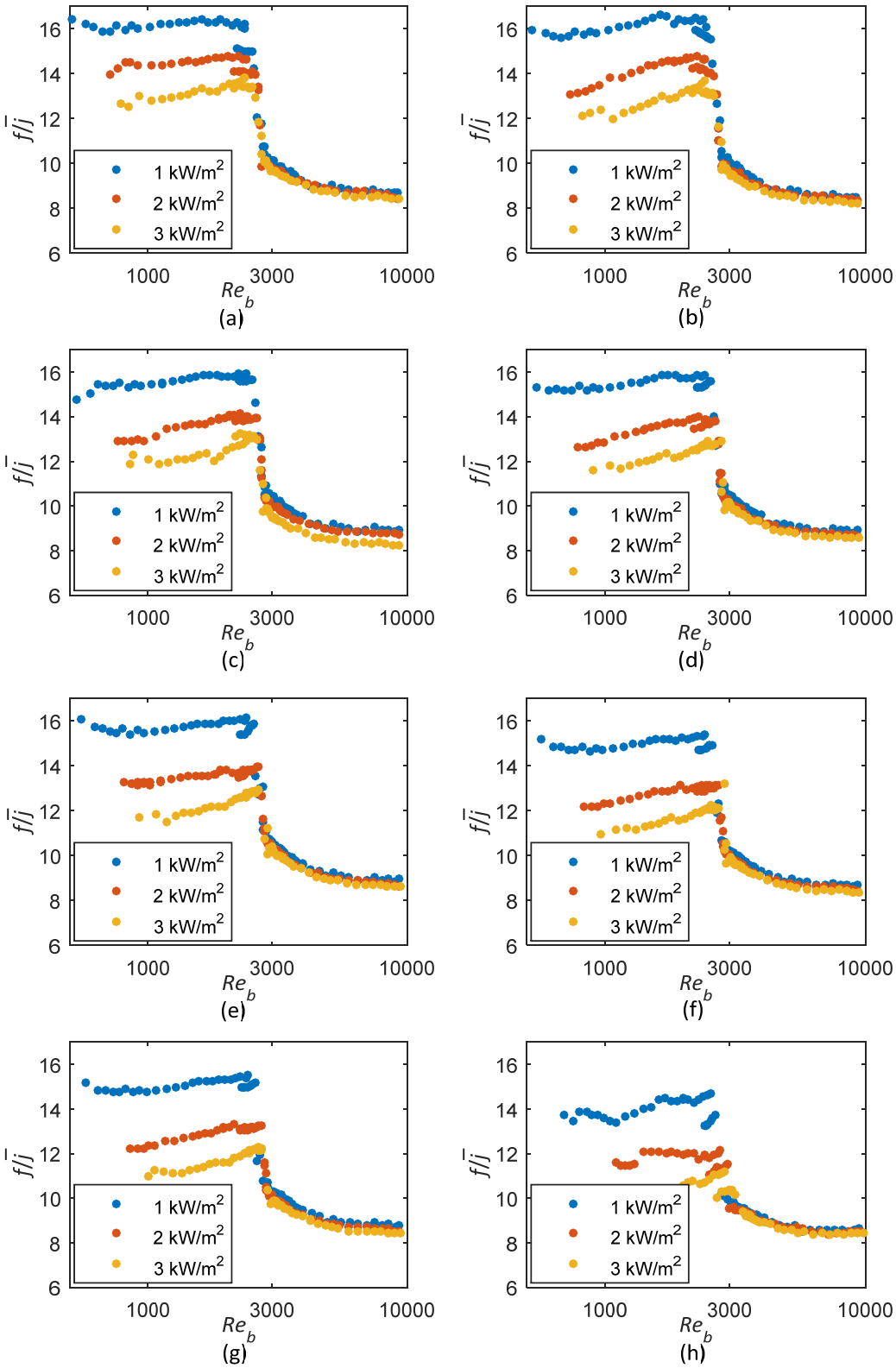

Fig. 7.7: Comparison of the friction factors divided by the average Colburn *j*-factors as a function of bulk Reynolds number at different heat fluxes across (a) 0 m ≤ *L* ≤ 2 m, (b) 0 m ≤ *L* ≤ 3 m, (c) 0 m ≤ *L* ≤ 4 m, (d) 0 m ≤ *L* ≤ 5 m, (e) 0 m ≤ *L* ≤ 6 m, (f) 0 m ≤ *L* ≤ 7 m, (g) 0 m ≤ *L* ≤ 8 m and (h) 8 m ≤ *L* ≤ 9.5 m.

Figure 7.7 compares the *f*/*j*-factors of the different tube lengths at different heat fluxes. This figure indicates that the laminar *f*/*j*-factors decreased significantly with increasing heat flux, thus free convection effects. Furthermore, at a heat flux of 1 kW/m^2, the laminar *f*/*j*-factors were approximately 16 for 0 m < *L* < 2 m (Fig. 7.7(a)), but decreased to approximately 14 when the flow was fully developed (Fig. 7.7(h)). As the Reynolds number was increased, free convection effects decreased and the difference between the *f*/*j*-factors of the different tube lengths and heat fluxes decreased and became negligible. It can be concluded from this graph that the *f*/*j*-factors in the laminar flow regime were a function of Grashof number (free convection effects), while it was a function of Reynolds number in the other flow regimes.

7.5. Correlations

Correlations were developed to determine the relationship between pressure drop and heat transfer (*f*/*j*-factors) of developing and fully developed flow in the different flow regimes. These correlations were then combined with Eq. 3.14 to obtain a correlation for the friction factor as a function of average Nusselt number. As these friction factor correlations were a function of Nusselt number, average Nusselt number correlations for developing and fully developed flow in the different flow regimes were also developed. The ranges and performance of the friction factor correlations (Section 7.5.1) and Nusselt number correlations (Section 7.5.2) are summarised in Section 7.5.3. It should be noted that although the friction factor and average Nusselt number correlations are not explicitly a function of tube length, *L*, it is valid for developing and fully developed data, because the bulk Reynolds number, Grashof number and Prandtl number for tube length *L*(*x*) are used. Furthermore, the Colburn *j*-factors and Nusselt numbers used in this chapter are the average values[1].

The friction factors and Colburn *j*-factors were calculated across eight different tube lengths and at three different heat fluxes. The solid markers in Fig. 7.8 to Fig. 7.11 represent the results at a heat flux of 1 kW/m^2, while the circles and diamonds represent the results at 2 kW/m^2 and 3 kW/m^2 respectively. Seven of the eight tube lengths contained both developing and fully developed flow (depending on the Reynolds number and heat flux), while the black markers (8 m < *L* < 9.5 m) contained fully developed flow only.

7.5.1. Friction factors

To determine the relationship between pressure drop and heat transfer for mixed convection conditions in the laminar flow regime, the *f*/*j*-factors were plotted against Grashof numbers in Fig. 7.8(a) and against the modified Grashof numbers in Fig. 7.8(c). A power curve fit was done through all the data (developing and fully developed flow) in Fig. 7.8(a) to obtain the following correlation:

$$\frac{f}{\bar{j}} = 109.71 Gr_b^{-0.215} \qquad 7.1$$

By substituting the Colburn *j*-factor with Eq. 3.14, the following correlation was obtained to calculate the friction factor as a function of average Nusselt number and bulk Grashof number:

[1] The overbar (-) for the average Colburn *j*-factors and Nusselt numbers is omitted in the text, because it does not print correctly in the text. However, it is included in the equations and graphs.

$$f = \frac{109.71\,\overline{Nu}}{Re_b Pr_b^{1/3} Gr_b^{0.215}} \tag{7.2}$$

The same procedure was then repeated for the bulk modified Grashof number in Fig. 7.8(c), because the temperature differences (required to calculate the Grashof number) are not always known, while the heat fluxes usually are:

$$\frac{f}{\bar{j}} = 115.01 Gr_b^{*-0.179} \tag{7.3}$$

The laminar friction factor as a function of average Nusselt number and bulk modified Grashof number can therefore be calculated using the following correlation:

$$f = \frac{115.01\,\overline{Nu}}{Re_b\, Pr_b^{1/3} Gr_b^{*0.179}} \tag{7.4}$$

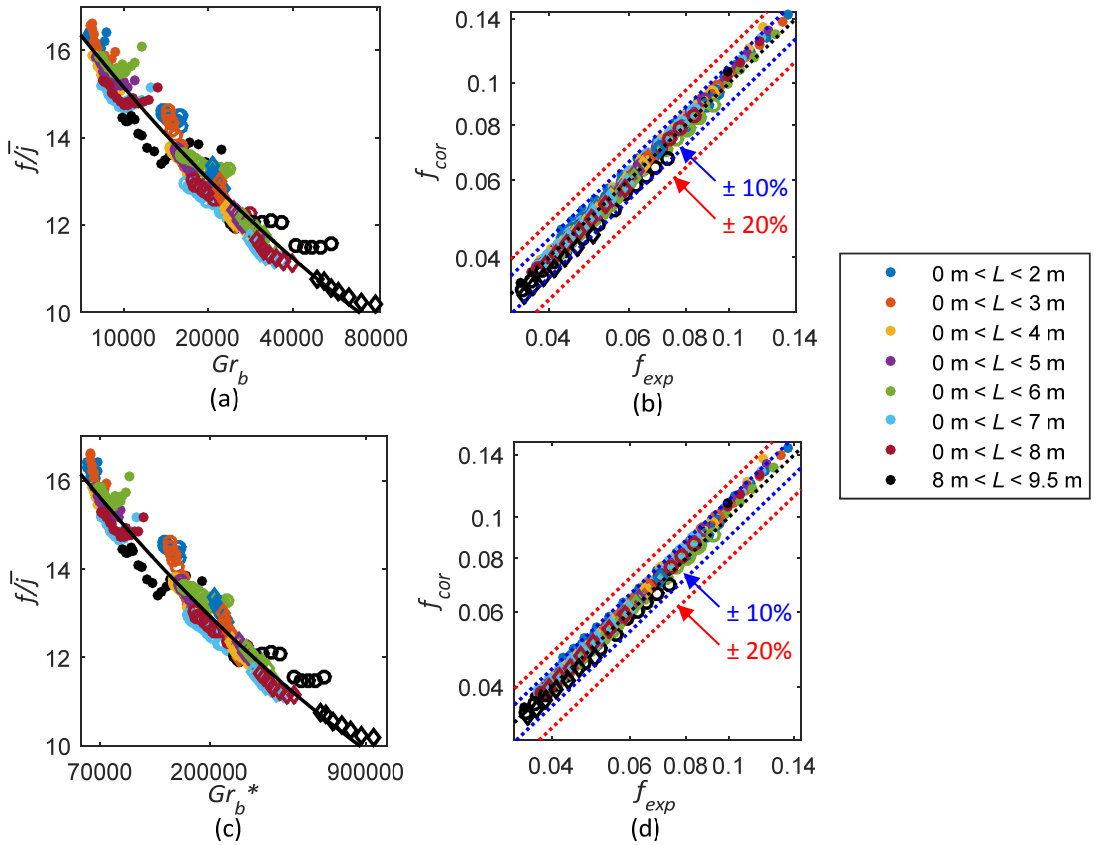

Fig. 7.8: Comparison of (a) *f*/*j* as a function of bulk Grashof number, (b) deviation between Eq. 7.2 and experimental data, (c) *f*/*j* as a function of bulk modified Grashof number and (d) deviation between Eq. 7.4 and experimental data. The solid markers represent the results at a heat flux of 1 kW/m², while the circles and diamonds represent the results at 2 kW/m² and 3 kW/m² respectively. The data are coloured according to the tube lengths, as specified in the legend.

Because the *f*/*j*-factors in the transitional, quasi-turbulent and turbulent flow regimes were a stronger function of Reynolds number than Grashof number, a single correlation for these three flow regimes was obtained by dividing the *f*/*j*-factors by $Pr_b^{0.42}$. The results ($(f/j)/Pr_b^{0.42}$) were plotted against the bulk Reynolds number in Fig. 7.9(a), and a rational curve fit was done to obtain the following correlation:

$$\frac{(f/\bar{j})}{Pr_b^{0.42}} = \frac{3.74\,Re_b - 8066}{Re_b - 2320} \qquad 7.5$$

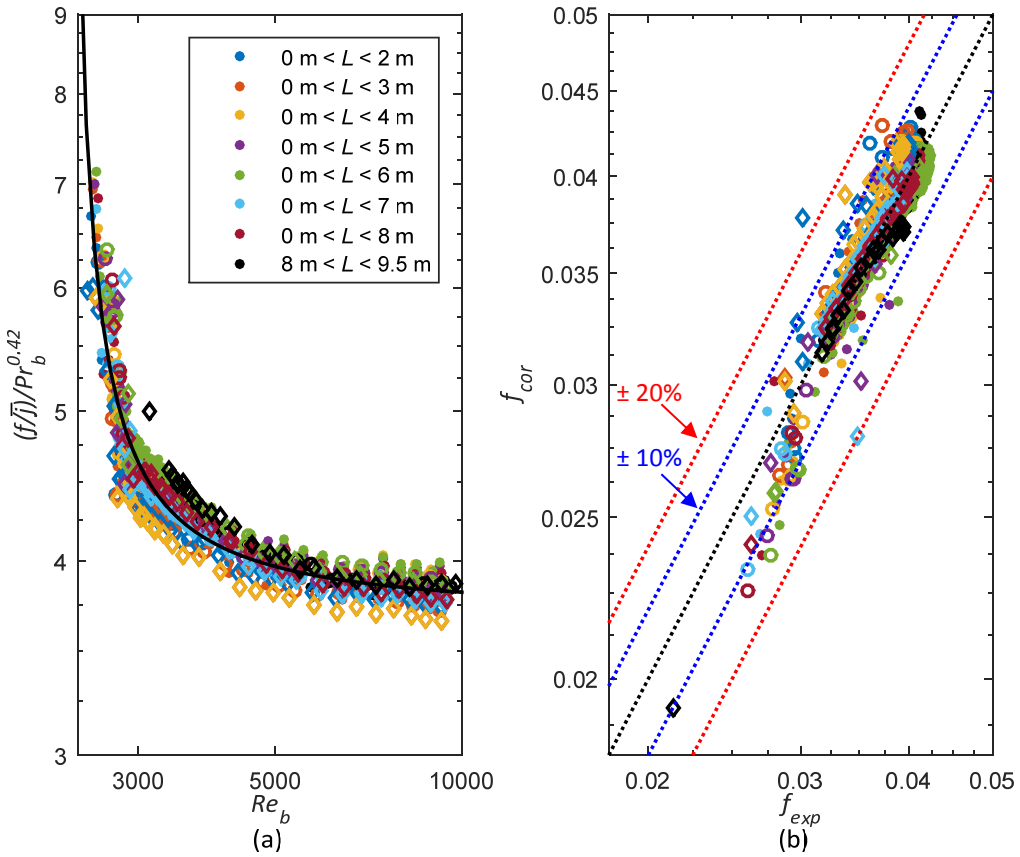

Fig. 7.9: (a) Comparison of $(f/j)/Pr^{0.42}$ as a function of bulk Reynolds number and (b) deviation between Eq. 7.6 and experimental data. The solid markers represent the results at a heat flux of 1 kW/m², while the circles and diamonds represent the results at 2 kW/m² and 3 kW/m² respectively. The data are coloured according to the tube lengths, as specified in the legend.

The following correlation was obtained to calculate the friction factor as a function of average Nusselt number for developing and fully developed flow in the transitional, quasi-turbulent and turbulent flow regimes:

$$f = \left(\frac{3.74\,Re_b - 8066}{Re_b - 2320}\right)\frac{\overline{Nu}}{Re_b Pr_b^{0.087}} \qquad 7.6$$

7.5.2. Average Nusselt numbers

Because Eqs. 7.2 and 7.4 are functions of the average Nusselt numbers, Eqs. 5.11 and 5.12 can be used to calculate the average Nusselt numbers across tube lengths $L(x)$, as a function of bulk Grashof numbers and bulk modified Grashof numbers respectively. The average Nusselt number correlations are a function of L, therefore it should be noted that Eqs. 7.2 and 7.4 can be used for both developing and fully developed flow.

To develop a correlation to predict the average Nusselt numbers of developing flow in the transitional flow regime, the Nusselt numbers were divided by $Gr_b^{-0.04}Pr_b^2$. The results $NuGr_b^{0.04}/Pr_b^2$ are plotted

as a function of bulk Reynolds number in Fig. 7.10(a) and the following transitional flow correlation was obtained with a linear curve fit:

$$\overline{Nu} = (0.00108\, Re_b - 2.49) Gr_b^{-0.04} Pr_b^2 \qquad 7.7$$

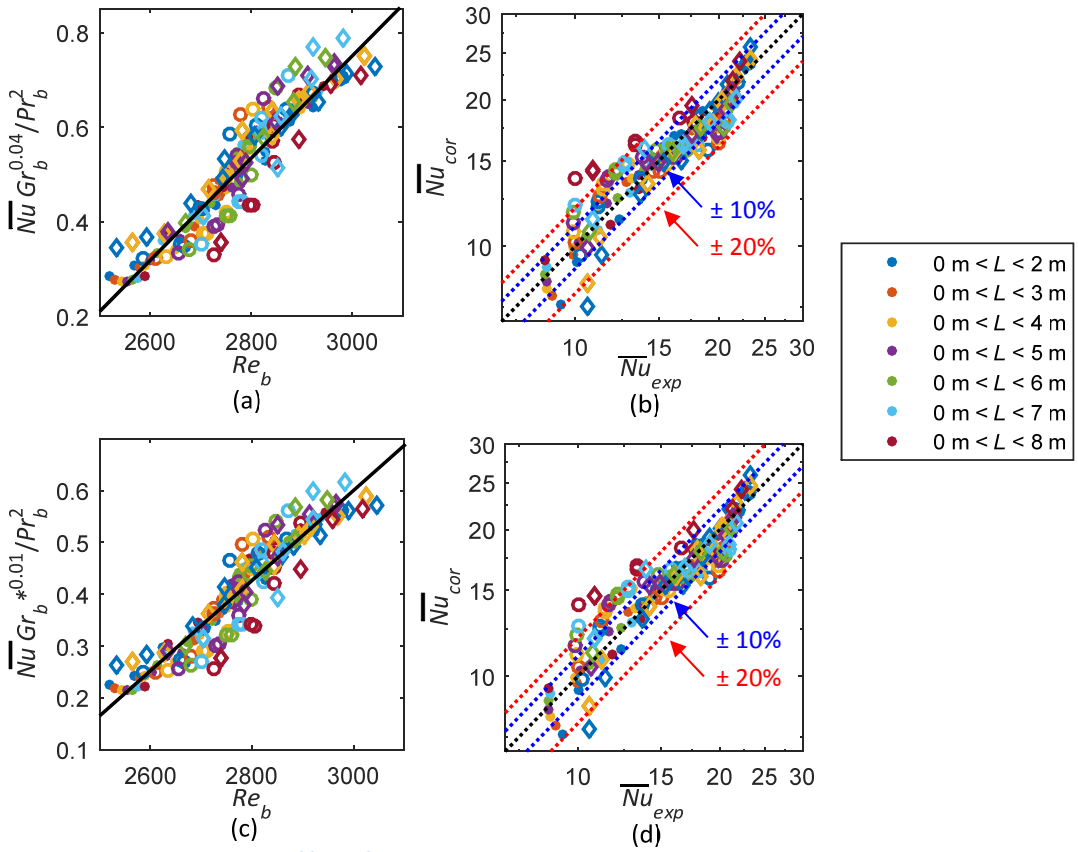

Fig. 7.10: Comparison of (a) $NuGr_b^{0.04}/Pr_b^2$ as a function of bulk Reynolds number, (b) deviation between Eq. 7.7 and experimental data, (c) $NuGr_b{}^{*\,0.01}/Pr_b^2$ as a function of bulk Reynolds number and (d) deviation between Eq. 7.8 and experimental data. The solid markers represent the results at a heat flux of 1 kW/m², while the circles and diamonds represent the results at 2 kW/m² and 3 kW/m² respectively. The data are coloured according to the tube lengths, as specified in the legend.

To calculate the Nusselt numbers in the transitional flow regime, Gnielinski [113] proposed using linear interpolation between the Nusselt numbers for laminar flow at a Reynolds number of 2 300 and the Nusselt numbers for turbulent flow at a Reynolds number of 10 000. However, to improve the accuracy of the heat transfer coefficients in the transitional flow regime, Gnielinski [45] proposed changing the turbulent Reynolds number to 4 000 [79]. Figure 6.6(c) indicates that both the start and end of transition were affected by free convection effects and varied along the tube length, while the method of Gnielinski did not account for free convection effects or developing flow. Therefore, although Eq. 7.7 also predicts the Nusselt numbers to increase linearly in the transitional flow regime, it accounts for free convection effects and does not require interpolation.

The same procedure was used for the bulk modified Grashof number and the following correlation for transitional flow was obtained by doing a linear curve fit through the results in Fig. 7.10(c):

$$\overline{Nu} = (0.00087\, Re_b - 2.01) Gr_b^{*-0.01} Pr_b^2 \qquad 7.8$$

Figure 7.4 indicates that the heat transfer coefficients in the quasi-turbulent and turbulent flow regimes were a strong function of Reynolds number and were not significantly affected by free convection effects. It was found by iteration that a correlation to predict the average Nusselt numbers in the quasi-turbulent and turbulent flow regimes can be obtained when the Nusselt numbers were divided by $Pr_b^{0.42}$. The results $Nu/Pr_b^{0.42}$ are plotted as a function of ($Re_b - 1\,000$) in Fig. 7.11(a), and a power curve fit was done to obtain the following correlation:

$$\overline{Nu} = [0.417\,(Re_b - 1000)^{0.499} - 8.2]Pr_b^{0.42} \qquad 7.9$$

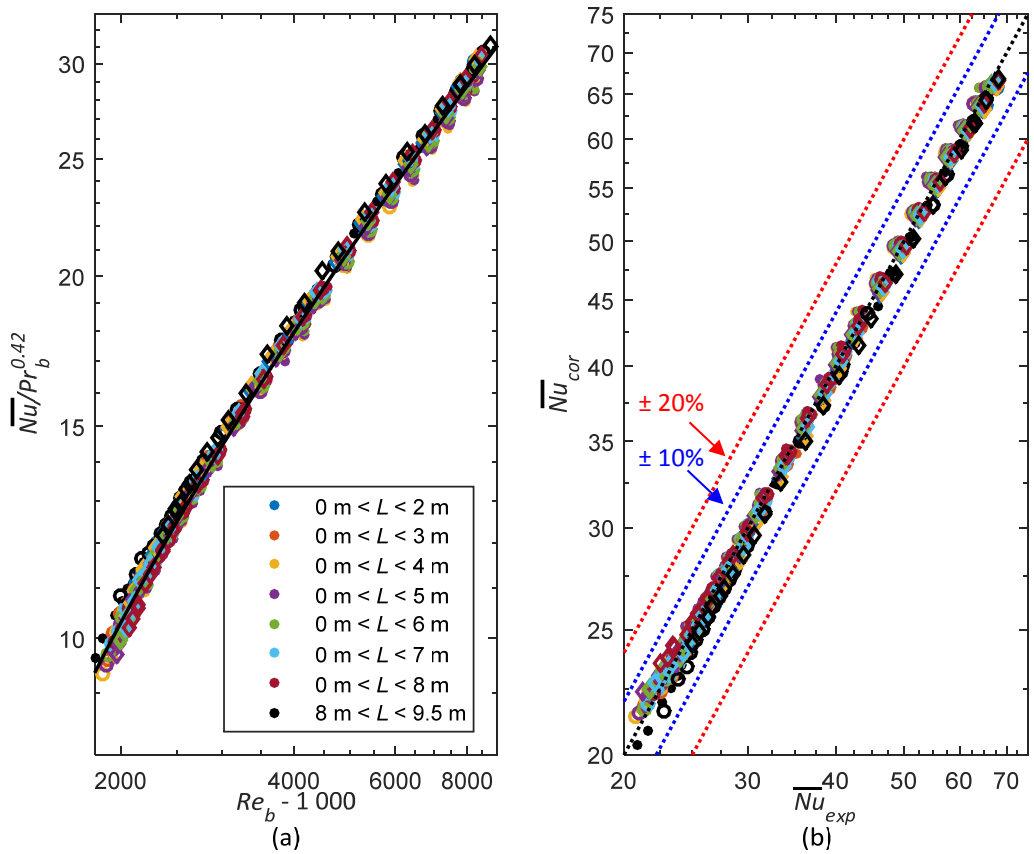

Fig. 7.11: Comparison of (a) $Nu/Pr_b^{0.42}$ as a function of ($Re_b - 1\,000$) and (b) deviation between Eq. 7.9 and experimental data. The solid markers represent the results at a heat flux of 1 kW/m², while the circles and diamonds represent the results at 2 kW/m² and 3 kW/m² respectively. The data are coloured according to the tube lengths, as specified in the legend.

The method of Churchill and Usagi [80] was used to obtain a single correlation that was valid for all four flow regimes:

$$\overline{Nu} = [\overline{Nu}_1^{10} + (\overline{Nu}_2^{-10} + \overline{Nu}_3^{-10})^{-1}]^{0.1} \qquad 7.10$$

Eq. 5.11 (laminar flow), Eq. 7.7 (transitional flow) and Eq. 7.9 (quasi-turbulent and turbulent flow) should be used to calculate Nu_1, Nu_2, and Nu_3 respectively, in terms of the Grashof number. Similarly, Eq. 5.12 (laminar flow), Eq. 7.8 (transitional flow) and Eq. 7.9 (quasi-turbulent and turbulent flow) should be used to calculate Nu_1, Nu_2, and Nu_3 respectively, in terms of the modified Grashof number.

7.5.3. Summary and performance of correlations

Table 7.1 summarises the valid ranges and performances of the friction factor and average Nusselt number correlations for developing and fully developed flow. Table 7.1 indicates that the laminar friction factor correlation could predict approximately all the data within 5%, while a single correlation for the transitional, quasi-turbulent and turbulent flow regimes could predict almost all the data (97%) within 10%. The average Nusselt number correlations could predict almost all the laminar, transitional, quasi-turbulent and turbulent data within 10%, 20%, and 5% respectively. Furthermore, the combined correlations, in terms of both the Grashof number and modified Grashof number, which could be used to calculate the Nusselt numbers in all the flow regimes, could predict 91% of the data within 10%.

Table 7.1: Summary of the ranges and performance of the friction factor (Section 7.5.1) and average Nusselt number (Section 7.5.2) correlations.

	Eq.	Data points	±5% [%]	±10% [%]	±20% [%]	Ave [%]	Range
Friction factors							
Laminar	7.2	495	92	100	100	2.4	$467 \leq Re \leq 3\,217$, $3 \leq Pr \leq 7.4$, $2.6 \leq Gr \leq 5\,589$, $541 \leq Gr^* \leq 4.01\times10^6$
	7.4	495	95	100	100	2.2	
Transitional, quasi-turbulent and turbulent	7.6	834	85	97	99.9	2.8	$2\,483 \leq Re \leq 9\,787$, $5.4 \leq Pr \leq 6.9$, $8.9\times10^2 \leq Gr \leq 3.2\times10^4$, $5.9\times10^4 \leq Gr^* \leq 3.7\times10^5$
Nusselt numbers							
Laminar‡	5.11	495	74	98	100	3.6	$48 \leq Re \leq 3\,217$, $2.9 \leq Pr \leq 282$, $5.5 \leq Gr \leq 4.5\times10^4$, $41 \leq Gr^* \leq 7.3\times10^6$
	5.12	495	77	95	100	3.6	
Transitional	7.7	179	51	76	95	7.1	$2\,520 \leq Re \leq 3\,361$, $5.4 \leq Pr \leq 6.8$, $2.8\times10^4 \leq Gr \leq 3.2\times10^4$, $6.1\times10^4 \leq Gr^* \leq 3.7\times10^5$
	7.8	179	53	75	93	7.3	
Quasi-turbulent and turbulent	7.9	653	99.8	100	100	1.4	$2\,804 \leq Re \leq 9\,787$, $5.5 \leq Pr \leq 6.9$, $8.9\times10^2 \leq Gr \leq 1.4\times10^4$, $5.9\times10^4 \leq Gr^* \leq 3.6\times10^5$
Laminar, transitional, quasi-turbulent and turbulent	*Gr*: 7.10	1 329	74	91	97	4.5	$512 \leq Re \leq 9\,787$, $3.8 \leq Pr \leq 6.9$, $8.9\times10^2 \leq Gr \leq 7.8\times10^4$, $5.9\times10^4 \leq Gr^* \leq 9.8\times10^5$
	*Gr**: 7.10	1 329	77	91	96	4.4	

‡These correlations were developed in Section 5.3.5.

7.6. Conclusions and recommendations

This chapter experimentally investigated the pressure drop and heat transfer characteristics of developing and fully developed flow in smooth tubes in the laminar, transitional, quasi-turbulent and turbulent flow regimes. It was found that the boundaries of the different flow regimes were the same for pressure drop and heat transfer and that a direct relationship between pressure drop and heat transfer existed in the transitional flow regime as well. In the laminar flow regime, the relationship

between pressure drop and heat transfer was a function of Grashof number (thus free convection effects), while it was a function of Reynolds number in the other three flow regimes. Correlations to predict the friction factors as a function of average Nusselt number, as well as correlations to predict the average Nusselt number, for developing and fully developed flow in all flow regimes were also developed.

The friction factor and average Nusselt number correlations that were developed in this chapter were developed using water data only, therefore the Prandtl numbers varied between three and seven. It is recommended that experiments should be conducted using air and different ethylene glycol-water mixtures in order to extend the ranges of the correlations with an order of magnitude lower and higher than that of water. Furthermore, as corrosion and scaling do not only affect the pressure drop in heat exchangers, but also the heat transfer characteristics, it is recommended that the influence of surface roughness on the relationship between pressure drop and heat transfer should also be investigated.

8. Flow Regime Maps

8.1. Introduction

In this chapter, the existing flow regime maps are evaluated using the experimental data from this study. Furthermore, new flow regime maps for both developing and fully developed flow, which can be used for both high and low Prandtl number fluids and a wide range of tube diameters are developed. Most of the results contained in this chapter were published in Everts and Meyer [50].

8.2. Maps from literature

An evaluation was conducted to determine which possible criteria (Richardson number or existing flow regime maps) are suitable to predict the convection flow regime of the experimental data of this study. The criterion used to distinguish the forced and mixed convection laminar data is as proposed by Metais and Eckert [13], i.e. mixed convection occurs when the Nusselt numbers are 10% higher than the corresponding forced convection Nusselt numbers. When validating the experimental data in Section 4.2, it was found that only 5% of the data fell into the forced convection flow regime. Therefore, in the evaluation that follows, 95% of the laminar data should fall into the mixed convection flow regime. In Fig. 8.1, Fig. 8.4 and Fig. 8.5, the data of this study will be grouped by tube diameter (4 mm or 11.5 mm), as well as which data (mostly) were mixed convection data.

The criterion proposed by Metais and Eckert [13] require the corresponding forced convection Nusselt number obtained using forced convection correlations; however, such correlations are not available in the transitional flow regime. The experimental data in Fig. 8.1-Fig. 8.5 were therefore coloured according to the ratio of h_t/h_b, because this can be used to gain insight into the free convection effects in all flow regimes. As will be discussed in Section 8.3.1, this criterion is suitable to compare results in a single test section, but not when the results of different tube diameters and test fluids are compared.

8.2.1. Richardson number

The Richardson number gives an indication of the relative magnitudes of free convection and forced convection effects. A general guideline in literature [3, 52-54, 60] is that the flow can be expected to be dominated by forced convection for $Ri \ll 1$, by free convection for $Ri \gg 1$ and by mixed convection for $Ri \approx 1$. However, it should be noted that the Richardson number was obtained by considering the boundary layer equations describing uniform upward flow over a heated vertical flat plate. Mills [55] suggested that when it is not obvious whether forced convection or free convection dominates, the Richardson number criterion for external flow should be used for internal flow to determine whether the flow is dominated by mixed convection. Therefore, the Richardson number is a typical parameter that should be investigated in this study.

Figure 8.1 compares the Reynolds numbers as a function of Richardson number of the experimental data (coloured according to the values of h_t/h_b) in the 4 mm and 11.5 mm test sections. The black dotted line indicates the Richardson number criterion for mixed convection ($Ri \approx 1$). Although 95% of the laminar experimental data were supposed to be in the mixed convection region, it follows from this figure that they fell incorrectly into the forced convection region because the Richardson numbers were significantly less than 1.

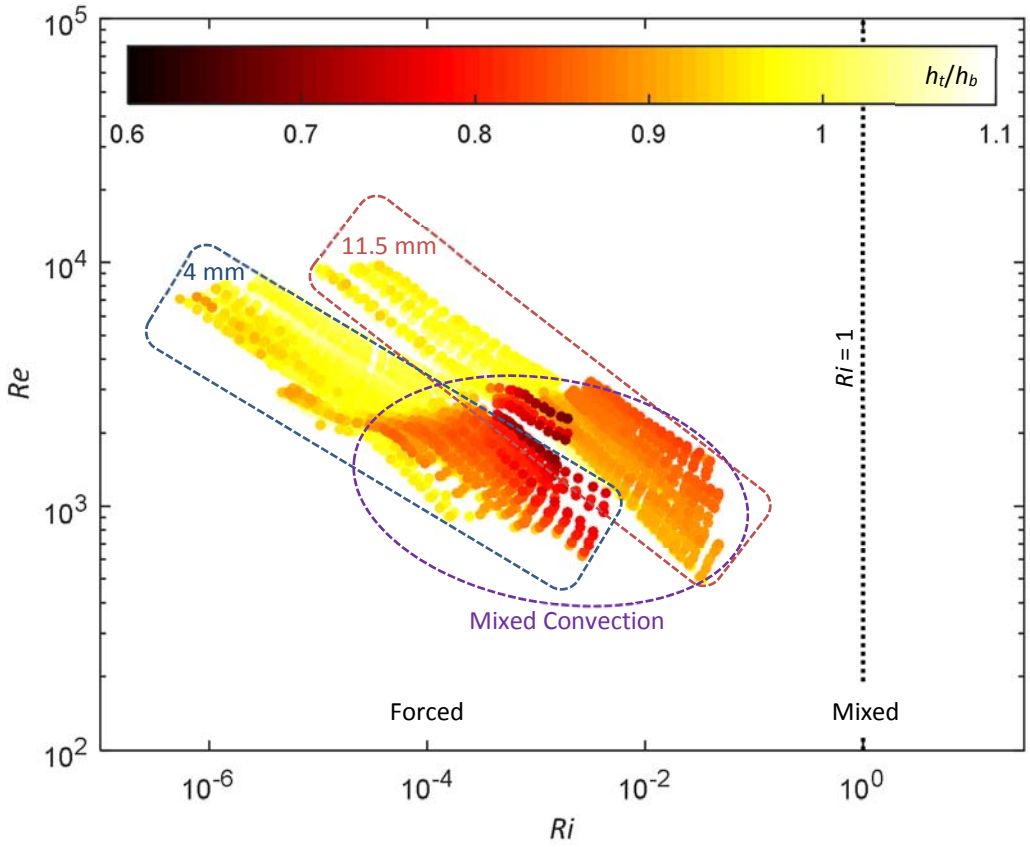

Fig. 8.1: Reynolds number as a function of Richardson number for the experimental data in the 4 mm and 11.5 mm test sections. The horizontal colour bar is coloured according to h_t/h_b. The mixed convection data are identified in the dotted purple oval.

8.2.2. Criterion of Shannon and Depew [20]

Shannon and Depew [20] conducted experiments using water in the laminar flow regime and concluded that free convection effects are significant when the product $Ra^{1/4}/Nu_{FC}$ is greater than 2. As they considered hydrodynamically fully developed flow, forced convection Nusselt numbers (Nu_{FC}) were obtained using the correlation of Siegel *et al*. [17]. Figure 8.2 compares the laminar experimental data (coloured according to the values of h_t/h_b) in the 4 mm and 11.5 mm test sections with the criterion of Shannon and Depew [20] (indicated by the vertical dotted line). The horizontal dotted line indicates the criterion proposed by Metais and Eckert [13] ($Nu/Nu_{FC} > 1.1$). Figure 8.2 indicates that although 68% of the data correctly fell into the mixed convection region, some mixed convection data fell incorrectly in the forced convection regions.

Figure 5.4 indicated that because the flow was simultaneously hydrodynamically and thermally developing in this study, the experimental data correlated better with the correlation of Shah and London [1] for simultaneously hydrodynamically and thermally developing flow, than with the correlation of Siegel *et al*. [17] for hydrodynamically fully developed flow. Similar to Fig. 8.2, Fig. 8.3 compares the experimental data of this study with the criterion of Shannon and Depew [20]; however, the forced convection Nusselt numbers (Nu_{FC}) were obtained using the correlation of Shah and London [1]. Figure 8.3 indicates that when the correct forced convection Nusselt number reference was used, only 64% of the data were correctly predicted to be dominated by mixed convection. Furthermore, the forced/mixed convection boundary was not predicted correctly. It should also be noted that this criterion is valid for laminar flow only.

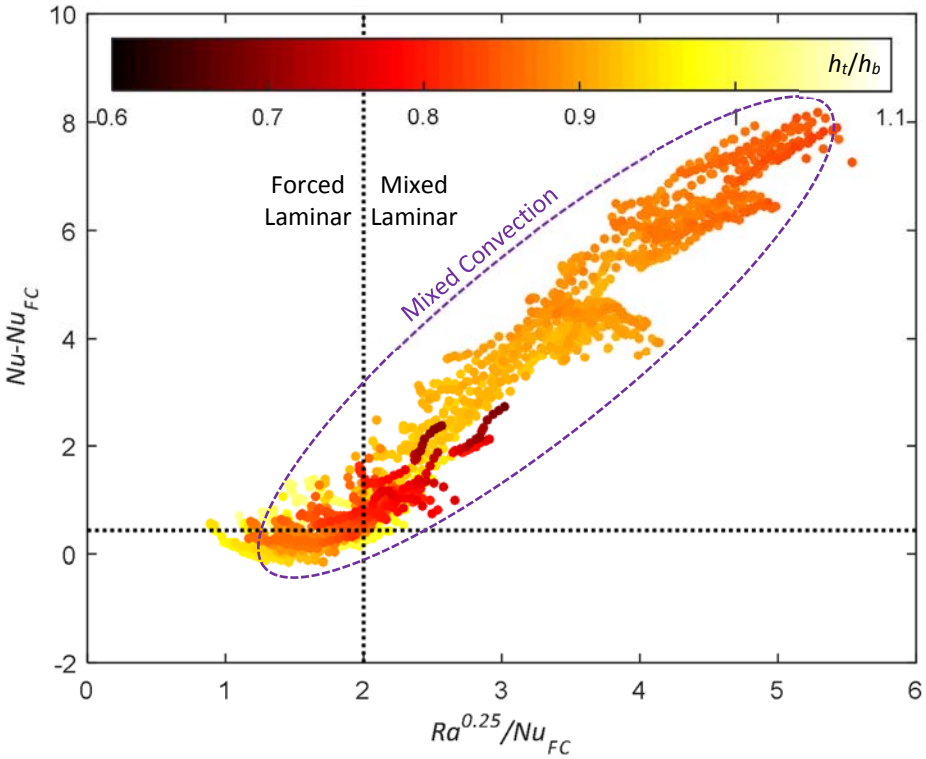

Fig. 8.2: Comparison of the laminar experimental data in the 4 mm and 11.5 mm test sections with the criteria of Shannon and Depew [20]. Nu_{FC} is the forced convection Nusselt number obtained using the correlation of Siegel *et al*. [17] for hydrodynamically fully developed flow. The horizontal colour bar is coloured according to h_t/h_b. The mixed convection data are identified in the dotted purple oval.

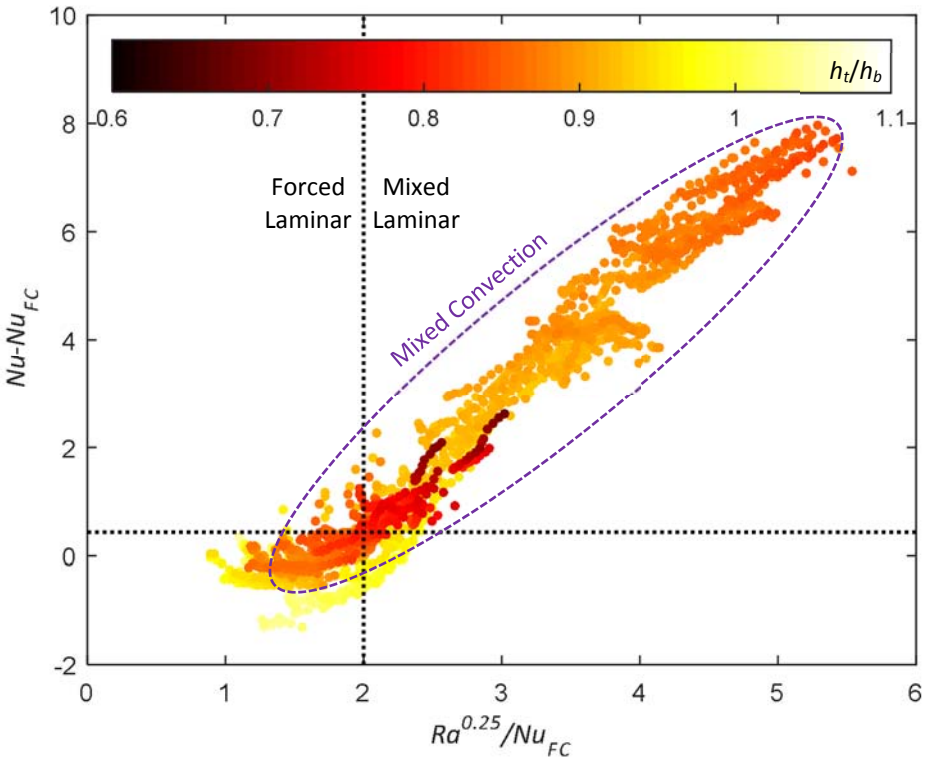

Fig. 8.3: Comparison of the laminar experimental data in the 4 mm and 11.5 mm test sections with the criteria of Shannon and Depew [20]. Nu_{FC} is the forced convection Nusselt number obtained using the correlation of Shah and London [1] for simultaneously hydrodynamically and thermally developing flow. The horizontal colour bar is coloured according to h_t/h_b. The mixed convection data are identified in the dotted purple oval.

8.2.3. Flow regime map of Metais and Eckert [13]

The experimental data of this study were plotted (and coloured according to h_t/h_b) on the flow regime map of Metais and Eckert [13] in Fig. 8.4. This flow regime map was developed for horizontal circular tubes with $10^{-2} < PrD/x < 1$, using a constant surface temperature boundary condition. Exact correlation was therefore not expected, because a constant heat flux boundary condition was used in this study and not a constant surface temperature boundary condition. Furthermore, as the values of PrD/x varied between 2.3×10^{-3} and 0.29 in this study, only 65% of the data fell into the specified ranges.

Because all the experimental data fell to the left of the forced/mixed convection boundary (indicated by the green line) in Fig. 8.4, it was expected to be forced convection data. However, using their criterion ($Nu/Nu_{FC} > 1.1$), 95% of the laminar data of this study were mixed convection data. Therefore, this map did not accurately predict the convection flow regime of the experimental data of this study.

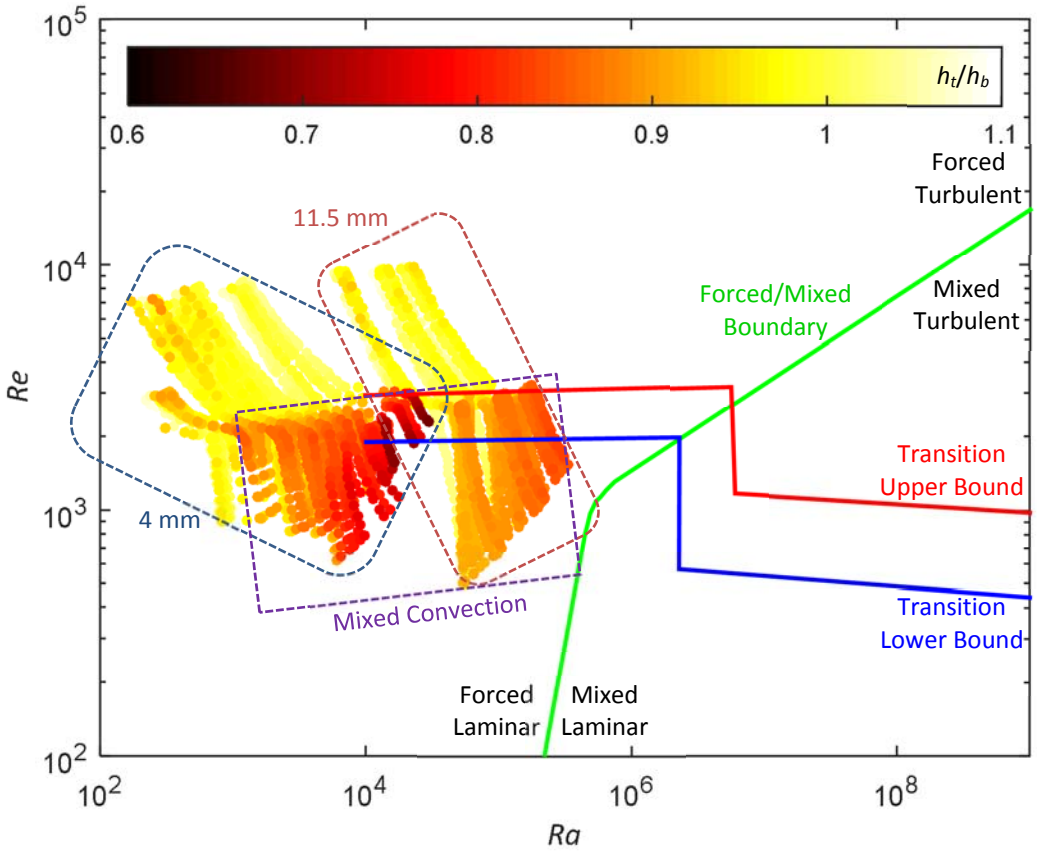

Fig. 8.4: Comparison of the flow regime map of Metais and Eckert [13] and the experimental data in the 4 mm and 11.5 mm test sections. The horizontal colour bar is coloured according to h_t/h_b. The mixed convection data are identified in the dotted purple rectangle.

8.2.4. Flow regime map of Tam *et al.* [15]

The experimental data of this study, as well as the experimental data of Strickland [106], were plotted (and coloured according to h_t/h_b) on the unified flow regime map of Tam *et al.* [15] in Fig. 8.5. This flow regime map was developed for horizontal tubes with a constant heat flux boundary condition. The boundary between forced and mixed convection was independent of the inlet geometry, while separate upper and lower boundaries of the transitional flow regime were included for the different

inlet geometries. For clarity purposes, only the transitional flow regime boundaries of the square-edged inlet were included in Fig. 8.5, because this inlet geometry was used in this study.

Figure 8.5 indicates that this flow regime map was primarily for Rayleigh numbers in the order of 10^5 to 10^8, which was high. This flow regime map was developed using the experimental data of Ghajar and Tam [16], who used the experimental data of Strickland [106] for the square-edged inlet. An analysis of the experiments conducted for the square-edged inlet [106] showed that distilled water was used for turbulent Reynolds numbers (3 639 < *Re* < 50 529 and 3.4 < *Pr* < 6.2), full concentration ethylene glycol was used in the laminar flow regime (281< *Re* < 3 328 and 96 < *Pr* < 158) and a mixture of 60% ethylene glycol (by mass fraction) and water was used for Reynolds numbers between 1 180 and 12 456. This covered the entire transitional flow regime as well as part of the laminar and quasi-turbulent flow regimes and the Prandtl number varied between 12.9 and 146. The mixed convection boundary in the laminar and transitional flow regimes was therefore developed using experimental data with Prandtl numbers between 12.9 and 158, while the Prandtl number in this study varied between three and seven.

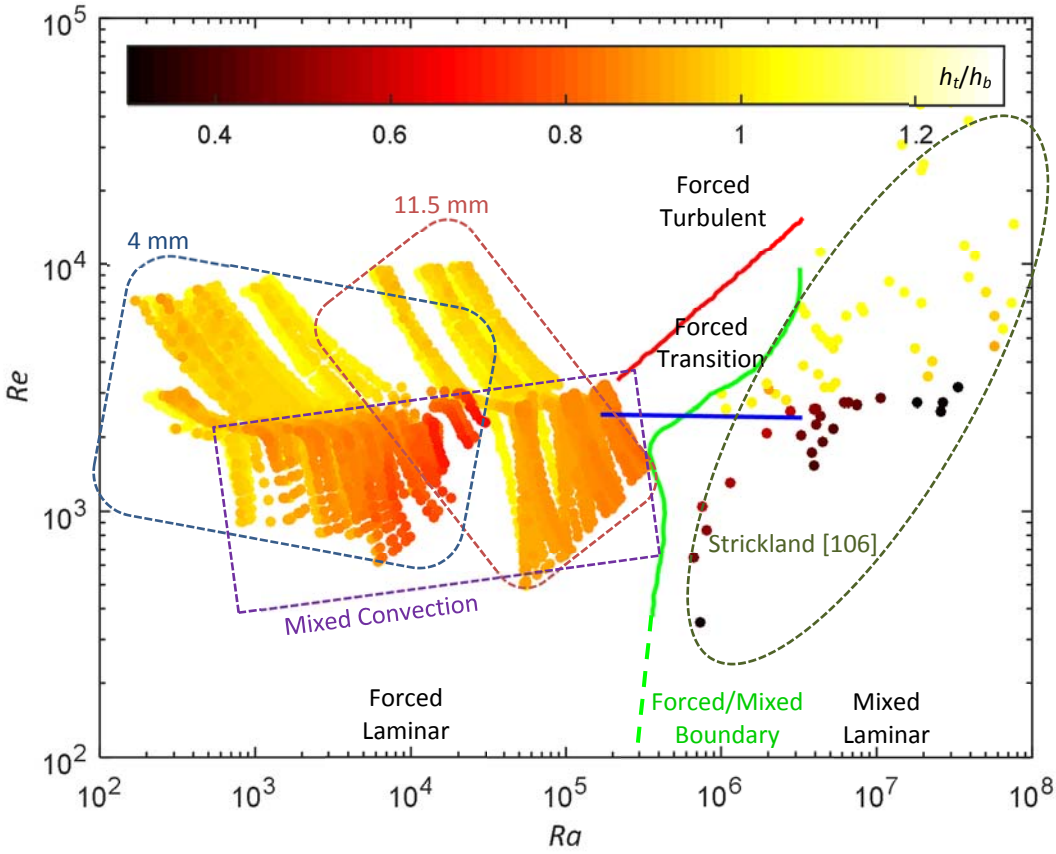

Fig. 8.5: Comparison of the flow regime map of Tam *et al*. [15] with the experimental data of the 4 mm and 11 mm test sections, as well as the experimental data of Strickland [106]. The horizontal colour bar is coloured according to h_t/h_b. The mixed convection data of this study are identified in the purple dotted rectangle.

As the Grashof number is a strong function of the inner tube diameter ($Gr \propto D^3$), free convection effects increased significantly with increasing tube diameter. The test section used by Strickland [106] had a relatively large inner diameter of 15.8 mm and the Grashof number varied between 1 000 and 2.5×10^5, which can be expected to be up to 62 times greater than when a 4 mm tube is used. Furthermore, the Grashof number is also a function of the surface-fluid temperature difference, which

was significantly higher for ethylene glycol than for water due to the low thermal conductivity and specific heat, as well as the high viscosity of ethylene glycol. This also led to significantly lower values of h_t/h_b compared with water. From the experimental data of Strickland [106] in Fig. 8.5, it follows that h_t/h_b decreased to as low as 0.3 in the laminar flow regime, while it did not decrease below 0.7 in the experimental data of this study.

The high Prandtl numbers of ethylene glycol, combined with the relatively high Grashof numbers (due to the large tube diameter and surface-fluid temperature difference), led to Rayleigh numbers between 6.7×10^5 and 7.4×10^7 in the study of Strickland [106]. This is of significant importance because the Rayleigh number was used on the *x*-axis of the flow regime map to distinguish between the forced and mixed convection data. Figure 8.5 indicates that this flow regime map could accurately predict the convection flow regime of the experimental results of Strickland [106]. However, it incorrectly predicted that all the data of this study should be in the forced convection flow regime (Rayleigh numbers in the order of 10^5 and less).

8.3. Proposed flow regime maps

Figures 8.1-8.5 indicate that there were no suitable criteria or flow regime map in literature to accurately predict the convection flow regime of the experimental data of this study. New, easy-to-use flow regime maps for developing and fully developed flow using different test fluids and tube diameters were therefore developed.

8.3.1. Flow regime map criteria

Metais and Eckert [13] defined the boundary between forced and mixed convection as the location where the heat transfer coefficients were 10% greater than the corresponding forced convection case ($Nu/Nu_{FC} > 1.1$), while Tam *et al*. [15] defined it as the location where h_t/h_b decreased below 0.8. To evaluate the suitability of the two criteria, the fully developed laminar Nusselt numbers were divided by 4.36 (fully developed forced convection laminar flow) and plotted against h_t/h_b in Fig. 8.6. The 10% increase in heat transfer coefficient criterion, $Nu/Nu_{FC} > 1.1$, which was used by Metais and Eckert [13], is indicated by the dotted black horizontal line. The dotted green vertical line indicates the heat transfer coefficient ratio criterion, $h_t/h_b < 0.8$, which was used by Tam *et al*. [15].

Figure 8.6 indicates that as the tube diameter was increased from 4 mm to 19 mm, using water as the test fluid, Nu/Nu_{FC} increased significantly from one to approximately four. However, there was only a slight decrease in h_t/h_b and it did not decrease below 0.8 in the 11.5 mm and 19 mm test sections. Although Nu/Nu_{FC} of the results of Strickland [106], who used pure ethylene glycol in a 15.8 mm test section, was approximately between the results of the 11.5 mm and 19 mm test sections, h_t/h_b was significantly lower. This was due to the increased circumferential and axial temperature differences, which were caused by the low thermal conductivity and specific heat, as well as the high viscosity of ethylene glycol.

As indicated by the Grashof number, free convection effects increased with increasing tube diameter, which explains why Nu/Nu_{FC} increased. As expected, the values of h_t/h_b in the 19 mm test section were less than in the 11.5 mm test section; however, the minimum h_t/h_b-value in the 4 mm test section was less than in the 11.5 mm and 19 mm test sections. There was thus no distinct trend between h_t/h_b and tube diameter. Figure 8.6 also indicates that h_t/h_b was very dependent on the fluid properties and differed significantly when the results of different test fluids, for example, water and ethylene glycol, were compared. Furthermore, it was found that the heat transfer coefficient ratio

criterion, $h_t/h_b < 0.8$, was too conservative for the experimental data of this study. At $h_t/h_b = 0.8$, Nu/Nu_{FC} in the 4 mm test section ranged between 1.16 and 1.4, which means that the Nusselt numbers were between 16% and 40% greater than the corresponding forced convection case. Furthermore, h_t/h_b in the 11.5 mm test section did not decrease below 0.83, while Nu/Nu_{FC} varied between 1.9 and 2.9. Figure 8.6 indicates that $h_t/h_b \leq 0.95$ was more appropriate for the results obtained using water, because this corresponds to the point where Nu/Nu_{FC} increased above 1.1 in the 4 mm test section. Although the flow regime maps of Metais and Eckert [13] and Tam *et al*. [15], as well as the Richardson number criterion, predicted the experimental data of this study as forced convection, free convection effects were present in 95% of the data in the laminar flow regime.

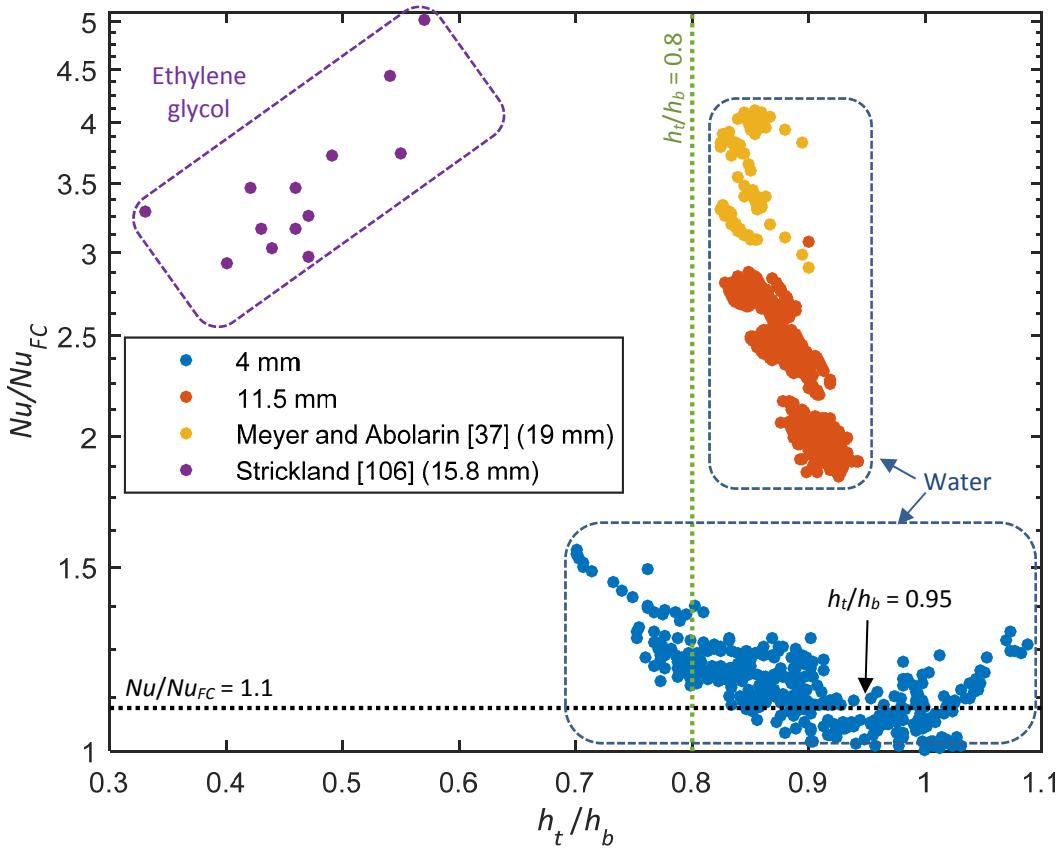

Fig. 8.6: Comparison of the experimental data of this study and literature [37, 106] in terms of Nu/Nu_{FC} (where $Nu_{FC} = 4.36$) against h_t/h_b at different heat fluxes for different tube diameters and test fluids.

Figure 8.6 also indicates that although h_t/h_b was an appropriate criterion for Strickland [106], the 10% increase in heat transfer coefficient criterion, $Nu/Nu_{FC} > 1.1$, was more suitable for this study, because it increased with increasing tube diameter and heat flux, which was known to increase free convection effects. It should be noted that h_t/h_b is a valuable tool to gain insight into the local free convection effects along the test section and how they are influenced by Reynolds number and heat flux, but it seems that care should be taken when different tube diameters and especially test fluids are compared, because it significantly affects the values of h_t/h_b.

8.3.2. Flow regime map for fully developed flow

In order to find a suitable parameter to be used on the *x*-axis of a graph with Reynolds number on the *y*-axis, the fully developed laminar experimental data of the 4 mm and 11.5 mm test sections were plotted as a function of Grashof number, Rayleigh number, Richardson number and Richardson-

Prandtl product in Fig. 8.7. The experimental data of Strickland [106] and Meyer and Abolarin [37] were also included to ensure that the flow regime map was valid for different tube diameters and test fluids. As this was for fully developed flow only, the theoretical fully developed forced convection Nusselt number of 4.36 was used for the forced convection Nusselt number reference, Nu_{FC}. The results were thus coloured according to $Nu/4.36$. The laminar data were identified using Eq. 6.3, while the fully developed data were identified using Eq. 5.3 (with $C_3 = 130$) and the data in the quasi-turbulent and turbulent flow regimes using Eq. 6.6.

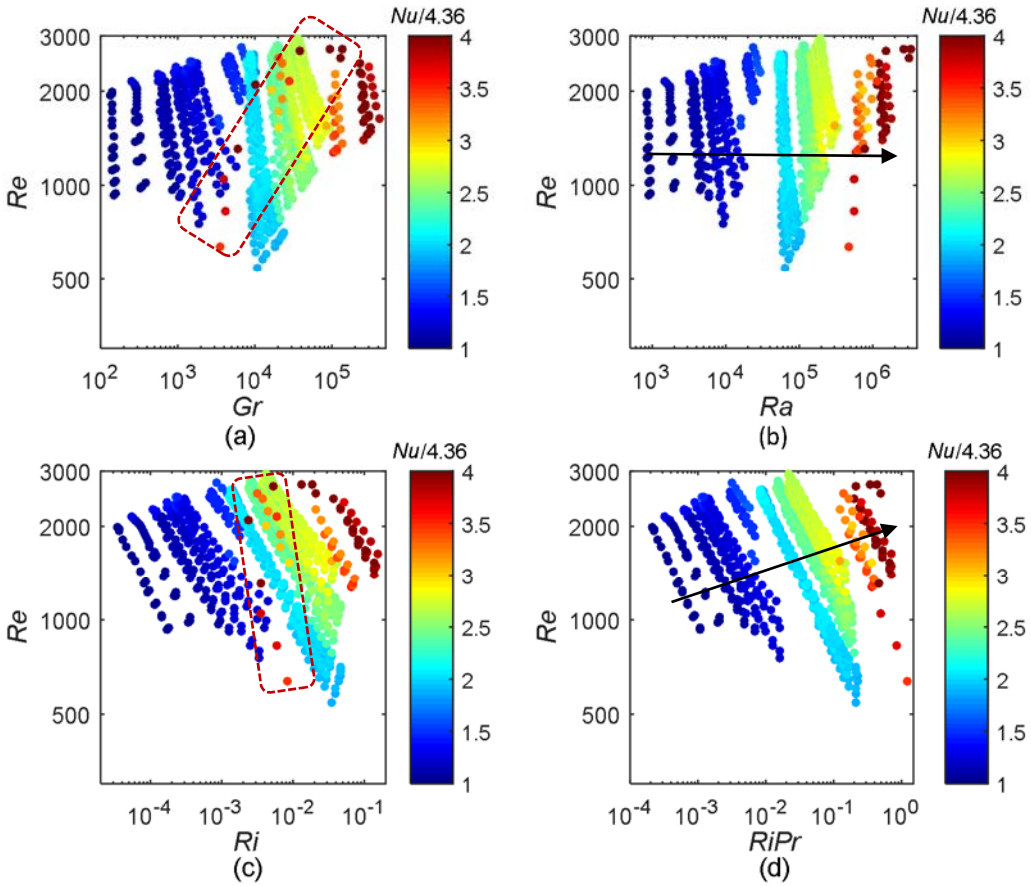

Fig. 8.7: Fully developed experimental data of this study and literature [37, 106] plotted as a function of (a) *Gr*, (b) *Ra*, (c) *Ri* and (d) *RiPr*. The data are coloured according to *Nu*/4.36.

The red dotted blocks in Fig. 8.7 indicate that not all the parameters were suitable to use on the *x*-axis, because 'red data' (mixed convection) fell into regions of 'blue data' (forced convection). Both the Rayleigh number (Fig. 8.7(b)) and Richardson-Prandtl product (Fig. 8.7(d)) would be suitable, because the colour changed gradually from dark blue (forced convection) to red (mixed convection) as free convection effects increased. As free convection effects increased horizontally (indicated by the black arrows) when the Rayleigh number (Fig. 8.7(b)) was used and not diagonally as when *RiPr* (Fig. 8.7(d)) was used, it was decided to use Rayleigh number on the *x*-axis of the flow regime maps for fully developed flow. Although the Rayleigh number was also used on the *x*-axis of the flow regime maps of Metais and Eckert [13] and Tam *et al*. [15], it was found that the predicted forced/mixed convection boundaries were not suitable for the experimental data of this study.

To develop a flow regime map that was valid for all flow regimes, Eqs. 6.3 and 6.6 were used to obtain the upper and lower boundaries of the transitional flow regime. However, Eq. 6.6 was multiplied by

1.2 to ensure a more conservative value for the end of the transitional flow regime. As free convection effects were negligible in the turbulent flow regime, Nu/Nu_{FC} was set to one for all Reynolds numbers greater than this boundary (Re_{qt}) and added to the laminar results of Fig. 8.7 in Fig. 8.8(a).

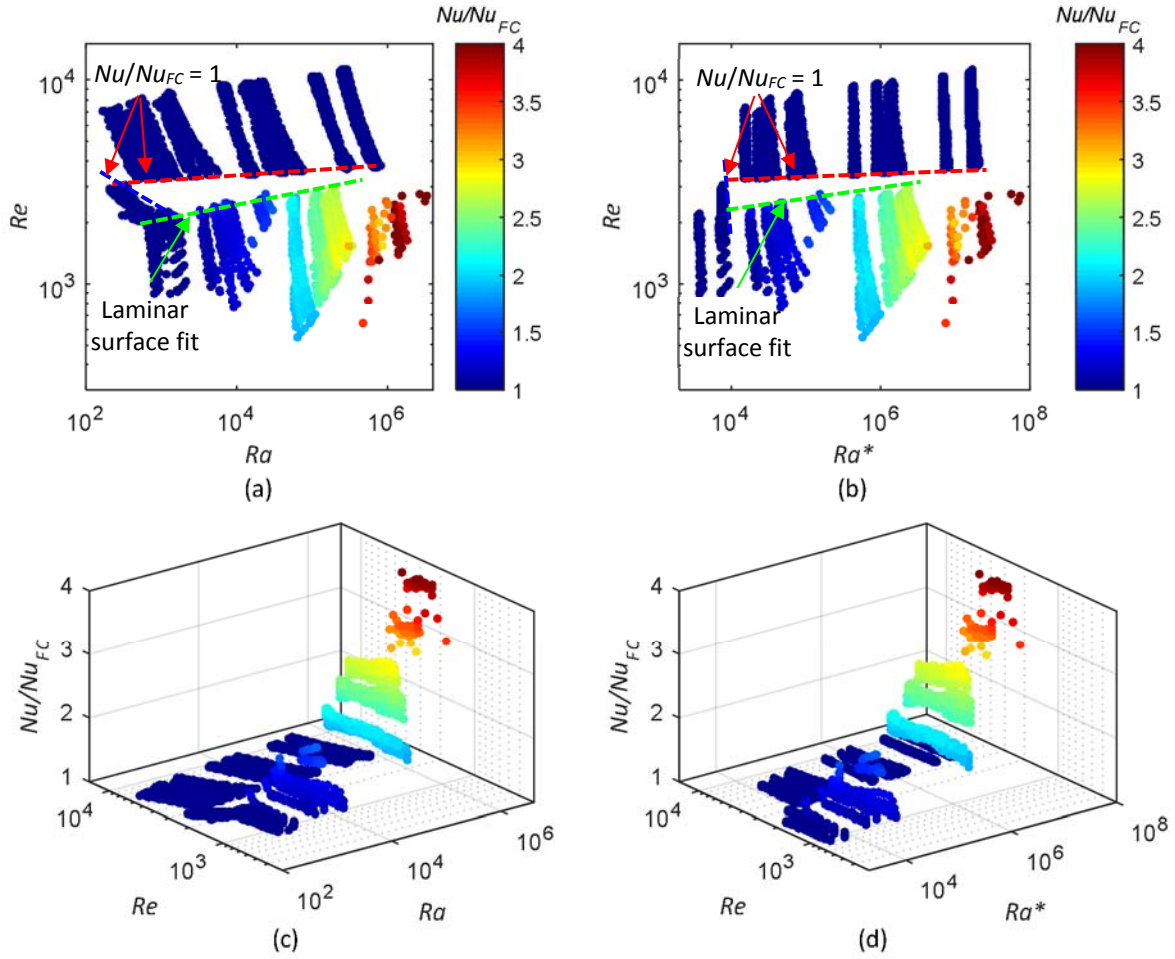

Fig. 8.8: Laminar, quasi-turbulent, turbulent and forced convection transitional data of this study and literature [37, 106] plotted as a function of *Re* against *Ra* and *Ra. The data are coloured according to Nu_{FC}, where Nu_{FC} = 4.36 for all data below the dotted green line. For all other data, Nu/Nu_{FC} = 1, where Nu_{FC} represents the corresponding forced convection Nusselt number from general literature.**

To the author's best knowledge, no experimental data in the transitional flow regime which specifically distinguished between forced and mixed convection were available at the time of writing. Therefore, the experimental data in the transitional flow regime (between the dotted green and red lines) at heat fluxes of 0.5 kW/m^2 and 1 kW/m^2 in the 4 mm test section were included, because it was known from Fig. 4.1 and Fig. 6.1 that forced convection conditions (Nu/Nu_{FC} = 1) existed at these two heat fluxes. These data were used as a guideline to obtain the forced/mixed convection boundary in the transitional flow regime. The experimental data in the transitional flow regime in the 11.5 mm test section, as well as at other heat fluxes in the 4 mm test section, were excluded because there was no available correlation which could be used as a forced convection reference to calculate Nu/Nu_{FC}. To obtain a flow regime map that was a function of heat flux and not temperature difference, the data were also plotted as a function of the modified Rayleigh number, *Ra**, in Fig. 8.8(b).

Figure 8.8(c) and (d) are three-dimensional plots of the results in Fig. 8.8(a) and (b). To generate the full flow regime map, a surface fit was done through the laminar heat transfer data using Ra and Ra^* respectively on the x-axis, Reynolds number on the y-axis and Nu/Nu_{FC} on the z-axis. Another surface fit was then done through the data on the Re_{cr}-line (using the laminar surface fit) and the Re_{qt}-line (using $Nu/Nu_{FC} = 1$) to fill the transitional flow regime gap in Fig. 8.8(a) and (b).

Figures 8.9 and 8.10 contain the flow regime maps for fully developed flow in terms of Ra and Ra^* respectively. In both flow regime maps, $Nu_{FC} = 4.36$ for all data below the Re_{cr}-line (Eqs. 8.1 and 8.5), while Nu_{FC} is the corresponding forced convection Nusselt number from general literature for all data above the Re_{qt}-line (Eqs. 8.2 and 8.6). In the transitional flow regime ($Re_{cr} < Re < Re_{qt}$, thus all the data between Eqs. 8.1 and 8.2, and Eqs. 8.5 and 8.6), correlations were not available for specifically forced convection and mixed convection data. Therefore, Nu/Nu_{FC} only gives an estimate (as it was not based on measurements) of whether free convection effects can be expected or not, and not the actual Nusselt number values.

Figures 8.9 and 8.10 indicate that $Ra < 4\,970$ and $Ra^* < 2.40\times10^4$ (indicated by the dotted yellow lines) can be used as Reynolds number independent criteria ($Nu/Nu_{FC} = 1.1$), which will ensure that the flow regime will most probably be forced convection. More conservative criteria ($Nu/Nu_{FC} = 1$) will be $Ra < 2\,520$ and $Ra^* < 1.02\times10^4$.

The equations of the transitional flow regime boundaries and the forced/mixed convection boundaries of the fully developed flow regime maps in Fig. 8.9 and Fig. 8.10 are summarised in Table 8.1. Proposed average Nusselt number correlations are also included in these flow regime maps (as well as the flow regime maps for developing flow in Section 8.3.3). However, it should be noted that these correlations were developed using water data only, while the flow regime maps are valid for high Prandtl number fluids as well. Therefore, other suitable Nusselt number correlations (for different test fluids) can be used in combination with the flow regime maps developed in this study.

Table 8.1: Equations of the transitional flow regime boundaries and forced/mixed convection boundaries, as well as the ranges of the flow regime maps as a function of *Ra* and *Ra.**

		Correlation	Eq.
Ra (Fig. 8.9)	Re_{cr}	$Re_{cr} = 1272\ Ra^{0.06834}$	8.1
	Re_{qt}	$Re_{qt} = 2846\ Ra^{0.02177}$	8.2
	$Re < Re_{cr}$	$FC/MC = 7.278\times10^{7}\ Ra^{-1.212} - 202.3$	8.3
	$Re_{cr} < Re < Re_{qt}$	$FC/MC = -1.123\times10^{5}\ Ra^{-0.4958} + 3950$	8.4
Ra^* (Fig. 8.10)	Re_{cr}	$Re_{cr} = 1730.9\ Ra^{*\,0.0549}$	8.5
	Re_{qt}	$Re_{qt} = 3056.4\ Ra^{*\,0.0217}$	8.6
	$Re < Re_{cr}$	$FC/MC = 2.73\times10^{9}\ Ra^{*\,-1.39} + 75.5$	8.7
	$Re_{cr} < Re < Re_{qt}$	$FC/MC = -3.338\times10^{4}\ Ra^{*\,-0.3112} + 3839$	8.8
Ranges		$546 \le Re \le 11\,247$, $3 \le Pr \le 139.4$, $26 \le Gr \le 4.2\times10^5$, $561 \le Gr^* \le 7\times10^6$	

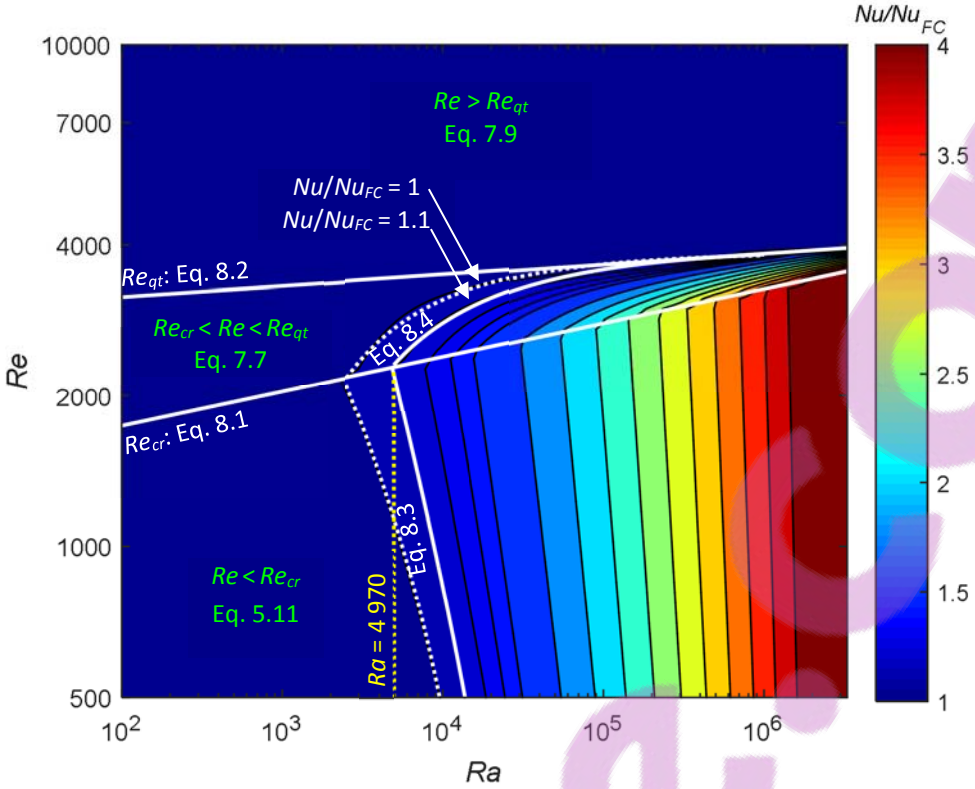

Fig. 8.9: Flow regime map for fully developed flow as a function of *Re* and *Ra*. Nu_{FC} = 4.36 for all data below Eq. 8.1, while Nu_{FC} is the corresponding forced convection Nusselt number from general literature for all data above Eq. 8.2. In the transitional flow regime ($Re_{cr} < Re < Re_{qt}$), Nu/Nu_{FC} only gives an estimate of whether free convection effects can be expected or not, and not the actual Nusselt number values.

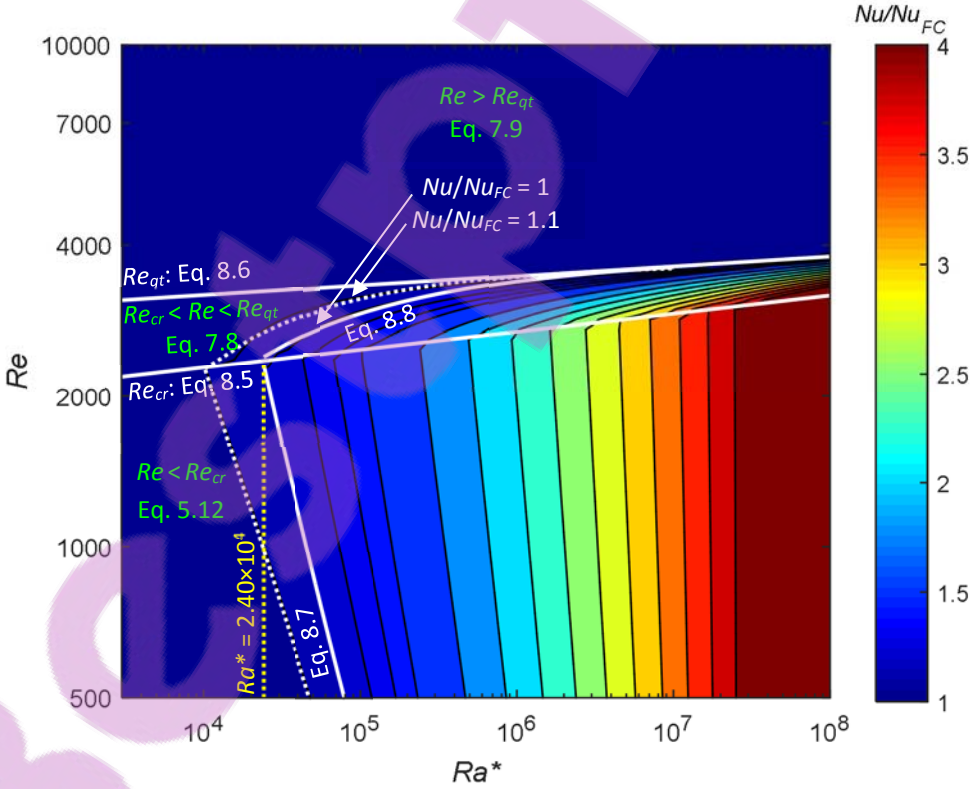

Fig. 8.10: Flow regime map for fully developed flow as a function of *Re* and *Ra. Nu_{FC} = 4.36 for all data below Eq. 8.5, while Nu_{FC} is the corresponding forced convection Nusselt number for all data above Eq. 8.6. In the transitional flow regime ($Re_{cr} < Re < Re_{qt}$), Nu/Nu_{FC} only gives an estimate of whether free convection effects can be expected or not, and not the actual Nusselt number values.**

The performance of the flow regime maps in Fig. 8.9 and Fig. 8.10 in the laminar flow regime was determined by comparing $Nu/4.36$ of the experimental data with the Nu/Nu_{FC} values in the flow regime maps, and the results are summarised in Table 8.2. This table indicates that both flow regime maps could predict approximately all the experimental data of this study, as well as from literature [37, 106], within 10%. It should therefore be possible to use these flow regime maps as reliable tools to predict the convection flow regime of fully developed flow in a wide range of tube diameters and Prandtl numbers.

Table 8.2: Ranges and performance of the flow regime maps in Fig. 8.9 and Fig. 8.10.

	This study only				This study and data from literature [37, 106]			
Range	$546 \leq Re \leq 2\,936$, $3 \leq Pr \leq 6.5$, $26 \leq Gr \leq 9.4\times10^4$, $610 \leq Gr^* \leq 1.2\times10^6$				$546 \leq Re \leq 2\,936$, $3 \leq Pr \leq 139.4$, $26 \leq Gr \leq 4.2\times10^5$, $561 \leq Gr^* \leq 7\times10^6$			
	n	±10% [%]	±20% [%]	Ave %	*n*	±10% [%]	±20% [%]	Ave %
Ra: Fig. 8.9	917	97	100	3.4	985	95	99.7	3.6
*Ra**: Fig. 8.10	916	99	100	2.8	984	98	100	3.0

8.3.3. Flow regime map for developing flow

The flow regime maps in literature were developed for fully developed flow. Therefore, the experimental data of both the mixed convection developing (MCD) and fully developed (FD) regions, as defined in Chapter 5, were plotted as a function of Grashof number, Rayleigh number, Richardson number and Richardson-Prandtl product in Fig. 8.11 to develop a flow regime map for developing flow. To ensure that the flow regime map was also applicable to high Prandtl number fluids and larger tube diameters, the experimental data of Strickland [106] and Meyer and Abolarin [37] were included. The laminar data were identified using Eq. 6.3, while the MCD data were identified using Eq. 5.1 (with $C_1 = 2.4$). The results were coloured according to Nu/Nu_{SL}, where Nu_{SL} was obtained using the correlation of Shah and London [1] (Eq. 2.17), which was valid for simultaneously hydrodynamically and thermally developing laminar flow using a constant heat flux boundary condition.

In general, it was found that the four parameters (*Gr*, *Ra*, *Ri* and *RiPr*) considered in Fig. 8.11 were not suitable to estimate the convection flow regime of developing flow. As indicated by the red dotted blocks, the colours in the graphs did not change gradually from dark blue to red as free convection effects increased, and 'blue data' fell into the 'red data' regions. Although the Rayleigh number was suitable for fully developed flow (Fig. 8.7), another parameter had to be added to the *x*-axis to account for developing flow.

The Grashof number, Rayleigh number, Richardson number and Richardson-Prandtl product in Fig. 8.11 were multiplied by (x/D) in Fig. 8.12 to account for developing flow. Figure 8.12 indicates that the parameter $Ri(x/D)$ (Fig. 8.12(c)) could produce the best, relatively smooth, contour, which changed from dark blue to red as free convection effects increased, for both water and ethylene glycol data. The red dotted blocks indicate the data that fell into the incorrect regions.

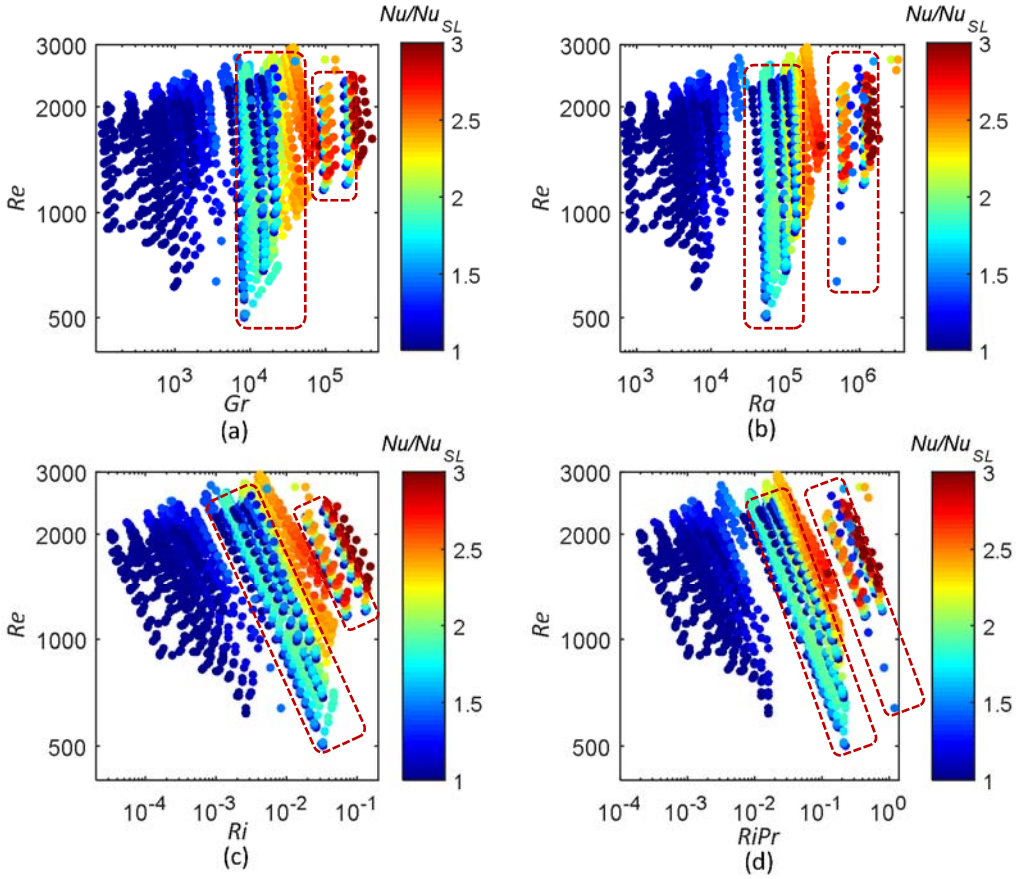

Fig. 8.11: MCD and FD experimental data of this study and literature [37, 106], plotted as a function of (a) *Gr*, (b) *Ra*, (c) *Ri* and (d) *RiPr*. The data are coloured according to Nu/Nu_{SL}.

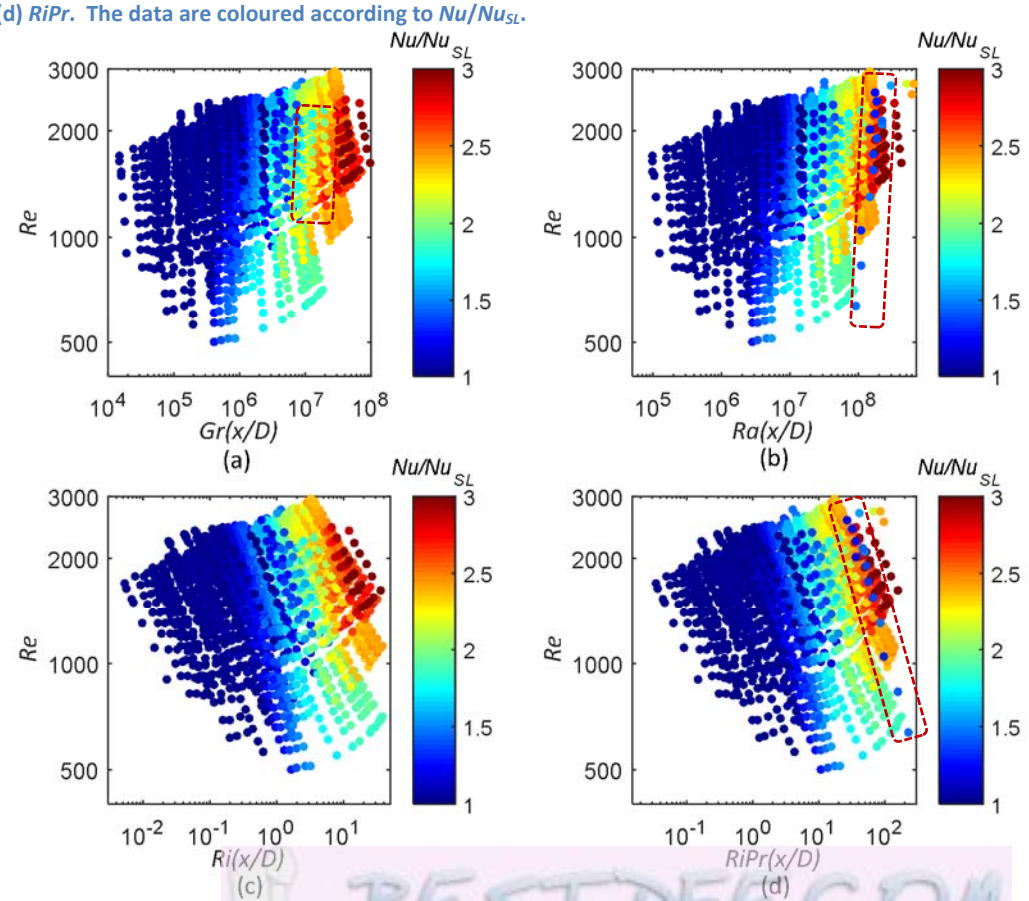

Fig. 8.12: MCD and FD experimental data of this study and literature [37, 106], plotted as a function of (a) *Gr*(*x*/*D*), (b) *Ra*(*x*/*D*), (c) *Ri*(*x*/*D*) and (d) *RiPr*(*x*/*D*). The data are coloured according to Nu/Nu_{SL}.

The Graetz number can also be used to account for axial position when the flow is still developing. Therefore, the Grashof number, Rayleigh number, Richardson number and Richardson-Prandtl product in Fig. 8.11 were divided by the Graetz number and the results are compared in Fig. 8.13. Although all the parameters might give reasonable results, best results were obtained using the parameters *Ra*/*Gz* (Fig. 8.13(b)) and *RiPr*/*Gz* (Fig. 8.13(d)). Approximately smooth contours (which changed from dark blue to red as the free convection effects increased) were obtained for both water and ethylene glycol data. It was decided to use *Ra*/*Gz* on the *x*-axis of the flow regime maps for developing flow, because free convection effects increased approximately horizontally (indicated by the black arrows) for *Ra*/*Gz* (Fig. 8.13(b)), while it increased diagonally for *RiPr*/*Gz* (Fig. 8.13(d)). The red dotted blocks indicate the data that fell into the incorrect regions.

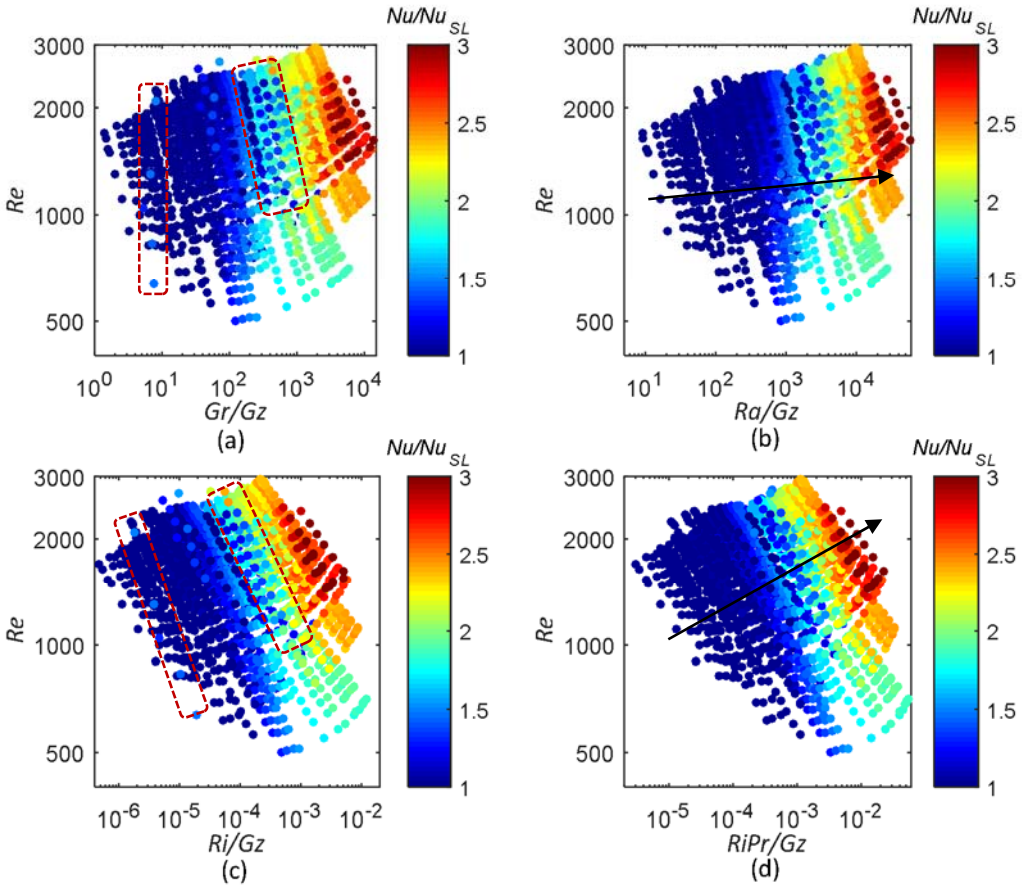

Fig. 8.13: MCD and FD experimental data of this study and literature [37, 106], plotted as a function of (a) *Gr*/*Gz*, (b) *Ra*/*Gz*, (c) *Ri*/*Gz* and (d) *RiPr*/*Gz*. The data are coloured according to Nu/Nu_{SL}.

Figures 8.12 and 8.13 indicate that both *Ri*(*x*/*D*) (Fig. 8.12(c)) and *Ra*/*Gz* (Fig. 8.13(b)) were suitable parameters to be used for the flow regime map. The same procedure as in Fig. 8.8 was followed to obtain the flow regime maps in terms of *Ri*(*x*/*D*) (Fig. 8.14) and *Ra*/*Gz* (Fig. 8.15). In both flow regime maps, $Nu_{FC} = Nu_{SL}$ for all data below the Re_{cr}-lines (Eqs. 8.9 and 8.13), while Nu_{FC} is the corresponding forced convection Nusselt number from general literature for all data above the Re_{qt}-lines (Eqs. 8.10 and 8.14). It should be noted that the values of Nu_{FC} given in the rest of this chapter are not only a function of Reynolds number and Prandtl number, but most importantly, they are a function of axial position, as the flow is developing. In the transitional flow regime ($Re_{cr} < Re < Re_{qt}$), Nu/Nu_{FC} only gives an estimate of whether free convection effects can be expected or not, and not the actual Nusselt number values.

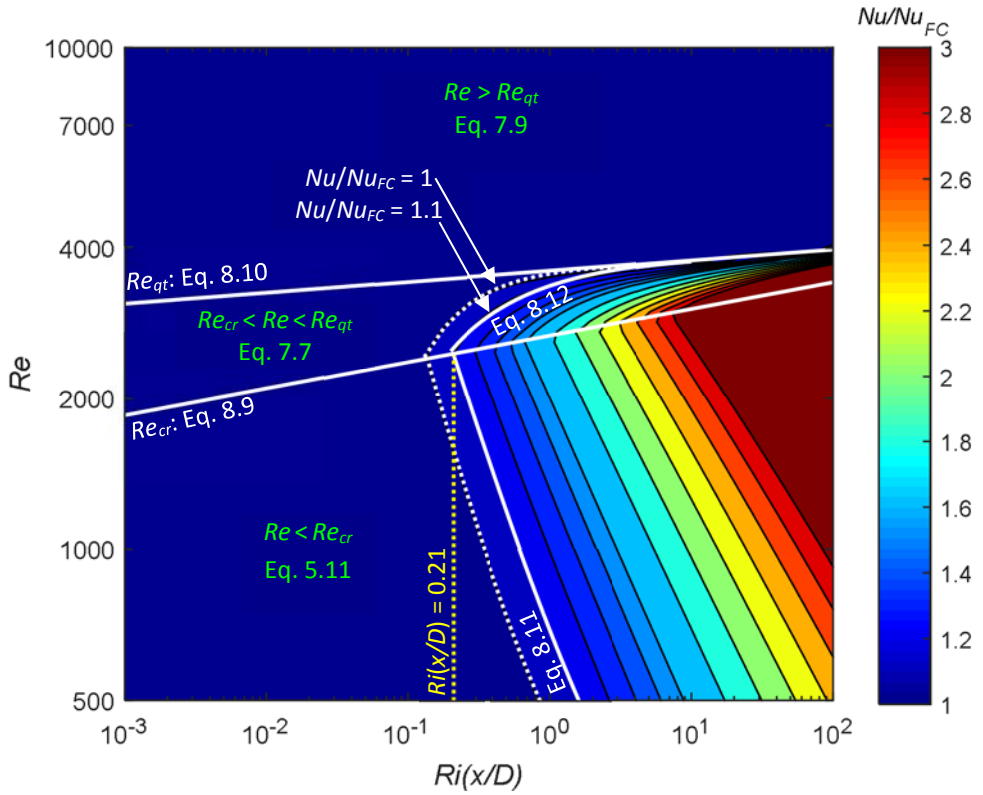

Fig. 8.14: Flow regime map for developing and fully developed flow as a function of *Re* and *Ri*(*x*/*D*). $Nu_{FC} = Nu_{SL}$ for all data below Eq. 8.9, while Nu_{FC} is the corresponding forced convection Nusselt number from general literature for all data above Eq. 8.10. In the transitional flow regime ($Re_{cr} < Re < Re_{qt}$), Nu/Nu_{FC} only gives an estimate of whether free convection effects can be expected or not, and not the actual Nusselt number values.

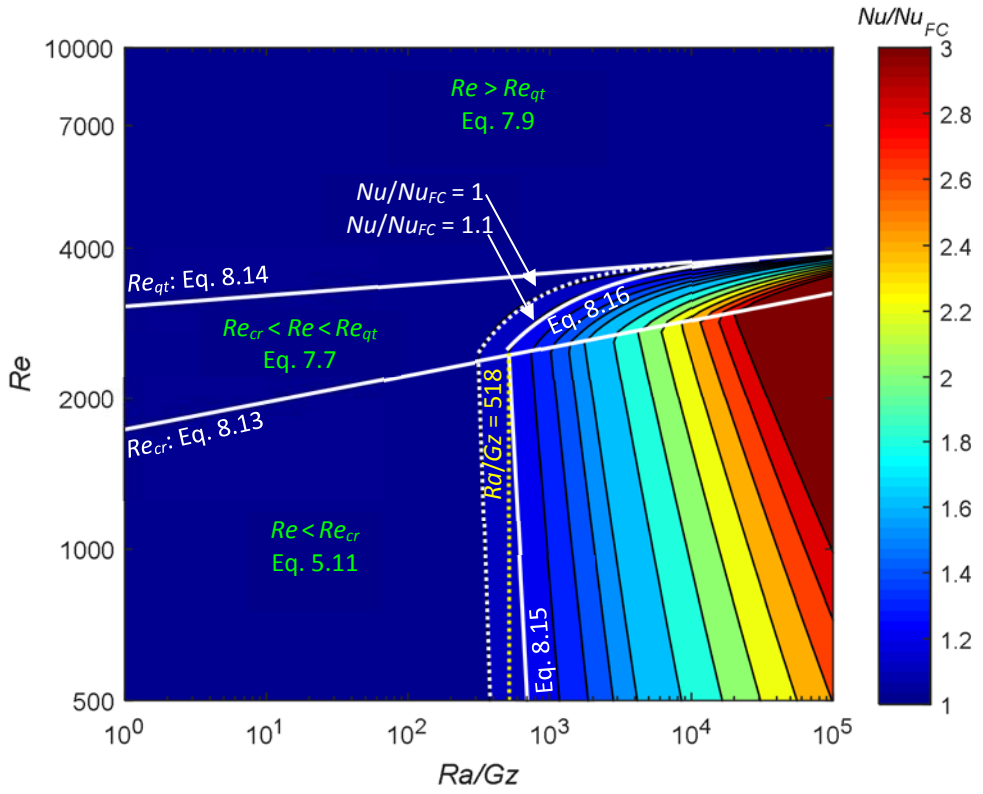

Fig. 8.15: Flow regime map for developing and fully developed flow as a function of *Re* and *Ra*/*Gz*. $Nu_{FC} = Nu_{SL}$ for all data below Eq. 8.13, while Nu_{FC} is the corresponding forced convection Nusselt number from general literature for all data above Eq. 8.14. In the transitional flow regime ($Re_{cr} < Re < Re_{qt}$), Nu/Nu_{FC} only gives an estimate of whether free convection effects can be expected or not, and not the actual Nusselt number values.

Figures 8.14 and 8.15 indicate that $Ri(x/D) < 0.21$ and $Ra/Gz < 518$ (indicated by the dotted yellow lines) can be used as Reynolds number independent criteria ($Nu/Nu_{FC} = 1.1$), which will ensure that the flow will most probably be forced convection. More conservative criteria ($Nu/Nu_{FC} = 1$) will be $Ri(x/D) < 0.14$ and $Ra/Gz < 318$. The equations of the transitional flow regime boundaries and the forced/mixed convection boundaries are summarised in Table 8.3, while the performance of the flow regime maps is summarised in Table 8.5.

Table 8.3: Equations of the transitional flow regime boundaries and forced/mixed convection boundaries, as well as the ranges of the flow regime maps as a function of *Ri*(*x*/*D*) and *Ra*/*Gz*.

		Correlation	Eq.
Ri(*x*/*D*) (Fig. 8.14)	Re_{cr}	$Re_{cr} = 2675.3\left(Ri(x/D)\right)^{0.0532}$	8.9
	Re_{qt}	$Re_{qt} = 3595.1\left(Ri(x/D)\right)^{0.0216}$	8.10
	$Re < Re_{cr}$	$FC/MC = 546.3\left(Ri(x/D)\right)^{-0.9212} + 145.7$	8.11
	$Re_{cr} < Re < Re_{qt}$	$FC/MC = -540.8\left(Ri(x/D)\right)^{-0.5939} + 3896$	8.12
Ra/*Gz* (Fig. 8.15)	Re_{cr}	$Re_{cr} = 1730.9(Ra/Gz)^{0.0549}$	8.13
	Re_{qt}	$Re_{qt} = 3056.4(Ra/Gz)^{0.0217}$	8.14
	$Re < Re_{cr}$	$FC/MC = 6.591 \times 10^{16}(Ra/Gz)^{-4.944} - 50.47$	8.15
	$Re_{cr} < Re < Re_{qt}$	$FC/MC = -3.582 \times 10^{4}(Ra/Gz)^{-0.512} + 3984$	8.16
Ranges		$502 \le Re \le 11\,247$, $3 \le Pr \le 139.4$, $2.7 \le Gz \le 5.5\times10^{3}$, $26 \le Gr \le 4.2\times10^{5}$, $561 \le Gr^* \le 7\times10^{6}$	

The same procedure was used to obtain flow regime maps in terms of the modified Grashof, Rayleigh and Richardson numbers, because the temperature difference (required to calculate the Grashof number for constant heat flux problems) is not always available (except when the heat transfer coefficients are known), while the heat flux usually is. Figures 8.16 and 8.17 contain the flow regime maps in terms of $Ri^*(x/D)$ and Ra^*/Gz respectively. In both flow regime maps, $Nu_{FC} = Nu_{SL}$ for all data below the Re_{cr}-line (Eqs. 8.17 and 8.21), while Nu_{FC} is the corresponding forced convection Nusselt number from general literature for all data above the Re_{qt}-line (Eqs. 8.18 and 8.22). In the transitional flow regime ($Re_{cr} < Re < Re_{qt}$), Nu/Nu_{FC} only gives an estimate of whether free convection effects can be expected or not, and not the actual Nusselt numbers. Figures 8.16 and 8.17 indicate that $Ri^*(x/D) < 1.64$ and $Ra^*/Gz < 4\,038$ (indicated by the dotted yellow lines) can be used as Reynolds number independent criteria ($Nu/Nu_{FC} = 1.1$), which will ensure that the flow regime will most probably be forced convection. More conservative criteria ($Nu/Nu_{FC} = 1$) will be $Ri^*(x/D) < 1$ and $Ra^*/Gz < 2\,364$.

Table 8.4 summarises the equations of the transitional flow regime boundaries and forced/mixed convection boundaries, and the performance of these flow regime maps is summarised in Table 8.5. The performance was determined by comparing Nu/Nu_{SL} of the experimental data and the Nu/Nu_{FC} values in the flow regime maps in Fig. 8.14 to Fig. 8.17. Table 8.5 indicates that all four flow regime maps could predict approximately 80% of the data within 10%, and almost all the data within 20%. The two flow regime maps (Fig. 8.16 and Fig. 8.17) which were a function of heat flux (Gr^*) performed slightly better than the flow regime maps (Fig. 8.14 and Fig. 8.15) which were a function of temperature difference (Gr).

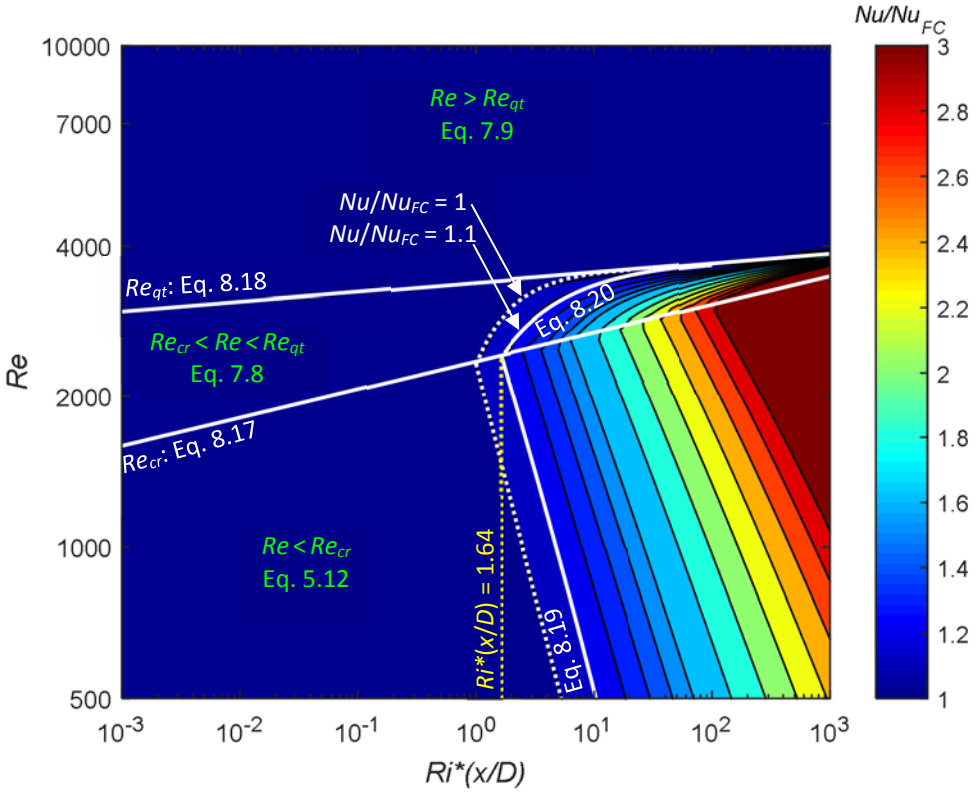

Fig. 8.16: Flow regime map for developing and fully developed flow as a function of *Re* and *Ri*(x/D)*. $Nu_{FC} = Nu_{SL}$ for all data below Eq. 8.17, while Nu_{FC} is the corresponding forced convection Nusselt number from general literature for all data above Eq. 8.18. In the transitional flow regime ($Re_{cr} < Re < Re_{qt}$), Nu/Nu_{FC} only gives an indication of whether free convection effects can be expected or not, and not the actual Nusselt number values.

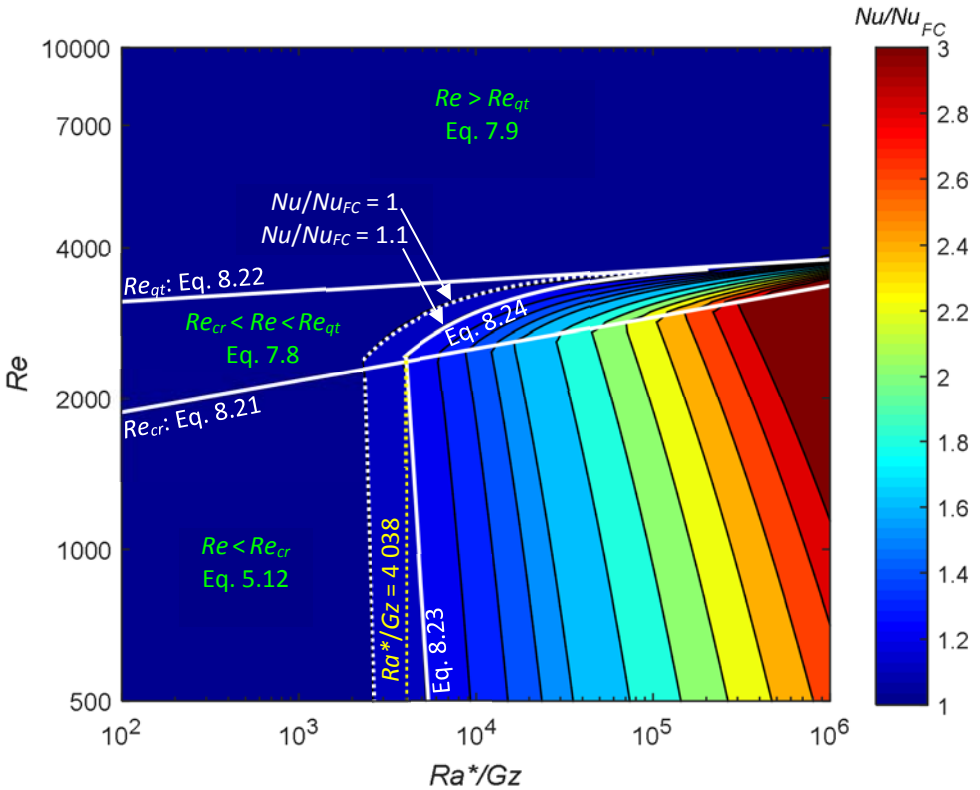

Fig. 8.17: Flow regime map for developing and fully developed flow as a function of *Re* and *Ra*/Gz*. $Nu_{FC} = Nu_{SL}$ for all data below Eq. 8.21, while Nu_{FC} is the corresponding forced convection Nusselt number from general literature for all data above Eq. 8.22. In the transitional flow regime ($Re_{cr} < Re < Re_{qt}$), Nu/Nu_{FC} only gives an indication of whether free convection effects can be expected or not, and not the actual Nusselt number values.

Table 8.4: Equations of the transitional flow regime boundaries and forced/mixed convection boundaries, as well as the ranges of the flow regime maps as a function of *Ri*(x/D)* and *Ra*/Gz*.

		Correlation	Eq.
Ri(x/D)* (Fig. 8.16)	Re_{cr}	$Re_{cr} = 2355.5\left(Ri^*(x/D)\right)^{0.0567}$	8.17
	Re_{qt}	$Re_{qt} = 3377.3\left(Ri^*(x/D)\right)^{0.0195}$	8.18
	$Re < Re_{cr}$	$FC/MC = 3724\left(Ri^*(x/D)\right)^{-0.7711} + 115.4$	8.19
	$Re_{cr} < Re < Re_{qt}$	$FC/MC = -1868\left(Ri^*(x/D)\right)^{-0.6159} + 3772$	8.20
Ra/Gz* (Fig. 8.17)	Re_{cr}	$Re_{cr} = 1401.3(Ra^*/Gz)^{0.0635}$	8.21
	Re_{qt}	$Re_{qt} = 2820.8(Ra^*/Gz)^{0.0215}$	8.22
	$Re < Re_{cr}$	$FC/MC = 5.8 \times 10^{22}(Ra^*/Gz)^{-5.373}$	8.23
	$Re_{cr} < Re < Re_{qt}$	$FC/MC = -1.224 \times 10^{4}(Ra^*/Gz)^{-0.543} + 3787$	8.24
Ranges		502 ≤ *Re* ≤ 11 247, 3 ≤ *Pr* ≤ 139.4, 2.7 ≤ *Gz* ≤ 5.5×10^3, 26 ≤ *Gr* ≤ 4.2×10^5, 561 ≤ *Gr** ≤ 7×10^6	

Table 8.5: Ranges and performance of the flow regime maps in Fig. 8.14 to Fig. 8.17 using developing and fully developed data.

	This study only				This study and data from literature [37, 106]			
Range	502 ≤ *Re* ≤ 2 936, 3 ≤ *Pr* ≤ 6.9, 2.7 ≤ *Gz* ≤ 689, 106 ≤ *Gr* ≤ 9.4×10^4, 569 ≤ *Gr** ≤ 1.2×10^6				502 ≤ *Re* ≤ 2 936, 3 ≤ *Pr* ≤ 139.5, 2.7 ≤ *Gz* ≤ 1 241, 106 ≤ *Gr* ≤ 4.2×10^5, 569 ≤ *Gr** ≤ 7.0×10^6			
	n	±10% [%]	±20% [%]	Ave %	*n*	±10% [%]	±20% [%]	Ave %
Ri(x/D): Fig. 8.14	1 776	77	97	6.7	2 174	79	95	6.6
Ra/Gz: Fig. 8.15	1 776	78	97	6.7	2 152	80	95	6.6
Ri(x/D)*: Fig. 8.16	1 777	82	99	5.7	2 159	84	96	5.9
Ra/Gz*: Fig. 8.17	1 747	83	99	5.7	2 085	84	96	5.9

To determine the validity/accuracy of the flow regime maps for Prandtl numbers less than one, the performance of the flow regime maps was determined using experimental data obtained using air as the test fluid. Apart from the experimental data of McComas and Eckert [19], it was found that limited experimental data obtained using air, which gives the Reynolds number, Nusselt number, Grashof number and axial position of each data point, were available in literature. The performance of the flow regime maps was determined using 70 experimental data points (220 < *Re* < 743, *Pr* ≈ 0.7, 0.13 < *Gr* < 1 000), and the flow regime maps could predict 86% of the data within 10% and all the data within 20%.

The flow regime maps in Fig. 8.14 to Fig. 8.17 were generated using developing flow and fully developed flow data. The validity/accuracy of these flow regime maps in the laminar flow regime using fully developed data only was determined by comparing Nu/Nu_{SL} of the experimental data and the Nu/Nu_{FC} values in the four flow regime maps, and the results are summarised in Table 8.6. Because all four flow regime maps could predict almost all the data within 20%, it is confirmed that these flow regime maps are valid for both developing and fully developed flow. It can therefore be concluded

that these four flow regime maps can be used as reliable tools to predict the convection flow regime for developing and fully developed flow in a wide range of tube diameters and Prandtl numbers.

Table 8.6: Performance of the flow regime maps in Fig. 8.14 to Fig. 8.17 using fully developed data only.

	This study only				This study and data from literature [37, 106]			
Range	546 ≤ Re ≤ 2 936, 3 ≤ Pr ≤ 6.5, 2.7 ≤ Gz ≤ 45, 137 ≤ Gr ≤ 9.4×10^4, 610 ≤ Gr^* ≤ 1.2×10^6				546 ≤ Re ≤ 2 936, 3 ≤ Pr ≤ 139.5, 2.7 ≤ Gz ≤ 1 241, 137 ≤ Gr ≤ 4.2×10^5, 610 ≤ Gr^* ≤ 7.0×10^6			
	n	±10% [%]	±20% [%]	Ave %	n	±10% [%]	±20% [%]	Ave %
$Ri(x/D)$: Fig. 8.14	917	73	95	7.1	985	72	94	7.4
Ra/Gz: Fig. 8.15	917	74	95	7.1	985	72	94	7.3
$Ri^*(x/D)$: Fig. 8.16	917	85	99	5.3	985	83	98	5.7
Ra^*/Gz: Fig. 8.17	917	85	99	5.3	985	84	98	5.6

8.4. Conclusions

A flow regime map is a valuable tool which can be used to determine whether free convection effects can be neglected (forced convection dominates) or whether it is significant (mixed convection dominates) for a given boundary condition and values of Re, Pr, Gr and x/D. It was found that although the existing constant heat flux boundary condition flow regime maps were accurate for high Prandtl number fluids, the flow regime maps became inaccurate once the Prandtl numbers and tube diameters were decreased, for example, when water was used in small diameter tubes.

The purpose of this chapter was to evaluate the existing flow regime maps using the experimental data of this study, which were obtained using water as the test fluid in test sections with inner diameters of 4 mm and 11.5 mm, as well as to develop new flow regime maps that could be used for both high and low Prandtl number fluids in a wide range of tube diameters. A total of six flow regime maps were developed and these flow regime maps are unique for four reasons. Firstly, they contained contour lines that showed the Nusselt number enhancements due to the free convection effects. Secondly, they were valid for a wide range of tube diameters and Prandtl numbers. Thirdly, the flow regime maps were developed as a function of temperature difference (Grashof number) and heat flux (modified Grashof number). Finally, four of the six flow regime maps were not only valid for fully developed flow, but also for developing flow. The two flow regime maps that were developed for fully developed flow could predict almost all the data within 10%. The four flow regime maps that were valid for developing and fully developed flow could predict approximately 80% of the data within 10% and almost all the data within 20%. It can be concluded that these flow regime maps can be used as reliable tools to predict the convection flow regime for developing and fully developed flow for a wide range of tube diameters and Prandtl numbers.

9. Summary, Conclusions and Recommendations

9.1. Summary

Heat exchangers have a wide range of applications and are commonly found in the process, petrochemical, petroleum, transport, sewage treatment, manufacturing and heating, ventilation and air-conditioning industries. Furthermore, heat exchangers are indispensable components in the cycles of fossil fuel, nuclear and solar power plants. Because the efficiency of generating energy and using energy directly depends on the effectiveness of heat exchangers, it is critical that sufficient design information is available so that heat exchanger effectiveness can be optimised. In the design process, a selection can be made between a flow regime that is laminar (low heat transfer coefficients and pressure drops) or turbulent (high heat transfer coefficients and pressure drops). Designers are usually advised to avoid the transitional flow regime because the flow is believed to be unstable and chaotic, and little design information is available. However, changes in operating conditions, design constraints, additional equipment, scaling and corrosion can cause heat exchangers to operate in or close to the transitional flow regime.

Although pressure drop and heat transfer are usually investigated independently, there exists a direct relationship that is often overlooked. Although this relationship has been extensively investigated for laminar and turbulent flow, no correlations were developed to quantitatively describe this relationship in the transitional flow regime. It is important to investigate this relationship, especially in the transitional flow regime, because there is a fundamental gap in the literature on this subject field. This is the first step before similar relationships can be developed for more complex geometries. Specifically, for complex geometries, it will be much easier for product developers to obtain either the heat transfer coefficients or the pressure drops, because this will save time and money. It is desirable to know this relationship because it will make it possible to calculate either the heat transfer coefficients or the friction factors when the other variable is available. Furthermore, it will also give additional insight into the trade-off between high heat transfer coefficients and low pressure drops during the design process.

Flow regimes in tubes have been extensively investigated from as early as 1883, especially focusing on laminar and turbulent flow, while research has been done on the transitional flow regime since the 1990s. As the density of fluids is dependent on temperature, the addition of heat to the tube wall leads to mixed convection. A flow regime map is a valuable tool that can be used to determine whether free convection effects can be neglected (forced convection) or whether they are significant (mixed convection). However, the existing flow regime maps for horizontal tubes with a constant heat flux boundary condition were primarily developed using high Prandtl number data and became inaccurate when low Prandtl number fluids in small diameter tubes were used, as in this study. Furthermore, it was developed using fully developed flow data and did not account for developing flow.

Another very important aspect for design engineers is the thermal entrance length, because it determines whether the heat transfer coefficients are dependent (developing flow) on or independent (fully developed flow) of axial tube position. When high Prandtl number fluids such as oil are used, the thermal entrance length can become very long, especially at high laminar Reynolds numbers (close to the transitional flow regime). Although the thermal entrance length has been defined for forced convection conditions, the differing behaviour of different Prandtl number fluids during mixed convection conditions led to gaps in literature not only regarding the thermal entrance length correlation, but also a single correlation that can be used to calculate the laminar heat transfer coefficients of both high and low Prandtl number fluids.

What further complicates the local heat transfer characteristics of mixed convection flow is the local laminar-turbulent transition that occurs along the tube length when the Reynolds number exceeds the critical Reynolds number. Although the transitional flow regime has been extensively investigated, previous studies focussed on the effects of inlet geometries, enhanced tubes, nanofluids, micro-channels, multiple circular tubes and annuli. Up to now, no experimental studies have been specifically devoted to the transitional heat transfer characteristics of developing flow, how it changes along the tube length, how it differs from that of fully developed flow and how it is affected by free convection effects. The lack of experimental data in the transitional flow regime is most probably the main reason for the limited understanding of and little design information on transitional flow that is available.

The purpose of this study was to experimentally investigate the local heat transfer and pressure drop characteristics of developing and fully developed flow of low Prandtl number fluids in smooth horizontal tubes for forced and mixed convection conditions. An experimental set-up was designed and built, and results were validated against literature. Two smooth circular test sections with inner diameters of 4 mm and 11.5 mm were used and the maximum length-to-diameter ratios were 1 373 and 872 respectively. Heat transfer and pressure drop measurements were taken at Reynolds numbers between 500 and 10 000 at different constant heat fluxes. A total of 648 mass flow rate measurements, 70 301 temperature measurements and 2 536 pressure drop measurements were taken. Water was used as the test fluid and the Prandtl number ranged between three and seven.

9.2. Conclusions

It was found that it was very challenging to experimentally obtain forced convection conditions. However, fully developed laminar forced convection conditions were successfully obtained by applying a very small heat flux. Furthermore, it was found that a longer thermal entrance length was required when the flow was simultaneously hydrodynamically and thermally developing, as in this study, than when the flow was hydrodynamically fully developed and thermally developing. A coefficient of at least 0.12 (and not 0.05 as suggested in most literature) was therefore suggested for simultaneously hydrodynamically and thermally developing forced convection laminar flow. As the heat flux and tube diameter were increased, free convection effects became significant, which not only led to increased Nusselt numbers, but also to a decreased thermal entrance length. Correlations were also developed to calculate the thermal entrance length for mixed convection conditions.

The boundaries between the flow regimes were defined mathematically, and terminology to define transitional flow characteristics were presented. Three different regions, namely forced convection developing (FCD), mixed convection developing (MCD) and fully developed (FD) were identified in the

local laminar heat transfer results. Nomenclature and correlations were developed to define and quantify the boundaries of these regions. Correlations were also developed to calculate the local and average laminar Nusselt numbers of mixed convection developing flow. The laminar-turbulent transition along the tube length occurred faster with increasing Reynolds number, due to the increased velocity of the fluid. Furthermore, this transition was also influenced by free convection effects. Free convection effects initially disturbed the fluctuations inside the test section, causing a slower laminar-turbulent transition compared with forced convection conditions. However, as the free convection effects were increased further, the fluctuations inside the test section were enhanced. The enhanced mixing caused the laminar-turbulent transition along the tube length to occur faster and the magnitude of the Nusselt numbers to increase.

In the transitional flow regime itself, it was found that the Reynolds number at which transition started was independent of axial position for both developing and fully developed flow and transition occurred at the same moment in time along the whole tube length. However, the end of transition was dependent on axial position when the flow was developing and occurred earlier as the flow approached fully developed flow. Once the flow was fully developed, the end of transition became independent of axial position. Free convection effects affected both the start and end of the transitional flow regime and caused the Reynolds number range of the transitional flow regime to decrease. Correlations were developed to determine the start and end of the transitional flow regime for developing and fully developed flow in mixed convection conditions.

The transitional flow regime across the tube length was divided into three regions. In the first region, the width of the transitional flow regime decreased significantly with axial position as the thermal boundary layer thickness increased and free convection effects were negligible. In Region 2, the width of the transitional flow regime decreased with axial position, due to the development of the thermal boundary layer and the mass flow rate and temperature fluctuations, as well as with free convection effects. In the fully developed region (Region 3), the width of the transitional flow regime was independent of axial position, but decreased significantly with increasing free convection effects. At high Grashof numbers, free convection effects even caused the transitional flow regime to become negligible when the flow was fully developed and the flow alternated between the laminar and the quasi-turbulent flow regimes.

It was found that the boundaries of the different flow regimes were the same for pressure drop and heat transfer and a relationship between pressure drop and heat transfer existed in all four flow regimes. In the laminar flow regime, this relationship between pressure drop and heat transfer was a function of Grashof number (thus free convection effects), while it was a function of Reynolds number in the other three flow regimes. Correlations to predict the friction factors as a function of average Nusselt number, as well as correlations to predict the average Nusselt number for developing and fully developed flow in all flow regimes, were developed.

Finally, a total of six flow regime maps were developed and these flow regime maps were unique for four reasons. Firstly, they contained contour lines that showed the Nusselt number enhancements due to the free convection effects. Secondly, they were valid for a wide range of tube diameters and Prandtl numbers. Thirdly, the flow regime maps were developed as a function of temperature difference (Grashof number) and heat flux (modified Grashof number). Finally, four of the six flow regime maps were not only valid for fully developed flow, but also for developing flow. The accuracy

of the flow regime maps was evaluated using the experimental data of this study, as well as experimental data in literature that were obtained using fluids with lower and higher Prandtl numbers and larger tube diameters. Therefore, these flow regime maps can be used as reliable tools to predict the convection flow regime for developing and fully developed flow for a wide range of tube diameters and Prandtl numbers.

Overall, it was concluded that free convection effects significantly affected the thermal entrance length, laminar-turbulent transition along the tube length, as well as the local heat transfer and pressure drop characteristics in the laminar and transitional flow regime. Furthermore, the heat transfer and pressure drop characteristics of developing and fully developed flow were significantly different, especially in the transitional flow regime. The thermal entrance length, heat transfer and pressure drop correlations, as well as the flow regime maps, that were developed in this study will not only enable designers to optimise the design of heat exchangers, but also improve the fundamental understanding of mixed convection developing and fully developed flow.

9.3. Recommendations

The following future work is recommended:

- The definition of the boundary between the quasi-turbulent and turbulent flow regimes can be improved by using experimental data with lower uncertainties (experiments conducted at higher heat fluxes) in the quasi-turbulent and turbulent flow regimes.
- The inflection point in the transitional flow regime is where the trend of the flow characteristics changes. The inflection point was found to be in the middle of the transitional flow regime and was prominent in both the heat transfer and pressure drop results, as well as when the relationship between pressure drop and heat transfer was investigated. The understanding of the heat transfer and pressure drop characteristics in the transitional flow regime can be improved by investigating the physical mechanism of the inflection point.
- When the Reynolds number exceeded the critical Reynolds number, four different regions were identified; however, the boundaries and heat transfer characteristics of these regions in the transitional flow regime were not quantified. The reason was that the laminar-turbulent transition along the tube length was significantly affected by fluid velocity as well as free convection effects, and therefore occurred faster with both increasing Reynolds number and Grashof number. This should be further investigated to develop correlations to determine the boundaries of the different regions in the transitional flow regime, as well as to predict the local Nusselt numbers as a function of axial position for transitional flow.
- Experimental data from literature were used to ensure that a wider range of Prandtl number data were available to use for interpretation and the development of correlations. To better investigate the influence of Prandtl number on the local heat transfer characteristics of developing and fully developed flow, experiments should be conducted using the same (or modified) experimental set-up, but with different concentrations of ethylene glycol-water mixtures as the test fluid. The results can then be compared with the low Prandtl number results obtained in this study. This will not only extend the experimental data base of the heat transfer and pressure drop results in the transitional flow regime, but will also improve the accuracy and extend the ranges of the correlations and flow regime maps that were developed in this study.

- For Prandtl numbers less than one, the thermal boundary layer develops faster than the hydrodynamic boundary. It will be valuable to conduct experiments using air ($Pr < 1$) to determine the validity/accuracy of the correlations and flow regime maps developed in this study for Prandtl numbers less than one. If necessary, the correlations and flow regime maps can then be modified to be valid for all Prandtl numbers.
- When the surface roughness of the tube is increased, the velocity and thermal boundary layers will be affected, which will not only affect the thermal entrance length and pressure drop, but also free convection effects and thus the heat transfer coefficients. Because the transitional flow regime is very dependent on free convection effects and developing flow, this will also significantly influence the heat transfer and pressure drop characteristics in the transitional flow regime, as well as the boundaries of the transitional flow regime. In order to investigate the influence of surface roughness on the heat transfer and pressure characteristics in all flow regimes, experiments should be conducted in three rough test sections with a length of 10 m but different values of relative surface roughness. The results can then be compared with the smooth tube results obtained in this study. Thermal entrance length, heat transfer and pressure drop correlations that account for surface roughness, developing flow and mixed convection conditions can then be developed. This will be of great value to design engineers because corrosion and scaling are common problems in heat exchangers, which not only increase the surface roughness of the tube, but also affect the performance of the heat exchangers.

References

[1] R.K. Shah, A.L. London, *Laminar Flow Forced Convection in Ducts*, Academic Press, New York, 1978.
[2] B.S. Gill, Relationship between pressure drop and heat transfer coefficient, *Hydrocarbon Processing*, Vol. 79(8), 2000.
[3] Y.A. Cengel, A.J. Ghajar, *Heat and Mass Transfer: Fundamentals and Applications*, 5th ed., McGraw-Hill, 2015.
[4] N.T. Obot, Smooth tube friction and heat transfer in laminar and transitional flow, *International Communications in Heat and Mass Transfer*, Vol. 19(3), pp. 299-310, 1992.
[5] R. Allen, E. Eckert, Friction and heat-transfer measurements to turbulent pipe flow of water (Pr = 7 and 8) at uniform wall heat flux, *Journal of Heat Transfer*, Vol. 86(3), pp. 301-310, 1964.
[6] F. Durst, S. Ray, B. Ünsal, O.A. Bayoumi, The development lengths of laminar pipe and channel flows, *J Fluids Eng Trans ASME*, Vol. 127(6), pp. 1154-1160, 2005.
[7] J.P. Meyer (keynote), Heat transfer in tubes in the transitional flow regime, *Proceedings of the 15th International Heat Transfer Conference (IHTC-15)*, Kyoto, Japan, 10-15 August 2014.
[8] H.K. Tam, L.M. Tam, A.J. Ghajar, Effect of inlet geometries and heating on the entrance and fully-developed friction factors in the laminar and transition regions of a horizontal tube, *Exp. Therm. Fluid Sci.*, Vol. 44, pp. 680-696, 2013.
[9] J.A. Olivier, J.P. Meyer, Single-phase heat transfer and pressure drop of the cooling of water inside smooth tubes for transitional flow with different inlet geometries (RP-1280), *HVAC R Res*, Vol. 16(4), pp. 471-496, 2010.
[10] L.M. Tam, A.J. Ghajar, Transitional heat transfer in plain horizontal tubes, *Heat Transfer Eng*, Vol. 27(5), pp. 23-38, 2006.
[11] Y. Mori, K. Futagami, S. Tokuda, M. Nakamura, Forced convective heat transfer in uniformly heated horizontal tubes, (1st report) Experimental study on the effect of buoyancy, *Int. J. Heat Mass Transf.*, Vol. 9, pp. 453-463, 1966.
[12] H.A. Mohammed, Y.K. Salman, The effects of different entrance sections lengths and heating on free and forced convective heat transfer inside a horizontal circular tube, *International Communications in Heat and Mass Transfer*, Vol. 37, pp. 769-784, 2007.
[13] B. Metais, E. Eckert, Forced, mixed, and free convection regimes, *Journal of Heat Transfer*, Vol. 86(2), pp. 295-296, 1964.
[14] A.J. Ghajar, L.M. Tam, Flow regime map for a horizontal pipe with uniform wall heat flux and three inlet configurations, *Exp. Therm. Fluid Sci.*, Vol. 10(3), pp. 287-297, 1995.
[15] H.K. Tam, L.M. Tam, A.J. Ghajar, C.W. Cheong, Development of a unified flow regime map for a horizontal pipe with the support vector machines, *AIP Conference Proceedings*, Hong Kong, pp. 608-613, 30 November-3 December 2009.
[16] A.J. Ghajar, L.M. Tam, Heat transfer measurements and correlations in the transition region for a circular tube with three different inlet configurations, *Exp. Therm. Fluid Sci.*, Vol. 8(1), pp. 79-90, 1994.
[17] R. Siegel, E.M. Sparrow, T.M. Hallman, Steady laminar heat transfer in a circular tube with a prescribed wall heat flux, *Applied Scientific Research*, Vol. 7, 1958.
[18] T.M. Hallman, *Combined free and forced convection in a circular tube*, PhD thesis, Purdue University, Lafayette, 1958.
[19] S. McComas, E. Eckert, Combined free and forced convection in a horizontal circular tube, *Journal of Heat Transfer*, Vol. 88(2), pp. 147-152, 1966.
[20] R.L. Shannon, C.A. Depew, Combined free and forced laminar convection in a horizontal tube with a uniform heat flux, *Journal of Heat Transfer*, Vol. 90(3), pp. 353-357, 1968.
[21] G.S. Barozzi, E. Zanchini, M. Mariotti, Experimental investigation of combined forced and free convection in horizontal and inclined tubes, *Meccanica*, Vol. 20, pp. 18-27, 1985.

[22] K.C. Cheng, J.W. Ou, Free convection effects on Graetz problem for large Prandtl number fluids in horizontal tubes with a uniform wall heat flux, *Proceedings of the 5th International Heat Transfer Conference (IHTC-5)*, Tokyo, Japan, pp. 159-163, 3-7 September 1974.
[23] M. Nishi, B. Ünsal, F. Durst, G. Biswas, Laminar-to-turbulent transition of pipe flows through puffs and slugs, *Journal of Fluid Mechanics*, Vol. 614, pp. 425-446, 2008.
[24] A.J. Ghajar, L.M. Tam, Laminar-transition-turbulent forced and mixed convective heat transfer correlations for pipe flows with different inlet configurations, *American Society of Mechanical Engineers, Heat Transfer Division, (Publication) HTD*, New York, United States, pp. 15-23.
[25] A.J. Ghajar, K.F. Madon, Pressure drop measurements in the transition region for a circular tube with three different inlet configurations, *Exp. Therm. Fluid Sci.*, Vol. 5(1), pp. 129-135, 1992.
[26] L.M. Tam, A.J. Ghajar, Effect of inlet geometry and heating on the fully developed friction factor in the transition region of a horizontal tube, *Exp. Therm. Fluid Sci.*, Vol. 15(1), pp. 52-64, 1997.
[27] L.M. Tam, A.J. Ghajar, The unusual behavior of local heat transfer coefficient in a circular tube with a bell-mouth inlet, *Exp. Therm. Fluid Sci.*, Vol. 16(3), pp. 187-194, 1998.
[28] A.J. Ghajar, C.C. Tang, W.L. Cook, Experimental investigation of friction factor in the transition region for water flow in minitubes and microtubes, *Heat Transfer Eng*, Vol. 31(8), pp. 646-657, 2010.
[29] H.K. Tam, L.M. Tam, A.J. Ghajar, S.C. Tam, T. Zhang, Experimental investigation of heat transfer, friction factor, and optimal fin geometries for the internally microfin tubes in the transition and turbulent regions, *J. Enhanced Heat Transf.*, Vol. 19(5), pp. 457-476, 2012.
[30] L.M. Tam, H.K. Tam, A.J. Ghajar, W.S. Ng, C.K. Wu, The effect of inner surface roughness and heating on friction factor in horizontal mini-tubes, *Proceedings of the 15th International Heat Transfer Conference (IHTC-15)*, Kyoto, Japan, 10-15 August 2014.
[31] J.P. Meyer, J.A. Olivier, Transitional flow inside enhanced tubes for fully developed and developing flow with different types of inlet disturbances: Part II - Heat transfer, *Int. J. Heat Mass Transf.*, Vol. 54(7-8), pp. 1598-1607, 2011.
[32] J.P. Meyer, J.A. Olivier, Transitional flow inside enhanced tubes for fully developed and developing flow with different types of inlet disturbances: Part I - Adiabatic pressure drops, *Int. J. Heat Mass Transf.*, Vol. 54(7-8), pp. 1587-1597, 2011.
[33] J.P. Meyer, J.A. Olivier, Heat transfer and pressure drop characteristics of smooth horizontal tubes in the transitional flow regime, *Heat Transfer Eng*, Vol. 35(14-15), pp. 1246-1253, 2014.
[34] J.P. Meyer, T.J. McKrell, K. Grote, The influence of multi-walled carbon nanotubes on single-phase heat transfer and pressure drop characteristics in the transitional flow regime of smooth tubes, *Int. J. Heat Mass Transf.*, Vol. 58(1-2), pp. 597-609, 2013.
[35] J. Dirker, J.P. Meyer, D.V. Garach, Inlet flow effects in micro-channels in the laminar and transitional regimes on single-phase heat transfer coefficients and friction factors, *Int. J. Heat Mass Transf.*, Vol. 77, pp. 612-626, 2014.
[36] D.D. Ndenguma, J. Dirker, J.P. Meyer, Transitional flow regime heat transfer and pressure drop in an annulus with non-uniform wall temperatures, *Int. J. Heat Mass Transf.*, Vol. 108, pp. 2239-2252, 2017.
[37] J.P. Meyer, S.M. Abolarin, Heat transfer and pressure drop in the transitional flow regime for a smooth circular tube with twisted tape inserts and a square-edged inlet, *Int. J. Heat Mass Transf.*, Vol. 117, pp. 11-29, 2018.
[38] D.D. Ndenguma, J. Dirker, J.P. Meyer, Heat transfer and pressure drop in annuli with approximately uniform internal wall temperatures in the transitional flow regime, *Int. J. Heat Mass Transf.*, Vol. 111, pp. 429-441, 2017.
[39] J.P. Meyer, M. Everts, A.T.C. Hall, F.A. Mulock Houwer, M. Joubert, L.M.J. Pallent, E.S. Vause, Inlet tube spacing and protrusion effects on multiple circular tubes in the laminar, transitional and turbulent flow regimes, *Int. J. Heat Mass Transf.*, Vol. 118, pp. 257-274, 2018.
[40] D. Taler, A new heat transfer correlation for transition and turbulent fluid flow in tubes, *Int. J. Therm. Sci.*, Vol. 108, pp. 108-122, 2016.

[41] V. Gnielinski, New equations for heat and mass-transfer in turbulent pipe and channel flow, *International Chemical Engineering*, Vol. 16(2), pp. 359-368, 1976.
[42] S.W. Churchill, Comprehensive correlating equations for heat, mass and momentum transfer in fully developed flow in tubes, *Industrial Engineering Chemistry Fundamentals*, Vol. 16(1), pp. 109-116, 1977.
[43] W. Yu-ting, L. Bin, M. Chong-fang, G. Hang, Convective heat transfer in the laminar-turbulent transition region with molten salt in a circular tube, *Exp. Therm. Fluid Sci.*, Vol. 33(7), pp. 1128-1132, 2009.
[44] J. Lu, S. He, J. Liang, J. Ding, J. Yang, Convective heat transfer in the laminar-turbulent transition region of molten salt in annular passage, *Exp. Therm. Fluid Sci.*, Vol. 51, pp. 71-76, 2013.
[45] V. Gnielinski, On heat transfer in tubes, *Int. J. Heat Mass Transf.*, Vol. 63, pp. 134-140, 2013.
[46] D. Taler, A. Korzeń, Numerical Modeling of Transient Operation of a Plate Fin and Tube Heat Exchanger at Transition Fluid Flow in Tubes, *Procedia Engineering*, Cracow, Poland, pp. 163-170, 23–26 May 2016.
[47] J.P. Meyer, M. Everts, Single-phase mixed convection of developing and fully developed flow in smooth horizontal circular tubes in the laminar and transitional flow regimes, *Int. J. Heat Mass Transf.*, Vol. 117, pp. 1251-1273, 2018.
[48] M. Everts, J.P. Meyer, Heat transfer of developing and fully developed flow in smooth horizontal tubes in the transitional flow regime, *Int. J. Heat Mass Transf.*, Vol. 117, pp. 1331-1351, 2018.
[49] M. Everts, J.P. Meyer, Relationship between pressure drop and heat transfer of developing and fully developed flow in smooth horizontal circular tubes in the laminar, transitional, quasi-turbulent and turbulent flow regimes, *Int. J. Heat Mass Transf.*, Vol. 117, pp. 1231-1250, 2018, 017.
[50] M. Everts, J.P. Meyer, Flow regime maps for smooth horizontal tubes at a constant heat flux, *Int. J. Heat Mass Transf.*, Vol. 117, pp. 1274-1290, 2018.
[51] F.M. White, *Fluid Mechanics*, 6th ed., McGraw-Hill, Singapore, 2009.
[52] J.P. Holman, *Heat Transfer*, 9th ed., McGraw-Hill, New York, 2002.
[53] S.M. Ghiaasiaan, *Convective Heat and Mass Transfer*, 1st ed., Cambridge University Press, United States of America, 2011.
[54] F. Kreith, *Principles of Heat Transfer*, Intext Educational Publisher, New York, 1976.
[55] A.F. Mills, *Heat and Mass Transfer*, Irwin, Chicago, 1995.
[56] A. Faghri, Y. Zhang, J.R. Howell, *Advanced Heat and Mass Transfer*, Global Digital Press, Columbia, 2010.
[57] J.C. Han, *Analytical Heat Transfer*, CRC Press, Boca Raton, 2016.
[58] P.S. Ghoshdastidar, *Heat Transfer*, 2nd ed., Oxford University Press, New Delhi, 2012.
[59] M.A. Ebadian, Z.F. Dong, Forced Convection, Internal Flow in Ducts, W.M. Rohsenow, J.P. Hartnett, Y.I. Cho (Eds.) *Handbook of Heat Transfer*, McGraw-Hill, Boston, pp. 5.1-5.137, 1998.
[60] J.H.IV Lienhard, J.H.V Lienhard, *A Heat Transfer Textbook*, 3rd ed., Phlogiston Press, Cambridge, 2008.
[61] A.E. Bergles, R.R. Simonds, Combined forced and free convection for laminar flow in horizontal tubes with uniform heat flux, *Int. J. Heat Mass Transf.*, Vol. 14(12), pp. 1989-2000, 1971.
[62] B.S. Petukhov, A.F. Polyakov, Experimental investigation of viscogravitational fluid flow in a horizontal tube, *Teplofiz. Vysok. Temp*, Vol. 5, pp. 87-95, 1967.
[63] S.W. Hong, S.M. Morcos, A.E. Bergles, Analytical and experimental results for combined forced and free laminar convection in horizontal tubes, *Proceedings of the 5th International Heat Transfer Conference (IHTC-5)*, Tokyo, pp. 154-158, 3-5 September 1974.
[64] O. Reynolds, An experimental investigation of the circumstances which determine whether the motion of water shall be direct or sinuous, and of the law of resistance in parallel channels, *Proceedings of the Royal Society of London*, Vol. 35(224-226), pp. 84-99, 1883.
[65] W. Aung, Mixed Convection in Internal Flow, S. Kakaç, R.K. Shah, W. Aung (Eds.) *Handbook of Single-Phase Convective Heat Transfer*, John Wiley & Sons, New York, pp. 15.11-15.51, 1987.

[66] G.D. Raithby, K.G.T. Hollands, Natural Convection, W.M. Rohsenow, J.P. Hartnett, Y.I. Cho (Eds.) *Handbook of Heat Transfer*, McGraw-Hill, Boston, pp. 4.1-4.99, 1998.
[67] J.D. Jackson, M.A. Cotton, B.P. Axcell, Studies of mixed convection in vertical tubes, *Int. J. Heat Fluid Flow*, Vol. 10(1), pp. 1-15, 1989.
[68] J. Orfi, N. Galanis, C.T. Nguyen, Laminar fully developed incompressible flow with mixed convection in inclined tubes, *International Journal of Numerical Methods for Heat & Fluid Flow*, Vol. 3(4), pp. 341-355, 1993.
[69] T. Maré, N. Galanis, S. Prétot, J. Miriel, Mixed convection with flow reversal in the entrance region of inclined tubes, *International Journal of Numerical Methods for Heat & Fluid Flow*, Vol. 15(7), pp. 740-756, 2005.
[70] S.W. Churchill, H. Ozoe, Correlations for laminar forced convection with uniform heating in flow over a plate and in developing and fully developed flow in a tube, *Journal of Heat Transfer*, Vol. 95(1), pp. 78-84, 1973.
[71] S.M. Morcos, A.E. Bergles, Experimental investigation of combined forced and free laminar convection in horizontal tubes, *Journal of Heat Transfer*, Vol. 97(2), pp. 212-219, 1975.
[72] G.K. Filonenko, Hydraulischer Widerstand von Rohrleitungen (Orig. Russ.), *Teploenergetika*, Vol. 1(4), pp. 40-44, 1954.
[73] X. Fang, Y. Xu, Z. Zhou, New correlations of single-phase friction factor for turbulent pipe flow and evaluation of existing single-phase friction factor correlations, *Nuclear Engineering and Design*, Vol. 241, pp. 897-902, 2011.
[74] C.F. Colebrook, Turbulent flow in pipes, with particular reference to the transition region between the smooth and rough pipe laws, *Journal of the Institution of Civil Engineers*, Vol. 11, pp. 133-156, 1938–1939.
[75] M. Everts, *Heat transfer and pressure drop of developing flow in smooth tubes in the transitional flow regime*, Master's dissertation, University of Pretoria, Pretoria, 2014.
[76] J.P. Abraham, E.M. Sparrow, W.J. Minkowycz, Internal-flow Nusselt numbers for the low-Reynolds-number end of the laminar-to-turbulent transition regime, *Int. J. Heat Mass Transf.*, Vol. 54(1-3), pp. 584-588, 2011.
[77] J.P. Abraham, E.M. Sparrow, J.C.K. Tong, Heat transfer in all pipe flow regimes: laminar, transitional/intermittent, and turbulent, *Int. J. Heat Mass Transf.*, Vol. 52(3-4), pp. 557-563, 2009.
[78] J.P. Abraham, E.M. Sparrow, J.C.K. Tong, Breakdown of laminar pipe flow into transitional intermittency and subsequent attainment of fully developed intermittent or turbulent flow, *Numer Heat Transfer Part B Fundam*, Vol. 54(2), pp. 103-115, 2008.
[79] D. Bertsche, P. Knipper, T. Wetzel, Experimental investigation on heat transfer in laminar, transitional and turbulent circular pipe flow, *Int. J. Heat Mass Transf.*, Vol. 95, pp. 1008-1018, 2016.
[80] S.W. Churchill, R. Usagi, A general expression for the correlation of rates of transfer and other phenomena, *AIChE Journal*, Vol. 18(6), pp. 1121-1128, 1972.
[81] H.L. Langhaar, Steady flow in the transition length of a straight tube, *Journal of Applied Mechanics*, Vol. 9, pp. A-55-A-58, 1942.
[82] S.G. Kandlikar, W.J. Grande, Evolution of microchannel flow passages - thermohydraulic performance and fabrication technology, *Proceedings of the ASME International Mechanical Engineering Congress and Exposition (ETCE2002)*, pp. 59-72, 17-22 November 2002.
[83] S.G. Kandlikar, D. Schmitt, A.L. Carrano, J.B. Taylor, Characterization of surface roughness effects on pressure drop in single-phase flow in minichannels, *Physics of Fluids*, Vol. 17(10), 2005, 100606.
[84] H. Nagendra, Interaction of free and forced convection in horizontal tubes in the transition regime, *Journal of Fluid Mechanics*, Vol. 57(2), pp. 269-288, 1973.
[85] ASHRAE, ASHRAE Handbook - Fundamentals, Fluid Flow, American Society of Heating Refrigerating and Air-Conditioning Engineers, Inc., Atlanta, 2009.
[86] R.M. Manglik, A.E. Bergles, Heat transfer and pressure drop correlations for twisted-tape inserts in isothermal tubes: Part II - Transition and turbulent flows, *Transactions - ASME: Journal of Heat Transfer*, Vol. 115(4), pp. 890-896, 1993.

[87] R.K. Shah, D.P. Sekulić, *Fundamentals of Heat Exchanger Design*, John Wiley & Sons Inc, New Jersey, 2003.
[88] A.M. Binnie, A double-refraction method of detecting turbulence in liquids, *Proceedings of the Physical Society*, Vol. 57(5), pp. 390-402, 1945, 302.
[89] E.K. Kalinin, S.A. Yarkho, Flow pulsations and heat transfer in the transition region between the laminar and turbulent flow regimes in a tube, *International Chemical Engineering*, Vol. 6(4), pp. 571-574, 1966.
[90] P. Zalzal, M. Ojha, C.R. Ethier, R.S.C. Cobbold, K.W. Johnston, Visualization of transitional pipe flow using the photochromic tracer method, *Physics of Fluids*, Vol. 6(6), pp. 2003-2010, 1994.
[91] I.J. Wygnanski, F.H. Champagne, On transition in pipe. Part 1. The origin of puffs and slugs and the flow in a turbulent slug, *Journal of Fluid Mechanics*, Vol. 59, pp. 281-351, 1973.
[92] H. Koizumi, Laminar-turbulent transition behavior of fully developed air flow in a heated horizontal tube, *Int. J. Heat Mass Transf.*, Vol. 45(5), pp. 937-949, 2002.
[93] M.A. El-Hawary, Effect of combined free and forced convection on the stability of flow in a horizontal tube, *Journal of Heat Transfer*, Vol. 102(2), pp. 273-278, 1980.
[94] L.M. Tam, A.J. Ghajar, H.K. Tam, S.C. Tam, Development of a flow regime map for a horizontal pipe with the multi-classification Support Vector Machines, *Proceedings of the 2008 ASME Summer Heat Transfer Conference (HT2008)*, Jacksonville, USA, pp. 537-547, 10-14 August 2008.
[95] R. Rayle, *Influence of orifice geometry on static pressure measurements*, American Society of Mechanical Engineers, 1959.
[96] F. Bozzoli, L. Cattani, S. Rainieri, Effect of wall corrugation on local convective heat transfer in coiled tubes, *Int. J. Heat Mass Transf.*, Vol. 101, pp. 76-90, 2016.
[97] F. Bozzoli, L. Cattani, S. Rainieri, F.S. Viloche Bazán, L.S. Borges, Estimation of the local heat-transfer coefficient in the laminar flow regime in coiled tubes by the Tikhonov regularisation method, *Int. J. Heat Mass Transf.*, Vol. 72, pp. 352-361, 2014.
[98] G. Maranzana, I. Perry, D. Maillet, Mini- and micro-channels: influence of axial conduction in the walls, *Int. J. Heat Mass Transf.*, Vol. 47(17), pp. 3993-4004, 2004.
[99] A. Bakker, R.D. LaRoche, E.M. Marshall, Laminar flow in static mixers with helical elements, The Online CFM Book, 2000.
[100] F.T. Ulaby, E. Michielssen, U. Ravaioli, *Fundamentals of Applied Electromagnetics*, 6th ed., Pearson, Boston, 2010.
[101] C.O. Popiel, J. Wojtkowiak, Simple formulas for thermophysical properties of liquid water for heat transfer calculations [from O°C to 150°C], *Heat Transfer Eng*, Vol. 19(3), pp. 87-101, 1998.
[102] A.J. Ghajar, J. Kim, Calculation of local inside-wall convective heat-transfer parameters from measurements of local outside-wall temperatures along an electrically heated circular tube, M. Kutz (Ed.) *Heat-Transfer Calculations*, McGraw-Hill, New York, pp. 23.23-23.27, 2006.
[103] P.F. Dunn, *Measurement and Data Analysis for Engineering and Science*, 2nd ed., CRC Press, United States of America, 2010.
[104] A.K. Kupper, *Combined free and forced convection in a horizontal tube under uniform heat flux*, Master's dissertation, University of British Columbia, Vancouver, 1968.
[105] J. Chen, *Heat transfer in high laminar, transition and lower turbulent flow regimes for square-edged contraction entrance in a circular tube*, PhD thesis, Oklahoma State University, Oklahoma, 1988.
[106] D.T. Strickland, *Heat transfer measurements in the transition region for a horizontal circular tube with a square-edged entrance*, Master's dissertation, Oklahoma State University, Stillwater, 1990.
[107] J.P. Meyer, C.C. Tang, Convective Heat Transfer of Nanofluids in Tubes, S.M. Sohel Murshed, C.A. Nieto de Castro (Eds.) *Nanofluids: Synthesis, Properties and Applications*, Nova Science Publishers, New York, pp. 155-192, 2014.
[108] L.M. Tam, *An experimental investigation of heat transfer and pressure drop in the transition region for a horizontal tube with different inlets and uniform heat flux*, PhD thesis, Oklahoma State University, Stillwater, 1995.

[109] S.M. Morcos, *Combined forced and free laminar convection in horizontal tubes*, PhD thesis, Iowa State University, Ames, 1974.
[110] R.K. Shah, Thermal entry length solutions for the circular tube and parallel plates, *Proceedings of the Third National Heat and Mass Transfer Conference*, India Institute of Technology, Bombay, pp. 1-12, 11-13 December 1975.
[111] D.K. Edwards, V.E. Denny, A.F. Mills, *Transfer Processes*, 2nd ed., Hemisphere, Washington, DC, 1979.
[112] E.N. Sieder, G.E. Tate, Heat transfer and pressure drop of liquids in tubes, *Industrial Engineering Chemistry*, Vol. 28, pp. 1429-1435, 1936.
[113] V. Gnielinski, Ein neues Berechnungsverfahren für die Wärmeübertragung im Übergangsbereich zwischen laminarer und turbulenter Rohrströmung, *Forschung im Ingenieurwesen*, Vol. 61(9), pp. 240-248, 1995.

APPENDICES

A. Calibration

A.1. Introduction

This appendix describes the calibration process of the Pt100 probes, thermocouples and pressure transducers. Sample calibration curves of the Pt100 probes, thermocouples and pressure transducers are also given.

A.2. Pt100 probe calibration

The Pt100 probes were calibrated between 15 °C and 65 °C at 2.5 °C intervals, using a DigiCal DCS2 digital thermometer with an accuracy of 0.03 °C. The Pt100 probes were placed with the thermometer inside a LAUDA PROLINE RP1845C thermostat-controlled bath with an accuracy of 0.01 °C. Once the thermostat-controlled bath reached the desired temperature, a measurement, consisting of 200 measuring points, was taken and the average of the 200 measuring points was used. The process was then repeated for decreasing temperatures (from 65 °C to 15 °C) to ensure that a constant curve was obtained, as well as to investigate the effect of hysteresis.

Figure A.1 contains a sample plot of the average temperature measurement of the Pt100 probe in the flow-calming section against the thermometer measurement. This figure indicates that there was no significant difference between the temperature measurements of the increasing and decreasing calibration runs and that the measured temperatures of the Pt100 probe were very close (within 0.2 °C, uncalibrated) to those of the thermometer.

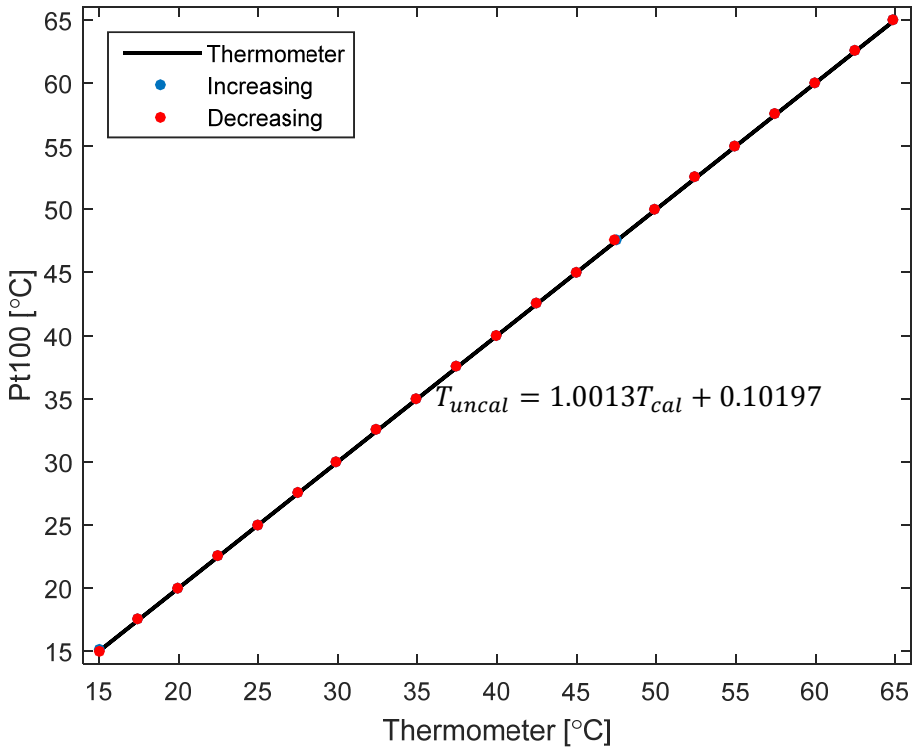

Fig. A.1: Temperature measurements of the Pt100 probe in the flow-calming section for increasing and decreasing calibration runs.

The average calibration factor of each Pt100 probe was obtained by doing a linear curve fit through the data of both calibration runs. The calibrated temperatures were then determined as follows:

$$T_{cal} = \frac{(T_{uncal} - c)}{m} \qquad \text{A.1}$$

Figure A.2 contains the uncalibrated and calibrated temperature measurements of the Pt100 probe inside the flow-calming section. This figure indicates that there was no significant difference between the calibrated measurements of the Pt100 probe and the measurements of the thermometer.

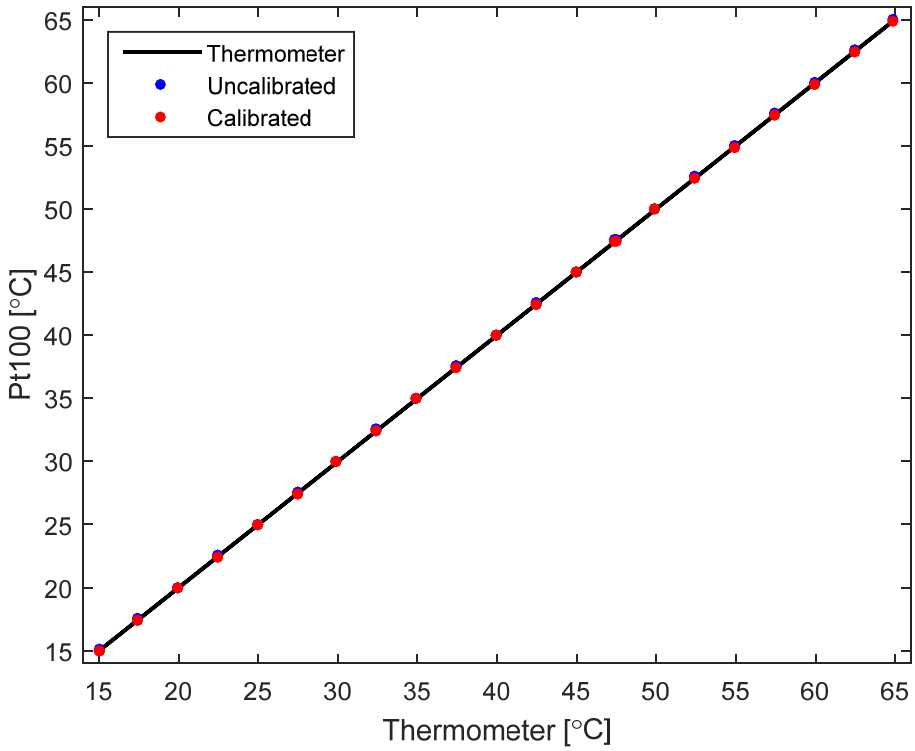

Fig. A.2: Calibrated and uncalibrated temperature measurements of the Pt100 probe inside the flow-calming section.

To confirm that the calibration was successful, the temperature difference between the thermometer and the Pt100 probe inside the flow-calming section before (filled markers) and after (empty markers) calibration are summarised in Fig. A.3. The uncertainty of the Pt100 probes was determined to be between 0.0305 °C and 0.0311 °C, which was less than the accuracy of 0.06 °C, which was specified by the manufacturer. Therefore, 0.06 °C was used as the uncertainty of the Pt100 probes and is indicated by the black dotted lines. The maximum temperature difference before calibration was 0.12 °C, and decreased to 0.016 °C after calibration. Because this temperature difference falls within the uncertainty of the Pt100 probe, it can be concluded that the calibration was successful.

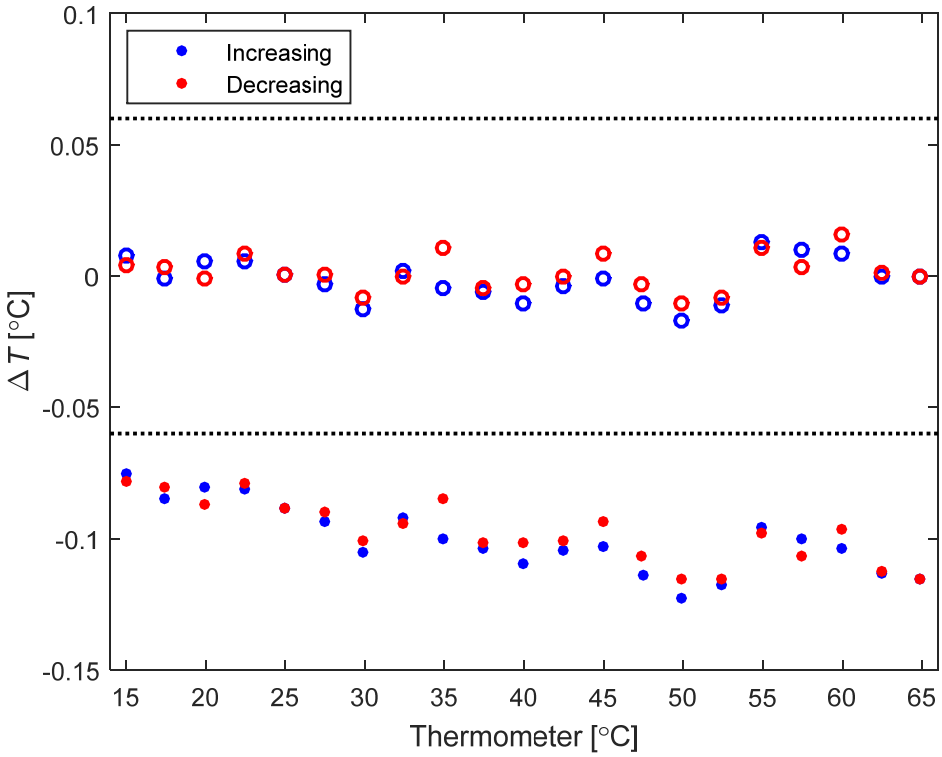

Fig. A.3: Temperature difference between the thermometer and the Pt100 probe in the flow-calming section before (filled markers) and after (empty markers) calibration.

A.3. Thermocouple calibration

In the past [7, 9, 31-34], the thermocouples were first calibrated using a thermostat-controlled bath and then soldered onto the test section. However, the properties of the thermocouple junction are likely to change during the attachment process. To improve the accuracy and reliability of the calibration factors, in situ calibration was used. Once the test section was completely built and inserted into the experimental set-up, insulated supply and return lines from the thermostat-controlled bath were connected to the test section. Water was therefore circulated through the test section and thermostat-controlled bath only and not through the entire experimental set-up, which decreased the calibration time significantly.

The thermocouples were calibrated using a thermostat-controlled bath (LAUDA PROLINE RP1845C) with an accuracy of 0.01 °C and the two Pt100 probes, which were calibrated to an accuracy of 0.06 °C. During the calibration process, the flow-calming section was replaced by an acetal manifold to avoid exposing the acrylic flow-calming section to high temperatures (the maximum operating temperature of extruded acrylic is 70 °C). The thermocouples were calibrated between 15 °C and 60 °C at 2.5 °C intervals using the water from the thermostat-controlled bath. Therefore, no heating was applied to the tubes using the power supplies. Once the thermostat-controlled bath reached the desired temperature and both Pt100 probes measured the same (within the uncertainty of the Pt100 probe) constant temperature, a measurement (consisting of 200 measuring points) was taken at a sampling frequency of 10 Hz. The process was also repeated for decreasing temperatures (from 60 °C to 15 °C) to ensure that a constant curve was obtained, as well as to investigate the effect of hysteresis.

Figure A.4 contains the uncalibrated and calibrated temperature measurements of the thermocouples along the tube length in the 11.5 mm test section at temperatures of approximately 15 °C, 30 °C, 45 °C

and 60 °C. The uncertainty of the thermocouples was determined to be between 0.0605 °C and 0.0649 °C. As this was less than the accuracy of 0.1 °C, which was specified by the manufacturer, 0.1 °C was used as the uncertainty of the thermocouples. The solid red line represents the temperatures measured by the Pt100 probes in the flow-calming section and mixer, and the dotted red lines indicate the thermocouple uncertainty of 0.1 °C. Figure A.4 indicates that the calibration was successful because all the calibrated temperature measurements fell within the dotted red lines. The average deviation between the thermocouple and Pt100 probe measurements along the 11.5 mm test section for temperatures between 20 °C and 60 °C was 0.43 °C before calibration and reduced to 0.009 °C after calibration. Similarly, for the 4 mm test section, the average deviation was 0.75 °C before calibration and reduced to 0.044 °C after calibration.

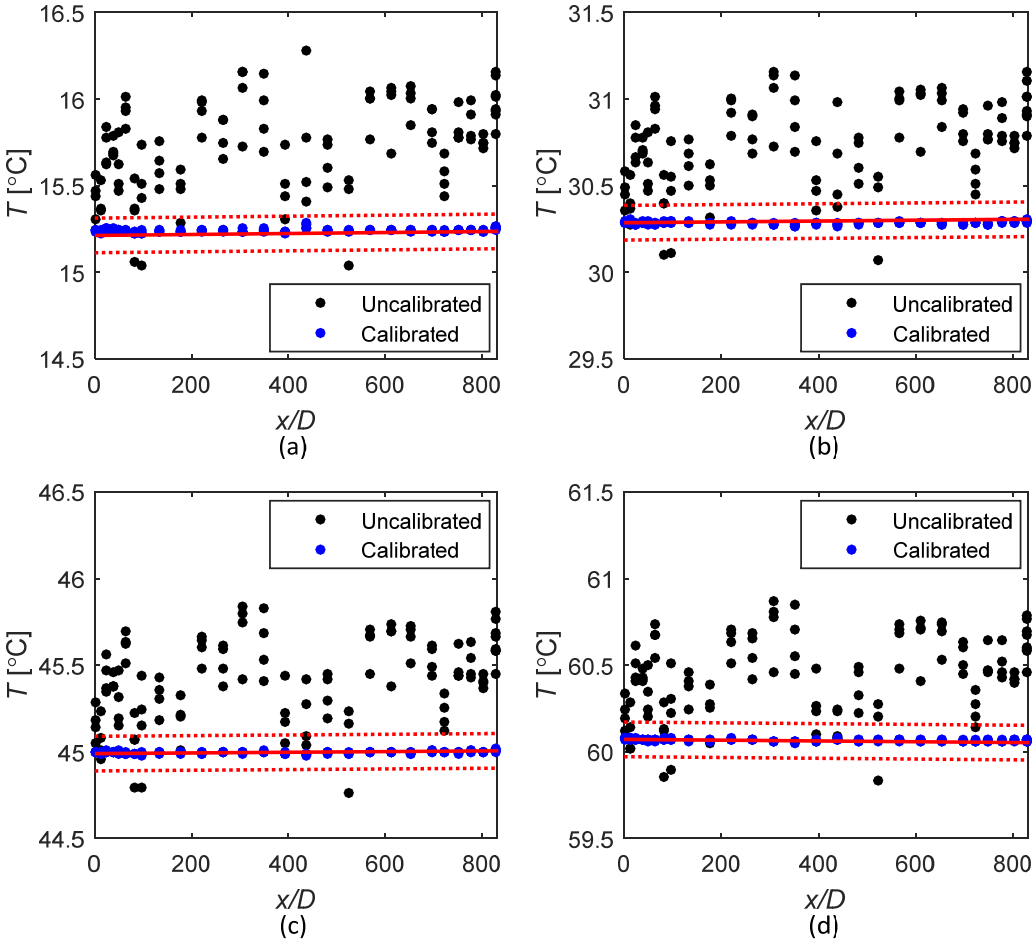

Fig. A.4: Local uncalibrated and calibrated temperatures as a function of axial position at temperatures of (a) 15.2 °C, (b) 30.3 °C, (c) 45.0 °C and (d) 60.1 °C.

The deviation between the thermocouple and Pt100 probe measurements in the 11.5 mm test section was less than in the 4 mm test section before and after calibration, which could be due to the different methods that were used to attach the thermocouples. The thermocouples were soldered to the 11.5 mm test section, while it was fixed to the 4 mm test section using a thermal adhesive with a thermal conductivity of 9 W/m.K. The lower thermal conductivity of the thermal adhesive compared with the solder possibly led to less accurate temperature measurements. Furthermore, the uncertainties of the thermocouples in the 4 mm test section were also slightly higher (maximum

uncertainty of 0.101 °C) than for the 11.5 mm test section (maximum uncertainty of 0.0649 °C). However, as the maximum deviation after calibration was less than the thermocouple uncertainty of 0.1 °C, it can be concluded that the calibration was successful in both test sections.

A.4. Pressure transducer calibration

Differential pressure transducers with interchangeable diaphragms were used to measure the pressure drop across the different tube lengths. One set of diaphragms was used between Reynolds numbers of 500 and 4 000 and another set between Reynolds numbers of 2 000 and 10 000. DP103 pressure transducers were used to measure the pressure drop across the 1.5 m and 2 m lengths, because diaphragms with a smaller full-scale (and thus higher accuracy) could be used in these pressure transducers. DP15 pressure transducers were used to measure the pressure drop across the other tube lengths. The accuracy of the diaphragms was 0.25% of the full-scale and different diaphragms were used to minimise the uncertainties of the pressure drop measurements. The diaphragms with a full-scale smaller than 2.5 kPa were calibrated using a Betz manometer with an accuracy of 2.5 Pa, while the other diaphragms were calibrated using a low pressure controlled air manometer with an accuracy of 10 Pa.

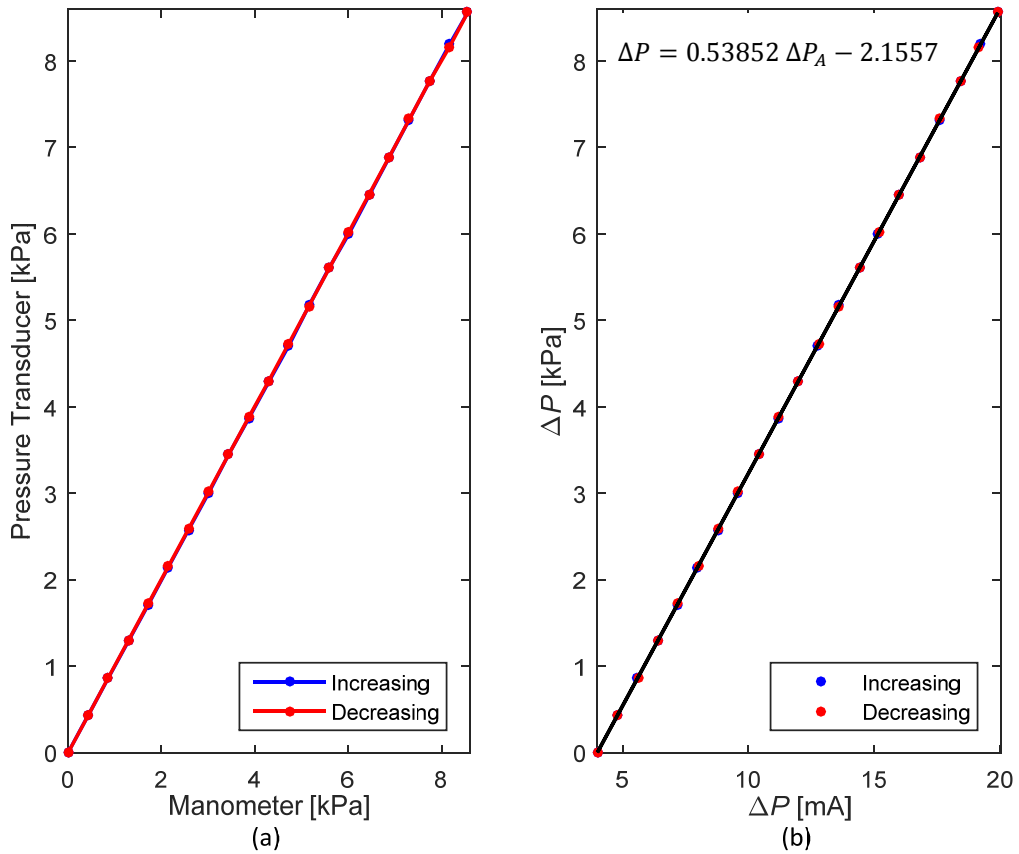

Fig. A.5: Pressure drop measurements using an 8.6 kPa diaphragm as a function of (a) the pressure drop measured by the manometer and (b) the current signal.

The amplifier was adjusted such that the zero of the manometer corresponded to 4 mA in the Labview program and the full-scale corresponded to 20 mA. The current signal obtained from the Labview program was converted to a pressure reading in MATLAB via interpolation. Figure A.5 contains sample plots of the pressure drop measurements using an 8.6 kPa diaphragm as a function of (a) the pressure

drop measured using the manometer and (b) the current signal. A linear curve fit was done to obtain the relationship between the pressure measurements and the current signals.

The equation of the linear curve fit was used during the data reduction of the actual tests. However, after each start-up of the pump, the pressure taps and pressure transducers were bled to ensure that there was no air in the system. A pressure reading, consisting of 200 measuring points, was then taken during no-flow conditions and the average was used as the offset. The no-flow condition was obtained by opening the bypass valve and closing the supply valve to ensure that there was water supply for the pump, but not through the test section. The final pressure transducer calibration equation for the 8.6 kPa diaphragm used in the data reduction program was thus:

$$\Delta P_{8.6\,\mathrm{kPa}} = 0.53852\,\Delta P_A - 2.1557 - \mathrm{offset} \qquad \text{A.2}$$

According to the manufacturer's specifications, the diaphragms have an accuracy of 0.25% of the full-scale value. The linear regression analysis and uncertainty analysis indicate that a maximum uncertainty of 0.17% was obtained at the full-scale of the 8.6 kPa diaphragm. As this was less than the accuracy which was specified by the manufacturer, 0.25% of the full-scale value was used as the uncertainty of the 8.6 kPa diaphragm. Due to the high accuracy manometers that were used to calibrate the pressure transducers, the uncertainties of the other pressure transducer diaphragms were also less than 0.25%, which was specified by the manufacturers. Therefore, 0.25% of the full-scale value was used as the uncertainty of all the pressure transducer diaphragms.

A.5. Conclusion

This appendix contained the calibration procedure and results of the Pt100 probes, thermocouples and pressure transducers. The Pt100 probes were calibrated in a thermostat-controlled bath with an accuracy of 0.01 °C, against a thermometer with an accuracy of 0.03 °C. The calculated uncertainty of the Pt100 probes was less than the accuracy which was specified by the manufacturer, therefore specified accuracy of 0.06 °C was used as the uncertainty of the Pt100 probes.

The thermostat-controlled bath and Pt100 probes were used to calibrate the thermocouples. In situ calibration was used for the thermocouples because the properties of the thermocouple junction were likely to change when the thermocouple was soldered to the test section. The average deviation between the thermocouple and Pt100 probe measurements along the 11.5 mm test section for temperatures between 20 °C and 60 °C was 0.43 °C before calibration and reduced to 0.009 °C after calibration. Similarly, for the 4 mm test section, the average deviation was 0.75 °C before calibration and reduced to 0.044 °C after calibration. The maximum thermocouple uncertainty in the 11.5 mm and 4 mm test sections was 0.0649 °C and 0.101 °C, while the accuracy of the thermocouples was specified by the manufacturers to be 0.1 °C. As the specified uncertainty was greater than the calculated uncertainties, 0.1 °C was used as the uncertainty of all the thermocouples.

To improve the accuracy of the pressure measurements, different sets of diaphragms were used for Reynolds numbers between 500 and 4 000 and Reynolds numbers between 2 000 and 10 000. The diaphragms with a full-scale smaller than 2.5 kPa were calibrated using a Betz manometer with an accuracy of 2.5 Pa, while the other diaphragms were calibrated using a low pressure controlled air manometer with an accuracy of 10 Pa. A linear curve fit was done to obtain the relationship between the pressure drop measurements and the current signals of each diaphragm. Due to the high accuracy manometers that were used to calibrate the pressure transducers, the uncertainties were less than

0.25%, which was specified by the manufacturers. Therefore, 0.25% of the full-scale value was used as the uncertainty of all the pressure transducer diaphragms.

A.6. Nomenclature

c	y-intercept
D	Inner diameter
m	Slope
P	Pressure
T	Temperature
x	Distance from inlet

A.6.1. Subscripts

8.6 kPa	Pressure transducer diaphragm with a full-scale of 8.6 kPa
A	Current signal
cal	Calibrated value
$uncal$	Uncalibrated value

B. Uncertainty Analysis

B.1. Introduction

An uncertainty analysis was conducted to determine the uncertainty of the parameters that were relevant to this study. The details of the uncertainty analysis method, accuracy of the instrumentation used, as well as the uncertainty analysis results, are given in this appendix.

B.2. Theory

Two types of errors, bias and precision, arise during measurement processes. The bias error determines the accuracy of the measurement and is normally specified by the manufacturer of the instrument. These errors result from calibration, imperfections in measuring equipment, etc. The precision error relates to the scatter in the data, because it determines the precision of the data. The precision errors are always present and are due to variations in the measurement process, electrical noise, etc. The magnitudes of the bias and precision errors correspond to the 95% probability that the actual error will not be more than the estimate. The uncertainty in a single measurement is based on the bias and precision and is calculated as follows [1]:

$$\delta x_i = \left(b_i^2 + p_i^2\right)^{1/2} \tag{B.1}$$

x_i is a single observation and δx_i represents the standard deviation multiplied with Student's *t*-variable [1]. The result *R* of a measurement is a function of several variables and is calculated from a group of equations.

$$R = R(x_1, x_2, x_3, \ldots, x_n) \tag{B.2}$$

Once the uncertainties of x_i are known, the uncertainty in *R* can be determined as follows:

$$\delta R = \frac{\partial R}{\partial x_i}\delta x_i \tag{B.3}$$

The sensitivity coefficient, δR, is used to determine the effect that x_i has on the overall uncertainty. The root sum square method can be used to determine the uncertainty for several independent variables:

$$\delta R = \left[\sum_{i=1}^{n}\left(\frac{\partial R}{\partial x_i}\delta x_i\right)^2\right]^{1/2} \tag{B.4}$$

The precision of the Pt100 probes, thermocouples and pressure transducers, which was used as the bias of the temperature and pressure drop measurements, was determined used linear regression analysis. Regression analysis determines a mathematical relation between two or more variables. The value of *x* is usually known and the value of *y* is obtained from measurements, therefore the uncertainty results from the *y* variable [1]. The uncertainty of the *y* variable is determined using Eq. B.5:

$$\delta y = \pm t S_{yx} \sqrt{\frac{1}{N} + \frac{1}{M} + \frac{(x_i - \bar{x})^2}{S_{xx}}} \quad \text{B.5}$$

where S_{xx} is defined as follows:

$$S_{xx} = \sum_{i=1}^{N} (x_i - \bar{x})^2 \quad \text{B.6}$$

S_{yx} is obtained by first calculating S_{xy} and the parameters a and b:

$$S_{xy} = \sum_{i=1}^{N} (x_i - \bar{x})(y_i - \bar{y}) \quad \text{B.7}$$

$$b = \frac{S_{xy}}{S_{xx}} \quad \text{B.8}$$

$$a = \bar{y} - b\bar{x} \quad \text{B.9}$$

$$y_{ci} = a + bx_i \quad \text{B.10}$$

$$S_{yx} = \sqrt{\frac{\sum_{i=1}^{N} (y_i - y_{ci})^2}{N - 2}} \quad \text{B.11}$$

To obtain the uncertainty in the x variable, the uncertainty in y is divided by the slope of the regression line.

$$\delta x = \frac{\delta y}{m} \quad \text{B.12}$$

B.3. Instruments

For all instruments, the bias was considered as the accuracy specified by the manufacturer. The precision was obtained from the standard deviation of the 200 measuring points which were logged during each measurement. This was then multiplied by Student's t-variable to fall within the 95% confidence region.

B.3.1. Pt100 probes

The Pt100 probes were calibrated between 15 °C and 65 °C at 2.5 °C intervals, using a DigiCal DCS2 digital thermometer with an accuracy of 0.03 °C. As a linear relationship between the Pt100 probes and thermometer existed, a linear curve fit was done to obtain the calibration curve. The accuracy of the thermometer was used as the bias, and the precision was calculated using Eqs. B.5 to B.12, while the overall uncertainty was calculated using Eq. B.1. The uncertainty of the Pt100 probes was calculated to be between 0.0305 °C and 0.0311 °C, which is less than the manufacturer's specified accuracy of 0.06 °C. To be conservative, an uncertainty of 0.06 °C was therefore used for the Pt100 probes.

B.3.2. Thermocouples

The Pt100 probes with an accuracy of 0.06 °C and a thermostat-controlled bath with an accuracy of 0.03 °C were used to calibrate the thermocouples between 15 °C and 60 °C at 2.5 °C intervals. Similar

to the Pt100 probes, a linear relationship existed between the thermocouples and Pt100 probes, therefore the calibration curve was obtained through a linear curve fit.

The accuracy of the Pt100 probe was used as the bias, and the precision was calculated using Eqs. B.5 to B.12, while the overall uncertainty was calculated using Eq. B.1. The uncertainty of the thermocouples was calculated to be between 0.0605 °C and 0.0649 °C for the 11.5 mm test section, and between 0.0602 °C and 0.101 °C for the 4 mm test section. Because this was less than the accuracy of 0.1 °C, which was specified by the manufacturer, 0.1 °C was used as the uncertainty of all the thermocouples.

It was found that the deviation between the thermocouple and Pt100 probe measurements in the 11.5 mm test section was less than in the 4 mm test section before and after calibration. This was probably due to the lower thermal conductivity of the thermal adhesive (used to attach the thermocouples to the 4 mm test section) compared with the solder (used to attach the thermocouples to the 11.5 mm test section), and explains why the uncertainties of the thermocouples in the 4 mm test section were slightly higher than in the 11.5 mm test section.

B.3.3. Coriolis flow meters

Three Coriolis flow meters with different capacities were used to measure the mass flow rate. The bias of the flow meters was 0.05% of the full-scale. Thus, the accuracy of the 108 ℓ/h, 330 ℓ/h and 2 108 ℓ/h flow meters was 0.054 ℓ/h, 0.165 ℓ/h and 1.09 ℓ/h respectively.

B.3.4. Pressure transducers

Differential pressure transducers with interchangeable diaphragms were used to measure the pressure drop across the different tube lengths in the 11.5 mm test section. DP103 pressure transducers were used to measure the pressure drop across the 1.5 m and 2 m lengths because diaphragms with a smaller full-scale (and thus higher accuracy) could be used in these pressure transducers. DP15 pressure transducers were used to measure the pressure drop across the other tube lengths. The diaphragms with a full-scale smaller than 2.5 kPa were calibrated using a Betz manometer with an accuracy of 2.5 Pa, while the other diaphragms were calibrated using a low pressure controlled air manometer with an accuracy of 10 Pa. The accuracies of the manometers were used as the bias of each pressure transducer. During the pressure transducer calibration, 21 data points, each consisting of 200 measuring points, were taken between zero and the maximum of each diaphragm. As a linear relationship between the pressure transducer and the manometer existed, a linear curve fit was done through the calibration points to obtain the calibration curve.

Similar to the Pt100 probe and thermocouple calibrations, the precision of the pressure transducers was calculated using Eqs. B.5 to B.12, while the overall uncertainty was calculated using Eq. B.1. Due to the high accuracy manometers that were used to calibrate the pressure transducers, the uncertainties were less than 0.25%, which was specified by the manufacturers. Therefore, 0.25% of the full-scale value was used as the uncertainty of all the pressure transducer diaphragms.

B.3.5. Power supplies

Two PS 8360-30 2U power supplies were used to heat the 11.5 mm test section. Both power supplies had a maximum power output of 3 kW, maximum voltage of 360 V and maximum current of 15 A. The accuracies of both measured voltages and currents were 0.2% of the nominal value.

As the 4 mm test section was heated by passing current through the stainless steel tube, a PS90 40-60 power supply with a higher current output was used. The power supply had a maximum power output of 3 kW, maximum voltage of 40 V and maximum current of 60 A. The voltage and current accuracies were both 0.2% of the nominal value.

B.3.6. Diameter

A split-ball instrument and a Vernier calliper with an accuracy of 20 µm were used to measure the inner diameter of the test sections.

B.3.7. Length

A measuring tape with an accuracy of 1 mm was used to measure the length of the test sections.

B.4. Fluid properties

The properties of water were calculated using the thermophysical equations of Popiel and Wojtkowiak [2], and the uncertainties associated with these equations are summarised in Table B.1.

Table B.1: Uncertainties of fluid properties.

Property	C_p [J/kg.K]	k [W/m.K]	Pr [-]	β [1/K]	ρ [kg/m^3]	μ [kg/m.s]
Uncertainty [%]	0.06	2	2.3	0.5	0.004	1

B.5. Calculated parameters

B.5.1. Temperatures

Both test sections contained 27 thermocouple stations, each with three or four thermocouples. A representative temperature at the thermocouple station was obtained by taking the average of the n thermocouples (with n = 3 or n = 4):

$$\bar{T}_s = \frac{T_1 + T_2 + \cdots + T_n}{n} \tag{B.13}$$

The uncertainty of this temperature was calculated as follows:

$$\delta\bar{T}_s = \left[\left(\frac{\delta T_1}{n}\right)^2 + \left(\frac{\delta T_2}{n}\right)^2 + \cdots + \left(\frac{\delta T_n}{n}\right)^2\right]^{1/2} \tag{B.14}$$

B.5.2. Heat transfer area

The uncertainty of the heat transfer area was:

$$A = \pi D l \tag{B.15}$$

$$\delta A = \left[\left(\frac{\partial A}{\partial D}\delta D\right)^2 + \left(\frac{\partial A}{\partial L}\delta L\right)^2\right]^{1/2}$$

$$\delta A = \left[(\pi L \delta D)^2 + (\pi D \delta L)^2\right]^{1/2} \tag{B.16}$$

B.5.3. Cross-sectional area

The uncertainty of the cross-sectional area was calculated as follows:

$$A_c = \frac{\pi}{4} D^2 \tag{B.17}$$

$$\delta A_c = \left[\left(\frac{\partial A_c}{\partial D} \delta D \right)^2 \right]^{1/2}$$

$$\delta A_c = \frac{\pi D}{2} \delta D \tag{B.18}$$

B.5.4. Flow velocity

The uncertainty of the flow velocity was:

$$V = \frac{\dot{m}}{\rho A_c} \tag{B.19}$$

$$\delta V = \left[\left(\frac{\partial V}{\partial \dot{m}} \delta \dot{m} \right)^2 + \left(\frac{\partial V}{\partial \rho} \delta \rho \right)^2 + \left(\frac{\partial V}{\partial A_c} \delta A_c \right)^2 \right]^{1/2}$$

$$\delta V = \left[\left(\frac{1}{\rho A_c} \delta \dot{m} \right)^2 + \left(-\frac{\dot{m}}{\rho^2 A_c} \delta \rho \right)^2 + \left(-\frac{\dot{m}}{\rho A_c^2} \delta A_c \right)^2 \right]^{1/2} \tag{B.20}$$

B.5.5. Reynolds number

The uncertainty of the Reynolds number was determined as:

$$Re = \frac{\dot{m} D}{\mu A_c} \tag{B.21}$$

$$\delta Re = \left[\left(\frac{\partial Re}{\partial \dot{m}} \delta \dot{m} \right)^2 + \left(\frac{\partial Re}{\partial D} \delta D \right)^2 + \left(\frac{\partial Re}{\partial \mu} \delta \mu \right)^2 + \left(\frac{\partial Re}{\partial A_c} \delta A_c \right)^2 \right]^{1/2}$$

$$\delta Re = \left[\left(\frac{D}{\mu A_c} \delta \dot{m} \right)^2 + \left(\frac{\dot{m}}{\mu A_c} \delta D \right)^2 + \left(-\frac{\dot{m} D}{\mu^2 A_c} \delta \mu \right)^2 + \left(-\frac{\dot{m} D}{\mu A^2} \delta A_c \right)^2 \right]^{1/2} \tag{B.22}$$

B.5.6. Heat flux

The uncertainty of the heat flux was calculated as follows:

$$\dot{q} = \frac{\dot{Q}_w}{A} = \frac{\dot{m} C_p (T_o - T_i)}{\pi D L} \tag{B.23}$$

$$\delta \dot{q} = \left[\left(\frac{\partial \dot{q}}{\partial \dot{m}} \delta \dot{m} \right)^2 + \left(\frac{\partial \dot{q}}{\partial C_p} \delta C_p \right)^2 + \left(\frac{\partial \dot{q}}{\partial T_o} \delta T_o \right)^2 + \left(\frac{\partial \dot{q}}{\partial T_i} \delta T_i \right)^2 + \left(\frac{\partial \dot{q}}{\partial D} \delta D \right)^2 + \left(\frac{\partial \dot{q}}{\partial L} \delta L \right)^2 \right]^{1/2}$$

$$\delta \dot{q} = \left[\left(\frac{C_p (T_o - T_i)}{\pi D L} \delta \dot{m} \right)^2 + \left(\frac{\dot{m} (T_o - T_i)}{\pi D L} \delta C_p \right)^2 + \left(\frac{\dot{m} C_p}{\pi D L} \delta T_o \right)^2 + \left(-\frac{\dot{m} C_p}{\pi D L} \delta T_i \right)^2 + \left(-\frac{\dot{m} C_p (T_o - T_i)}{\pi D^2 L} \delta D \right)^2 + \left(\frac{-\dot{m} C_p (T_o - T_i)}{\pi D L^2} \delta L \right)^2 \right]^{1/2} \tag{B.24}$$

B.5.7. Heat transfer coefficient

The uncertainty of the heat transfer coefficient was:

$$h = \frac{\dot{q}}{(T_s - T_b)} \tag{B.25}$$

$$\delta h = \left[\left(\frac{\partial h}{\partial \dot{q}}\delta\dot{q}\right)^2 + \left(\frac{\partial h}{\partial T_s}\delta T_s\right)^2 + \left(\frac{\partial h}{\partial T_b}\delta T_b\right)^2\right]^{1/2}$$

$$\delta h = \left[\left(\frac{1}{T_s - T_b}\delta\dot{q}\right)^2 + \left(\frac{-\dot{q}}{(T_s - T_b)^2}\delta T_s\right)^2 + \left(\frac{\dot{q}}{(T_s - T_b)^2}\delta T_b\right)^2\right]^{1/2} \tag{B.26}$$

B.5.8. Nusselt number

The uncertainty of the Nusselt number was determined as follows:

$$Nu = \frac{hD}{k} \tag{B.27}$$

$$\delta Nu = \left[\left(\frac{\partial Nu}{\partial h}\delta h\right)^2 + \left(\frac{\partial Nu}{\partial D}\delta D\right)^2 + \left(\frac{\partial Nu}{\partial k}\delta k\right)^2\right]^{1/2}$$

$$\delta Nu = \left[\left(\frac{D}{k}\delta h\right)^2 + \left(\frac{h}{k}\delta D\right)^2 + \left(-\frac{hD}{k^2}\delta k\right)^2\right]^{1/2} \tag{B.28}$$

B.5.9. Colburn *j*-factor

The uncertainty of the Colburn *j*-factor was:

$$j = \frac{Nu}{RePr^{1/3}} \tag{B.29}$$

$$\delta j = \left[\left(\frac{\partial j}{\partial Nu}\delta Nu\right)^2 + \left(\frac{\partial j}{\partial Re}\delta Re\right)^2 + \left(\frac{\partial j}{\partial Pr}\delta Pr\right)^2\right]^{1/2}$$

$$\delta j = \left[\left(\frac{1}{RePr^{1/3}}\delta Nu\right)^2 + \left(-\frac{Nu}{Re^2 Pr^{1/3}}\delta Re\right)^2 + \left(-\frac{1}{3}\frac{Nu}{RePr^{4/3}}\delta Pr\right)^2\right]^{1/2} \tag{B.30}$$

B.5.10. Graetz number

The uncertainty of the Graetz number was determined as follows:

$$Gz = \frac{RePrD}{L} \tag{B.31}$$

$$\delta Gz = \left[\left(\frac{\partial Gz}{\partial Re}\delta Re\right)^2 + \left(\frac{\partial Gz}{\partial Pr}\delta Pr\right)^2 + \left(\frac{\partial Gz}{\partial D}\delta D\right)^2 + \left(\frac{\partial Gz}{\partial L}\delta L\right)^2\right]^{1/2}$$

$$\delta Gz = \left[\left(\frac{PrD}{L}\delta Re\right)^2 + \left(\frac{ReD}{L}\delta Pr\right)^2 + \left(\frac{RePr}{L}\delta D\right)^2 + \left(\frac{-RePrD}{L^2}\delta L\right)^2\right]^{1/2} \tag{B.32}$$

B.5.11. Grashof number

The uncertainty of the Grashof number was calculated as follows:

$$Gr = \frac{g\beta(T_s - T_m)D^3}{\nu^2} = \frac{g\beta\rho^2(T_s - T_m)D^3}{\mu^2} \quad \text{B.33}$$

$$\delta Gr = \left[\left(\frac{\partial Gr}{\partial \beta}\delta\beta\right)^2 + \left(\frac{\partial Gr}{\partial \rho}\delta\rho\right)^2 + \left(\frac{\partial Gr}{\partial T_s}\delta T_s\right)^2 + \left(\frac{\partial Gr}{\partial T_m}\delta T_m\right)^2 + \left(\frac{\partial Gr}{\partial D}\delta D\right)^2 + \left(\frac{\partial Gr}{\partial \mu}\delta\mu\right)^2\right]^{1/2}$$

$$\delta Gr = \left[\left(\frac{g\rho^2(T_s - T_m)D^3}{\mu^2}\delta\beta\right)^2 + \left(\frac{2g\beta\rho(T_s - T_m)D^3}{\mu^2}\delta\rho\right)^2 + \left(\frac{g\beta\rho^2 D^3}{\mu^2}\delta T_s\right)^2 + \left(\frac{-g\beta\rho^2 D^3}{\mu^2}\delta T_m\right)^2 + \left(\frac{3g\beta\rho^2(T_s - T_m)D^2}{\mu^2}\delta D\right)^2 + \left(\frac{-2g\beta\rho^2(T_s - T_m)D^3}{\mu^3}\delta\mu\right)^2\right]^{1/2} \quad \text{B.34}$$

B.5.12. Modified Grashof number

The uncertainty of the modified Grashof number was determined as follows:

$$Gr^* = \frac{g\beta\dot{q}D^4}{\nu^2 k} = \frac{g\beta\rho^2\dot{q}D^4}{\mu^2 k} \quad \text{B.35}$$

$$\delta Gr^* = \left[\left(\frac{\partial Gr^*}{\partial \beta}\delta\beta\right)^2 + \left(\frac{\partial Gr^*}{\partial \rho}\delta\rho\right)^2 + \left(\frac{\partial Gr^*}{\partial \dot{q}}\delta\dot{q}\right)^2 + \left(\frac{\partial Gr^*}{\partial D}\delta D\right)^2 + \left(\frac{\partial Gr^*}{\partial \mu}\delta\mu\right)^2 + \left(\frac{\partial Gr^*}{\partial k}\delta k\right)^2\right]^{1/2}$$

$$\delta Gr^* = \left[\left(\frac{g\rho^3\dot{q}D^4}{\mu^2 k}\delta\beta\right)^2 + \left(\frac{2g\beta\rho\dot{q}D^4}{\mu^2 k}\delta\rho\right)^2 + \left(\frac{g\beta\rho^2 D^4}{\mu^2 k}\delta\dot{q}\right)^2 + \left(\frac{4g\beta\rho^2\dot{q}D^3}{\mu^2 k}\delta D\right)^2 + \left(\frac{-2g\beta\rho^2\dot{q}D^4}{\mu^3 k}\delta\mu\right)^2 + \left(\frac{-g\beta\rho^2\dot{q}D^4}{\mu^2 k^2}\delta k\right)^2\right]^{1/2} \quad \text{B.36}$$

B.5.13. Rayleigh and modified Rayleigh numbers

The uncertainty of the Rayleigh number was calculated as follows:

$$Ra = GrPr \quad \text{B.37}$$

$$\delta Ra = \left[\left(\frac{\partial Ra}{\partial Gr}\delta Gr\right)^2 + \left(\frac{\partial Ra}{\partial Pr}\delta Pr\right)^2\right]^{1/2}$$

$$\delta Ra = \left[(Pr\delta Gr)^2 + (Gr\delta Pr)^2\right]^{1/2} \quad \text{B.38}$$

Similarly, for the modified Rayleigh number:

$$\delta Ra^* = \left[(Pr\delta Gr^*)^2 + (Gr^*\delta Pr)^2\right]^{1/2} \quad \text{B.39}$$

B.5.14. Richardson and modified Richardson numbers

The uncertainty of the Richardson number was determined as follows:

$$Ri = \frac{Gr}{Re^2} \tag{B.40}$$

$$\delta Ri = \left[\left(\frac{\partial Ri}{\partial Gr}\delta Gr\right)^2 + \left(\frac{\partial Ri}{\partial Re}\delta Re\right)^2\right]^{1/2}$$

$$\delta Ri = \left[\left(\frac{1}{Re^2}\delta Gr\right)^2 + \left(\frac{-2Gr}{Re^3}\delta Re\right)^2\right]^{1/2} \tag{B.41}$$

Similarly, for the modified Rayleigh number:

$$\delta Ri^* = \left[\left(\frac{1}{Re^2}\delta Gr^*\right)^2 + \left(\frac{-2Gr^*}{Re^3}\delta Re\right)^2\right]^{1/2} \tag{B.42}$$

B.5.15. Friction factor

The uncertainty of the friction factor was:

$$f = \frac{2\Delta P D}{\rho V^2 L} = \frac{\Delta P \rho D^5 \pi^2}{8\dot{m}^2 L} \tag{B.43}$$

$$\delta f = \left[\left(\frac{\partial f}{\partial \Delta P}\delta \Delta P\right)^2 + \left(\frac{\partial f}{\partial D}\delta D\right)^2 + \left(\frac{\partial f}{\partial \rho}\delta \rho\right)^2 + \left(\frac{\partial f}{\partial V}\delta V\right)^2 + \left(\frac{\partial f}{\partial L}\delta L\right)^2\right]^{1/2}$$

$$\delta f = \left[\left(\frac{2D}{\rho V^2 L}\delta \Delta P\right)^2 + \left(\frac{2\Delta P}{\rho V^2 L}\delta D\right)^2 + \left(-\frac{2\Delta P\, D}{\rho^2 V^2 L}\delta \rho\right)^2 + \left(-\frac{4\Delta P\, D}{\rho V^3 L}\delta u\right)^2 + \left(-\frac{2\Delta P\, D}{\rho V^2 L^2}\delta L\right)^2\right]^{1/2} \tag{B.44}$$

B.6. Results

This section gives the uncertainty analysis results of the Reynolds number, Graetz number, Nusselt number, Colburn *j*-factor, Grashof and modified Grashof numbers, Rayleigh and modified Rayleigh numbers, Richardson and modified Richardson numbers, as well as the friction factor, as a function of bulk Reynolds number. The uncertainties are also summarised in Table 3.3 and Table 3.4 for three different heat fluxes in the 11.5 mm and 4 mm test sections. Sample calculations for the Reynolds number, Nusselt number, Colburn *j*-factor and friction factors are given in Everts [3].

The Reynolds number and Graetz number uncertainties as a function of bulk Reynolds number are summarised in Fig. B.1 for different heat fluxes in the 4 mm and 11.5 mm test sections. Figure B.1(a) indicates that the Reynolds number uncertainty decreased with increasing Reynolds number from approximately 1.6% at a Reynolds number of 900, to 1.5% just before transition started. In the transitional flow regime, the Reynolds number uncertainty increased to approximately 2% (depending on the heat flux applied) due to the fluctuations that occurred in this flow regime. From Eq. B.1, it follows that the uncertainties consist of two components, namely the bias and precision. During transition, severe mass flow rate fluctuations occurred, which led to greater standard deviations, and thus greater precision errors and mass flow rate uncertainties. Because the Reynolds number depended on the mass flow rate, these uncertainties increased as well. The Reynolds number

uncertainty remained approximately constant at 1.5% for all Reynolds numbers and heat fluxes in the quasi-turbulent and turbulent flow regimes.

Figure B.1(b) indicates that the Reynolds number uncertainty in the 11.5 mm test section decreased from 1.6% at a Reynolds number of 700, to 1% at a Reynolds number of 2 000, and then remained constant as the Reynolds number was increased further. The increasing Reynolds number uncertainty due to the mass flow rate fluctuations in the transitional flow regime was not obtained in the 11.5 mm test section, because the mass flow meters were located upstream of the 11.5 test section, while it was located downstream of the 4 mm test section (Fig. 3.1). Therefore, the mass flow meter could measure the fluctuations in flow rate when the flow was in the transitional flow regime for the 4 mm test section, but not for the 11.5 mm test section.

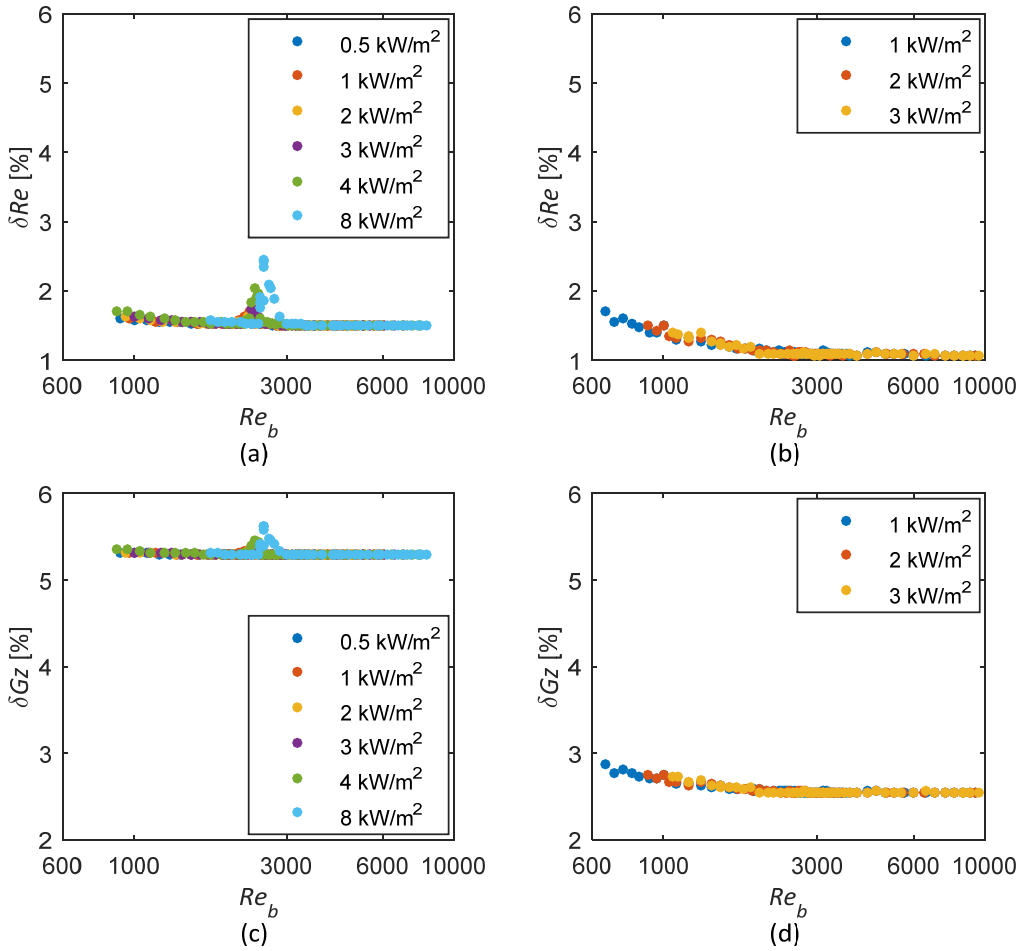

Fig. B.1: Reynolds number uncertainty in the (a) 4 mm test section and (b) 11.5 mm test section, and Graetz number uncertainty in the (c) 4 mm test section and (d) 11.5 mm test section, as a function of bulk Reynolds number for different heat fluxes.

Three different flow meters were used during the experiments in the 11.5 mm test section to minimise the uncertainty of the mass flow rate measurements. For Reynolds numbers less than 1 200, a flow meter with a maximum flow rate of 108 ℓ/h was used, while a large flow meter with a maximum limit of 2 180 ℓ/h was used for Reynolds numbers greater than 4 600. For mass flow rates in-between, a flow meter with a maximum capacity of 330 ℓ/h was used. This explains the slight (visible but negligible) discontinuities in the Reynolds number uncertainties at bulk Reynolds numbers of 1 200

and 4 600 in Fig. B.1(b). As the Reynolds number uncertainty is not only a function of the velocity of the fluid, but also the density, viscosity and tube diameter, there was no significant difference between the Reynolds number uncertainties where different flow meters were used. Furthermore, the Reynolds number uncertainty remained approximately constant for all heat fluxes.

Figure B.1(c) and (d) indicate that, as expected, the Graetz number uncertainties in both test sections were higher than the Reynolds number uncertainties, because the Graetz number is also a function of the diameter and length of the test section. Furthermore, the uncertainties in the 11.5 mm test section (Fig. B.1(d)) were significantly less than for the 4 mm test section (Fig. B.1(c)) due to the larger tube diameter and longer tube length. The trend of the Reynolds number and Graetz number uncertainties was similar, because the Prandtl number, tube diameter and tube length uncertainties, which are used in addition to the Reynolds number uncertainty in the calculation of the Graetz number uncertainty, are approximately independent of Reynolds number.

The Nusselt number and Colburn *j*-factor uncertainties for different heat fluxes in the 4 mm and 11.5 mm test sections are summarised in Fig. B.2. Figure B.2(a) and (b) indicate that the laminar Nusselt number uncertainties were approximately independent of Reynolds number, but decreased with increasing heat flux. The laminar Nusselt number uncertainties were less than 10% and 5% for forced and mixed convection conditions respectively. This was due to the increased temperature differences, which led to decreased temperature uncertainties. From Eq. B.28, it follows that the Nusselt number uncertainty was a function of the heat transfer coefficient uncertainty, which was, in turn, a function of the temperature uncertainty, as well as the heat flux uncertainty. The surface-fluid temperature difference decreased with increasing heat flux, which led to increased uncertainties. Furthermore, as the heat flux was calculated using Eq. 3.6, it depended on the temperature difference between the inlet and outlet of the test section, which also decreased with decreasing heat flux or increasing Reynolds number. When the tube diameter was increased, the surface-fluid temperature differences increased, which explains why, at the same heat flux, the Nusselt number uncertainties in the 11.5 mm test section (Fig. B.2(b)) were lower than in the 4 mm test section (Fig. B.2(a)).

In the transitional flow regime, the Nusselt number uncertainties increased to approximately 10% (depending on the heat flux and tube diameter) due to the temperature fluctuations. The increased standard deviation of the temperature measurements led to increased precision errors and temperature uncertainties. The Nusselt number uncertainties in the quasi-turbulent and turbulent flow regimes increased with increasing Reynolds number due to the decreasing surface-fluid temperatures, as well as the decreasing temperature difference between the inlet and outlet of the test section. The average Nusselt number uncertainty at a Reynolds number of 6 000 was 13%.

Figure B.2(c) and (d) indicate that, as expected, the Colburn *j*-factor uncertainties in both test sections were slightly higher than the Nusselt number uncertainties, because the Colburn *j*-factor is also a function of Reynolds number and Prandtl number. However, as the Reynolds number and Prandtl number uncertainties were small and not significantly affected by Reynolds number, the trends of the Nusselt number and Colburn *j*-factor uncertainties were similar.

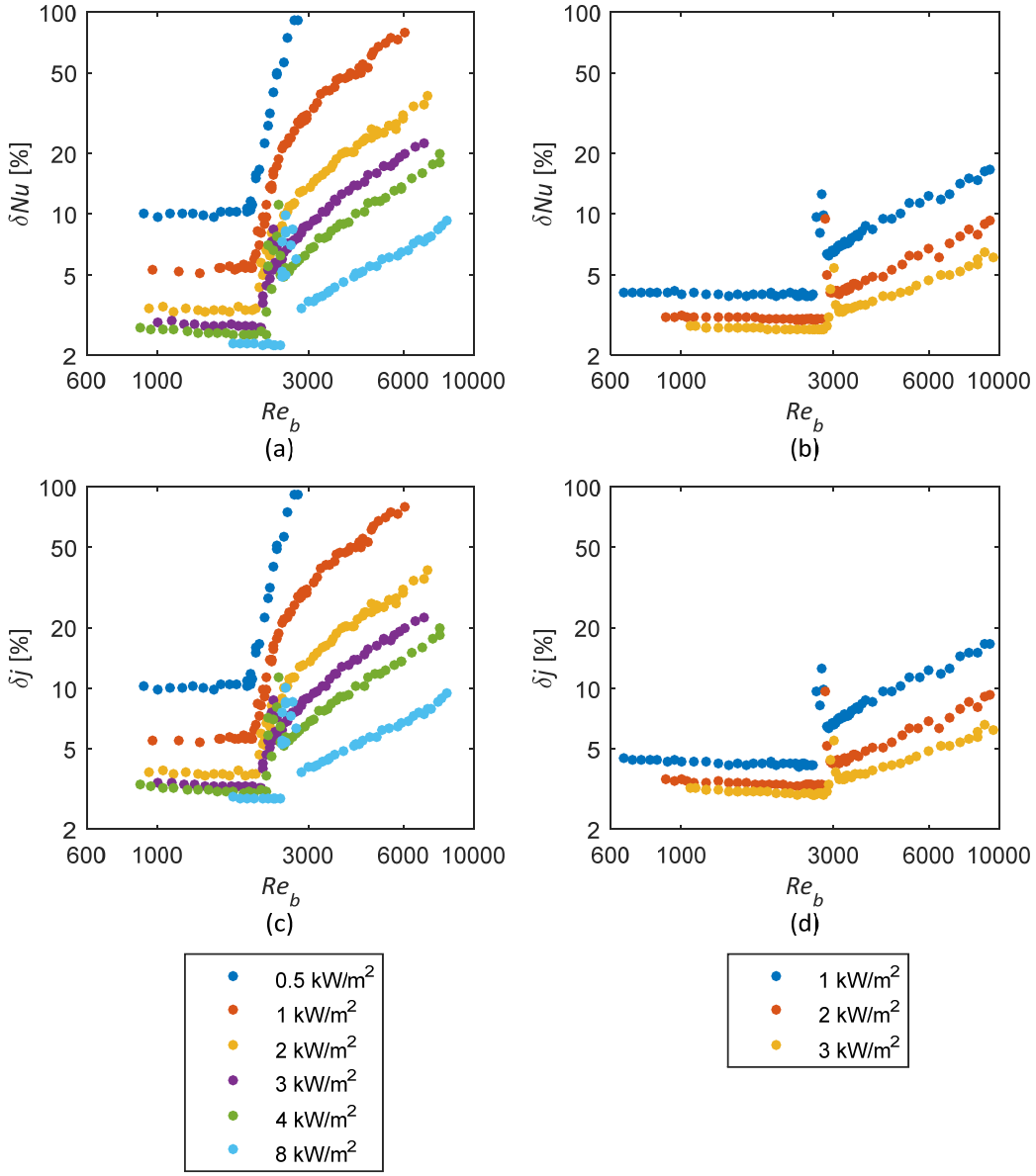

Fig. B.2: Nusselt number uncertainties in the (a) 4 mm test section and (b) 11.5 mm test section, and Colburn *j*-factor uncertainties in the (c) 4 mm test section and (d) 11.5 mm test section, as a function of bulk Reynolds number for different heat fluxes.

The uncertainties for the Grashof numbers and Rayleigh numbers, as well as the modified Grashof numbers and modified Rayleigh numbers, for different heat fluxes in the 4 mm and 11.5 mm test sections are summarised in Fig. B.3. The Grashof number and Rayleigh number uncertainties are represented by the filled markers, while the empty markers represent the modified Grashof number and modified Rayleigh number uncertainties. Because the Grashof number is a function of the surface-fluid temperature difference, the trend of the Grashof number and Rayleigh number uncertainties in Fig. B.3 is similar to the Nusselt number and Colburn *j*-factor uncertainties in Fig. B.2. The uncertainties increased with decreasing heat flux, increasing Reynolds number and decreasing tube diameter, due to the increased temperature uncertainties caused by the decreasing surface-fluid temperature differences.

In the laminar flow regime, the Grashof number and Rayleigh number uncertainties were approximately independent of Reynolds number. Figure B.3(a) indicates that the Grashof number uncertainty at a heat flux of 1 kW/m^2 in the 4 mm test section was approximately 8%, but decreased to 6% when the heat flux was increased to 3 kW/m^2. As the tube diameter was increased to 11.5 mm (Fig. B.3(b)), the Grashof number uncertainties at a heat flux of 3 kW/m^2 decreased significantly to approximately 2%. In the transitional flow regime, the temperature fluctuations caused the Grashof number (as well as the Rayleigh number) uncertainties to increase. Both Grashof number and Rayleigh number uncertainties increased significantly with increasing Reynolds number and decreasing heat flux in the quasi-turbulent and turbulent flow regimes due to the decreasing surface-fluid temperature differences.

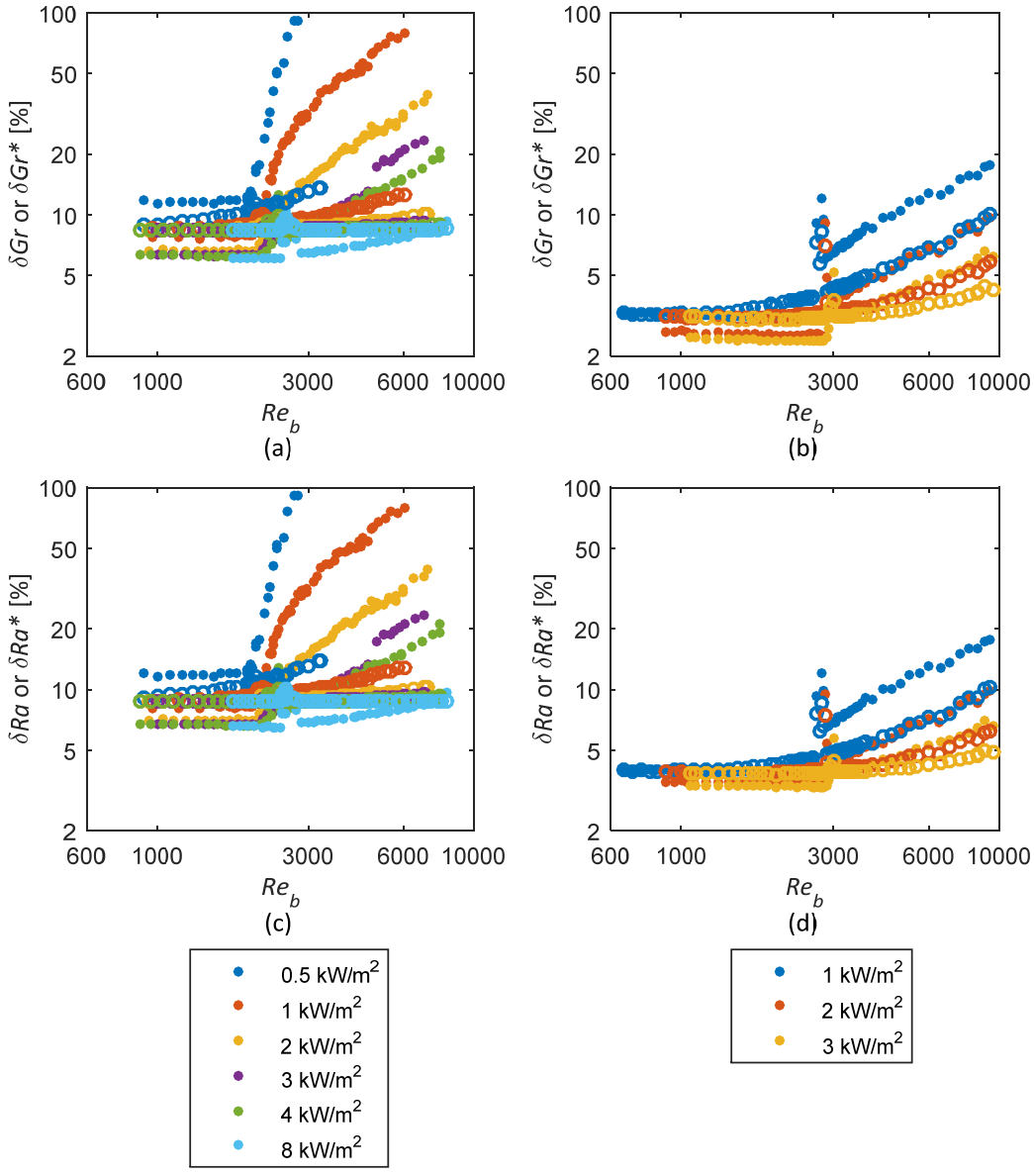

Fig. B.3: Grashof number and modified Grashof number uncertainties in the (a) 4 mm test section and (b) 11.5 mm test section, and Rayleigh number and modified Rayleigh number uncertainties in the (c) 4 mm test section and (d) 11.5 mm test section, as a function of bulk Reynolds number for different heat fluxes. The Grashof number and Rayleigh number uncertainties are represented by the filled markers, while the empty markers represent the modified Grashof number and modified Rayleigh number uncertainties.

Because the modified Grashof number is a function of heat flux (which remained constant due to the constant heat flux boundary condition), the change in modified Grashof number and modified Rayleigh number uncertainties (empty markers) with Reynolds number, was less than for the Grashof numbers and Rayleigh numbers (filled markers). However, the uncertainties still increased slightly with increasing Reynolds number, because the heat flux uncertainty was a function of the temperature difference between the inlet and outlet of the test section, which decreased with increasing Reynolds number. As expected, the modified Grashof number and modified Rayleigh number uncertainties decreased with increasing heat flux due to the increasing temperature difference between the inlet and outlet of the test section.

Figure B.3 indicates that the modified Grashof number and modified Rayleigh number uncertainties were in general less than the Grashof number and Rayleigh number uncertainties respectively, in the quasi-turbulent and turbulent flow regimes. However, this was not true for the laminar and transitional flow regimes, because the Grashof number and Rayleigh number uncertainties were significantly affected by the surface-fluid temperature difference, and thus heat flux. In the laminar flow regime, the uncertainties of the Grashof numbers and Rayleigh numbers were in general less than for the modified Grashof and modified Rayleigh numbers.

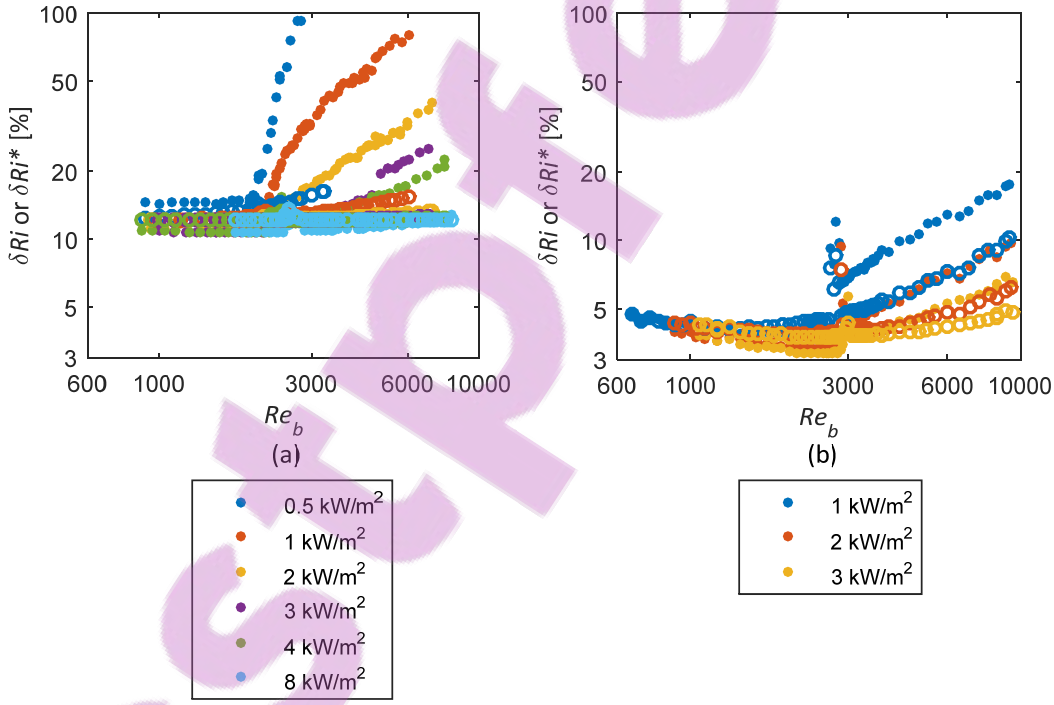

Fig. B.4: Richardson number and modified Richardson number uncertainties in the (a) 4 mm test section and (b) 11.5 mm test section as a function of bulk Reynolds number for different heat fluxes. The Richardson number uncertainties are represented by the filled markers, while the empty markers represent the modified Richardson number uncertainties.

The Richardson number (filled markers) and modified Richardson number (empty markers) uncertainties as a function of bulk Reynolds number for different heat fluxes in the 4 mm and 11.5 mm test sections are summarised in Fig. B.4. The Richardson number uncertainties were slightly higher than the Grashof number uncertainties in Fig. B.3, because it is also a function of the Reynolds number uncertainty. Similar to the Grashof number uncertainties, the Richardson number uncertainties decreased with increasing heat flux, decreasing Reynolds number, as well as increasing tube diameter,

mainly due to the increasing surface-fluid temperature differences. Although it is not clear from the 4 mm results in Fig. B.4(a), it follows from Fig. B.4(b) that the Richardson number uncertainties in the laminar flow regime decreased with increasing Reynolds numbers. This is due to the Richardson number being a function of the Reynolds number uncertainties, which decreased with increasing Reynolds number (Fig. B.1).

Figure B.5 compares the friction factor uncertainties as a function of bulk Reynolds number for different tube lengths in the 11.5 mm test section at different heat fluxes. Figure B.5 indicates that the laminar friction factor uncertainties across the tube lengths 0 m < L < 2 m, 0 m < L < 3 m and 8 m < L < 9.5 m were higher than for the other tube lengths. This was due to the limitations of the pressure transducer diaphragms, because smaller suitable diaphragms were not commercially available. The laminar friction factors for the other tube lengths were approximately 10% at the minimum Reynolds number, and decreased to approximately 2% just before transition started. In the transitional flow regime, the uncertainties increased to approximately 20% due to the fluctuations inside the test section. In the quasi-turbulent and turbulent flow regimes, the uncertainties decreased with increasing Reynolds number, and the uncertainties varied between 1% and 3% in the turbulent flow regime. Figure B.5 also indicates that the heat flux did not significantly affect the friction factor uncertainties.

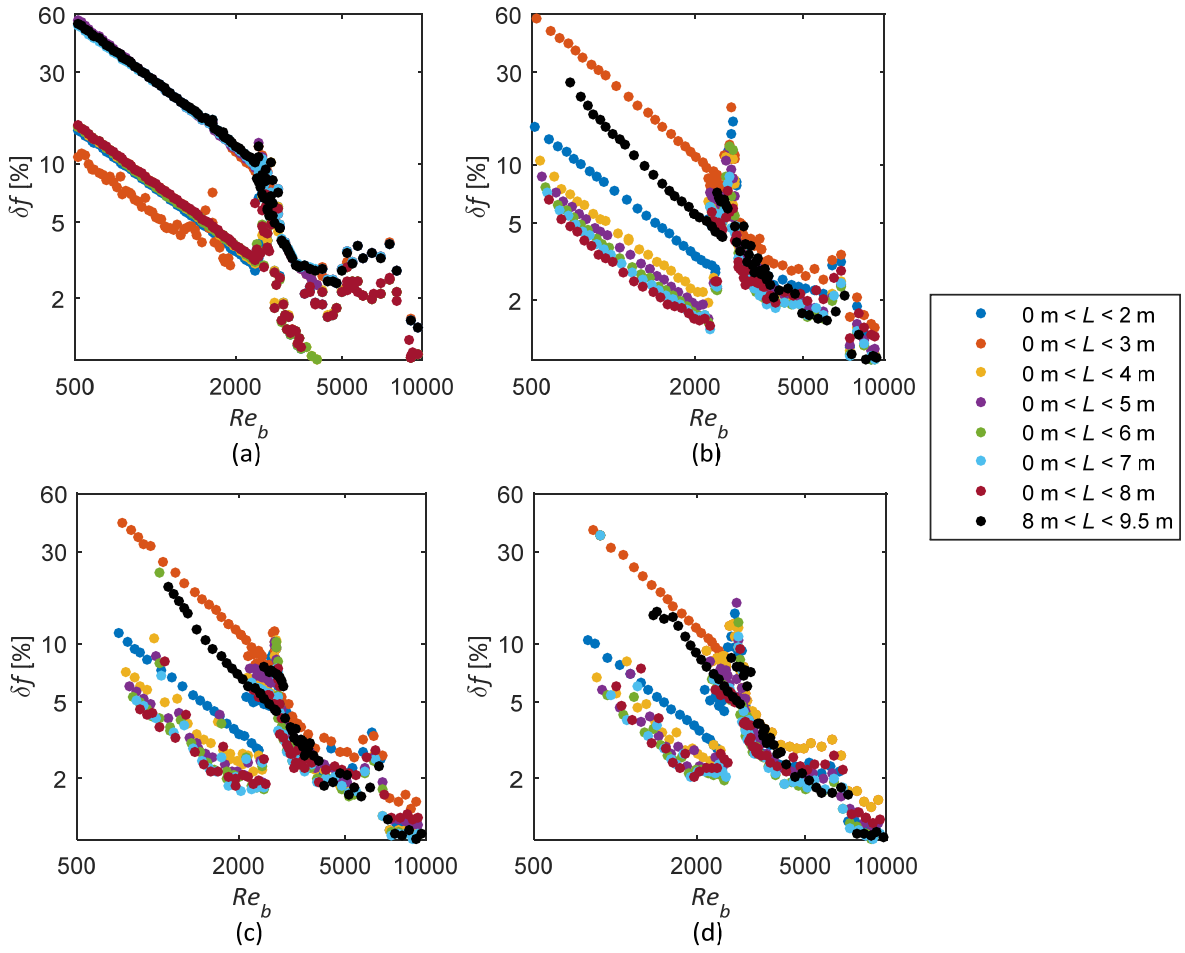

Fig. B.5: Friction factor uncertainties as a function of bulk Reynolds number across different tube lengths in the 11.5mm test section at heat fluxes of (a) 0 kW/m² (isothermal flow), (b) 1 kW/m², (c) 2 kW/m² and (d) 3 kW/m².

B.7. Conclusions

This appendix contained the uncertainty analysis method, accuracy of the instrumentation used, as well as the uncertainty analysis results. Linear regression analysis was used to determine the bias of the Pt100 probes, thermocouples and pressure transducers. For all the other instruments, the bias was considered as the accuracy of the instrument, which was specified by the manufacturer. The precision was obtained from the standard deviation of 200 measuring points, which was then multiplied by Student's *t*-variable to fall within the 95% confidence region.

The Reynolds number uncertainties were approximately 1.5% in the laminar and turbulent flow regimes, and increased to 2% in the transitional flow regime due to the mass flow rate fluctuations that occurred in this flow regime. A similar trend was found in the Graetz number uncertainties; however, the Graetz number uncertainties were higher because they are also a function of the Prandtl number, tube diameter and tube length uncertainties.

The laminar forced convection Nusselt number uncertainties were less than 10%, while the laminar mixed convection uncertainties were less than 5%, and decreased with increasing heat flux. The temperature fluctuations in the transitional flow regime caused the uncertainties to increase to approximately 10% (depending on the heat flux). The Nusselt number uncertainties in the quasi-turbulent and turbulent flow regimes increased with increasing Reynolds number and the average Nusselt number uncertainty at a Reynolds number of 6 000 was 13%. The Colburn *j*-factor uncertainties were similar, but slightly higher, than the Nusselt number uncertainties.

The Grashof number and Rayleigh number uncertainties were similar and increased with decreasing heat flux, increasing Reynolds number and decreasing tube diameter, due to the increased temperature uncertainties caused by the decreasing surface-fluid temperature differences. Because the modified Grashof number is a function of heat flux (which is a function of the temperature difference between the inlet and outlet of the test section and not the surface-fluid temperature difference), the change in modified Grashof number and modified Rayleigh number uncertainties with Reynolds number was less than for the Grashof numbers and Rayleigh numbers. However, the uncertainties still increased slightly with increasing Reynolds number. The Richardson number uncertainties were higher than the Grashof number uncertainties, and also decreased with increasing heat flux, decreasing Reynolds number, as well as increasing tube diameter. Furthermore, the Richardson number uncertainties decreased with increasing Reynolds number in the laminar flow regime due to the decreasing Reynolds number uncertainties.

The laminar friction factor uncertainties across the tube lengths 0 m < *L* < 2 m, 0 m < *L* < 3 m and 8 m < *L* < 9.5 m were higher than for the other tube lengths due to the limitations of the pressure transducer diaphragms. The laminar friction factor uncertainties for the other tube lengths were approximately 10% at the minimum Reynolds number and decreased to approximately 2% just before transition started. In the transitional flow regime, the uncertainties increased to approximately 20% due to the fluctuations inside the test section. In the quasi-turbulent and turbulent flow regimes, the friction factor uncertainties decreased with increasing Reynolds number, and the uncertainties varied between 1% and 3% in the turbulent flow regime.

B.9. References

[1] P.F. Dunn, *Measurement and Data Analysis for Engineering and Science*, 2nd ed., CRC Press, United States of America, 2010.

[2] C.O. Popiel, J. Wojtkowiak, Simple formulas for thermophysical properties of liquid water for heat transfer calculations [from O°C to 150°C], *Heat Transfer Eng*, Vol. 19(3), pp. 87-101, 1998.

[3] M. Everts, *Heat transfer and pressure drop of developing flow in smooth tubes in the transitional flow regime*, Master's dissertation, University of Pretoria, Pretoria, 2014

B.10. Nomenclature

A	Area	m^2
a	Best-fit intercept	
b	Bias/ best-fit slope	
C_p	Constant pressure specific heat	J/kg.K
D	Diameter	m
f	Friction factor	
g	Gravitational acceleration	m/s^2
Gr	Grashof number	
Gr^*	Modified Grashof number	
Gz	Graetz number	
h	Heat transfer coefficient	$W/m^2.°C$
j	Colburn *j*-factor	
k	Thermal conductivity	W/m.K
L	Length	m
M	Number of measuring points	
m	Slope of regression line	
$\dot{m}$	Mass flow rate	kg/s
N	Number of data points	
n	Total	
Nu	Nusselt number	
ΔP	Pressure drop	
Pr	Prandtl number	Pa
p	Precision	
$\dot{Q}_w$	Water heat transfer rate	W
$\dot{q}$	Heat flux	W/m^2
R	Result	
Ra	Rayleigh number	
Ra^*	Modified Rayleigh number	
Re	Reynolds number	
Ri	Richardson number	
Ri^*	Modified Richardson number	
S_{xx}	Sum of the squares of x	
S_{xy}	Sum of the squares of x and y	
S_{yx}	Standard error of best-fit	
T	Temperature	°C
t	Student's *t*-variable	
V	Velocity	m/s
x	*x*-axis variable	
y	*y*-axis variable	

B.10.1 Superscripts

-	Average

B.10.2 Subscripts

b	Bulk
c	Cross-section
ci	Calculated value
i	Index/inlet
m	Mean
o	Outlet
s	Surface

B.10.3 Greek letters

β	Thermal expansion coefficient	1/K
δ	Uncertainty	
μ	Dynamic viscosity	kg/m
ν	Kinematic viscosity	m^2/s
ρ	Density	kg/m^3